Annual Report 2013

Physik-Department

Lehrstuhl für Funktionelle Materialien
mit dem
Fachgebiet Physik Weicher Materie

Technische Universität München

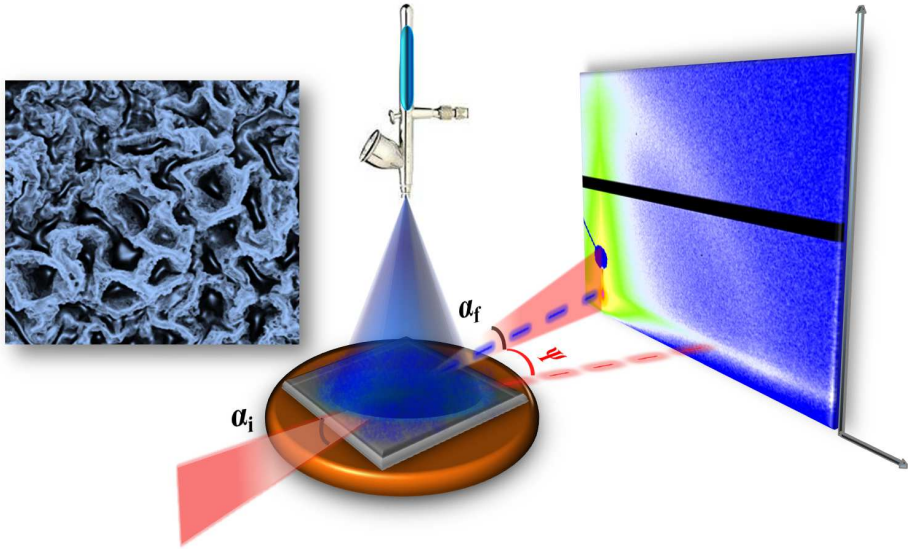

Prof. Dr. Winfried Petry
Chair of Functional Materials
Physik-Department

Deputy chairman for Prof. Dr. Winfried Petry:
Prof. Dr. Peter Müller-Buschbaum

Prof. Dr. Christine M. Papadakis
Soft Matter Physics Group

Physik-Department
Technische Universität München
James-Franck-Straße 1
85748 Garching

Secretaries: Marion Waletzki
Susanna Fink

Tel.: +49(0)89 289 12452
Fax: +49(0)89 289 12473

Email: peter.mueller-buschbaum@ph.tum.de
papadakis@ph.tum.de
marion.waletzki@ph.tum.de
susanna.fink@ph.tum.de
http://www.functmat.ph.tum.de
http://www.softmatter.ph.tum.de

Editor: Dr. Martine Philipp

Cover-page picture:

A schematic representation of the experimental setup for grazing-incidence small-angle x-ray scattering (GISAXS) measurements on an in-situ spray deposited ZnO nanostructured film.

1 Preface

It is a great pleasure to present in the name of the staff of the Chair of Functional Materials the annual report for the year 2013. It provides an overview of our teaching, research, and development activities. Our research activities are focused on functional materials and cover a broad range from soft matter physics to developments in methods and instrumentation. We examine the fundamental physics of material properties using mainly scattering methods (neutrons-, x-ray and light scattering). The general goal of our research is to explain the functional characteristics of soft condensed matter from the knowledge of the molecular dynamics and nanostructure.

In 2013, the chair activities covered the specific areas of water-based polymer systems, thin polymer films, polymer films for application in photovoltaics, polymer-hybrid systems, dynamics, and methodological and instrumental developments. The activities in the fields of polymer films for energy related application such as photovoltaic devices and energy storage have developed into a core part of the work. In the network of the Bavarian Collaborative Research Project 'Solar Technologies go Hybrid' (SolTec) at TUM, the keylab 'TUM.solar', headed by Prof. Müller-Buschbaum, is successfully operated in its second year. It bundles the research activities in the field of solar energy conversion and storage.

The in-house experiments available in the laboratories of the chair were supplemented by the lively activities at numerous large scale facilities, comprising synchrotron radiation and neutron scattering experiments. In particular in-situ and in-operando experiments were very successful in 2013. For example, a first in-situ investigation of an operating organic solar cell was pioneered by the Müller-Buschbaum group. The Papadakis group had very successfully extended the in-situ investigations of solvent vapor treatment of block copolymer films. The in-house SAXS/WAXS instrument was upgraded to improve the potential of GISAXS and GIWAXS measurements to bridge the gap between conventional in-house x-ray scattering experiments and work at third generation synchrotron sources.

In 2013, the Chair of Functional Materials comprised 9 fellows, 30 PhD students, 5 diploma students, 25 master students, 14 bachelor students, 8 student assistants and 9 administrative and technical staff members. 4 PhD theses were accomplished; moreover, 5 diploma and 9 master theses as well as 14 bachelor theses were finished. As all the years before, we had the pleasure to host several guests from abroad which stimulated a lively scientific atmosphere.

In general, all members of the chair were very active at conferences and workshops, participating with both talks and posters. Moreover, important conferences were organized by members of the chair. In particular, the international workshop 'GISAXS 2013' was organized by Prof. Müller-Buschbaum with colleagues from DESY. It brought together different communities working in the field of thin films, nanostructures, surfaces and interfaces, to gain insights to the very powerful method of grazing incidence small angle x-ray scattering and related techniques. The first workshop on Fluorescence Correlation Spectroscopy in Polymer Science was organized at TU München by Prof. Papadakis with Dr. Wöll from Universität Konstanz. The possibilities of this method — which only recently has been applied to polymeric systems — were discussed. In addition, two Edgar-Lüscher Seminars were again organized, this year on the subjects 'Physik von Zukunftsmaterialien' and 'Energiewandlung und Energiespeicherung'. The 3rd Colloquium of the Munich School of Engineering 'Research towards innovative energy systems and materials' took place in Garching. The chair participated in the biannual meeting with the colleagues from the Munich research reactor MLZ in Grainau. Everybody enjoyed the extensive discussions in combination with a fascinating landscape a lot!

Regarding teaching activities of the chair, we offered general physics lectures for teachers for vocational schools (Papadakis). Specialized lectures comprised 'Polymer physics' (Müller-Buschbaum) and 'Nanostructured soft materials' (Papadakis). Prof. Papadakis acted again as a women's representative of the Physics Department. In this context, she organized again the Day of the Female Physicist as well as the first one-day trial studies for female high school students. Moreover Prof. Müller-Buschbaum is heading the activities in the 'Network Renewable Energies (NRG)' in the Munich School of Engineering (MSE).
This annual report comprises a selection of the different research topics and projects carried out in the individual groups of the chair. It highlights the dedicated and successful research activities and collaborations with other groups and large scale facilities. We wish all chair members a fruitful continuation and a successful year 2014.

Peter Müller-Buschbaum and Christine Papadakis April 2014

Contents

2 Water based polymer systems

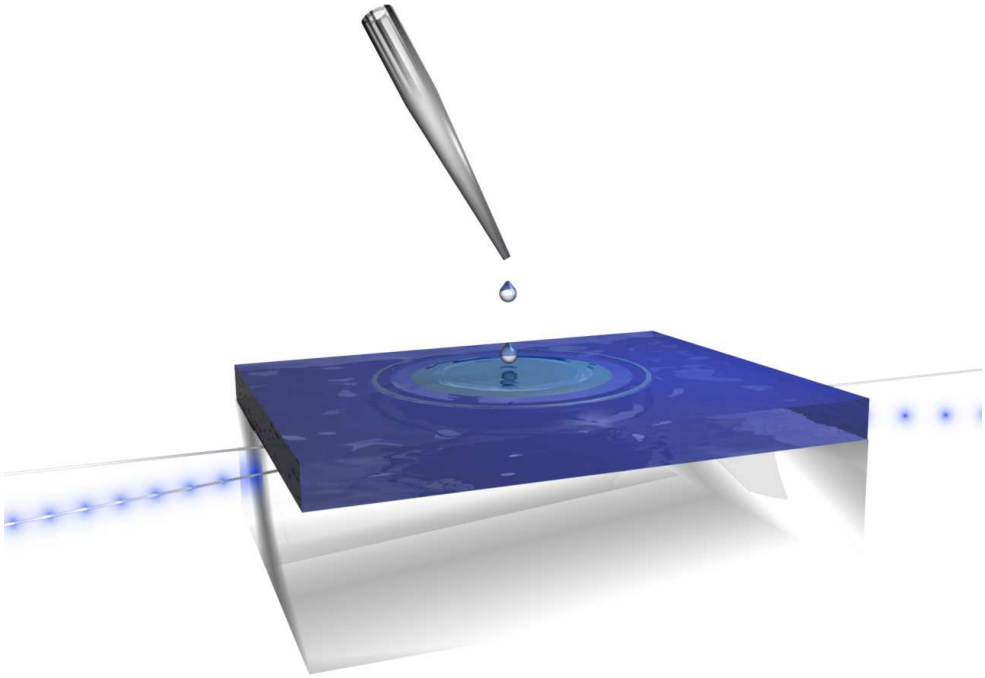

2.1 Investigation of a multiresponsive hydrogel based on poly-(methoxydiethylenglycol acrylate) (PMDEGA) with azobenzene moieties

D. Magerl, A. Miasnikova[1], A. Laschewsky[1,2], P. Müller-Buschbaum

[1] Institut für Chemie, Universität Potsdam, Potsdam, Germany
[2] Fraunhofer Institut für Angewandte Polymerforschung, Potsdam-Golm, Germany

Hydrogels are chemically or physically cross-linked polymers that build-up networks in which large amounts of water, i.e. more than the volume of the polymer, can be stored. Stimuli responsive hydrogels are polymers that respond to a small external stimulus (physical or chemical) with a strong change in its properties. An example of a thermoresponsive hydrogel, a hydrogel that responds strongly to temperature changes, is poly(methoxydiethylenglycol acrylate) (PMDEGA). It has a lower critical solution temperature (LCST) of about 40 °C, i.e. below this temperature the polymer dissolves well in water, forming hydrogen bonds with the surrounding water molecules, but when heated above the LCST it precipitates from water. Addition of hydrophpobic comonomers to the chain is reported to decrease the LCST [1]. In our study we investigate a statistical copolymer of MDEGA and its azo-dye-functionalized acrylate analogue, azoMDEGA. The latter has an azobenzene ring at a double bond that is responsive to light in a way that the double bond flips from a trans to a cis state when illuminated with UV-light. Upon this flipping the hydrophilicity of the monomer changes, which in turn should shift the LCST. The investigated polymer was polymerized by our coworkers from Potsdam and has an azoMDEGA content of 5.2 mol%. Silicon substrates were precleaned in an acidic bath and treated with oxygen plasma to improve hydrophilicity and thus inhibit dewetting of the thin films. Thin films of P(MDEGA-stat-azoMDEGA) were produced by spin coating from chloroform solution. The thickness of the dry films is 114 nm. Measurement of the absorption characteristics was done in transmission by UV-Vis spectroscopy. Therefore another sample was prepared on a glass substrate by solution casting. To illuminate the samples a light emitting diode with a maximum emission at a wavelength of 360 nm was used.

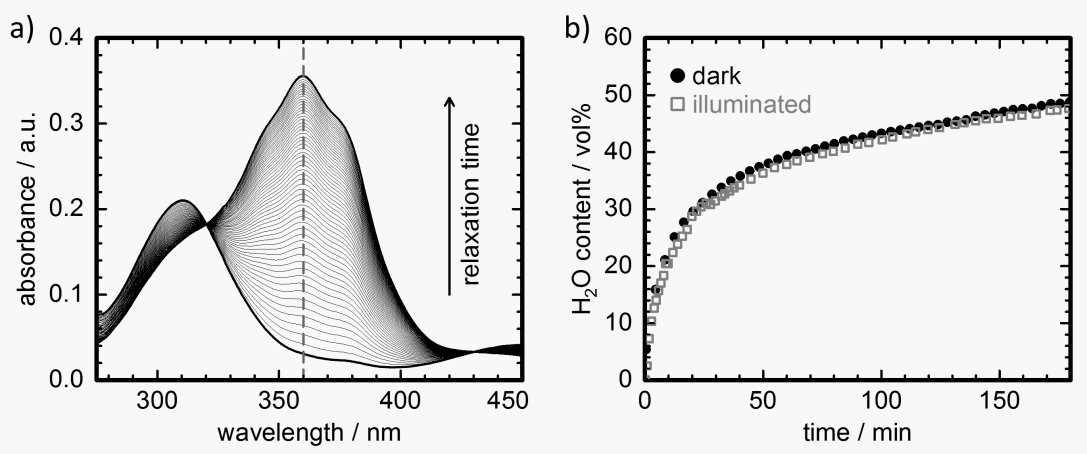

Figure 2.1:
a) UVVis spectra of the film before (top thick line) and after (bottom thick line) illumination with UV-light. The thin lines show the decay with time as indicated by the arrow. b) Increasing water content of two different thin films upon exposure with water vapor. Filled circles: Film kept in the dark; open squares: Film illuminated with UV-light.

Absorption characteristics of the film before and after illumination are shown in Fig. 2.1a. Before illumination the film shows strong absorption around 360 nm (upper bold curve) which corresponds to the energy required to switch the double bond to its excited state. After illumination

of the film with UV-light for 30 minutes the absorption is strongly decreased (lower bold curve) because most of the double bonds are in their excited state. Leaving the film in the dark relaxes the double bonds back to their ground state over time which is measured in steps of 15 minutes as indicated by the arrow. The individual absorption curves are shown by the thin curves and finally overlap perfectly with the absorption behavior measured before illumination.
After proofing the general ability to switch the double bonds the swelling behavior of two films was measured. One was kept in the dark so all the bonds should be in the trans state. The other was continuously illuminated with UV-light. Both films were exposed to high relative humidity and their changing thickness was monitored with white light interferometry over a period of 180 minutes. The temperature during the swelling was 13 °C which is well below the LCST. From the measured thickness the volume fraction of the water inside the film was calculated. The evolution of the water content with time is shown in Fig. 2.1b. The two films show no difference in their swelling behavior which suggests that the changes in the side groups do not influence the bonding of the water molecules to the chains while well below the LCST.

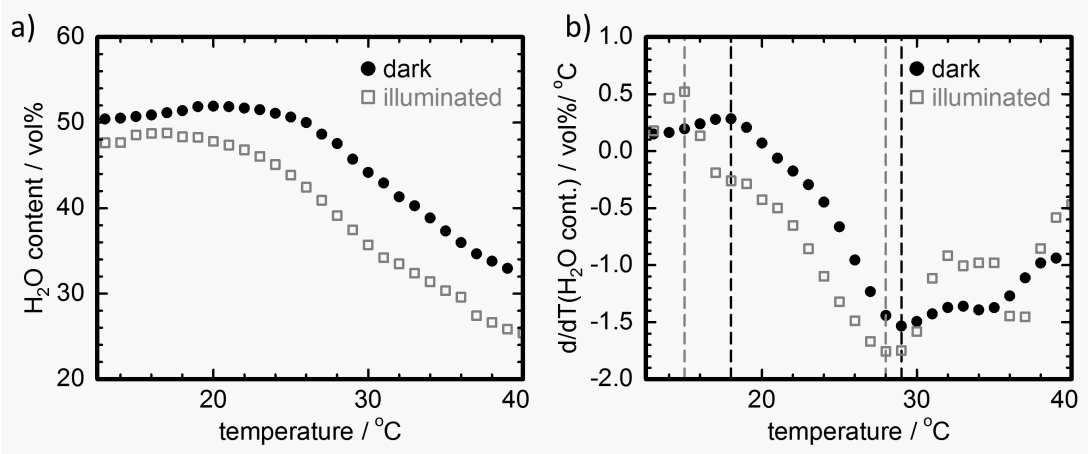

Figure 2.2:
a) Water content change with temperature of thin films exposed to water vapor. b) Derivative of data shown in a). In both graphs filled circles correspond to the film kept in the dark, open squares belong to the film illuminated with UV-light.

After this 3 hours of swelling at constant temperature the temperature is increased in steps of 1 °C. At each step the temperature is kept fixed for 10 minutes to let the system reach equilibrium. The temperature range covered crosses the LCST and therefore a reduction of the water content within the thin films upon heating can be observed, as seen in Fig. 2.2a. The two curves show a clear shift in the transition temperature and in order to quantify the temperature difference more accurately the derivative is calculated (see Fig. 2.2b). Two different points in the derivative can be evaluated: The onset of the transition (last point before the water content decreases), and the inflection point where the decrease is strongest. These two are marked with the striped lines on the left side and the center of the graph, respectively. The measurements show that a downshift of 1-3 °C of the transition temperature upon illumination with UV-light occurs. This agrees well with the findings in solution, which were accomplished by cloud point measurements [2]. We successfully show that the switching of the multiresponsive copolymer P(MDEGA-stat-azoMDEGA) by UV-light is possible in thin films. Furthermore it is shown that the switching changes the transition temperature of the thermoresponsive part.

[1] A. Laschewsky, E. D. Rekai, E. Wischerhoff, *Macromol. Chem. Phys.* **202**, 276-286 (2001)

[2] A. Miasnikova, C. A. Benítez-Montoya, A. Laschewsky, *Macromol. Chem. Phys.* **214**, 1504–1514 (2013)

2.2 Immense elastic nonlinearities existing at the volume phase transition of PNIPAM solutions

M. Philipp, U. Müller[1], R. Aleksandrova[1], R. Sanctuary[1], P. Müller-Buschbaum, J. K. Krüger[1]

[1] University of Luxembourg, Luxembourg, Luxembourg

Stimuli-responsive polymers undergo sharp demixing transitions when subjected to external stimuli, like changes of temperature, pH or ionic strength. They have great potential in various fields of application, like biomedicine and biotechnology (e.g. [1]). Amongst the stimuli-responsive polymers, poly(N-isopropylacrylamide) (PNIPAM) has attracted particular attention because of its sharp demixing transition in aqueous environment at about 32 °C. The PNIPAM molecules are subjected to a coil-to-globule transition when the aqueous PNIPAM solution is heated above its demixing transition temperature T_c. This molecular collapse is followed by aggregation of PNIPAM chains, leading to PNIPAM-rich aggregates with diameters of several 100 nm embedded in a water-rich phase [2].

Due to large volume changes occurring at the demixing transition of manifold PNIPAM systems, this transition is often denominated as a volume phase transition. As we could recently show, not only the mass density, but also the isothermal compressibility is closely related to the order parameters of this demixing transition [3]. In the present study, we demonstrate for the first time the importance of elastic nonlinearities arising in the vicinity of a liquid-liquid phase transition, studying phase separating PNIPAM solutions. The focus lies amongst others on the question in how far these elastic nonlinearities govern the phase separation of PNIPAM solutions.

Stress-strain experiments, which are commonly applied to access the elastic properties of solids, are not feasible for liquids and gels. In contrast, Brillouin spectroscopy allows probing thermally induced sound waves at GHz frequencies propagating within liquids. Due to the probed high frequencies, this technique permits interferences with viscoelastic properties to be overcome and determines high frequency clamped elastic properties. Our Brillouin spectroscopic investigations were complemented by measurements of mass density in order to be able to determine both the changes of linear and nonlinear elastic properties of phase separating dilute and semi-dilute aqueous PNIPAM solutions [3-5].

The Brillouin spectroscopic investigations were performed on a modified six-pass tandem Brillouin spectrometer of the Sandercock type in collaboration with the group of Prof. Krüger at the University of Luxembourg. The evolution of mass density versus temperature was determined by means of a DMA 5000 M densitometer from Anton Paar, Austria. The PNIPAM homopolymer (M_n = 20 - 25 kg/mol) was purchased from Sigma-Aldrich Chemie GmbH, Taufkirchen. Details of the experimental investigations, the evaluation of the Brillouin spectra and the interpretation of the data are given in [3-5]. The hypersonic velocity v_L determined from the Brillouin spectra permits calculating the longitudinal elastic modulus (linear elastic constant) according to $c_{11} = \rho v_L^2$, where ρ denotes the mass density. A third order elastic constant (nonlinear elastic constant), $c_{111} + 2c_{112}$, can also be calculated from the measured datasets, using the concept of mode Grüneisen parameters, which was originally introduced in solid state physics [4]. The linear and nonlinear elastic constants are represented versus temperature in Fig. 2.3a for a 6 mass% aqueous PNIPAM solution and pure water. In Fig. 2.3b are indicated the third order elastic constants for different semi-dilute PNIPAM solutions and pure water.

The main outcome of this study is as follows. We are able to directly observe for the first time immense nonlinear elastic constants across a liquid-liquid phase transition, using aqueous PNIPAM solutions. Note that third order elastic constants of about -1300 GPa are one order of magnitude stronger than those typically observed for other strain-softening systems. It clearly

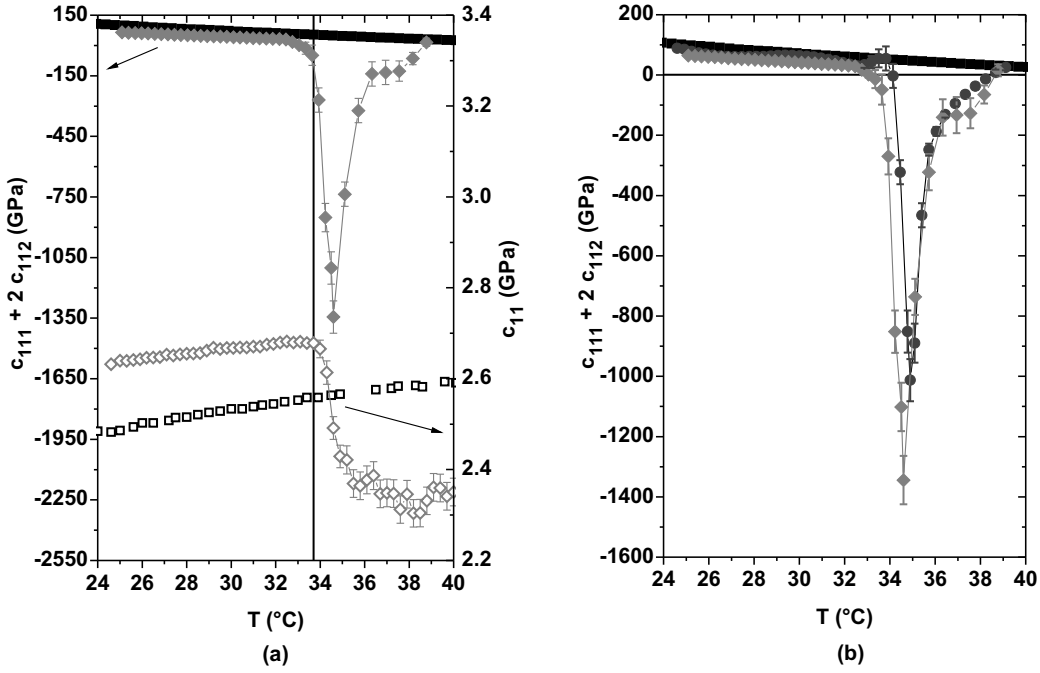

Figure 2.3:
a) Comparison of the temperature evolution of the linear elastic constant c_{11} and a nonlinear elastic constant $c_{111} + 2c_{112}$ across the demixing transition of a a 6 mass% aqueous PNIPAM solution (diamonds) and pure water (squares). b) Temperature evolution of the nonlinear elastic constants for pure water (squares), the 3 mass% (dots), the 6 mass% (diamonds) PNIPAM solutions.

follows from Fig. 2.3a that Hooke's law is far from being valid at such demixing transitions. The occurence of such a strong strain-softening allows for better understanding the crucial role of elastic nonlinearities in the vicinity of demixing transitions. It seems that the immense strain-softening strongly endorses the formation of phase separated PNIPAM solutions. First insights into the molecular reasons for the existence of this immense strain-softening are gained [4]. The study evidences the need for addressing fundamental questions related to the universal role played by elastic nonlinearities at phase transitions within soft materials.

M.P. thanks the Fonds National de la Recherche (Luxembourg) for the receipt of a Marie Curie cofunded AFR Postdoc grant.

[1] M. A. Cole, N. H. Voelcker, H. Thissen, H. J. Griesser, *Biomaterials* **30**, 1827-1850 (2009)

[2] A. Meier-Koll, V. Pipich, P. Busch, C. M. Papadakis, P. Müller-Buschbaum, *Langmuir* **28**, 8791-8798 (2012)

[3] M. Philipp, U. Müller, R. Aleksandrova, R. Sanctuary, P. Müller-Buschbaum, J. K. Krüger, *Soft Matter* **8**, 11387-11395 (2012)

[4] M. Philipp, U. Müller, R. Aleksandrova, R. Sanctuary, P. Müller-Buschbaum, J. K. Krüger, *Soft Matter* **9**, 5034-5041 (2013)

[5] M. Philipp, U. Müller, R. Aleksandrova, R. Sanctuary, P. Müller-Buschbaum, J. K. Krüger, *Soft Matter* **9**, 9887-9896 (2013)

2.3 Micellar solutions of symmetrical triblock copolymers poly(styrene-*b*-(methoxy diethylene glycol acrylate)-*b*-styrene) – a time-resolved SAXS investigation

J. Adelsberger, A. M. Bivigou-Koumba[1], A. Miasnikova[1], A. Golosova, S. S. Funari[2], A. Laschewsky[1], P. Müller-Buschbaum, C. M. Papadakis

[1] Institut für Chemie, Universität Potsdam, Germany

[2] DESY, Hamburg, Germany

Amphiphilic triblock copolymers with hydrophobic end blocks and a hydrophilic middle block form flower-like micelles in aqueous solution with the hydrophobic and the hydrophilic block forming the core and the shell, respectively. The hydrophilic blocks either fold back, and both hydrophobic blocks are located in the same core, or they bridge different cores, which, at sufficiently high polymer concentrations, results in the formation of a micellar gel. Special properties arise when the middle block is thermoresponsive, i.e. water-soluble and swollen below the cloud point (CP) and water-insoluble and collapsed above (lower critical solution temperature (LCST)-type behavior). We have previously synthesized and characterized a novel thermoresponsive polymer, namely poly(methoxy diethylene glycol acrylate) (PMDEGA) [1,2]. The transition at the CP is sharp and virtually without hysteresis, which has been attributed to the fact that PMDEGA can only act as H-bond acceptor, not as H-bond donor, which limits the possibilities to form intramolecular H-bonds. Moreover, the CP is sensitive to molar mass and can in this way be adjusted within a broad temperature range (20-40°C). By block copolymerizing PMDEGA with short PS end blocks, new triblock copolymers with a thermoresponsive middle block, namely poly(styrene-*b*-(methoxy diethylene glycol acrylate)-*b*-styrene) (P(S-*b*-MDEGA-*b*-S)), could be synthesized.Triblock copolymers with short PS blocks and significantly longer PMDEGA blocks are directly soluble in water. In contrast to the PMDEGA homopolymer, the triblock copolymers consistently showed hysteresis upon cooling. Here, we focus on P(S_{11}-*b*-$MDEGA_{96}$-*b*-S_{11}) triblock copolymer solutions of different concentrations. Temperature jumps from below the CP to above and back, i.e. from the one-phase state to the phase-separated state, were carried out, and time-resolved small-angle X-ray (SAXS) experiments allowed us to follow the structural changes.

The triblock copolymer P(S_{11}-*b*-$MDEGA_{96}$-*b*-S_{11}) (Fig. 2.4) was synthesized by two successive radical addition fragmentation chain transfer (RAFT) polymerization steps. It was dissolved in D_2O 2 days before the SAXS experiment at $c = 50$ mg ml^{-1} or 300 mg ml^{-1}, and the solutions were kept in the fridge. The CP is 36.6°C.

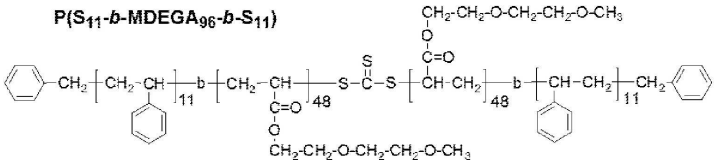

Figure 2.4:
Structure of PS-PMDEGA-PS.

SAXS measurements were carried out at beamline A2 at DESY. The X-ray wavelength was $\lambda = 0.15$ nm. A 2D MarCCD detector was mounted at a sample-detector distance of 1.04 m. The sample solution was installed in a custom-made sample holder between Kapton foil, and SAXS curves were measured for 5 min at 34°C. Then, the temperature was increased rapidly to 38°C, and SAXS measurements were carried out for 30 min. Afterwards, the temperature was rapidly decreased back to 34°C. The temperature changes took ca. 20 s with an overshoot of less than 0.6°C. The measuring times per SAXS image were always 30 s. The curves were azimuthally averaged, and the background from D_2O and the cell was subtracted. The scattered SAXS intensity, $I(q)$, was modeled using the following expression: $I(q) = P_{mic}(q)S_{HS}(q) + S_{OZ}(q) + I_{bkg}$ where $P_{mic}(q)$ is the form factor of spherical core-shell micelles with a polydisperse core, $S_{HS}(q)$

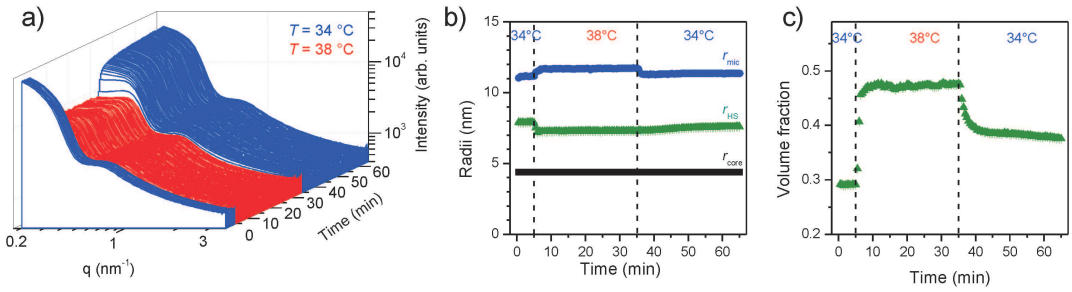

Figure 2.5:
a) SAXS curves of P(S_{11}-*b*-MDEGA$_{96}$-*b*-S_{11}) at 300 mg ml^{-1} in D_2O in dependence on time. b), c) Resulting core radius r_{core}, micellar radius r_{mic}, hard-sphere radius r_{HS} and volume fraction of correlated micelles, η.

the structure factor of hard spheres, S_{OZ} the Ornstein-Zernike term for thermal fluctuations, and I_{bkg} the incoherent background.
Figure 2.5a shows the SAXS curves in dependence on time: first at 34°C, then during rapid heating from 34°C to 38°C and finally during rapid cooling to 34°C. As soon as the temperature is increased, the curve shape changes significantly. The changes take ca. 2 min. In contrast, during cooling through the CP, the system needs ca. 15 min to switch back to the swollen state. Thus, the swelling is much slower than the collapse, probably because the large aggregates need to dissolve before the micellar shells can swell. This hysteresis is in accordance with previous observations using turbidimetry at very low polymer concentration (1 mg ml^{-1}).
Upon heating through the CP, r_{mic}, increases from 11.2 nm at 34°C to 11.7 nm at 38°C within 3 min and decreases back to 11.3 nm within 2 min when the sample is cooled back to 34°C. The hard-sphere radius, r_{HS}, decreases upon heating from 7.9 nm to 7.3 nm within 1 min. Interestingly, no change of r_{HS} is encountered upon cooling back, not even during the remaining 30 min. The volume fraction increases from 0.29 at 34°C to 0.47 at 38°C within 3.5 min. Upon cooling, the volume fraction η decreases again and reaches a value higher than the initial one, namely 0.38. This decrease proceeds slowly, it takes 7 min. Thus, a significant hysteresis is encountered.
The SAXS results presented give insight into the structure of the triblock copolymer solutions: Strong overlap between the micelles is encountered below the CP. The most prominent change during heating through the CP is the rapid and strong increase of the volume fraction of the micelles, i.e. their correlation increases drastically. In contrast, the micellar radius and the hard-sphere radius only change slightly. The hard-sphere radius decreases, as expected. Interestingly, the micellar radius increases slightly upon heating above the CP; possibly, this stretching of the shell blocks occurs during the release of water. The changes upon cooling are reversible but slower than upon heating, and the correlation between micelles becomes stronger than initially, which may explain the hysteresis observed previously. Larger aggregates could not be detected in any of the experiments, since the q-range is limited, and their scattering contribution would be expected at even lower q-values. Scattering methods can thus reveal the kinetics of the structural changes in this novel thermoresponsive system. Significant differences with the often studied PNIPAM system are obvious, such as the absence of the collapse of the micellar shell.
This work is funded by DFG within the priority program "Intelligente Hydrogele".

[1] A. Miasnikova, A. Laschewsky, G. De Paoli, C. M. Papadakis, P. Müller-Buschbaum, S. S. Funari, *Langmuir* **28**, 4479-4490 (2012)

[2] A. Miasnikova, A. Laschewsky, *J. Polym. Sci. A: Polym. Chem.* **50**, 3313-3323 (2012)

2.4 Collapse and aggregation of a micellar solution of symmetrical triblock copolymers poly(styrene-*b*-(methoxy diethylene glycol acrylate)-*b*-styrene)

J. Adelsberger, X. Shen, A. M. Bivigou-Koumba[1], A. Miasnikova[1], P. Busch[2], A. Laschewsky[1], P. Müller-Buschbaum, C. M. Papadakis

[1] Institut für Chemie, Universität Potsdam, Germany
[2] MLZ, Garching, Germany

Amphiphilic triblock copolymers with hydrophobic end blocks and a hydrophilic middle block form flower-like micelles in aqueous solution with the hydrophobic and the hydrophilic block forming the core and the shell, respectively. The hydrophilic blocks can either fold back or bridge different cores, which, at sufficiently high polymer concentrations, results in the formation of a micellar gel. Special properties arise when the middle block is thermoresponsive, i.e. water-soluble and swollen below the cloud point (CP) and water-insoluble and collapsed above (lower critical solution temperature (LCST)-type behavior). We have previously synthesized and characterized a novel thermoresponsive polymer, namely poly(methoxy diethylene glycol acrylate) (PMDEGA) [1,2]. The transition at the CP is sharp and virtually without hysteresis, which has been attributed to the fact that PMDEGA can only act as H-bond acceptor, not as H-bond donor, which limits the possibilities to form intramolecular H-bonds. By block copolymerizing PMDEGA with short PS end blocks, new triblock copolymers with a thermoresponsive middle block, namely poly(styrene-*b*-(methoxy diethylene glycol acrylate)-*b*-styrene) (P(S-*b*-MDEGA-*b*-S)), could be synthesized. Here, we present results from temperature-resolved SANS experiments around the CP on a P((S-d_8)$_{11}$-*b*-MDEGA$_{200}$-*b*-(S-d_8)$_{11}$) triblock copolymer solution in D_2O having a relatively high concentration.
P((S-d_8)$_{11}$-*b*-MDEGA$_{200}$-*b*-(S-d_8)$_{11}$) was synthesized by RAFT (Fig. 2.6). It was dissolved in D_2O 12 days before the SANS experiment at a concentration of 300 mg ml^{-1}and was kept in the fridge. Its CP is 36°C.

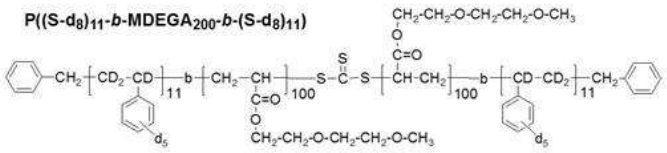

Figure 2.6:
Structure of P((S-d_8)$_{11}$-*b*-MDEGA$_{200}$-*b*-(S-d_8)$_{11}$)

SANS measurements were carried out at the instrument KWS-2 of JCNS at FRM II, Garching. The neutron wavelength was $\lambda = 0.7$ nm with a spread $\Delta\lambda/\lambda = 20\%$. Sample-detector distances of 2 m and 8 m were chosen. The sample was mounted in an oven. After each change of temperature, the waiting time before the measurement was 10 min. Measuring times were 5 or 10 min. The curves were azimuthally averaged and the background from D_2O and the cell were subtracted. The intensities were brought to absolute scale. The scattered SANS intensity, $I(q)$, was modeled using the following expression: $I(q) = P_{mic}(q)S_{HS}(q) + P_{Guinier}(q) + I_{bkg}$ where $P_{mic}(q)$ is the form factor of spherical core-shell micelles with a polydisperse core, $S_{HS}(q)$ the structure factor of hard spheres, $P_{Guinier}(q)$ the Guinier law used to model the forward scattering from large aggregates and I_{bkg} the background. The scattering length densities of the P(S-d_8) core and of D_2O were fixed during fitting. The resolution function was taken into account.
Figure 2.6a shows representative SANS curves. At temperatures up to 26°C, typical scattering from correlated micelles is observed. At temperatures between 37.5°C and 39°C, strong scattering appears at $q < 0.4$ nm^{-1}. Above 40°C, forward scattering appears at very small q-values (below 0.1 nm^{-1}). Thus, the structural changes at the CP are complex.

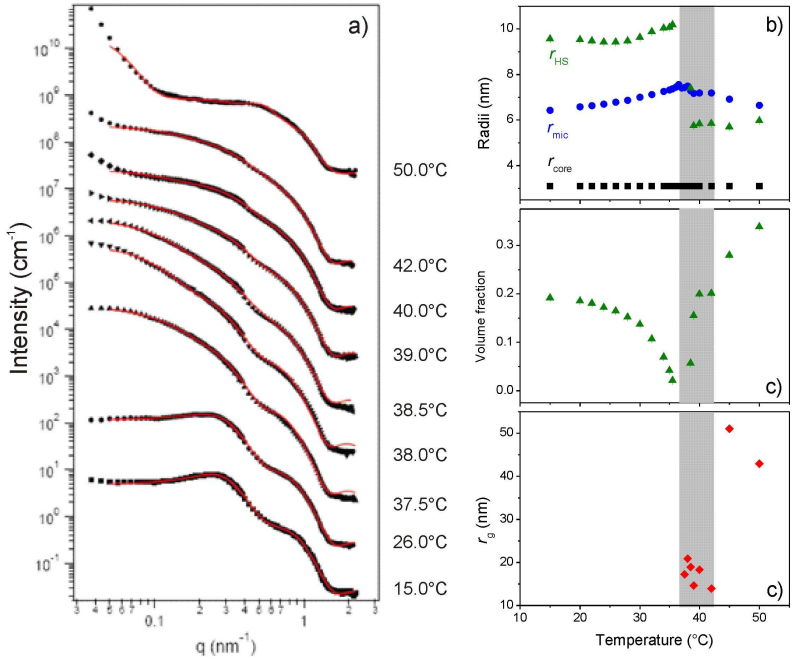

Figure 2.7:
a) Representative SANS curves of P((S-d_8)$_{11}$-*b*-MDEGA$_{200}$-*b*-(S-d_8)$_{11}$) at 300 mg ml^{-1} in D_2O in dependence on temperature. b)-d) Resulting core radius r_{core}, micellar radius r_{mic}, hard-sphere radius r_{HS}, volume fraction of correlated micelles and aggregate radius.

The fitting results are compiled in Fig. 2.7b-d. Best fits were obtained when the core radius was fixed at 3.1 nm. The micellar radius, r_{mic}, increases from 6.4 nm to 7.5 nm upon heating towards the CP (Fig. 2.7b), and decreases again above 36.5°C to 6.7 nm. The absence of a discontinuity at the CP is in line with our previous results on a similar triblock copolymer [1]. The hard-sphere radius, r_{HS}, is 9.5 nm at 15°C. It increases above 30°C to a value of 10.2 nm and then decreases within 3.5 K to 5.7 nm where it stays up to 50°C. The correlation between the micelles decreases as the CP is approached: The volume fraction, η, decreases from 0.19 at 15°C to 0.02 at 35.5°C (Fig. 2.7c). At temperatures between 36°C and 38°C, the structure factor is very weak, and η is close to zero. Only at 38.5°C, it takes again a positive value and increases steeply to 0.34 at 50°C. Thus, the correlation is lost, as the CP is approached from below. Above 37.5°C, aggregates form, which, up to 42°C, have a radius of gyration $r_g = 17.3 \pm 2.6$ nm (Fig. 2.7d). Only at higher temperatures, they are larger with $r_g = 43$-51 nm. The latter values are only approximate since the q-range is not sufficient to determine them precisely.
To summarize, the transition region of this triblock copolymer ranges from 37.5°C to 42.5°C and is thus rather broad. Below the CP, it forms core-shell micelles which are correlated in a liquid-like manner. The micellar radius changes only weakly at the CP, whereas the micellar distance decreases discontinuously at the CP. The correlation between micelles gets gradually lost as the CP is approached. This decrease may be at the origin of the gel-sol-transition observed in dynamic mechanical measurements [1]. At the CP, large aggregates are formed which grow with temperature. The core-shell structure of the micelles is preserved above the CP. Scattering methods can thus reveal the temperature-dependent structure in this novel thermoresponsive system. Significant differences with the often studied PNIPAM system are obvious, such as the absence of the collapse of the micellar shell.
This work is funded by DFG within the priority program "Intelligente Hydrogele".

[1] A. Miasnikova, A. Laschewsky, G. De Paoli, C. M. Papadakis, P. Müller-Buschbaum, S. S. Funari, *Langmuir* **28**, 4479-4490 (2012)

[2] A. Miasnikova, A. Laschewsky, *J. Polym. Sci. A: Polym. Chem.* **50**, 3313-3323 (2012)

2.5 Kinetics of aggregation in thermoresponsive triblock copolymers – influence of concentration, start and target temperature

J. Adelsberger, I. Grillo[1], A. M. Bivigou Koumba[2], A. Laschewsky[2], P. Müller-Buschbaum, C. M. Papadakis

[1] Institut Laue-Langevin, Grenoble, France
[2] Institut für Chemie, Universität Potsdam, Potsdam, Germany

Thermoresponsive polymers have received increasing attention because they respond with a strong change of conformation and solubility to a small variation of temperature across their cloud point, i.e. they show lower critical solution temperature (LCST) behavior. A widely used LCST polymer is poly(N-isopropyl acrylamide) (PNIPAM) which has a cloud point of ≈ 32°C. The kinetics of the transition, such as the switching time and the reversibility, is of importance for many applications. We have investigated triblock copolymers consisting of a long hydrophilic PNIPAM middleblock and two short hydrophobic polystyrene (PS) endblocks. In aqueous solution, they form flower-like core-shell micelles or, above the critical gel concentration, micellar hydrogels. When heated above the LCST, the PNIPAM block becomes hydrophobic and releases water from the micellar shell, which consequently collapses. The collapsed micelles form large aggregates. These changes are reversible [1]. We have investigated the aggregation behavior in dependence on polymer concentration and on the start and target temperatures [2]. This way, we obtain information on the role of intermicellar bridging and on the role of the temperatures for the reversibility of the switching.

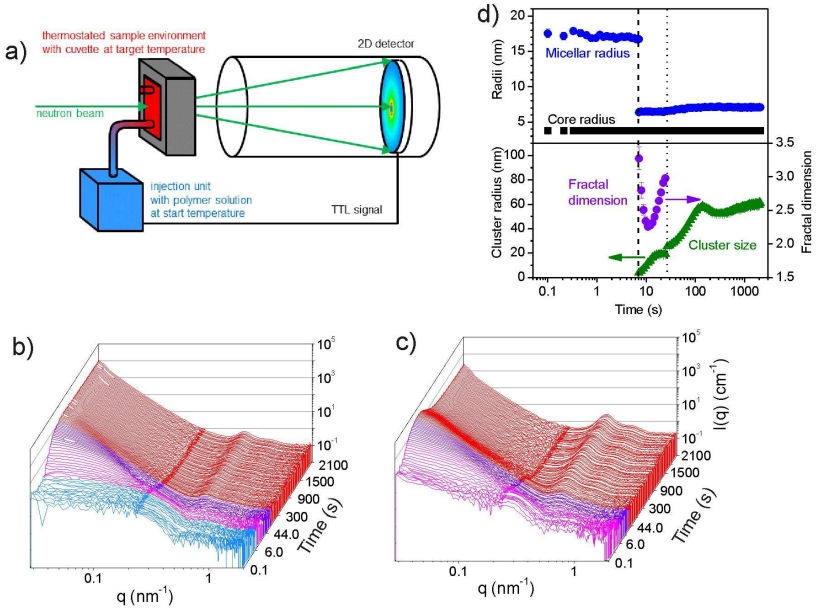

Figure 2.8:
a) Scheme of the setup of the experiment. SANS curves b) at 20 mg/ml during a jump from 29.6°C to 34.6°C and c) at 200 mg/ml during a jump from 20.0°C to 42.8°C. d) Micellar and cluster radius as well as size and fractal dimension of the clusters for the jump in b).

Time-resolved small-angle neutron scattering (SANS) experiments allowed us to investigate the kinetics of the collapse of the micellar shell and the cluster formation with an excellent time

resolution (0.1 s) and gave information on a wide range of length scales. For that purpose, a stopped-flow apparatus was used at beamline D22 at ILL (Fig. 2.8a). The triblock copolymer solutions (P(S-d_8)$_{11}$-*b*-NIPAM$_{220}$-*b*-S-d_8)$_{11}$ at 20, 50 or 200 mg/ml in D_2O) were kept in a reservoir at a temperature below the cloud point (20.0°C or 29.6°C. The target temperatures were chosen at 34.6°C or 42.8°C. To realize a fast temperature jump, the solution was injected into the preheated sample cell, and the time-resolved measurement was started. The curves were fitted using a model for spherical core-shell micelles together with different form and structure factors for their clusters [3,4].
The SANS curves during two jumps are shown in Fig. 2.8b-c. Four time regimes are distinguished by the appearance of forward scattering, its shape and the presence of a correlation peak. For high concentrations and high target temperatures, the first time regime below the cloud point is not resolved (Fig. 2.8c).

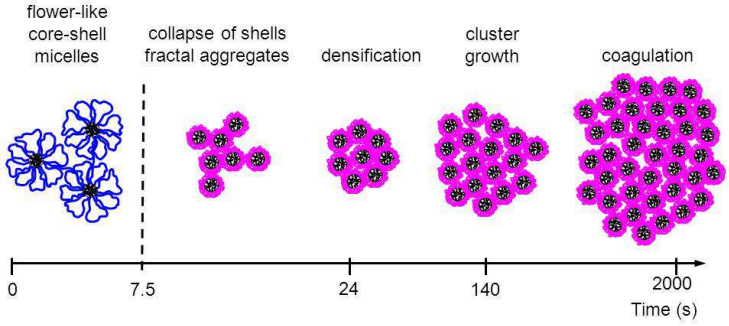

Figure 2.9:
Scheme of cluster formation and growth for the four different regimes.

The most important results are compiled in Fig. 2.8d. In all cases, the micellar radius decreases very rapidly and relaxes to slightly higher values during the later stages after crossing the cloud point. Right after the cloud point is passed, the collapsed micelles form small imperfect clusters with voids; thus, their correlation is of fractal type. Only later, the clusters are dense enough to be described by a liquid-like structure. They grow first by attachment of additional micelles from solution; this process depends on the polymer concentration and thus the degree of intermicellar bridging. Eventually, the clusters grow by coagulation. Their final surface structure depends on the target temperature: For 34.6°C, a concentration gradient is present in the beginning which transforms into a rough cluster surface. For 42.8°C, the behavior is opposite.
Thermoresponsive triblock copolymer solutions thus show a complex collapse and aggregation behavior (Fig. 2.9). We suggest that, in applications, where fast switching back is needed, prolonged heating above the cloud point should be avoided because then large aggregates form which presumbably dissolve only slowly. Moreover, we find that the behavior in the triblock copolymers is much more complex than the one in PNIPAM homopolymers.
This work was funded by the DFG within the project SPP1259 'Intelligent Hydrogels'.

[1] A. Jain, A. Kulkarni, A. M. Bivigou Koumba, W. Wang, P. Busch, A. Laschewsky, P. Müller-Buschbaum, C. M. Papadakis, *Macromol. Symp.* **291-292**, 221 (2010).

[2] J. Adelsberger, A. Kulkarni, A. Jain, W. Wang, A. M. Bivigou-Koumba, P. Busch, V. Pipich, O. Holderer, T. Hellweg, A. Laschewsky, P. Müller-Buschbaum, C. M. Papadakis, *Macromolecules* **43**, 2490 (2010)

[3] J. Adelsberger, E. Metwalli, A. Diethert, I. Grillo, A. M. Bivigou-Koumba, A. Laschewsky, P. Müller-Buschbaum, C. M. Papadakis, *Macromol. Rapid Commun.* **33**, 254 (2012)

[4] J. Adelsberger, I. Grillo, A. Kulkarni, M. Sharp, A. M. Bivigou-Koumba, A. Laschewsky, P. Müller-Buschbaum, C. M. Papadakis, *Soft Matter* **9**, 1685 (2013)

2.6 The collapse and aggregation of thermoresponsive poly(2-oxazoline) gradient copolymers: A time-resolved SANS study

S. Jaksch, A. Schulz[1], K. Kyriakos, J. Zhang, I. Grillo[2], R. Jordan[1], C. M. Papadakis

[1] Professur für Makromolekulare Chemie, Department Chemie, TU Dresden

[2] Institut Laue-Langevin, Grenoble, France

Thermoresponsive polymers in aqueous solution respond reversibly to small temperature stimuli by strong changes in their solubility and chain conformation, i.e. they show lower critical solution temperature (LCST) behavior. Thus, they have received increased attention as smart materials, e.g. for biomedical applications. Theoretical predictions for the collapse transition at the cloud point have been made for equilibrium conditions and have put forward the cooperativity of hydrogen bonding to the polymer as an important parameter for the nature of the transition. Time-resolved small-angle neutron scattering (TR-SANS) may provide detailed structural information. Poly(2-oxazoline)s (POx, Fig. 2.10) are well suited for biomedical applications because of their excellent biocompatibility, but also because thermoresponsive poly(alkyl-2-oxazoline)s with ethyl, *iso*- or *n*-propyl side groups show a very sharp collapse transition in aqueous solution and nearly no hysteresis.

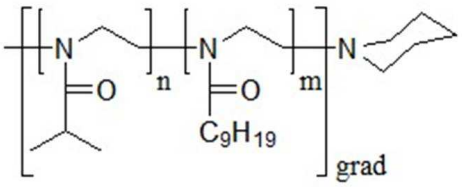

Figure 2.10: Structure of P[*i*PrOx$_n$NOx$_m$]$_{grad}$ copolymers.

We present here investigations of aqueous solutions of poly[(2-*iso*-propyl-2-oxazoline)$_{48}$-(2-*n*-nonyl-2-oxazoline)$_2$]$_{grad}$ (P[*i*PrOx$_{48}$NOx$_2$]$_{grad}$). In our recent SANS study [1], we found that immediately above the cloud point, small aggregates (formed already below the cloud point) are predominant, and only at higher temperatures, large aggregates are present in significant number. The question arises, whether the small aggregates are stable with time, or whether large aggregates will appear at the expense of the small ones. To address this question, we have carried out TR-SANS investigations during temperature jumps across the cloud point. The target temperatures were chosen to be either in the intermediate regime, i.e. just above the cloud point, or in the high-temperature regime. This way, we were able to follow the changes in chain conformation as well as the aggregate formation as a function of time.

SANS experiments were performed at instrument D22 at ILL in Grenoble. Rapid temperature changes were enabled by a modified Biologic SFM-300 [2]. The sample solution was equilibrated at the start temperature in the reservoir while the cuvette in the neutron beam was preheated to the target temperature in a custom-made sample holder. The sample was injected into the cuvette, and data acquisition was started simultaneously. The accumulation time was 3-30 s. Each temperature jump was repeated at least twice, and the resulting SANS curves were averaged. The neutron wavelength was $\lambda = 8.0$ Å and the sample-detector distances (SDD) 4.0 m and 14.0 m. The resulting 2D images were azimuthally averaged, corrected for background scattering as well as the detector sensitivity and brought to absolute units. The curves were modeled by a form factor of small fractals [3], giving the size of the single chain, ξ, and its fractal dimension, D, which is related to the Flory exponent ν, i.e. the chain conformation, by $\nu = 3/(D + 2)$. Forward scattering was modeled using a Porod law.

Figure 2.11a and b shows the SANS curves taken during the temperature jumps into the intermediate and the high-temperature regime. Initially, the slope of the forward scattering increases; afterwards, it stays constant. The cloud point at 24.5 °C is reached immediately after injection,

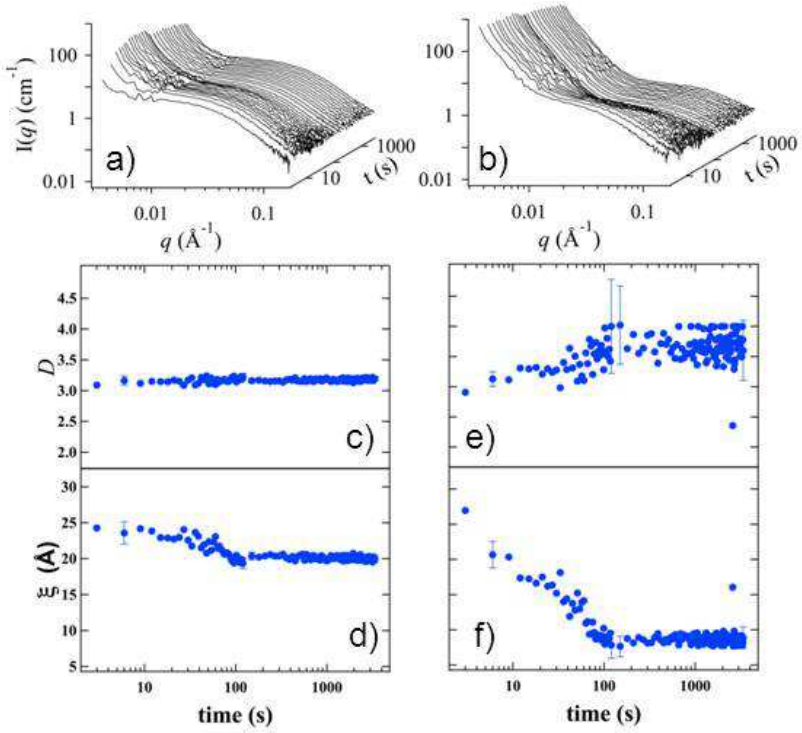

Figure 2.11:
TR-SANS curves of P[iPrOx$_{48}$NOx$_2$]$_{grad}$ in D_2O taken during the temperature jumps. Start temperature 23.0 °C. Target temperature a) 27.0 °C and b) 30.0 °C. Corresponding fitting parameters: c), d) fractal dimension, D and e), f) fractal size, ξ.

and the temperature becomes stable at the target value after ca 100 s. The results of the fits are shown in Fig. 2.11c-f. For the jump into the intermediate regime, the fractal dimension, D, is constant at 3.1-3.2, which corresponds to a Flory exponent $\nu = 0.58$-0.59, i.e. the solvent is good. The size ξ is initially 24.2 ± 1.5 Å, i.e. a relatively high value. Thus, P[iPrOx$_{48}$NOx$_2$]$_{grad}$ forms small aggregates already below the cloud point because of intermolecular bridging by the hydrophobic n-nonyl groups of the NOx monomers. ξ decreases to 19.3 ± 0.7 Å during the first 126 s, which reflects the collapse of these small aggregates. For the temperature jump into the high-temperature regime, the decay at $q > 0.02$ Å^{-1} changes shape during the first 100 s. Afterwards, no more changes are observed. The fractal dimension D is constant at 3.1 ± 0.1 during the first 30 s, then it increases and reaches 3.5 ± 0.7 110 s after the injection, i.e. ν decreases from 0.59 ± 0.01 to 0.54 ± 0.07. The initially good solvent thus becomes slightly worse, but not yet a theta solvent. ξ decreases from 23 ± 2 Å to 8 ± 2 Å 110 s after the injection, i.e. the small aggregates collapse. This means that the final solvent quality is worse and the collapse is stronger than for the jump into the intermediate regime, as expected.
The present results confirm that the gradient copolymers form small aggregates already below the CP. Moreover, the intermediate regime found in our previous work is stable.
This project is supported by DFG (Pa771/6-2).

[1] S. Salzinger, S. Huber, S. Jaksch, P. Busch, R. Jordan, C. M. Papadakis, *Colloid Polym. Sci.* **290**, 385 (2012)

[2] J. Adelsberger, E. Metwalli, A. Diethert, I. Grillo, A. M. Bivigou-Koumba, A. Laschewsky, P. Müller-Buschbaum, C. M. Papadakis, *Macromol. Rapid Commun.* **33**, 254 (2012)

[3] J. Teixeira, *J.* Appl. Crystallogr. **21**, 781 (1988)

2.7 Cononsolvency in PNIPAM aqueous solutions - A time resolved SANS study

K. Kyriakos, M. Philipp, J. Adelsberger, S. Jaksch, I. Grillo[1], A. Miasnikova[2], A. Laschewsky[2], P. Müller-Buschbaum, C. M. Papadakis

[1] ILL, Grenoble, France

[2] Universität Potsdam, Potsdam-Golm, Germany

Poly(N-isopropyl acrylamide) (PNIPAM) shows thermoresponsive behavior, which makes it a very promising material for a wide range of applications, ranging from drug delivery to microfluidic valves [1,2]. More recently, the behavior of PNIPAM in mixed solvents of water (H_2O) and alcohols (e.g. methanol MeOH) has attracted strong interest. Separately they act as good solvents for PNIPAM, but interestingly their mixtures act as a poor one. This phenomenon, termed cononsolvency, manifests itself in a strong decrease of the lower critical solution temperature (LCST) upon the addition of e.g. MeOH to aqueous solutions of PNIPAM. Various theories have been put forward to explain the true origin of this behavior but no decisive conclusion has been reached.

We report here on a time-resolved small angle neutron scattering (SANS) experiment on aqueous solutions of PNIPAM homopolymers and micelle forming P(S-b-NIPAM) diblock copolymers (PS stands for polystyrene) upon the addition of MeOH. The focus here is on the influence of different methanol volume ratios on the aggregation process of the collapsed, hydrophobic chains or micelles for PNIPAM and P(S-b-NIPAM) respectively. To this end, three different volume ratios of d-MeOH were added to aqueous (in D_2O) polymer solutions of an initial polymer concentration of 20 mg/ml; namely 10 %, 15 % and 20 % v/v of d-MeOH were added by using a stopped-flow set-up (Biologic SFM 300). To elucidate the kinetics of the phase separation and the subsequent aggregation, time-resolved SANS experiments were perfomed at the high flux instrument D22 in ILL, Grenoble. Two sample to detector distances of 4.0 m and 14.4 m were selected, that together with a wavelength of λ = 8 Å resulted in a q range from 0.003 to 0.15 Å^{-1}.

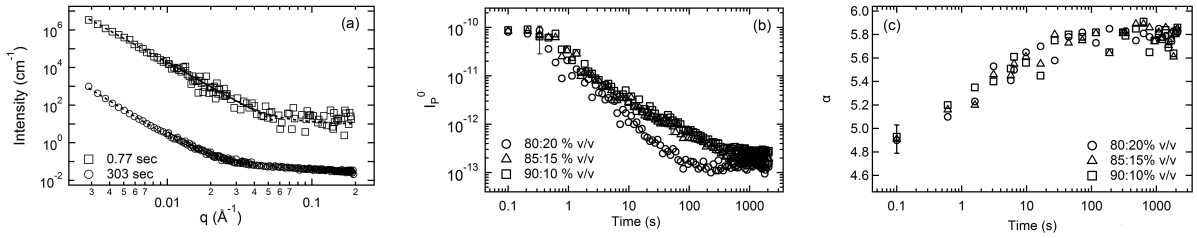

Figure 2.12: a) Representative SANS curves of PNIPAM homopolymer for mixing ratio D_2O:d-MeOH of 80:20 v/v % for selected time frames. The lines are fitting curves to the open symbols. For clarity the curves were shifted vertically by a factor of 10^3 (0.77 sec). b) Porod intensity I_P^0 and c) Porod exponent α for all mixing ratios are presented as a function of time.

In Fig. 2.12a representative SANS curves of PNIPAM homopolymer for a mixing ratio 80:20 v/v of D_2O:d-MeOH are shown. The strong forward scattering indicates large aggregates of collapsed PNIPAM chains. Moreover, in the high q-region, an additional small contribution is observed, due to scattering arising from density fluctuations inside the aggregates. To account for these contributions, a combination of a Porod term and an Ornstein-Zernicke term was used. The Porod intensity (I_{Porod}) (Fig. 2.12b) decreases with time reflecting the decrease of the specific surface of the aggregates or in other words the increase of their size. Interestingly, the comparison between the different mixing ratios shows a dependence of the followed aggregation path on the methanol content; the more methanol is present, the earlier the increase of the aggregates size starts and the larger the final size. The Porod exponent (α) has an initial value

of 4.8 and increases to 5.8 until 100 s after mixing. These values are larger than the expected for spheres with smooth surface (e.g. $\alpha = 4$), which may be assigned to a gradient of the SLD along the surface normal of the aggregates. The increase of α means that the interfaces become sharper.
Figure 2.13a shows representative SANS curves of P(S-*b*-NIPAM) for a mixing ratio 80:20 v/v of D_2O:*d*-MeOH. The first curves decay smoothly. After ca. 15 s, a minimum appears at $q \approx 0.015$ Å^{-1} and moves to lower q values with time. For the first curves a generalized Guinier-Porod model and for the later stages a model describing spheres with a Gaussian size distribution was used. In Fig. 2.13b the aggregate radius is presented as a function of time. The initial value of R = 150 Å is much bigger than the size of a single collapsed micelle, thus we postulate that aggregates exist right from the beginning. Interestingly, we observe that for the first 1 s, the aggregate radius remains almost constant before it starts to increase. After a fast growth process that lasts approx. 25 s, for all three systems we observe a transition to a kinetically frozen regime, where the radius increases much more slowly than in the beginning. In aggreement with the observations for the homopolymer, the final aggregate radius increases with the volume fraction of the methanol, reaching final values between 440 and 490 Å.

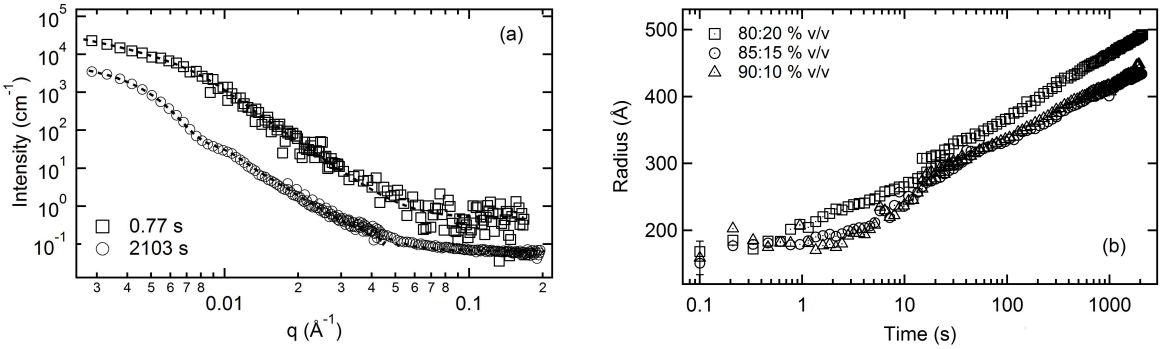

Figure 2.13: (a) Representative SANS curves of P(S-*b*-NIPAM) for mixing ratio D_2O:*d*-MeOH of 80:20 v/v for selected time frames. The lines are fitting curves to the open symbols. For clarity the curve at 0.77 s was shifted vertically by a factor of 100. (b) Aggregate radii as a function of time for all three mixing ratios.

To summarize, we studied the phase separation induced by the addition of MeOH to aqueous solutions of PNIPAM and P(S-*b*-NIPAM). In both cases the aggregation path depends on the methanol volume fraction; the more methanol is present the earlier the aggregation starts and the larger is the final aggregate radius. In particular, for the diblock copolymer we observe an unusual aggregation process that deviates from the known models describing the aggregation of colloidal systems (i.e. RCLA, DCLA) and at the later stages enters a kinetically frozen regime where the radius increases at a very slow rate.

The project is supported by DFG within the priority program SPP1259 "Intelligente Hydrogele" (Pa771/4).

[1] S. Cammas, K. Suzuki, S. Cone, Y. Sakurai, K. Kataoka, T. Okano, *J. Controlled Release* **48**, 157 (1997)

[2] A. Nykänen, N. Nuopponen, A. Laukkanen, S. P. Hirvonen, M. Rytelä, O. Turunen, H. Tenhu, R. Mezzenga, O. Ikkala, J. Ruokolainen *Macromolecules* **40**, 5827 (2007)

2.8 Temperature-resolved mesoscopic structures of the novel thermoresponsive diblock copolymer P((S-d_8)$_{11}$-*b*-MDEGA$_{571}$)

L. Augsbach, K. Kyriakos, A. Miasnikova[1], A. Laschewsky[1], Z. Di[2], P. Müller-Buschbaum, C. M. Papadakis

[1] Institut für Chemie, Universität Potsdam, Germany
[2] MLZ, Garching, Germany

Thermoresponsive polymers are stimuli-responsive polymers that undergo an abrupt physical change in response to a small variation of temperature. Such transitions are often fast and reversible which make such polymers interesting, among others, for biomedical applications.
Poly(methoxydiethylenglycol acrylate) (PMDEGA) is a novel thermoresponsive polymer that shows lower critical solution temperature (LCST) behavior in aqueous solution and has transition temperatures in the range of 37 °C to 45 °C [1]. Along with the collapse of PMDEGA above the cloud point T_C, the collapsed polymers form large aggregates at higher temperatures. To many applications, core-shell micellar structures are of interest. They can be created by using block copolymers of polystyrene (PS) and a PMDEGA block. The diblock P(S-*b*-MDEGA) forms star-like micelles.
To investigate the micellar structures around the cloud point, we use small-angle neutron scattering (SANS). We report here on SANS experiments on P((S-d_8)$_{11}$-*b*-MDEGA$_{571}$) in D_2O with a concentration of 100 mg/ml at temperatures between 25 °C and 48 °C, i.e. around the cloud point at 38.5 °C. We measured at three sample-detector distances (1.36 m, 4.00 m, 20.00 m) at the KWS-2 instrument in MLZ. A wavelength of 4.5 Å was used. Figure 2.14a shows representative intensity curves. At 25 °C a pronounced peak between 0.01 Å^{-1} and 0.02 Å^{-1} is observed, which is due to the interaction between micelles. With increasing temperature, this peak becomes weaker and the forward scattering increases.

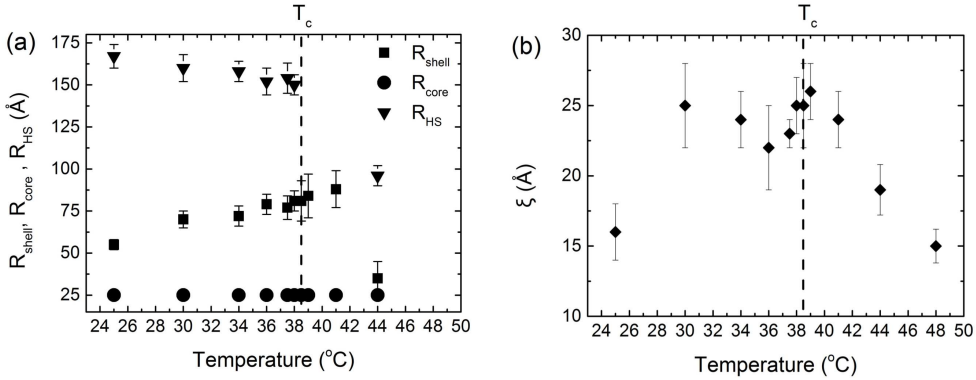

Figure 2.14:
a) Representative SANS curves of P((S-d_8)$_{11}$-*b*-MDEGA$_{571}$) in D_2O at 100 mg/ml. b) SANS curve at T = 44 °C and contributions to the fitting model.

To elucidate the structural changes accompanying the phase transition, we fit the curves with models including the form factor of the micelles and a structure factor charactering their correlations.

$$I(q) = P_{mic}(q) \cdot S_{HS}(q) + I_{Porod}(q) + I_{OZ}(q) + I_{bkg}$$

P_{mic}(q) is the form factor of spherical core-shell micelles, S_{HS}(q) the hard-sphere structure factor, I_{Porod}(q) the Porod model describing the forward scattering due to large clusters and I_{OZ}(q)

is the Ornstein-Zernike structure factor describing the semidilute PMDEGA solution in the micellar shells. A representative model fit is given in Fig. 2.14b for a temperature of $44\,^{\circ}\mathrm{C}$ which is well above the CP. Good agreement is obtained.
The important information about the structure of the micelles obtained from the models, are the micellar radius, and the correlation between the micelles. As expected for semidilute systems, the hard-sphere radius is bigger than the micellar radius. As appears from Fig. 2.15a the core radius was kept constant. The shell radius increases below the CP and for the intermediate region and drops abruptly only at higher temperatures. Despite the fact that R_{mic} does not change significantly, aggregates are formed. The correlation length ξ of the PMDEGA blocks within the shell is constant below and decreases above the CP, as expected due to the tightly packed micelles in the clusters (Fig. 2.15b). The phase transition induces a significant change on the structure of the micelles and, more interestingly, this transition happens over a broad temperature range and through intermediate stages This is in agreement with our previous results on similar PMDEGA systems [2].

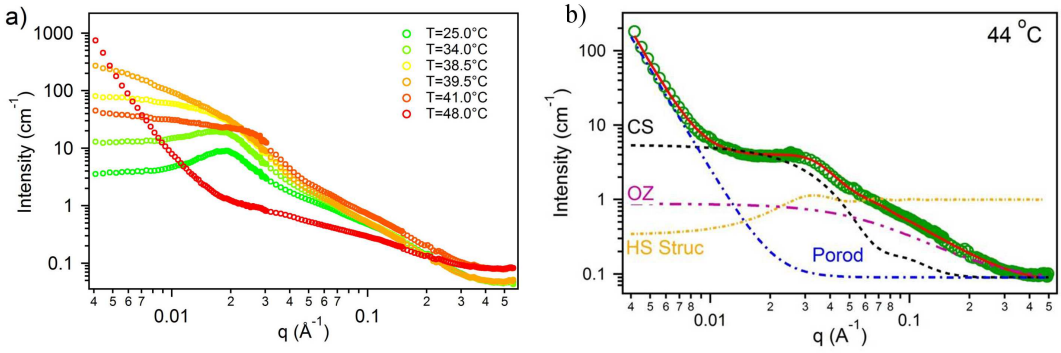

Figure 2.15:
a) Core and shell radius for different temperatures. b) Correlation length for different temperatures.

To summarize, we studied a P((S-d_8)$_{11}$-*b*-MDEGA$_{571}$) diblock copolymer in D_2O with a concentration of 100 mg/ml at various temperatures around the T_C. By using different models for the temperatures below, above and for the intermediate regions, we were able to get information about the mesoscopic structures and temperature induced structural changes.
This project is funded by DFG (Pa771/4-3).

[1] A. Miasnikova, A. Laschewsky, *J. Polym. Sci., Part A: Polym. Chem.* **50**, 3313 (2012)

[2] A. Miasnikova, A. Laschewsky, G. De Paoli, C. M. Papadakis, P. Müller-Buschbaum, S. S. Funari, *Langmuir* **28**, 4479 (2012)

2.9 Polymeric nanoparticles for drug delivery

N. Vishnevetskaya, M. Dyakonova, A. Bogomolova[1], S. K. Filippov[1], C. M. Papadakis

[1] Institute of Macromolecular Chemistry, Prague, Czech Republic

Polymer-drug conjugates based on the copolymer N-(2-hydroxypropyl) methacrylamide (HPMA) bearing the anticancer drug doxorubicin and a defined amount of hydrophobic moieties (cholesterol and its derivatives) are therapeutically highly potent, because they have the appropriate size, good solubility in bio-acceptable solutions and biocompatibility [1]. In aqeous solution, these amphiphilic conjugates form micelles are formed by self-assembly. The hydrophobic cholesterol-derived moieties, differing in chemical structure, and the drug are bound by a pH-sensitive hydrazone bond. This hydrazone bond is relatively stable at neutral pH (blood pH), but breaks under mild acidic conditions, such as in the acidic intracellular environment (endosomes in tumor cells) and releases both the drug (doxorubicin) and cholesterol (which then is eliminated from the body). Figure 2.16 shows a schematic of the expected self-assembly and release process.

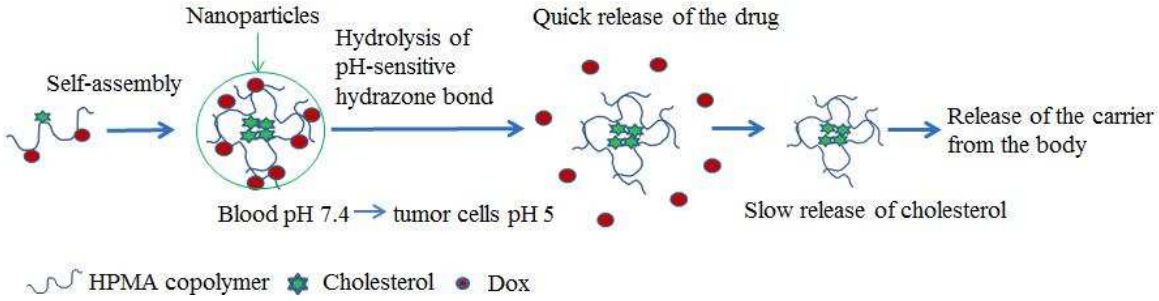

Figure 2.16:
Schematic of the self-assembly process of pH-sensitive HPMA copolymer Dox conjugates in aqueous solution as well as their biodegradation at low pH by hydrolysis.

The micelle formation of various copolymers in phosphate buffer solution and their size was investigated using fluorescence correlation spectroscopy (FCS) by adding the fluorescence dye rhodamine 6G as a probe. We have compared the values of the hydrodynamic radii of the micelles and the critical micelle concentrations (CMC) in very dilute solutions (as in blood) of the copolymers as well as the kinetics during time and pH changes. Representative results are presented in Fig. 2.17, showing copolymers I and III, with 5-cholestanone and Lev-Cholesterol derivatives, respectively. From previous studies, it is known that these show a growth of the particles at pH 5, which are thus more effectively accumulated in solid tumors due to the enhanced permeation and retention (EPR) effect [1]. We find that above the CMC, both HPMA copolymers form micelles, due to the hydrophobic interactions between the cholesterol-containing moieties. The value of the CMC depends on the content of the hydrophobic groups and is found at ca. 0.05 mg/mL for both copolymers, because they have nearly the same content of cholesterol moieties (Fig. 2.17a). An increase of polymer concentration leads to a step-like increase of the hydrodynamic particle radius, indicating formation of the aggregates above a certain threshold in concentration. In the solution of more hydrophilic copolymer I an additional aggregation of the micelles over time is observed (Fig. 2.17b). The copolymers show fast kinetics during change of pH from neutral to mildly acidic, namely the growth of the particle size at pH 5 with subsequent disintegration of the micelles (Fig. 2.17c). The more hydrophobic copolymer III with Lev-Cholesterol derivative shows a more stable hydrodynamic particle radius.

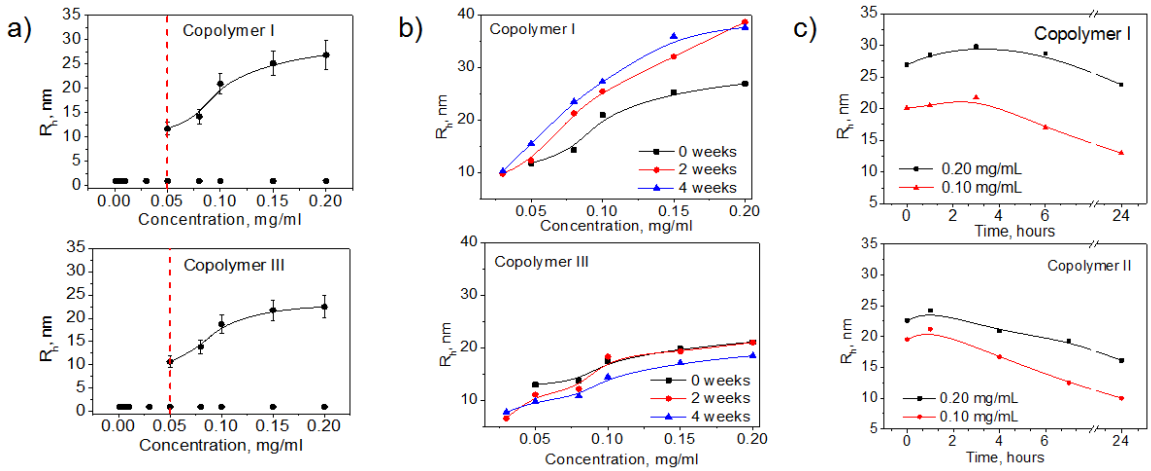

Figure 2.17:
Concentration dependence of the hydrodynamic radii, the vertical dashed line indicate the CMC (a), the kinetics during time, namely 4 weeks, (b) and during pH change from 7.4 to 5.0 (c) at room temperature.

Time-resolved small-angle neutron scattering (SANS) measurements during a temperature jump experiment show that the structures of the copolymers are temperature independent and provide detailed information on the micellar core-shell structures. The conjugate-I-Dox, which is slightly more hydrophobic, shows stable behavior. The structure of the micelles (ellipsoids connected by polymer chains [2]) is unchanged with time (Fig. 2.18a). In contrast, the conjugate-III-Dox consists of homogeneous spheres with different radii. Most probably, the cholesterol-HPMA linkage is hydrolysable at neutral pH and the structure converts to a system consisting of cholesterol crystals with time (Fig. 2.18b), thus the system is.

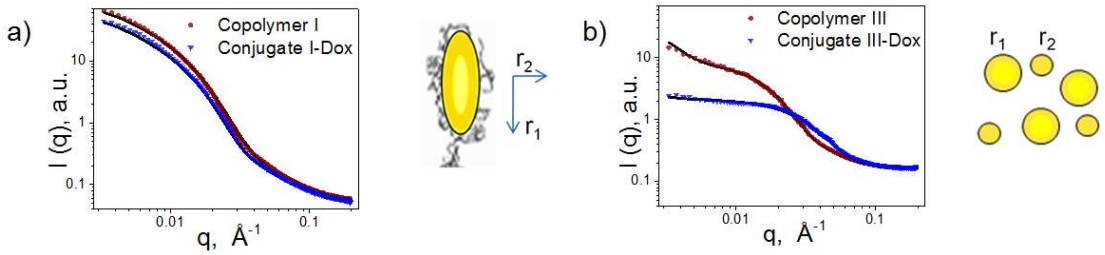

Figure 2.18:
Scattered intensity I(q) as a function of the scattering vector q for conjugates I (a) and III (b), with 5-cholestanone and Lev-cholesterol derivatives respectively, at room temperature and their schematic structures.

Thus, the obtained results are in good agreement with the previous investigations [2] and prove that the structures of the pH-sensitive cholesterol-HPMA linkage and of cholesterol itself have an influence on the nanoparticle formation and behavior in solution.

The project was carried out in terms of two year European Master program in Materials Science, MaMaSELF.

[1] P. Chytil, T. Etrych, L. Kostka, K. Ulbrich, *Macromol. Chem. Phys.* **213**, 858-867 (2012)

[2] S. K. Filippov , P. Chytil, P. V. Konarev, M. Dyakonova, C. M. Papadakis, A. Zhigunov, J. Plestil, P. Stepanek, T. Etrych, K. Ulbrich, D. I. Svergun, *Biomacromolecules* **13**, 2594-2604 (2012)

2.10 Stimuli-responsive reversible hydrogels from triblock polyelectrolytes and polyampholytes

M. Dyakonova, M. T. Popescu[1], A. Heine, K. Kyriakos, M. Philipp, I. Grillo[2] S. Jaksch[3], C. Tsitsilianis[1], C. M. Papadakis

[1] University of Patras, Department of Chemical Engineering, Greece
[2] Institut Laue-Langevin, Grenoble, France
[3] MLZ, Garching, Germany

Injectable hydrogels may be created from triblock copolymers featuring oppositely charged blocks, such as poly(acrylic acid) (PAA) and poly(2-vinylpyridine) (P2VP) or quaternized P2VP (P2VPQ). We have investigated the structures of P(AA_{163}-$2VPQ_{1397}$-AA_{163}) using SANS and SAXS. The behavior of the polyampholyte P(AA_{163}-$2VPQ_{1397}$-AA_{163}) depends on the pH-dependent behavior of the end blocks: pH variation leads to a change of charge density of both blocks and hence determines the charge asymmetry [1].

SANS experiments were carried out at instrument D22 at the Institut Laue-Langevin (ILL) in Grenoble, France, using the wavelength of 0.8 nm and sample-detector distances (SDD) of 3.98 m and 13.98 m. SAXS experiments were performed using the Ganesha 300 XL SAXS instrument with λ = 0.154 nm and SDD = 0.40 m. All measurements were carried out at 26°C.
SANS curves of the quaternized polyampholyte system containing 4 wt% of polymer at pH 7.0, 5.0 and 3.0 are presented in Fig. 2.19. All curves have different shape. The electrostatically driven coil-globule transition of the polyampholyte thus depends strongly on the charge asymmetry. Low charge asymmetry at pH 7.0 causes the collapse of the chain into a globule consisting of a core composed of hydrophobic domains of complexed negatively charged groups of the PAA end blocks and the positively charged groups of the long P2VPQ middle block. At pH 7.0, modeling with polydisperse spheres was successfully applied. The resulting sphere radius R was determined at 37.1 $\pm$ 1.9 nm with a polydispersity of 0.27 $\pm$ 0.01. Moreover, inside the core a loose network is formed by the P2VPQ chains complexed with PAA, having a correlation length, ξ = 2.6 $\pm$ 0.6 nm. Thus, relatively, large and unconnected spheres are formed, which explains that the solutions are viscous liquids.
Decreasing the pH of the solution to 5.0, the net charge imbalance increases due to the smaller fraction of negatively charged PAA units (Fig. 2.19a, triangles). The curve was modeled using the form factor of spherical core-shell particles and a structure factor of small fractal aggregates. The core radius is found at R_c = 3.4 $\pm$ 1.1 nm with a micellar radius, R_m of 8.2 $\pm$ 0.8 nm. These small core-shell micelles form fractal aggregates having a radius of 17.8 $\pm$ 1.3 nm and a fractal dimension d_f of 2.8 $\pm$ 0.2.

At pH 3.0, the polyampholyte forms a steady gel which was attributed to the known fact that most PAA units turn hydrophobic when crossing the pK_a point and act as additional frozen crosslinks which increase the stiffness of the gel [1]. Oppositely charged units in the triblock copolymer associate and form micelles. At higher concentration, the middle blocks are able to bridge the micelles, leading to a transient network of interconnected particles. At pH 3.0, the Percus-Yevick structure factor for hard-sphere interaction was included together with the form factor for spherical core-shell micelles and an Ornstein-Zernicke term for scattering from polymer network. From the form factor, a mean core radius of R_c = 2.7 $\pm$ 0.9 nm and a shell thickness of 12.2 $\pm$ 1.6 nm is obtained, whereas the structure factor results in a hard-sphere radius R_{HS} = 30.8 $\pm$ 2.1 nm and a volume fraction η = 0.21 $\pm$ 0.08. Scattering at $q > 0.4$ nm^{-1} was attributed to the fluctuations of the network of interconnected P2VPQ chains, and was modeled by an Ornstein-Zernicke function, resulting in a correlation length ξ = 1.3 $\pm$ 0.5 nm. The sample thus forms a three-dimensional micellar gel where the PAA micelles are partially bridged by the P2VPQ middle blocks.

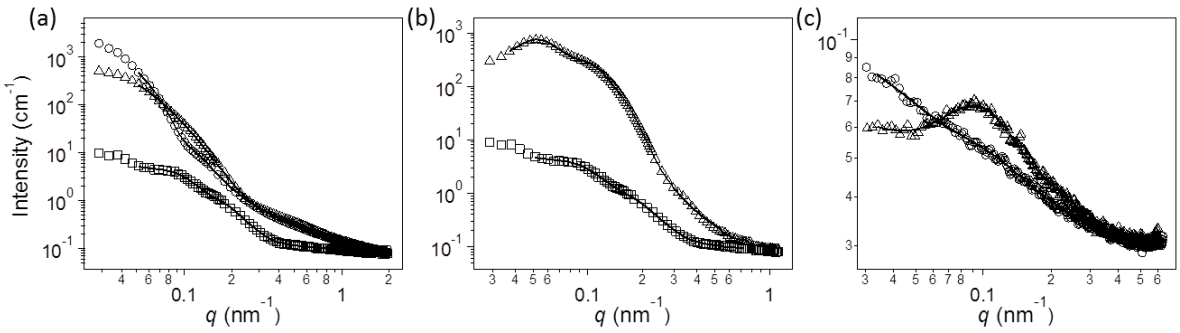

Figure 2.19:
SANS curves I(q) as a function of the momentum transfer q (a) for quaternized polyampholyte solutions at concentration 4 wt% at 26°C at pH 7.0 (circles), pH 5.0 (triangles) and pH 3.0 (squares), measured at D22, ILL, Grenoble. (b) of hydrogels from 4 wt% of P*t*BA-P2VP-P*t*BA (triangles) or PAA-P2VPQ-PAA (squares). (c) SAXS curves of the hydrogels with 4 wt% at 26°C at pH 3.0 of P*t*BA-P2VP-P*t*BA (triangles) or P*t*BA-P2VP-P*t*BA in a 0.15M NaCl solution (circles). The solid lines represent fits.

The conformational properties of hydrogels from triblock polyelectrolytes poly(*tert*-butyl acrylate-*b*-2-vinyl pyridine-*b*-*tert*-butyl acrylate) (P(tBA$_{163}$-2VP$_{1397}$-tBA$_{163}$)) with hydrophobic P*t*BA end blocks, were investigated with SANS and compared with the ones from polyampholyte hydrogels. These systems have interesting mechanical properties previously studied with rheology [1]. In dependence on the nature of the end blocks, two systems feature different aggregation mechanisms, which in turn, results in different rheological properties [1]. The analysis of the SANS curves from P(tBA$_{163}$-2VP$_{1397}$-tBA$_{163}$) solutions at pH 3.0 confirmed the existence of network formation (Fig. 2.19b, triangles). The gel formed by the polyelectrolyte is much stiffer than the polyampholyte gel, which was explained by different association mechanism depending on the nature of the end blocks [1]. The hydrophobic P*t*BA end blocks agglomerate and form spherical particles with a core size of 14.6 $\pm$ 1.3 nm, which are screened against unfavourable contacts with water by the P2VP shell. The hard-sphere radius is 55.5 $\pm$ 1.9 nm, thus much higher than in P(AA$_{163}$-2VPQ$_{1397}$-AA$_{163}$). This difference in micellar distance is attributed to the partial neutralization of protonated P2VP(CH$_3$)$^+$ groups with PAA units in P(AA$_{163}$-2VPQ$_{1397}$-AA$_{163}$), which leads to less extended middle blocks.

By SAXS, the influence of the ionic strength of the solution on the structure of the hydrogel from polyelectrolyte P(tBA$_{165}$-2VP$_{828}$-tBA$_{165}$) was studied (Fig. 2.19c). As in the previous case, the polyelectrolyte network consists of core-shell structures, where the hydrophobic P*t*BA chains form the core and hydrophilic P2VP chains from a micellar shell. Addition of NaCl causes the formation of less stretched conformations of P2VP, thus, the micelles tend to approach each other. While the core size does not change dramatically (3.7 $\pm$ 0.6 nm), the shell thickness and the hard-sphere radius are significantly decreased (0.65 $\pm$ 0.05 nm and 1.67 $\pm$ 0.08 nm compared to the salt-free solution). This is a result of a weakened P2VP chain stretching after influencing the ionization strength. Small-angle scattering thus allows detailed structural characterization of these complex, nanostructured networks.
This project was supported by DAAD in the framework of the IKYDA program.

[1] N. Stavrouli, T. Aubry, C. Tsitsilianis, *Polymer* **49**, 1249 (2008)

2.11 Core-shell bottle brush copolymers with poly(propylene oxide)-*b*-poly(ethylene oxide) side chains

C. Psylla, K. Kyriakos, J. Zhao[1], S. Pispas[1], C. M. Papadakis

[1] Theoretical and Physical Chemistry Institute, National Hellenic Research Foundation, Athens, Greece

Block copolymers based on poly(propylene oxide) (PPO) and poly(ethylene oxide) (PEO) copolymers have been found to form micellar core-shell structures which make them very good candidates for a wide range of applications. Recently, novel molecular architectures where P(PO-*b*-EO) chains are grafted on a poly(*b*–hydroxystyrene) (PHOS) backbone have been synthesized and studied with respect to their thermal behavior [1]. Both, the length and composition of the side chains were varied. By inverting the sequence of the monomer addition, two different molecular structures were achieved, with either PPO or PEO linked to the backbone. The high grafting density along the backbone results in strong interactions between the side chains, particularly close to the backbone, resulting in chain extension of the polymer backbone. However, the phase behavior of the bottlebrush copolymers, like side chain conformation and crystallization are poorly understood. We report here on small- and wide-angle x-ray scattering experiments (SAXS and WAXS) on systems of various architectures and molecular compositions. The focus is on the effect of the molecular architecture and the composition on the crystallization and the microphase separation. Samples with different volume fraction and sequence of PEO and PPO segments in the side chains are termed as gPE and gEP depending on whether the PO or EO blocks are closer to the backbone. More specifically, the polymers under our current study are gPE, which contains 59 wt% PPO and the PO segments are close to the backbone, and gEP, which contains 15 wt% PPO and the EO segments are close to the backbone respectively. We used the SAXS instrument Ganesha 300XL with a wavelength λ = 1.54 Å and the sample-detector-distances (SDD) of 101 and 401 mm. The samples were mounted in holders between mica sheets, were heated to $80\,^{\circ}\mathrm{C}$ with 5 minutes equilibration time and then cooled to $-80\,^{\circ}\mathrm{C}$ with a cooling rate of $80\,^{\circ}\mathrm{C}/\mathrm{min}$. Then, they were heated in steps of $5\,^{\circ}\mathrm{C}$ with equilibration times of 5 minutes after each step. The measuring times were 10 minutes at the SDD of 101 mm and betweeen 10 and 30 minutes at the SDD of 401 mm.

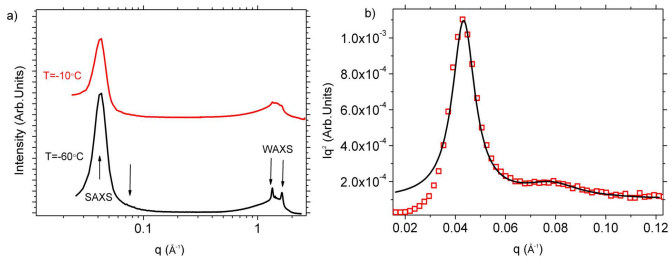

Figure 2.20:
a) Representative SAXS and WAXS curves for the sample gPE at $-60\,^{\circ}\mathrm{C}$ and $-10\,^{\circ}\mathrm{C}$. b) Representative fit of a Lorentzian function to the experimental data in the SAXS regime at $-35\,^{\circ}\mathrm{C}$.

Both samples showed Bragg reflections in the WAXS range as well as peaks due to the microphase seperation in the SAXS range. Figure 2.20a shows representative SAXS curves of gPE for two temperatures, below and above T_m, which lies at $-10\,^{\circ}\mathrm{C}$ and has been determined seperately by DSC measurements at low temperatures. The PEO blocks crystallize, as evident from the two Bragg reflections, at 1.34 $\mathrm{Å}^{-1}$ and 1.62 $\mathrm{Å}^{-1}$, which vanish above T_m. At q_1^*= 0.0424 $\mathrm{Å}^{-1}$

and q_2^*= 0.0792 Å^{-1}, peaks due to the microphase seperation are present at temperatures up to $10\,^{\circ}$C. Above, only the first peak persists.
Information about the morphology is obtained by fitting Lorentzian functions to experimental peaks in the SAXS regime (Fig. 2.20b). The peak positions, q_1^* and q_2^* , as well as the peak widths were used to determine the morphology, the repeat distance and the domain size, using the Scherrer equation. For gPE, the repeat distance is found at $D = 165$ Å up to $-10\,^{\circ}$C and continuously decreases above (Fig. 2.21a). The morphology of the sample is hexagonal: $q_2^*/q_1^* = 1.78 - 1.84$, which is similar to $\sqrt{3}$.

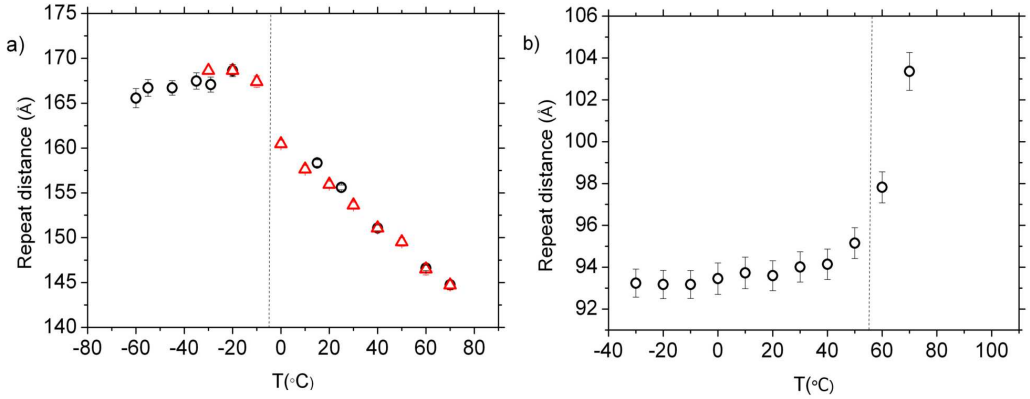

Figure 2.21:
Repeat distance versus temperature for sample gPE from a) two seperate measurements and b) for sample gEP.

The same procedure and analysis were followed for sample gEP. The PEO segments crystallize giving rise to two scattering peaks due to the Bragg reflections at q_1^*= 1.34 Å^{-1} and q_2^*= 1.62 Å^{-1}, as before. In the SAXS range, the sample gEP exhibits lamellar structure ($q_2^*/q_1^* = 2$) with a repeat distance $D = 94$ Å, which continuously increases above $50\,^{\circ}$C (Fig. 2.21b). Moreover, the peak at q_2^* is present at temperatures up to $90\,^{\circ}$C, i.e the lamellar structure persists.
To summarize, we studied the mesostructure and the crystalline structure in bulk samples of graft copolymers with densely grafted side chains, i.e bottle brush copolymers. Significant effects of the chain architecture, i.e the sequence of PEO and PPO in the side chains and the volume fraction of PPO are observed on both the crystalline structure of the PEO block and the mesostructure.

[1] J. Zhao, G. Mountrichas, G. Zhang, S. Pispas, *Macromolecules.* **43**, 1771 (2010)

2.12 Novel thermoresponsive polymers in various architectures

C. Psylla, S. Ottinger, K. Kyriakos, A. Miasnikova[1], A. Laschewsky[1], P. Müller-Buschbaum, C. M. Papadakis

[1] Universität Potsdam, Potsdam-Golm, Germany

Thermoresponsive polymers have a vast range of applications applications including drug delivery, tissue engineering and gene delivery. Among them, poly(N-isopropylacrylamide) (PNIPAM) has a very prominent place, since it exhibits a sharp phase transition at 32 ^{o}C, thus it has been thoroughly studied, and several applications based on it have been developed. Nevertheless, novel thermoresponsive systems have been designed, featuring new characteristics. Poly(methoxy diethylene glycol acrylate) (PMDEGA) is a new thermoresponsive polymer, which exhibits a cloud point in the range 35-45 ^{o}C, i.e. exactly in the physiological window which is interesting for bioapplications [1,2]. Its monomer, bearing the shortest diethylene side chain to achieve solubility, is sterically similar to the PNIPAM monomer. Despite that, it exhibits different thermoresponsive behavior: the transition takes place over a wide temperature range and during cooling, no significant hysteresis is observed. The latter is due to the fact that PMDEGA acts only as an acceptor of H bond, therefore no interchain H bonds are formed after the collapse.

We report here on fluorescence correlation spectroscopy (FCS) experiments on various amphiphilic block copolymer systems P(S-*b*-MDEGA) of different molecular architectures (PS stands for polystyrene). These amphiphilic systems form micellar structures when dissolved in H_2O. Three different architectures are studied: a P(S_{11}-*b*-$MDEGA_{172}$) diblock, a P(S_9-*b*-$MDEGA_{360}$-*b*-S_9) triblock and a P(S_9-*b*-$MDEGA_{219}$)$_3$ three-arm star block copolymer. A ConfoCor 2 from Carl Zeiss Jena GmbH was used together with a He-Ne laser (λ = 543 nm). All measurements were conducted at room temperature. Thus information on the critical micelle concentration (CMC) and the hydrodynamic radius of the unimers and the micelles is obtained, taking advantage of the unique ability of the method to adress the very dilute regime of polymer solutions. To realize the experiment, mixtures of Rhodamine 6G- labeled polymers and identical non labeled ones were produced, keeping always the concentration of the labeled chains below 10^{-8} M, to avoid saturation of the pin diode.

Figure 2.22a presents the autocorrelation functions obtained for all studied concentrations for P(S_9-*b*-$MDEGA_{219}$)$_3$. For concentrations lower than the CMC only a single, fast decay is observed which is assigned to single polymers, while for higher concentrations an additional slow decay is present, an indication of micelles that diffuse more slowly. Thus the CMC could be determined for this system at a c = (5.3$\pm$2.1)$\times 10^{-8}$ M. In a similar way, the CMC values for the diblock and the triblock were determined at c = (1.41$\pm$0.32)$\times 10^{-8}$ M and (7.07$\pm$2.03)$\times 10^{-8}$ M, respectively. The small differences can be assigned to the steric hindrances arising from the different architectures. To quantify the hydrodynamic radii, we fitted an exponential decay to the curves at $c < CMC$ and double exponential for micelles and single chains at $c > CMC$. A representative example of the fit is presented in Fig. 2.23a. From this analysis, the diffusion times τ_D of the two species was determined. The hydrodynamic radii of the unimers and of the micelles was determined using the Stokes-Einstein equation $R_h = k_B T/6\pi\eta D$ at the last step of this analysis.

The results are compiled in Fig. 2.23a. The hydrodynamic radius R_h is presented as a function of the polymer concentration for all three systems. As expected, below the CMC, only one species is observed with $R_h \sim 1$ nm, thus only single polymer chains are observed. As soon as the concentration is higher than the CMC, micelles are formed with a hydrodynamic radius that varies for the different architectures; for the diblock copolymer R_h = 12.5 ± 0.4 nm, for the triblock copolymer R_h = 12.1 ± 0.5 nm and for the star copolymer R_h = 10.2 ± 0.2 nm. Interestingly the micellar hydrodynamic radii do not depend strongly on the architecture.

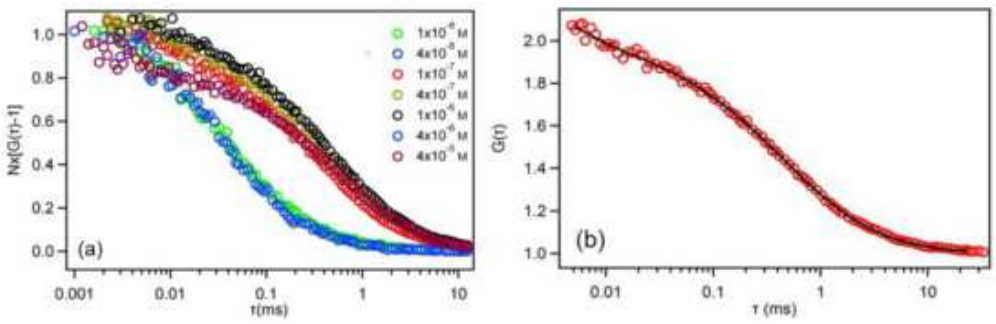

Figure 2.22:
a) FCS correlation functions of the P(S_{11}-*b*-MDEGA$_{172}$) diblock for different polymer concentrations. b) Representative fit of an exponential function to the experimental data collected for $c = 4\times10^{-5}$ M.

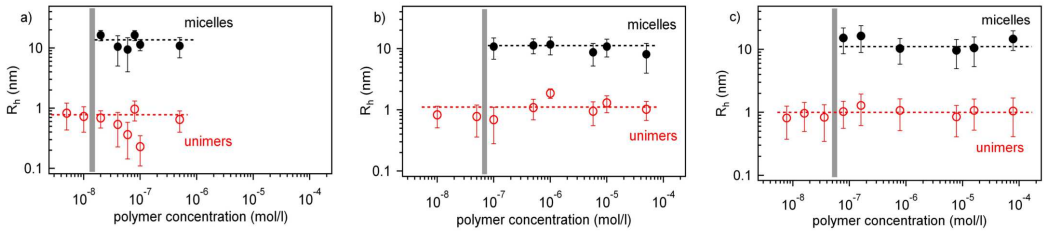

Figure 2.23:
Hydrodynamic radii as a function of polymer concentration for all three architectures: a) diblock, b) triblock and c) three arm star block copolymer. In all cases, the grey bar indicates the CMC.

To summarize, we have performed FCS experiments on amphiphilic copolymers of the novel thermoresponsive PMDEGA with PS as the hydrophobic block of various architectures. The focus is on the effect of the chain architecture on the behavior of the polymer in the dilute regime. Interestingly, we observe that the star block copolymer exhibits a CMC value close to the ones observed for the other systems. Also no apparent effect of the architecture on the hydrodynamic radii of the micelles is observed.

Financial support by DFG within the priority program 'Intelligente Hydrogele' is gratefully acknowledged (Pa771/4).

[1] A. Miasnikova, A. Laschewsky, G. De Paoli, C. M. Papadakis, P. Müller-Buschbaum, S. Funari, *Langmuir* **28**, 4479 (2012)

[2] A. Miasnikova, A. Laschewsky, *J. Polym. Sci. Part A: Polym. Chem.* **50**, 3313 (2012)

2.13 Networks from amphiphilic star block copolymers

X. Zhang, K. Kyriakos, C. Patrickios[1], M. Rikkou-Kalourkoti[1], E. N. Kitiri[1], C. M. Papadakis

[1] University of Cyprus, Nicosia, Cyprus

Amphiphilic polymer co-networks are networks composed of hydrophilic and hydrophobic blocks [1]. Hydrophilic and hydrophobic blocks microphase-separate when swollen with water. This way, a large internal interface is created which makes it a versatile soft material. Applications of such bio-compatible soft matter include scaffolds for tissue engineering and materials for soft contact lenses.
Our networks were prepared by sequential group transfer polymerization (GTP) of monomers and cross linker. 2-(Dimethylamino) ethyl methacrylate (DMAEMA) was used as the hydrophilic monomer, 2-ethylhexyl methacrylate (EHMA) or lauryl methacrylate (LauMA) were used as hydrophobic monomers in different network architectures, and ethylene glycol dimethacrylate (EGDMA) served as the cross linkers. The resulting structure consists of interconnected amphiphilic star block copolymers named amphiphilic cross-linked star (CLS) polymer co-network[1]. The number of elastic chains and dangling chains is equal. Both types of blocks are connected to the cores which are formed by EGDMA. There are two types of cores in the CLS networks (Fig. 2.24). The larger cores are named primary cores and have higher functionality than the smaller cores (secondary cores). The primary cores are connected only to secondary cores, and vice versa.

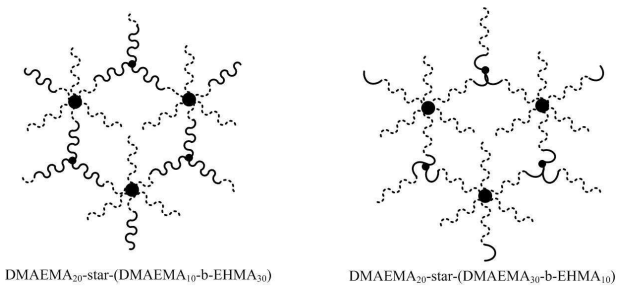

Figure 2.24:
Schematic representations of two cross-linked star block copolymer networks investigated by us. Hydrophilic DMAEMA blocks are represented by dashed lines, whereas hydrophobic EHMA blocks are represented by solid lines. The larger and smaller dots are the primary and secondary cores, respectively.

We investigate such networks from various acrylic blocks which differ in composition, water solubility and mechanical properties. We use small- and wide-angle X-ray scattering (SAXS, WAXS) to study the structures of different network architectures, i.e. the microphase-separated morphology. Currently, we have investigated two types of co-networks: the EHMA system and the LauMA system. The glass transition temperature of both systems is low. SAXS/WAXS measurements were carried on the GANESHA SAXS instrument. The sample-detector distances (SDD) were chosen to be 101 mm, 401 mm and 1051 mm which covered both the small- and wide-angle scattering range. The temperature was held steady at 298 K.

The SAXS curves of both systems (Figs. 2.25 and 2.26) feature a strong increase towards low momentum transfers q, indicating the presence of large scale inhomogeneities, which are typical for chemically cross-linked networks. A correlation peak and a bump are observed around $0.3\,\mathrm{nm}^{-1}$. The latter may reflect the form factor of the cross-linkers and the densely packed

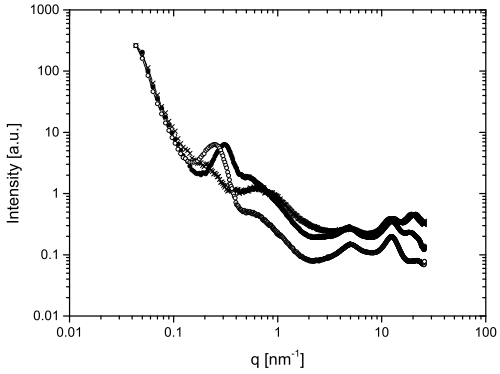

Figure 2.25:
SAXS profile of EHMA system (DMAEMA$_{20}$-star-(DMAEMA$_{10}$-b-EHMA$_{30}$), • . DMAEMA$_{20}$-star-(DMAEMA$_{20}$-b-EHMA$_{20}$), ○ . DMAEMA$_{20}$-star-(DMAEMA$_{30}$-b-EHMA$_{10}$), ×) at 298 K swollen with water.

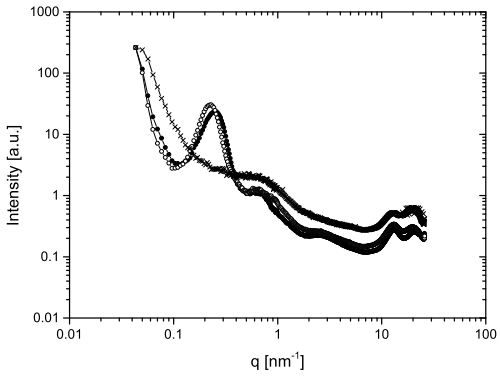

Figure 2.26:
SAXS profile of LauMA system (DMAEMA$_{20}$-star-(DMAEMA$_{10}$-b-LauMA$_{30}$), • . DMAEMA$_{20}$-star-(DMAEMA$_{20}$-b-LauMA$_{20}$), ○ . DMAEMA$_{20}$-star-(DMAEMA$_{30}$-b-LauMA$_{10}$), ×) at 298 K swollen with water.

hydrophobic blocks around them. The correlation peak points to well-defined distance between these hydrophobic domains. However, in both systems, when the number of monomers on hydrophobic block is reduced to 10, the peak vanishes with only the bump left. In this case, the hydrophobic domains are thus uncorrelated. Besides, the peaks in the WAXS region ($q > 2\,nm^{-1}$) reflect an ordering at small length scales, presumably within the densely packed hydrophobic domains. Comparing the EHMA and the LauMA systems, the LauMA system shows a higher correlation peak, i.e. stronger contrast, and the position of the peak shifts to lower q. Thus, the LauMA system microphase-separates more strongly and a microstructure with larger domains is created.
To summarize, we studied the cross-linked amphiphilic co-networks with SAXS/WAXS. The materials pronounced microphase-separation. Further work will address the model fitting.

[1] M. Vamvakaki, C. S. Patrickios, *Langmuir* **23**, 10433-10437 (2007)

3 Thin polymer films

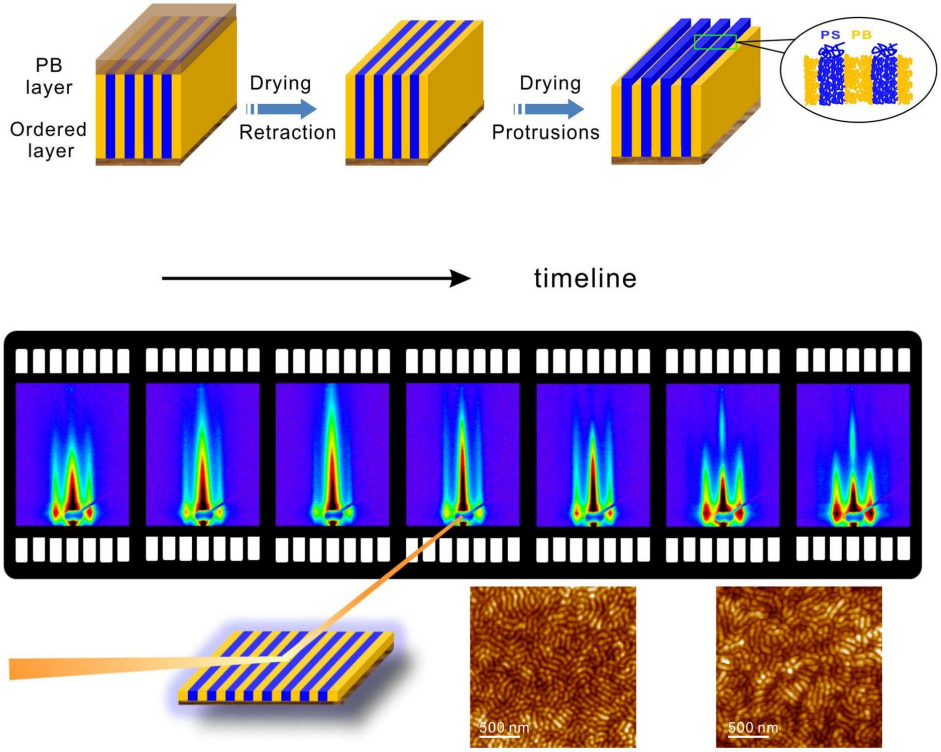

3.1 Molecular order and dynamics of nanometric thin layers of poly(styrene-*b*-1,4-isoprene) diblock copolymers

W. K. Kipnusu[1], M. M. Elmahdy[1], M. Tress[1], M. Fuchs[1] , E. U. Mapesa[1], D.-M. Smilgies[2], J. Zhang, C. M. Papadakis, F. Kremer[1]

[1] Institute of Experimental Physics I, Leipzig University, Germany
[2] Cornell University, Ithaca, NY, USA

Structure and molecular dynamics of nanometric thin films of diblock copolymers is a topic of current research interest due to the potential applications of these materials in emerging nanotechnologies. In thin films of poly(styrene-*block*-1,4-isoprene) P(S-*b*-I), the isoprene blocks are under two types of constraints coming from the stiffer polystyrene domains in the mesophases and the externally imposed confinement due to film thickness. How these types of confinement impact on molecular dynamics is of particular attention.
In the present work, grazing-incidence small-angle X-ray scattering (GISAXS), atomic force microscopy (AFM) and broadband dielectric spectroscopy (BDS) are combined to investigate the morphology and molecular dynamics in thin films of two lamellae-forming P(S-*b*-I) samples having isoprene volume fractions (f_{PI}) of 0.43 and 0.55 with identical molar masses of the styrene blocks [1]. GISAXS probes both the morphology in the entire film and near the film surface, while AFM shows the surface topography and BDS together with the use of novel nano-structured electrodes reveals the molecular dynamics taking place at different time and length scales. This study aims to answer the following questions: (i) How do the molecular dynamics of P(S-*b*-I) differ from the dynamics of the respective homopolymers? and (ii) what is the impact of external (layer thickness) and internal (mesophases) constraints on segmental and chain (normal mode of PI) dynamics? This report shows the GISAXS and BDS results of P(S-*b*-I) films for $f_{PI} = 0.55$.

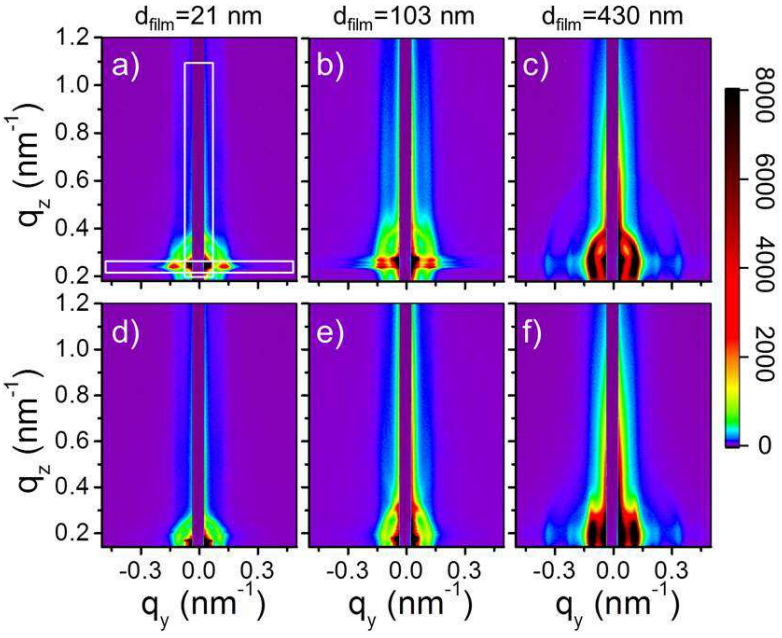

Figure 3.1:
2D GISAXS images of P(S-*b*-I) films with $f_{PI} = 0.55$. a)-c) incident angle $\alpha_i = 0.14°$ for film thicknesses a) 21 nm, b) 103 nm and c) 430 nm. d)-f) are images taken at $\alpha_i = 0.09°$ for same samples. The narrow vertical rectangles are the shadows of the rod-like beam stop.

By taking images at incident angles above and below the critical angle of the P(S-*b*-I) film ($\alpha_i = 0.14°$ and 0.09◦) GISAXS was used to elucidate the inner film structures as well as the near-surface structures (Fig. 3.1). Comparing the images taken at $\alpha_i = 0.14°$ for different film thicknesses, significant differences are observed: Bragg rods are observed at $q_y \approx 0.11$–0.14 nm^{-1} indicative of a lateral nanostructure, presumably perpendicular lamellae. With increasing film thickness, they become more pronounced (Fig. 3.1a-c). For the highest film thickness, higher-order Bragg rods appear at $q_y = 0.22$ nm^{-1} and 0.34 nm^{-1} (Fig. 3.1c) which indicate that a significant fraction of the film features perpendicular lamellae which are well correlated. The surface-sensitive GISAXS measurements of the thinnest and the intermediate film (Fig. 3.1d-e) indeed do not show any Bragg rods, except for the thickest film (Fig. 3.1f).

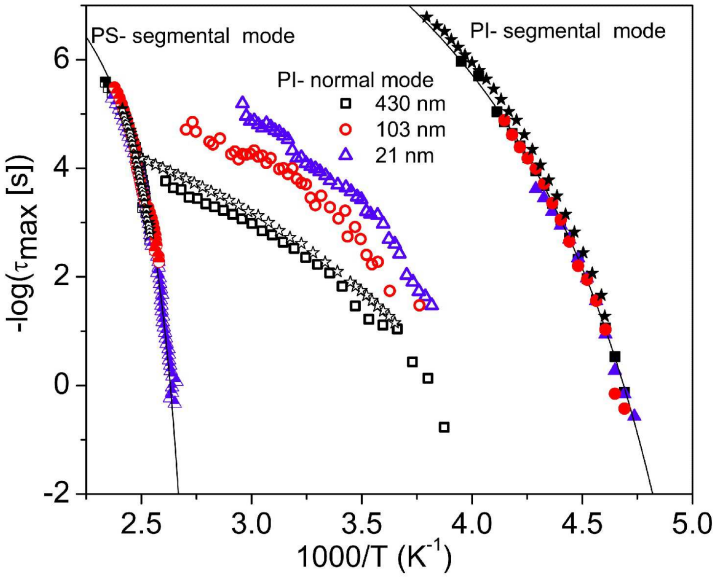

Figure 3.2:
Activation plots of the relaxation rates corresponding to the segmental mode of the isoprene blocks (filled symbols), normal mode of the isoprene blocks (open symbols) and segmental mode of the styrene blocks (half-filled symbols) of P(S-*b*-I) films with $f_{PI} = 0.55$. For comparison, the bulk PI and PS homopolymers with $M_w = 44500$ g/mol (PI-42) and 58900 g/mol (PS-58), respectively, are included (stars). The solid lines are Vogel–Fulcher–Tammann (VFT) fits to the experimental data.

The segmental relaxation times (τ_α) of isoprene and styrene blocks collapse into one curve for different film thicknesses and the corresponding bulk homopolymers (Fig. 3.2).The T_g values obtained from the VFT fits at $\tau = 100$ s are quantitatively identical (within experimental accuracy) to the calorimetrically determined T_g of the bulk P(S-*b*-I) and their corresponding homopolymers. This shows that the T_g for the investigated samples is independent of the film and the lamellar thicknesses. This corroborates the fact that glassy dynamics in polymers takes place at a length scale of a few segments (about 2-3 monomers) corresponding to about 1 nm, which is far below the lamellar and film thicknesses used in this study. On the other hand, the normal mode relaxation of the isoprene blocks becomes faster with decreasing film thickness. This trend is similar to what was observed for the case of PI homopolymers where it was attributed to relaxation of terminal subchains when parts of the chains are anchored to the substrate [2]. In P(S-*b*-I), it can be affected by several factors including the interactions of the monomers with each other, confinement due to stiffer styrene matrix leading to osmotic constraints and coupling between lamellae of thicker films resulting to long-range ordering as revealed by GISAXS.

This project is funded by SFB/102 and DFG Pa771/10-1.

[1] W. K Kipnusu, M. M. Elmahdy, M. Tress, M. Fuchs, E. U. Mapesa, D.-M. Smilgies, J. Zhang, C. M. Papadakis, F. Kremer, *Macromolecules* **46**, 9729-9737 (2013)

[2] E. U. Mapesa, M. Tress, G. Schulz, H. Huth, C. Schick, M. Reiche, F. Kremer, *Soft Matter* **9**, 10592-10598 (2013)

3.2 Density profile in thin films of polybutadiene on silicon oxide substrates: A time-of-flight neutron reflectometry study

E. T. Hoppe, A. Sepe, M. Haese-Seiller[1], J.-F. Moulin[1], C. M. Papadakis

[1] MLZ, Garching, Germany

The properties of polymers near a solid interface are of importance for applications such as lubricants and adhesives. The question whether and in which way the polymer properties change near a solid interface has been studied in numerous works focusing on, among others, the chain conformation, the mass density and the chain mobility. The term interphase has been used for a near-solid layer in the polymer melt with properties different from the bulk. Theoretical works revealed that the (cigar-shaped) chains align with their long axes parallel to the interface. Recent chemically realistic simulations of 1,4-polybutadiene near graphite (an attractive interface), revealed monomer layering near the interface which extends over a distance of roughly twice the polymer radius of gyration, i.e. over a few nanometers [1]. Experimentally, the polymer/solid interface is not easily accessible, unlike the polymer surface. Interface-sensitive methods specific to the polymer/solid interface are thus highly desired. Neutron reflectometry (NR) may give such information on the buried interface.

In the present work, we use time-of-flight NR (TOF-NR) to address the question of possible density changes in a PB film near a SiO_x substrate. The choice of PB is due to its low glass transition temperature which minimizes the risk of having residual solvent from the preparation in the film. To compare with our previous results obtained with surface plasmon resonance and optical waveguide spectroscopy on PB films on glass [2], a substrate similar to glass was prepared by thermally oxidizing a Si wafer which results in a 2500 Å thick SiO_x surface layer. Fully deuterated PB-d_6 was used to minimize the incoherent background in TOF-NR. We characterized the substrate using contact angle measurements, atomic force microscopy (AFM) and TOF-NR and use the resulting characteristics for the interpretation of the TOF-NR curves of the PB-d_6 film on this substrate.

(100) silicon wafers having a thickness of 4 mm and a diameter of 100 mm (4″) from Si-Mat, Germany, were used as substrates. They were cleaned in an acid bath, dry thermally oxidized at 1200°C, cleaned once more in the same way and rinsed with fully deuterated toluene (toluene-d_8). PB-d_6 having a molar mass of 55 kg/mol was purchased from Polymer Source Inc., Canada. The substrate was spin-coated for 60 s at 2000 rpm with a 2 wt.-% solution of PB-d_6 in toluene-d_8, resulting in a film thickness of ca. 1100 Å. The thin film was dried for 10 min in vacuum at room temperature to remove volatile solvent. The TOF-NR measurements were started within 30 min. They were carried out using the REFSANS instrument (Helmholtz-Zentrum Geesthacht) at FRM II (Garching, Germany). Neutron wavelengths $\lambda = 2 - 15$ Å were chosen together with incident angles $\alpha_i = 0.2°$, 0.8° and 2.0°. Measuring times were 1 h, 6 h and 37-40 h, respectively. The beam impinged through the side of the Si wafer. While the positions of the Kiessig fringes measured at different α_i values coincide, their amplitude is affected by the resolution. The minimal layer thickness that is resolved within the measured spectra is estimated at $d_{min} \approx 20$ Å. Motofit was used as software for fitting. Two approaches to model the SLD profile in the polymer film were used: (i) Constant layer thickness model: A certain number of layers was fixed at the film/substrate interface and the film surface, and their layer thicknesses and scattering length densities (SLD) was allowed to vary. The minimum layer thickness was 20 Å, i.e. the resolution limit. (ii) Variable layer thickness model: Layers of thickness 20 Å were used near the film/substrate interface and the film surfaces, and their number was increased until no more variation of the SLD of the outermost layers with respect to the neighboring bulk PB-d_6 film or to air was observed. In both approaches, the thickness of the homogenous part of the film was allowed to vary, while its SLD was given by the critical value of q_z.

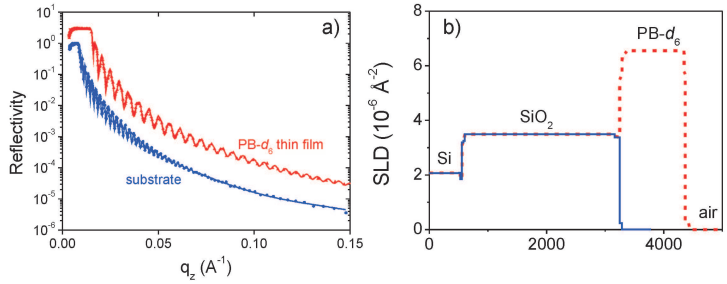

Figure 3.3:
a) TOF-NR curves of the substrate (blue circles) and of the PB-d_6 thin film (red triangles, shifted vertically by a factor of 3) together with the fits (lines). b) Corresponding SLD profiles from the variable layer thickness model.

The TOF-NR curve of the substrate, $R(q_z)$, features regular Kiessig fringes due to the SiO_x layer (Fig. 3.3a). The SLD profile corresponding to the best fit of the variable layer thickness model (Fig. 3.3b)results in an overall thickness of the SiO_x layer of 2768 Å with a surface width of 46 Å . Reasonable SLD values are obtained for Si and SiO_x.
The TOF-NR curve of thin PB-d_6 film on this substrate shows Kiessig fringes having a complex shape and a larger period (Fig. 3.3a). The critical value is now higher than for the substrate and corresponds to the literature value of the SLD of PB-d_6. The fit using the variable layer thickness model was carried out using the substrate parameters as fixed parameters and shows good agreement (Fig. 3.3a). The corresponding SLD profile consists of the homogeneous bulk part of the PB-d_6 film (Fig. 3.3b) and shows a decrease of the SLD of PB-d_6 at the interface to air which may be due to surface roughness. Moreover, a decrease of the SLD of PB-d_6 near the substrate is observed which we attribute to an increase of the free volume in the PB-d_6 melt. To calculate an average free volume of the interphase we use the model shown in Fig. 3.4. The SLD of the SiO_x surface decays over a smaller height than the SLD of PB-d_6 increases. Assuming that an interphase of PB-d_6 containing higher free volume (indicated by the white circles) is present near the rough SiO_x surface, we estimate a free volume of 5.7 %.

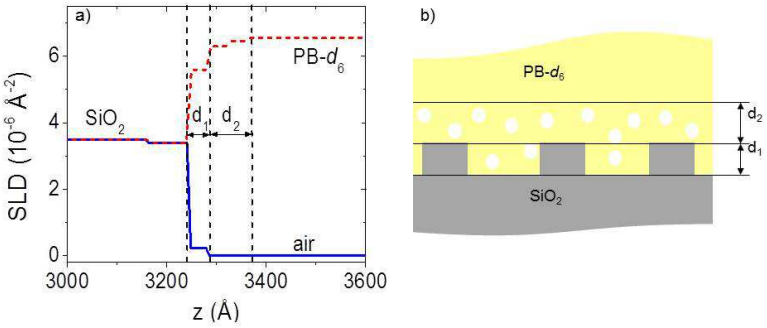

Figure 3.4:
a) SLD profiles of the thermally oxidized Si wafer (full blue line) and the PB-d_6 film on this substrate (dashed red line). b) Sketch of the interface. White circles: excess free volume. The rough surface of SiO_x is sketched as rectangles.

In summary, a thin film of PB-d_6 near a SiO_x interface was investigated. PB-d_6 may equilibrate more easily than other polymers because of its lower molar mass and its significantly lower T_g. TOF-NR curves could be measured with excellent statistics (down to reflectivities of 1.5×10^{-6}) and allow quantifying the mass density profile near the substrate.
This work was funded by DFG (Pa771/7-1) within the DFG priority program SPP 1369 (Polymer-Solid Contacts: Interfaces and Interphases).

[1] L. Yelash, P. Virnau, K. Binder, W. Paul, *Phys. Rev. E* **82**, 050801 (2010)

[2] E. T. Hoppe, A. Sepe, M. Haese-Seiller, J.-F. Moulin, C. M. Papadakis, *Langmuir* **29**, 10759-10768 (2012)

3.3 Structural rearrangment of diblock copolymer thin films having perpendicular lamellae during solvent vapor annealing

J. Zhang, D. Posselt[1], A. Sepe, X. Shen, J. Perlich[2], D.-M. Smilgies[3], C. M. Papadakis

[1] Roskilde University, IMFUFA, Denmark
[2] DESY, Hamburg, Germany
[3] Cornell University, Ithaca, NY, USA

The structural rearrangements in block copolymer thin films have attracted considerable interest since vapor treatment is frequently used for annealing defects hampering applications. In-situ, real-time grazing-incidence small-angle X-ray scattering (GISAXS) is a very powerful method to determine the structural changes of block copolymer thin films with high time resolution and statistical relevance [1].
In the present work, we focus on poly(styrene-*b*-butadiene) (P(S-*b*-B)) diblock copolymers having a molar mass of 215.8 kg/mol which shown perpendicular lamellar orientation. Perpendicular lamellae have severe geometrical constraints because the normal of the lamellar interfaces lies in the film plane and changes of the lamellar thickness are not easily accommodated. To investigate the structural changes during vapor treatment and drying, two different incident angles, one below ($\alpha_i = 0.10°$) and one above ($\alpha_i = 0.18°$) the critical angle of the polymer, were used in the GISAXS experiments. This way, we could discriminate surface-near order from the one in the bulk of the film. Cyclohexane was used to treat the samples; it is a good solvent for PB and a theta solvent for PS. Time-resolved GISAXS was performed at beamline BW4 at DESY.

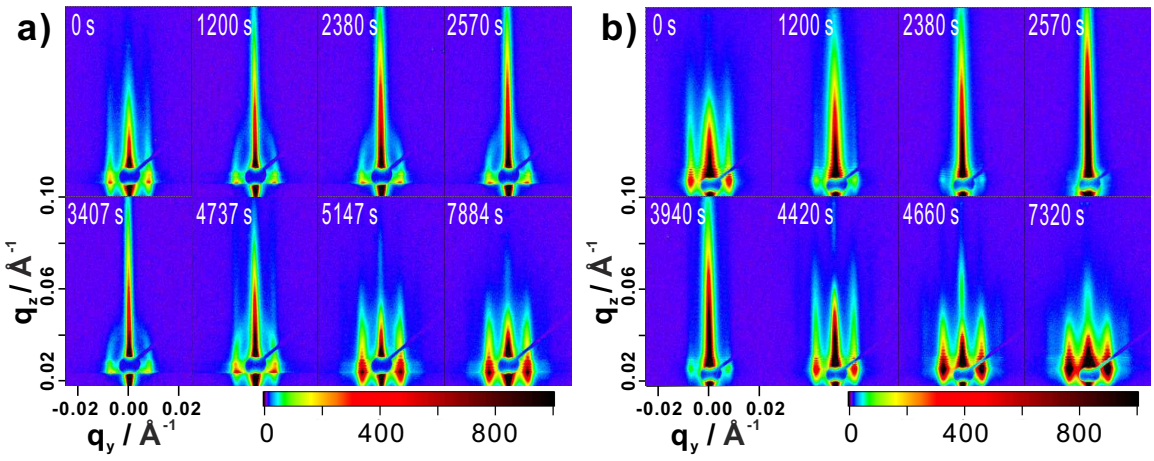

Figure 3.5:
2D GISAXS images during swelling (top row) and drying (bottom row). a) $\alpha_i = 0.18°$, b) $\alpha_i = 0.10°$. The times after the beginning of the vapor treatment are indicated. The intensity scale is given on bottom.

At $\alpha_i = 0.18°$, the scattering signal is an average over the entire film thickness. The BRs bent inwards during the swelling (Fig. 3.5a top). We attribute this bending to tilting of the lamellae away from the purely perpendicular orientation. During drying, the straight BRs reappeared (Fig. 3.5a bottom) in such a way that, initially, they were very long along q_z with very weak intensity; then, their intensity increased while their length decreased. Thus, we propose that the purely perpendicular orientation is lost due to the solvent uptake during swelling, while it is reinstalled during drying. At the end of the drying, the BRs became short again. At $\alpha_i = 0.10°$, during swelling (Fig. 3.5b, top row) the intensity of the BRs became weaker and weaker, which may be attributed to a loss of lamellar order near the film surface. During drying, a modulation appeared in-plane, i.e. at $q_y = 0$. Both the narrow and elongated DBRs and the modulation

appeared during the drying are due to the the protrusion of one block at the film surface. Since the solvent is slightly selective for the PB domains, the PS domains are more quickly depleted of the solvent and turn solid earlier than the PB domains. This means a characteristic time is passed after which there is practically no solvent left in the PS domains, while the PB domains are still swollen with solvent. Further evaporation leads to a collapse of the swollen PB domains to a level below the interface of the already rigid PS domains. This way, the protrusion structure is formed during drying.

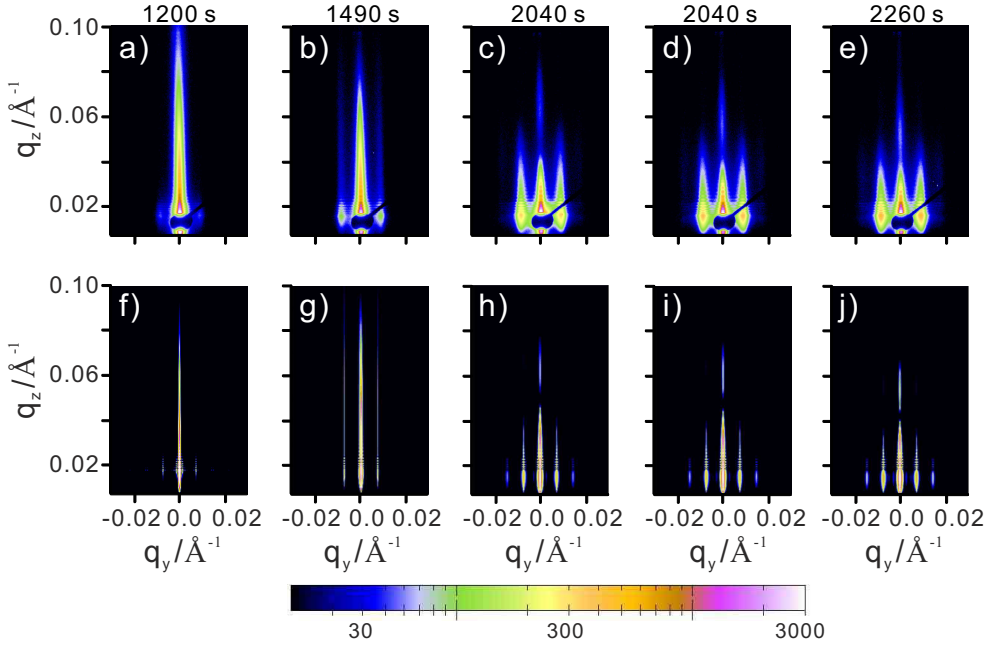

Figure 3.6:
Images of five representative measured GISAXS scattering patterns measured at $\alpha_i = 0.10°$ (upper row) and corresponding simulations (lower row). The height of the box particles is 0 Å(f), 43 Å(g), 157 Å(h), 166 Å(i) and 189 Å(j), respectively. The times after the beginning of the drying are given. The intensity is represented on a logarithmic scale.

To proof the above speculation, we simulated 2D images at $\alpha_i = 0.10°$ using the IsGISAXS software which calculates the diffuse scattering in the framework of the distorted-wave Born approximation. Figure 3.6 shows the simulated 2D images together with the corresponding measured ones. It has to be noted that the specular reflection is not included in the IsGISAXS algorithm, thus, it does not appear in the simulated images (Fig. 3.6f-j). To capture the protruding perpendicular lamellae, they were modeled as box-shaped particles on top of a homogeneous film, described by the parameters width, height, orientation and distribution. The interference function was calculated using the 1D paracrystalline model. During drying, the height of the particles was adapted to fit the positions of the minima of the in-plane modulation. The measured and calculated 2D images agree with each other very well; thus, we attribute the modulation to the formation of protrusions. Moreover, the length variation of the BRs (initially very long with weak intensity, later short with high intensity) is also reproduced by the model.
This project is funded by DFG (Pa771/10-1).

[1] Z. Di, D. Posselt, D.-M. Smilgies, R. Li, M. Rauscher, I.-I. Potemkin, C. M. Papadakis, *Macromolecules* **45**, 5185 (2012)

[2] C. M. Papadakis, K. Almdal, K. Mortensen, D. Posselt, *Europhys. Lett.* **36**, 289 (1996)

3.4 Microphase separation nanostructure in binary blend diblock copolymer thin films prepared by spin-coating

J. Zhang, K. Kyriakos, S. Jaksch, J. Perlich[1], D. Posselt[2], D.-M. Smilgies[3], C. M. Papadakis

[1] DESY, Hamburg, Germany
[2] Roskilde University, IMFUFA, Denmark
[3] Cornell University, Ithaca, NY, USA

Nanostructures obtained from self-assembly of block copolymers have gained great attention due to their facile, simple and cost-effective characteristics with many promising applications in nanotechnology, such as ultrahigh-density data storage media, molecular sieves, dielectric reflectors, and sensors [1]. Although self-assembly of block copolymers offer a rich variety of periodic nanoscale patterns, and researchers have succeeded in finding conditions that lead to very long range order of the domains, there are still major challenges to manipulate the self-assembly process to realize these promising applications.

In the present work, we use a binary blend of compositionally symmetric poly(styrene-*b*-butadiene) (P(S-*b*-B)) diblock copolymers differing in molar mass. In thin film geometry, the high molar mass copolymer, 215.8 kg/mol, $(\text{P(S-}b\text{-B)})_\alpha$, forms perpendicular lamellae, whereas the low molar mass copolymer, 28 kg/mol, $(\text{P(S-}b\text{-B)})_\beta$, forms parallel lamellae. We thus expect a complex structure of mixed orientations in the thin films from the blends of these copolymers. Thin films were prepared by spin coating the polymer solution onto silicon wafers. The dependence of the morphology on volume fraction of low molar mass ϕ_β copolymer was studied by means of grazing-incidence small-angle X-ray scattering (GISAXS).

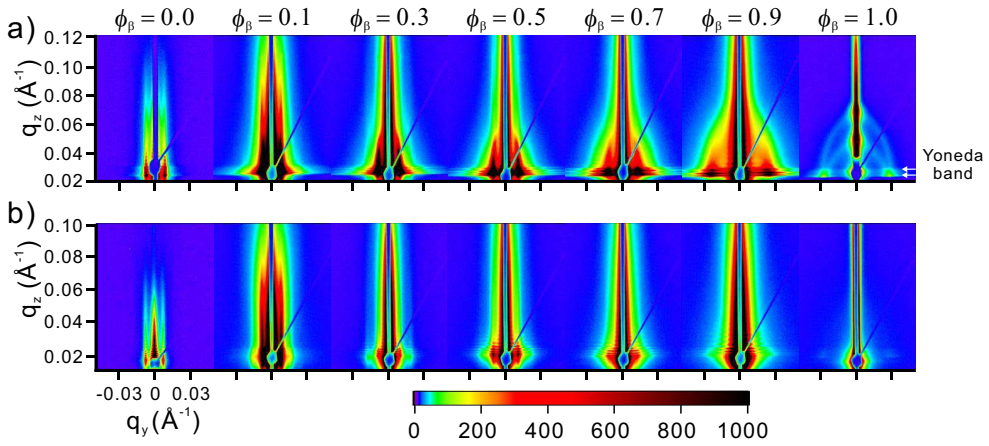

Figure 3.7:
2D GISAXS images of as-prepared films for different compositions. The ϕ_β values are given on top. The incident angles are a) $0.18°$ and b) $0.10°$. The intensity scale is given below the images. The Yoneda band is delimited by the q_z values corresponding to k_{cP} and k_{cS}, marked by white arrows in a).

Figures 3.7a and b show the 2D GISAXS images from the binary blend thin films measured at incident angles of $0.18°$ (averaging over the entire film thickness, Fig. 3.7a) and $0.10°$ (being surface sensitive, Fig. 3.7b), respectively. We discuss them first qualitatively. The image of the thin film from pure $(\text{P(S-}b\text{-B)})_\alpha$ at $\alpha_i = 0.18°$ displays first-order Bragg rods (BRs) which are strongly extended along q_z, i.e., normal to the film surface. This extension results from the protrusion of the PS blocks at the film surface, as shown by us previously [2]. The GISAXS image of the film from pure $(\text{P(S-}b\text{-B)})_\beta$ at $\alpha_i = 0.18°$ shows a pair of first-order diffuse Debye-Scherrer

rings (DDSRs), with their intensities being enhanced between the Yoneda peaks of (P(S-*b*-B)) and SiOx. In addition, the intensities of the DDSRs are significantly enhanced near q_y = 0; i.e., a significant fraction of the lamellae is parallel to the film surface [3]. At α_i = 0.18° , the 2D GISAXS images of the binary blend thin films show BRs for ϕ_β = 0.1-0.7, whereas the one of the blend with ϕ_β = 0.9 features a scattering arc, i.e. a part of the DDSR (Fig. 3.7a). This means, for ϕ_β = 0.1-0.7, the films predominantly feature perpendicular lamellae whereas the lamellae are tilted in the thin film with ϕ_β = 0.9.

In the surface-sensitive 2D GISAXS images taken at at α_i = 0.10°, BRs are present for pure $(\text{P(S-}b\text{-B)})_\alpha$ (Fig. 3.7b), indicating the presence of perpendicular lamellae with protrusions in the near-surface region. In contrast, the GISAXS image of pure $(\text{P(S-}b\text{-B)})_\beta$ is nearly featureless. The 2D GISAXS images show BRs for ϕ_β= 0.1-0.5, indicating the presence of the perpendicular lamellae in the near-surface region; whereas they are featureless for ϕ_β= 0.7 and 0.9. We conclude that the parallel lamellae disappear by adding only 10 volume percent of $(\text{P(S-}b\text{-B)})_\alpha$ (i.e. long diblock copolymers); thus, the long diblock copolymer dominates the lamellar orientation.

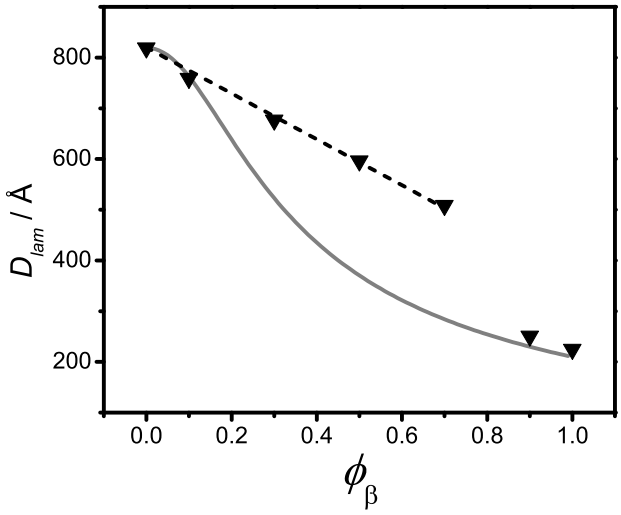

Figure 3.8: Reduced lamellar thickness in dependence on the volume fraction of $(\text{P(S-}b\text{-B)})_\beta$.

To quantitatively analyze the data, the lamellar thicknesses were obtained by q_y profiles created from the experimental 2D GISAXS images of all blends. The lamellar thickness, D_{lam}, of all blends together with the pure diblock copolymers from GISAXS are represented in Fig. 3.8 (solid triangles) in dependence on ϕ_β. Firstly, the data were compared with the one phase model proposed by Court and Hashimoto (solid line) [4]. It is found that the data can not be described by the one phase model. Secondly, an intriguing result emerging from the data is that D_{lam} decreases linearly for ϕ_β = 0.1-0.7 (dashed line). This is a great advantage for nanofabrication applications using diblock copolymer thin films as a template, because the periodicity of the nanostructure can simply be tailored by mixing two diblock copolymers instead of having to use *de novo* synthesized diblock copolymers with the appropriate molar mass.

This project is funded by DFG (Pa771/10-1).

[1] S. Park, D. H. Lee, J. Xu, B. Kim, S. W. Hong, U. Jeong, T. Xu, T. P. Russell, *Science* **323**, 1030 (2009)

[2] J. Zhang, D. Posselt, A. Sepe, X. Shen, J. Perlich, D.-M. Smilgies, C. M. Papadakis, *Macromol. Rapid Commun.* **34**, 1289 (2013)

[3] Z. Di, D. Posselt, D.-M. Smilgies, C. M. Papadakis, *Macromolecules* **43**, 418 (2010)

[4] F. Court, T. Hashimoto, *Macromolecules* **35**, 2566 (2002)

3.5 Structural changes in lamellar diblock copolymer thin films upon swelling in nonselective solvents

A. A. Rudov[1], E. S. Patyukova[1], I. V. Neratova[2], P. G. Khalatur[2], D. Posselt[3], C. M. Papadakis, I. I. Potemkin[1]

[1] Physics Department, Lomonosov Moscow State University, Russian Federation
[2] Institute for Advanced Energy Related Nanomaterials, University of Ulm
[3] IMFUFA, Department of Science, Systems and Models, Roskilde University, Denmark

Control of nanodomains orientation in block copolymer films is one of the key problems for many applications including growth of ultrahigh-density nanowire arrays for storage media, for instance. However, the most common way of preparation, spin-coating, often results in non-equilibrium structures and usually reveals many defects. In order to approach equilibrium, the film may be equilibrated by solvent vapor annealing (SVA). Absorption of vapor molecules during SVA makes the system three-component (two blocks and condensed solvent), where structural changes are strongly influenced by the interaction of the two polymer blocks with the solvent, the distribution of solvent in the film, etc. The present work addresses the swelling of lamellae-forming diblock copolymer films using dissipative particle dynamics (DPD) computer simulations and mean-field calculations.

The simulations are performed in a tetragonal box of a constant volume $V = 40 \times 40 \times 100$ with periodic boundary conditions in the x and y directions (i.e., in the film plane). The total number of the particles in the box is $N = 3 \times 40^2 \times 100$. There are four different types of particles in the system: solvent particles, A- and B-beads forming diblock copolymers, and the particles forming the walls at $z = 0$ (bottom) and $z = L_z$ (top) (denoted by W). The W-particles are arranged to form smooth, dense walls which prevent escape of all other particles from the system. The forces acting between any pair of DPD particles are taken to be the same nature for both mobile and frozen particles. Initially, the volume above the film is filled with single-site solvent particles, and the polymer volume fraction in the box corresponds to 40 %. We fix the number of the beads in each block at 10, so the total number of the beads in the polymer chain is $n = 20$. The force keeping the beads in the chains is described by Hooke's law. Initially, the polymer film and the solvent are completely separated from each other. To prove convergency to the equilibrium structure, each time we prepare two different initial structures of the dry film (spatially homogeneous and lamellar) and let them relax during the swelling process. We restrict ourselves to the analysis of a nonselective solvent.

To induce the parallel lamellar orientation in computer simulations, the repulsion of the B blocks from the wall is set to be higher than the one of A. After annealing of the polymer film, the parallel lamellar structure is formed (Fig. 3.9a, left picture). The dry film is in the strong segregation regime. The decrease of the interaction parameter between A and the solvent leads to the swelling of the film. One can distinguish two regimes of lamellar swelling: Affine swelling of the film, i.e. swelling of individual lamella with their number in the film being fixed, and then a reduction of the lamellar thickness and an increase of the number of lamellae (Fig. 3.9a). The latter effect is due to the weakening of the incompatibility between A and B monomer units in the presence of the solvent which makes the blocks less stretched. On the other hand, the AB interfacial area per molecule increases; i.e., the chains become more coiled. Therefore, the number of the lamellae grows and their thickness decreases. The initial swelling of the lamellae is related to a finite size effect along the film normal, namely the finite number of the lamellae. Structural changes in the film correspond to the lower free energy if the upper layer is complete. Any terraces formation in the upper layer at the length scale of the simulation box (nanoscale) costs extra surface energy, especially in the case of poor solvent. Therefore, if the fraction of the absorbed solvent is small and the increasing area of AB interfaces is insufficient to form an

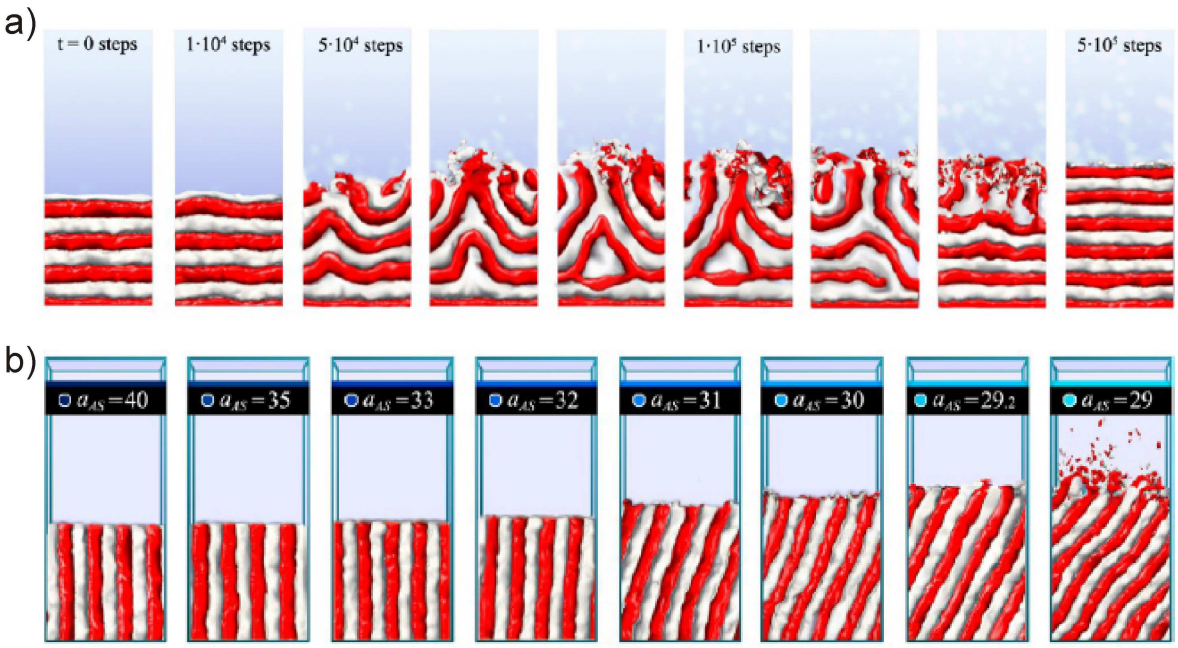

Figure 3.9:
a) Time evolution of the parallel lamellar structure during swelling. b) Snapshots of the perpendicular lamellar structure during swelling.

additional complete AB layer, the alternative process of swelling of the fixed number of lamellae is the only way to provide the film swelling.
The perpendicular lamellar orientation is stable if the interactions of both blocks with the substrate are similar. Therefore, the interaction parameters of A and B blocks with the bottom substrate are chosen to be equal. We consider two initial structures of the film: perpendicular lamellae and spatially disordered ones. In both cases, a dry film with perpendicular lamellae is formed after annealing (Fig. 3.9b, left picture). The regime of the lamella thickening is absent for the perpendicular lamellae, as expected. The absorbed solvent makes the perpendicular lamellae thinner (e.g., along the x-axis). This leads to an increase of the lamellar area in the y- and z-directions, if the number of lamellae remains the same. Keeping in mind the fixed area of the film, the increase of the lamellar dimension in the y-direction results in a zigzag bending of the lamellae. In order to fulfill the space filling condition in the x-direction the lamellae must tilt (Fig. 3.9b).
In conclusion, we have demonstrated using DPD simulations that the structural changes in thin films of symmetric diblock copolymers follow significantly different pathways depending on the initial lamellar orientation.
This work is funded by Russian Foundation for Basic Research, the Ministry of Education and Science (Russian Federation) and by DFG within the project Pa771/10-1. The simulations were performed on multiteraflop supercomputers Lomonosov and Chebyshev at Moscow State University.

[1] A. A. Rudov, E. S. Patyukova, I. V. Neratova, P. G. Khalatur, D. Posselt, C. M. Papadakis, I. I. Potemkin, *Macromolecules* **46**, 5786 (2013)

3.6 GIWAXS simulations to understand side chain influences on crystal structure in thin films

E. M. Herzig, V. Gevaerts[1], M. Kirkus[1], K. H. Hendriks[1], M. M. Wienk[1], J. Perlich[2], R. A. J. Janssen[1], P. Müller-Buschbaum

[1] TUe, Eindhoven, The Netherlands
[2] DESY, Hamburg, Germany

Organic solar cells can be fabricated from polymers or small molecules. Similar as for polymer systems the solubility properties of small molecules depend on the side chains. However, side chains also influence how these molecules arrange with respect to each other and therefore other parameters relevant for solar cell performance are influenced. In a systematic study of side chain position in the small π-conjugated molecule based on diketopyrrole and bithiophene (DPP2T) we have used various methods from spectroscopy and microscopy to scattering to characterize these custom synthesized molecules. In combination with the comparison of measured grazing incidence wide angle X-ray (GIWAXS) data and GIWAXS simulations it was possible to clearly show, how the orientation and packing of these molecules changes with side group position. Furthermore, we were able to relate this directly to the solar cell performance of the different molecules [1].
To achieve this quantitative analysis we use the powerful software package simDiffraction developed by Breiby and co-authors [2]. With this code it is possible to calculate the scattering patterns of particular molecules in a chosen unit cell. The comparison to experimental data allows to identify the origin of various scattering peaks and a quantitative determination of possible unit cell parameters allowing conclusions to certain molecular arrangements within the thin films.

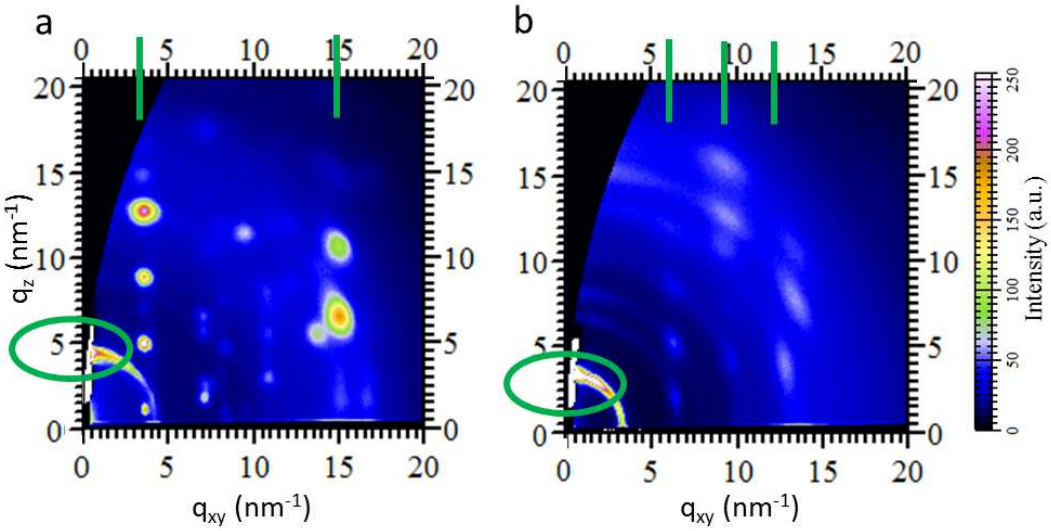

Figure 3.10:
2 dimensional GIWAXS data of a) DPP2T-4 and b) DPP2T-5. Green marks show position of dominant features of scattering pattern.

The GIWAXS data shown in Fig. 3.10a shows the scattering pattern of a neat DPP2T-4 film where the terminal thiophene carries a hexyl chain in the 4^{th} position while Fig. 3.10b shows the same data for a neat DPP2T-5 film where the hexyl chain is found at the 5^{th} position. The well defined diffraction spots found for both samples indicate a significant ordering throughout both thin films. The q-value of the diffraction ring with a peak in vertical direction is found for DPP2T-4

at 4.5 nm^{-1} and for DPP2T-5 at 3.4 nm^{-1}. This indicates a change in real space separation from 1.4 to 1.8 nm respectively. Furthermore, characteristic, vertically repeating diffraction spots are seen at different q_{xy} positions for both samples.
To more thoroughly understand the origin of these main features the simulation of the molecules within a simple P1 space group arrangement, i.e. a rectangular unit cell without particular symmetries, is sufficient. Figures 3.11c and d show simulated GIWAXS patterns that closely correspond to the observed patterns.

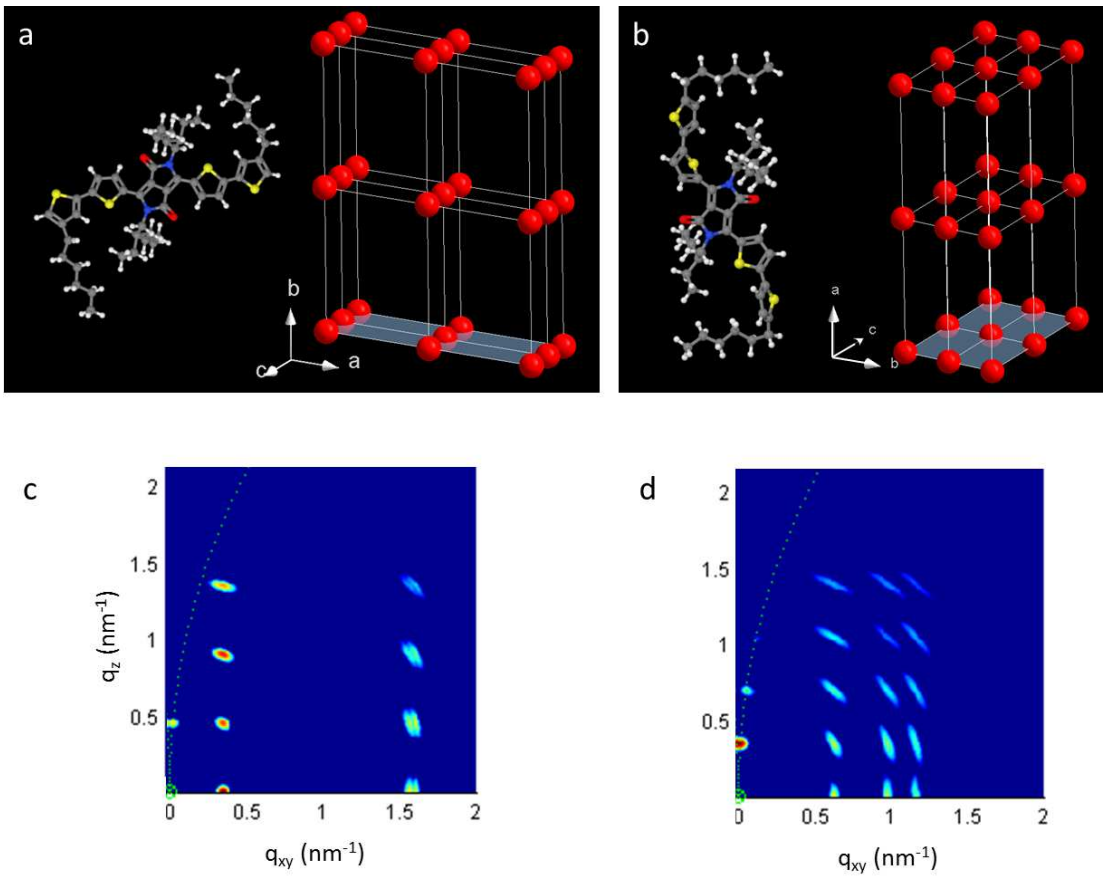

Figure 3.11:
Possible conformation of a) DPP2T-4 and b) DPP2T-5 and the corresponding unit cell arrangement used for the calculated 2 dimensional scattering patterns for c) DPP2T-4 and d) DPP2T-5.

The unit cells used to obtain these patterns are shown in Fig. 3.11 a and b. Possible decorations of the unit cell positions are the molecular conformations shown next to the unit cell arrangement. While the exact conformation cannot be determined with this measurement, the general geometry of the molecule will be within the a-b plane of the unit cell. This reveals that the π-π-stacking distance is significantly smaller for DPP2T-4 than for DPP2T-5 explaining why solar cells with DPP2T-4 have higher current and therefore higher efficiency. A more detailed account on these and related systems can be found in reference [1].

[1] V. S. Gevaerts , E. M. Herzig , M. Kirkus , K. H. Hendriks , M. M. Wienk , J. Perlich , P. Müller-Buschbaum, R. A. J. Janssen, *Chem. Mater.* **26**, 916-926 (2014)

[2] D. W. Breiby, O. Bunk, J. W. Andreasen, H. T. Lemke, M. M. Nielsen, *J. Appl. Cryst.* **41**, 262-271 (2008)

3.7 Hierarchically structuring of hybrid materials with the breath figure method

A. Hassan, V. Körstgens, P. Müller-Buschbaum

Structures found in nature often exhibit superior properties such as, strength, stability or weight, For example the honeycomb structure is build-up by using minimum beeswax and shows very good properties like space filling, good structural stability, high mechanical strength and low density. To artificially prepare the highly ordered honey-comb structure as a particular patterned thin film with a 2D or 3D array of pores, the so called breath figures or moist casting methods have been established [1].
Before 1994 breath figures did not receive any attention, although it had been studied already 100 years ago. Almost 20 years ago Widawski et al. [2] illustrated the method for the preparation of porous film structures. Using this technique, we obtain porous thin film with pore sizes from nanometers to micrometers. The pore size of the thin film realized via the breath figure method depends on different parameters such as boiling point and volatility of the organic solvent, miscibility with water, humidity, concentration of the polymer, temperature, type of the substrate and most important the casting technique.
Materials with a high hydrophobicity are of great interest, because of special properties as for example dirt repelling. As a consequence, these materials have applications in e.g. snow preventing, heat conduction and oxidation and self-cleaning surfaces [3]. A super hydrophobic membrane or surface can also be produce via the breath figure method. Furthermore, because of the environment friendly, simplicity, versatility and robustness of this method, it has number of application in many other fields such as like photoelectric conversion, photo catalysis, antireflection, hydrophobicity, high mechanical strength and cell adhesion.
In the moist casting method the substrate is exposed to moisture or a high humidity. After casting the polymer solution on the substrate, the solvent starts to evaporate and the polymer surface cool down as compared to the environment. Due to the temperature difference, water droplets from the humid air condensate on the polymer film surface. Initially, this condensation takes place on an unstructured liquid polymer solution surface, which gives rise to droplets with a small size distribution. As long as more solvent evaporate form the polymer solution, more water droplets from the atmosphere condensate on the thin film. These water droplets merge with already deposited droplets and the pore size becomes larger. After evaporating the solvent and water from the solution, the ordered porous thin film structure is obtained [4].
A number of different realizations of moisture casting have been reported to get nano- and micro- porous thin films. Examples are drop casting, solution casting with high humidity, spin coating with high humidity, the airflow technique, coating on the water, the cold stage technique and an emulsion technique. The technique used in my preset investigation is spin coating under high humidity.
As polymer we use a commercial polyacrylate, also known as paraloid-72. It is a copolymer of copolymer consisting of methyl acrylate (MA) and ethyl methacrylate (EMA). Porous thin films having breath figures were prepared using this polyacrylate copolymer with different solvent (chloroform, toluene, THF) with 5 different concentration (50, 10, 15, 20, 25mg/ml) and with different rotational speed in the spin coating process (500, 1000 and 2000 rpm). The spin coating is done for 60 seconds.
As an example optical microscope (OM) images of the sample surfaces obtained for five different concentrations with a spin coating speed of 1000 rpm are shown in Fig. 3.12. Different porous structures are seen. With increasing concentration of the solution the porous structure becomes more prominent and thus better visible in the OM images. At a low polymer concentration such as 0.5 mg/ml the pores are less well defined because of the fast evaporation of the solvent and little aggregation of the water droplets on the surface of the polymer solution. If

the concentration of the polymer solution is above 10 mg/ml, the viscosity of the solution is higher and films becomes thicker, which makes the porous thin film structure more prominent as compere to the dilute solution.

Figure 3.12:
OM images of Paraloid-72 films out of chloroform solutions with 3 different polymer concentrations (50, 150, and 250 mg/ml).

The pore size increases with increasing the concentration of the polymer solution as extracted from the OM data. In contrast to the number of pores, the average diameter of the pores decreases with increasing the polymer concentration of the solution (see Fig. 3.13). This might be caused by an increase in the viscosity of the solution which decreases the degree of the water droplets sinking into the solution.

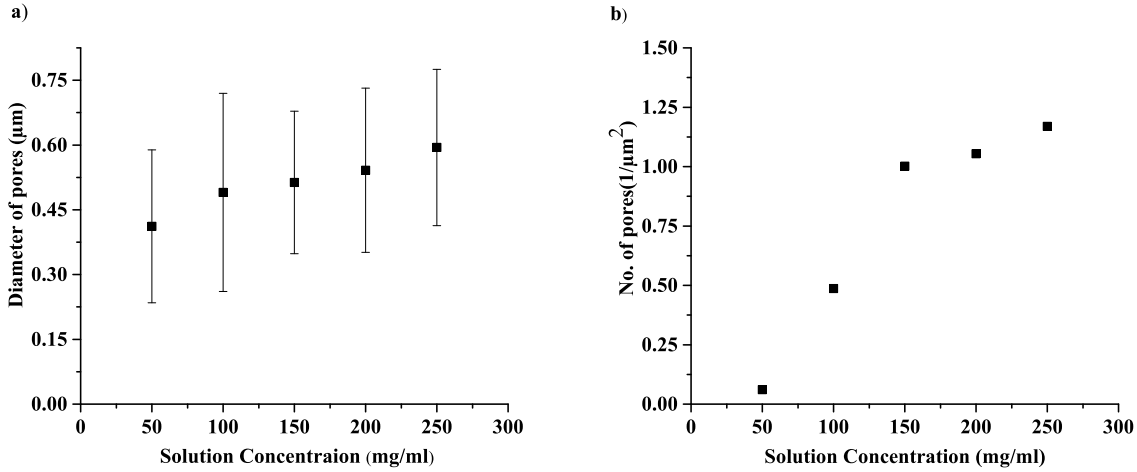

Figure 3.13:
a) Average diameters of the pores and b) number of pores as function of the polymer concentration of the solution as extracted from OM data.

In conclusion, the number of pores and the average diameter of the pores can be tuned with changing the polymer concentration of the solution. The influence of the other solvents used to prepare the polymer solution is under investigation. In further investigation, titanium dioxide nanoparticles will be added to the porous thin films. The homogeneity versus a preferential distribution at pore boundary of the nanoparticles will be probed.

[1] L. Heng, B. Wang, M. Li, Y. Zhang, L. Jiang, *Materials* **6**, 460-482 (2013)

[2] G. Widawski, M. Rawiso, B. Francois, *Nature* **369**, 387-389 (1994)

[3] M. Hernandez-Guerrero, M. H. Stenzel, *Polym. Chem.* **3**, 563-577 (2012)

[4] Y. Zheng, Y. Kubowaki, M. Kashiwagi, K. Miyazaki, *J. Mech. Sci. Techn.* **25**, 33-36 (2011)

3.8 Arrangement of maghemite nanoparticles in P(S-*b*-NIPAM) diblock copolymer films

Y. Yao, E. Metwalli, B. Su, V. Körstgens, D. Moseguí-González, L. Song, G. Santoro[1], S. V. Roth[1], P. Müller-Buschbaum

[1] DESY, Hamburg, Germany

Block copolymers with embedded magnetic nanoparticles have attracted strong interest as a method to fabricate hybrid nanocomposites for wide potential applications in functional devices. Furthermore, the control over the alignment of the nanoparticles within the polymer matrix is essential for producing well-aligned, highly-oriented metal-polymer nanopatterns. It can be achieved by using a guiding polymer matrix [1]. In this work, we have investigated the alignment of maghemite (γ-Fe_2O_3) nanoparticles within poly(styrene-*b*-N-isopropylacrylamide), denoted P(S-*b*-NIPAM), diblock copolymer films. The employed maghemite nanoparticles were coated with PS chains. We have studied the emerged morphologies as function of the nanoparticle concentration of the metal-polymer hybrid film by using atomic force microscopy (AFM), scanning electron microscope (SEM) and grazing incidence small-angle x-ray scattering (GISAXS).

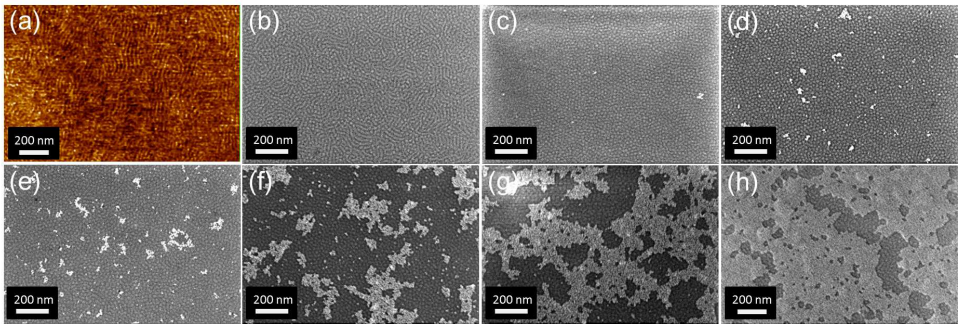

Figure 3.14:
a) AFM phase image of the particle free P(S-*b*-NIPAM) diblock copolymer film. b-h) SEM images of the metal oxide-polymer hybrid films with different nanoparticles concentrations: 0 wt%, 0.1 wt%, 0.5 wt%, 1 wt%, 3 wt%, 7 wt%, and 15 wt%.

Hybrid films of the diblock copolymer containing the maghemite nanoparticles were prepared by spin-coating on precleaned Si substrates, which were cut into 2.5*2.5 cm^2 pieces. To achieve a defined silicon oxide layer on the surface, Si substrates were cleaned in a base solution composed of 350 ml H_2O, 30 ml H_2O_2 and 30 ml NH_3 at 76 $^\circ C$. The polymer-nanoparticle solutions were prepared in 1,4-dioxane and the concentration of polymer was kept fixed at 45 mg/ml for all prepared films. Several hybrid films were prepared with various nanoparticles concentrations, viz, 0, 0.1, 0.5, 1, 3, 7, and 15 wt%. According to the theoretical phase diagram of block copolymers, a cylindrical morphology is expected for the bare P(S-*b*-NIPAM) diblock polymer (f_{PS} = 0.34). The surface of particle-free P(S-*b*-NIPAM) diblock copolymer film was examined by AFM and SEM (Fig. 3.14a-b) in real space, respectively. Both measurements indicate a microphase separation with a parallel cylindrical morphology. Upon incorporation of maghemite nanoparticles into the diblock polymer matrix, the surface morphology dramatically changes to the highly ordered perpendicular cylinders. Parallel to perpendicular morphological transition is attributed to a competition of entropy and enthalpy terms in the hybrid film. Localized maghemite nanoparticles within the PS domain of the P(S-*b*-NIPAM) block copolymer is achieved by using PS coating covered around nanoparticles [2]. Furthermore, the PS coating of

the nanoparticles favors the enthalpic interaction parameter between nanoparticles and polymer matrix, and an ordering of the copolymer matrix is enhanced. From Fig. 3.14b-c it is seen that the nanoparticles are highly dispersed in the diblock copolymer matrix at low concentration. However, at higher nanoparticles content nanoparticles aggregates are formed and monotonically increase in size with increasing nanoparticles concentration (Fig. 3.14d-h). Particularly, at concentration $\geq$ 7 wt%, the magnetic nanoparticles aggregates form interpenetrating network cluster with a percolation path and cover large area of the film surface.

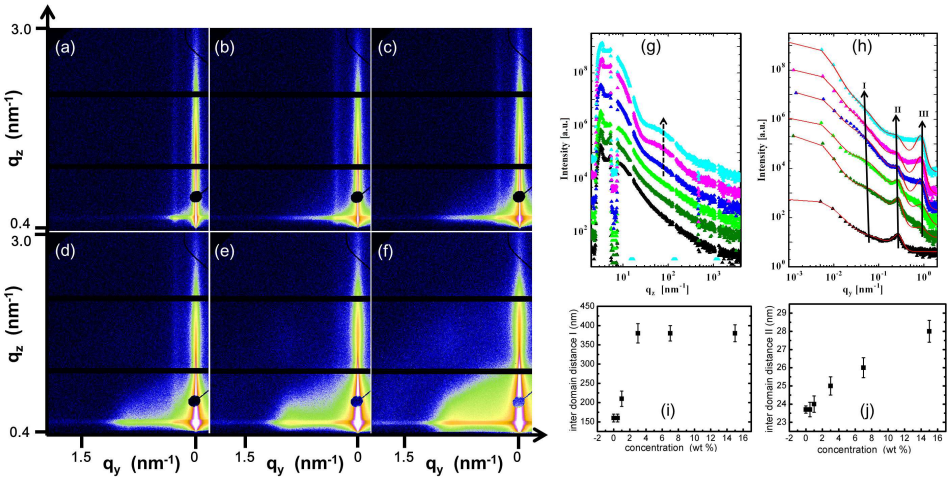

Figure 3.15:
a)-f) 2D GISAXS data of the metal oxide-polymer hybrid films with different nanoparticles concentrations: 0 wt%, 0.5 wt%, 1 wt%, 3 wt%, 7 wt%, and 15 wt%. g) Vertical line cuts and h) horizontal line cuts of the 2D GISAXS data (symbols) and fit (red solid line) with different nanoparticles concentrations: 0 wt%, 0.5 wt%, 1 wt%, 3 wt%, 7 wt%, and 15 wt% from bottom to top. i)-j) Inter-domain distance is plotted as a function of nanoparticles concentrations corresponding to the arrows I or II out of horizontal line cuts.

To obtain more statistical relevant data of the film structure, GISAXS measurements were performed at beamline P03 (DESY, Hamburg). The selected wavelength was λ = 0.0957 nm. The incident angle was set to α_i = 0.35°. A sample-detector distance of 2.54 m was used. The 2D GISAXS patterns show significant changes with the incorporation of the maghemite nanoparticles. From the q_y profiles, the particle-free polymer shows a characteristic peak (marked with II in Fig. 3.15h), which corresponds to an inter-domain spacing D of 23.7 nm. Upon nanoparticles incorporation, D values increases from 23.7 $\pm$ 0.2 nm to 28 $\pm$ 0.6 nm for the nanoparticle concentrations up to 15 wt% (Fig. 3.15j). The increase is attributed to the selective swelling of the nanoparticles in the PS domains. An additional broad peak (I) (Fig. 3.15h) which indicates an increased characteristic distances of 160 $\pm$ 10 nm to 380 $\pm$ 22 nm (Fig. 3.15i) is attributed to the nanoparticles aggregates. The peak III (Fig. 3.15h) indicates the form factor contribution of isolated nanoparticles (constant diameter 6 $\pm$ 0.5 nm).
In summary, the particle-free P(S-*b*-NIPAM) diblock copolymer film shows an ordered parallel cylinder nanostructure. Incorporation of maghemite nanoparticles induces morphological transition to perpendicular cylinder alignment. The PS domains swell the embedded nanoparticles up to a critical concentration. Coalescence of nanoparticles at high particle content appears to move up on top of the polymer film surface and form large size particle aggregates.

[1] E. Metwalli, J.-F. Moulin, J. Perlich, W. Wang, A. Dietert, S. V. Roth, P. Müller-Buschbaum, *Langmuir* **25**, 11815 (2009)

[2] J. J. Chiu, B. J. Kim, E. J. Kramer, D. J. Pine, *J. Am. Chem. Soc.* **14**, 5036 (2005)

3.9 Investigation of the near-interface composition in pressure sensitive adhesives at the adhesive-adherent interface

M. Schindler, S. Pröller, T. Geue[1], P. Müller-Buschbaum
[1] PSI, Villigen, Switzerland

The formation of mechanical bonds between different kinds of materials using pressure-sensitive adhesives (PSAs) is still conquering new fields of application [1]. Their fast and permanent tack, the low force necessary for bonding compared to the release energy, as well as the low weight of the joint or the nearly residual free removal from the adherent are just some of many important features of PSAs, which make them the candidate of choice for the establishment of mechanical joints in many cases. Reasons for this are for example their comparably low costs or the fact that the structure of the joined parts does not need to be weakened compared to e.g. the use of screws. Very different kinds of materials, e.g. paper, glass, polymers and metal can not only be joint by common adhesives like epoxies, but also by PSAs [2]. Earlier measurements using X-ray reflectivity (XRR) have shown that the freshly cast film exhibits an enrichment of one component at the surface, e.g. in case of a statistical copolymer [3-5]. This enrichment results in an altered adhesive performance. The even more important aspect in adhesion science is the inner structure and composition of the adhesive-adherent interface. This buried interface is no longer accessible with X-rays due to high absorption.

The tool of choice in this study is neutron reflectivity (NR), offering very low absorption and no beam damage, providing information about possible enrichment layers at the interface of cleaned silicon and the model PSA P(EHA-stat-20dMMA). It is a statistical copolymer consisting of 80% ethylhexylacrylate and 20% deuterated methylmethacrylate. Partial deuteration of the MMA component enhances the contrast in the neutron scattering experiment. Two different cleaning procedures (acidic and basic) have been applied to silicon substrates to alter the surface chemistry and thereby change the polymer-substrate interactions [6]. Figure 3.16a shows NR measurements with the corresponding fit for the surfaces of both samples.

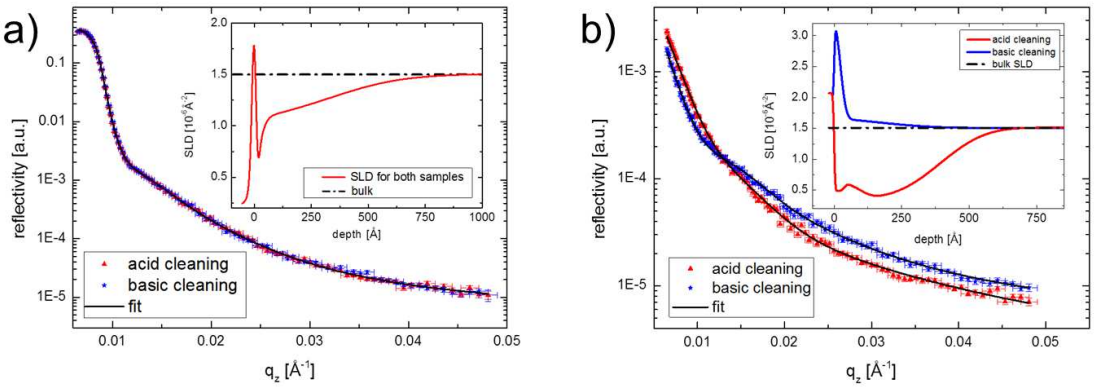

Figure 3.16:
a) NR of the adhesive-air interfaces: Both samples show the same near-surface composition as can be seen from the SLD profile in the inset. b) NR of the adhesive-adherent interfaces: Acid cleaning (red triangles) leads to an EHA enrichment, basic cleaning (blue stars) to a MMA enrichment at the interface to silicon. The SLD profiles are shown in the inset.

It is clearly visible that the different cleaning routines do not affect the surface-near region and both films therefore show the same composition in this measurement. As already mentioned

an expected MMA-enrichment is found at the very surface [4,5]. Figure 3.16b reveals the differences for the two silicon treatments: While the basic cleaning results in a hydrophilic surface, attracting the more polar MMA, the acid cleaning provides a more hydrophobic surface which is favored by the less polar EHA[7]. This leads to two very different SLD profiles, depicted in the inset.

The resulting SLD profiles of the adhesive can be translated into a gray scale-coded compositional map. These maps are shown in Fig. 3.17. The white color corresponds to pure EHA while the color black represents pure dMMA, mixtures of the two components result in different shades of gray. The y-axis denotes the distance to the interface. Remarkably, very strong differences can be seen in the interface composition of the polymer on the two differently cleaned silicon substrates. This opposite behavior shows the enormous sensitivity of the polymer composition to the surface chemistry of the adherent, which might be somewhat surprising due to the fact that both samples were prepared in principle on the same adherent (silicon).

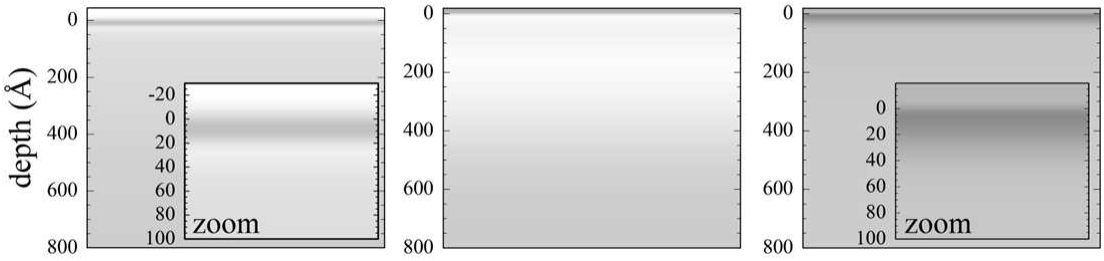

Figure 3.17:
Gray scale-coded representations of the obtained near-surface (left) and near-interface (center, right) composition profiles. For better visibility a zoom-in of the first 100$\mathring{A}$ is presented in the insets. The acidic cleaned silicon interface is shown in the center, the basic cleaned silicon on the right.

Thus, in summary neutron reflectivity, being able to access buried interfaces, is a very powerful tool for the investigation of adhesive-adherent interfaces. For P(EHA-stat-20dMMA) on Si with different surface energies a marked change in the interface-near region in the adhesive composition was observed. Other adherents have been studied as well. The analysis of the corresponding data is still in progress. This comparison will lead to a better understanding and possibly prediction of bond strength and also bond duration, two very important quantities in adhesive applications.

[1] P. Minghetti, F. Cilurzo, L. Tosi, A. Casiraghi, L. Montanari, *AAPS Pharm. Sci. Tech.* **4(8)**, 53–61 (2003)

[2] E. Maurer, S. Loi, D. Wulff, N. Willenbacher, P. Müller-Buschbaum, *Physica B*, **357**, 144–147 (2005)

[3] A. Diethert, K. Ecker, Y. Peykova, N. Willenbacher, P. Müller-Buschbaum, *ACS Appl. Mater. Interfaces* **3**, 2012-2021 (2011)

[4] A. Diethert, E. Metwalli, R. Meier, Q. Zhong, R. A. Campbell, R. Cubitt, P. Müller-Buschbaum, *Soft Matter* **7**, 6648-6659 (2011)

[5] M. Schindler, A. Kriele, P. Müller-Buschbaum, *J. Adhes.* **88**, 684-698 (2012)

[6] M. Schindler, S. Pröller, T. Geue, P. Müller-Buschbaum, *Macromol. React. Eng.* **7**, 549-554 (2013)

[7] P. Müller-Buschbaum, L. Schulz, E. Metwalli, J.-F. Moulin, R. Cubitt, *Langmuir* **24**, 7639-7644 (2008)

3.10 Reduced sheet resistance in poly(3,4-ethylendioxythiophene): poly(styrenesulfonate) with surfactant additive and multilayers

J. Schlipf, C. M. Palumbiny, P. Müller-Buschbaum

In recent years electronics made from organic materials, especially organic light emitting diodes (OLED), have seen a steady rise on the consumer market and are nowadays applied in many devices. Organic photovoltaics for instance are believed to become an alternative to conventional inorganic solar cells, even more, as their power conversion efficiency has recently surpassed 12 %. Two of their main advantages over conventional technologies are low cost and flexibility. But these two advantages are often not realized in current devices because of the brittleness and high cost of indium tin oxide (ITO) which is commonly used as a transparent electrode (TE). To circumvent this issue, many alternative materials are investigated for use as TE.
Among them poly(3,4-ethylenedioxythiophene):poly(styrenesulfonate) (PEDOT:PSS) has attracted high interest, as it is already used as an electrode blocking layer in organic solar cells. While the conductivity of pristine PEDOT:PSS is usually below 1 S cm^{-1} it can be enhanced by several orders of magnitude via so-called "doping". This often is achieved through the addition of high-boiling solvents to the PEDOT:PSS solution before processing; some examples are dimethyl sulfoxide (DMSO), glycerol or ethylene glycol (EG). The latter has also been used by Kim et al. [1] for a post-treatment of the annealed PEDOT:PSS film in a bath of EG - leading to an increased conductivity of 1418 S cm^{-1}. A study by Vosguerichtian et al. [2] revealed, that with the addition of a surfactant (DuPont Zonyl® FS-300, an aqueous solution with 40 % solid Zonyl content) to the aqueous PEDOT:PSS solution, wetting on hydrophobic surfaces becomes possible - which is important to form PEDOT:PSS multilayers as annealed PEDOT:PSS films are hydrophobic.

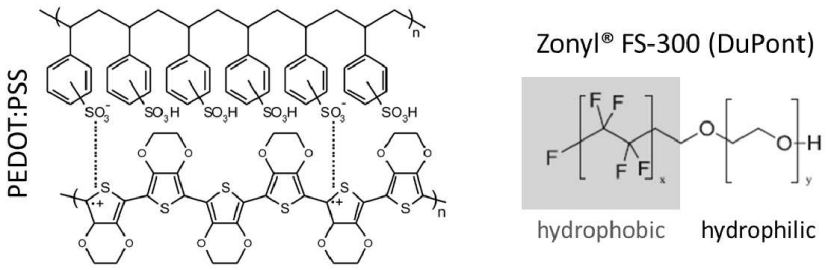

Figure 3.18: PEDOT:PSS and Zonyl molecules

In this work, the EG post-treatment has been applied to films formed from PEDOT:PSS solution with a certain amount of Zonyl solution added. To get a better idea of the electronic effect of the surfactant, a series of PEDOT:PSS films with varying Zonyl content - 0, 0.1, 1 and 10 wt% of Zonyl solution - has been produced with and without subsequent post-treatment in a bath of EG for three minutes. To further investigate the impact of multilayers on the sheet resistance, samples with one to four layers of EG post-treated PEDOT:PSS films were produced for 0.1 wt% and 1 wt% of Zonyl solution respectively. On all samples, four-point probe measurements were conducted and the sheet resistance was calculated using equation 3.1.

$$R_{sq} = \frac{\pi}{ln(2)} \frac{U}{I} \tag{3.1}$$

The results are shown in Fig. 3.19, with the value for ITO as given by the manufacturer depicted for comparison (number 15). The sheet resistances for untreated PEDOT:PSS films are much too high to be used as TE (numbers 1, 3, 8 and 13 in the figure). For pristine PEDOT:PSS with EG

post-treatment (number 2 in the figure) it is 100 $\Omega\,\square^{-1}$ and therefore in the range given by Kim et alteri. The addition of a small amount of Zonyl already reduces the sheet resistance to 70 $\Omega\,\square^{-1}$. The sheet resistance decreases almost linearly with additional layers, reaching a minimum of 30 $\Omega\,\square^{-1}$ for four layers (numbers 7 and 12 in the figure), a value comparable to ITO. For 10 wt% of Zonyl solution the sheet resistance is slightly higher, which may be an indication that this ratio is already to high as Zonyl is an insulating material and remains in the final film.

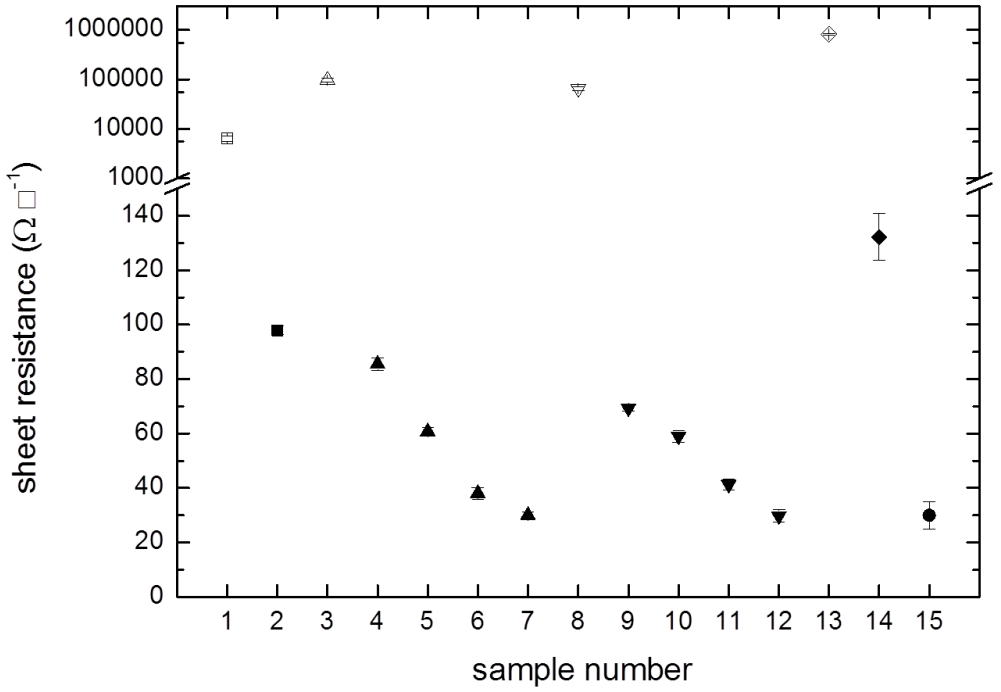

Figure 3.19: Numbers 1−14 series of PEDOT:PSS films with varying Zonyl content (indicated by symbol shape), EG post-treatment (full symbols) and multilayers: pristine without (1) and with EG post-treatment (2), 0.1 wt% Zonyl solution (3) with EG post-treatment and increasing number of layers (4-7), 1 wt% Zonyl solution (8) with EG post-treatment and increasing number of layers (9-12), 10 wt% Zonyl solution (13) with EG post-treatment (14); 15 ITO

To evaluate the quality of TE, equation 3.2 connects the sheet resistance with the transmission:

$$T(\lambda) = \left(1 + \frac{188.5}{R_{sq}} \frac{\sigma_{op}(\lambda)}{\sigma_{dc}} \right)^{-2} \tag{3.2}$$

Using $\frac{\sigma_{dc}}{\sigma_{op}(\lambda)}$ as a figure of merit (FoM) to compare different types of TE, a value of 35 is considered necessary for the use in most practical devices, whereas LCD screens and similar devices need TE with a FoM of at least 50. UV-Vis transmission measurements on our samples showed that four layers of Zonyl:PEDOT:PSS still exhibit a 79% transmission, whereas one layer transmits almost 92%. This corresponds to FoM of 50 or 73 respectively, which are comparable to the values of ITO or graphene (around 120).
In total, the low sheet resistance combined with the good light transmission allow the application of PEDOT:PSS as TE to fully utilize the advantages of ITO-free organic electronics.

[1] Y. H. Kim, C. Sachse, M. L. Machala, C. May, L. Müller-Meskamp, K. Leo, *Adv. Funct. Mater.* **21**, 1076-1081 (2011)

[2] M. Vosguerichtian, D. J. Lipomi, Z. Bao, *Adv. Funct. Mater.* **22**, 421-429 (2012)

4 Polymer films for applications in photovoltaics

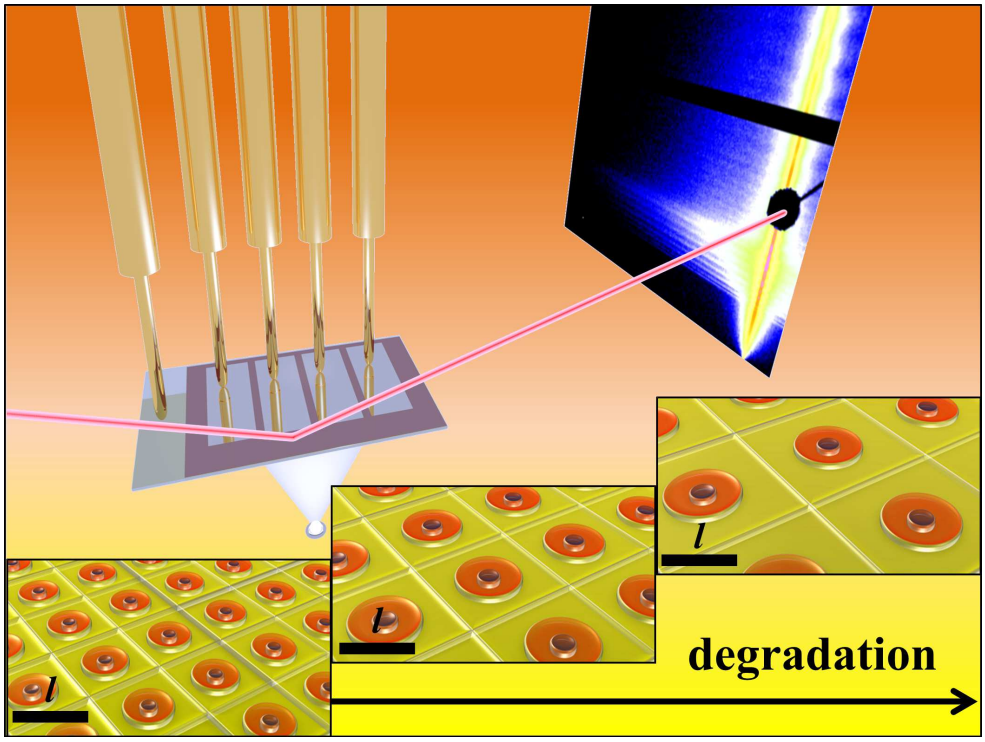

4.1 The effect of fluorination in manipulating the nanomorphology in the PTB7:PC_{71}BM bulk heterojunction system

S. Guo, J. Ning, V. Körstgens,Y. Yuan, E. M. Herzig, S. V. Roth, J. Perlich[1], P. Müller-Buschbaum

[1] DESY, Hamburg, Germany

Rapid progress has been envisioned on the solution-processed organic solar cells in the past decade, and the efficiency has exceeded the threshold for commercial application of 10%. [1] Combined with the attempting advantages of lightweight, flexibility, and potentially low cost, polymer-based solar cells have become one of the most promising technology in the field of renewable green energy. In this work, the record setting system, the PTB7-Fxx:PC_{71}BM family with incorporation of different amounts of fluorine atoms at same position along the polymer backbone, was thoroughly investigated, to address the relation between the morphology and efficiency. Atomic force microscopy (AFM) is used to reveal the real space information of the active layer surfaces. Together with the reciprocal space information probed by grazing incidence small angle x-ray scattering (GISAXS) measurements, the whole morphology of the active layer is obtained. As a result, the best polymer for PTB7-Fxx:PC_{71}BM BHJ solar cells can be identified, and the reason is clarified.

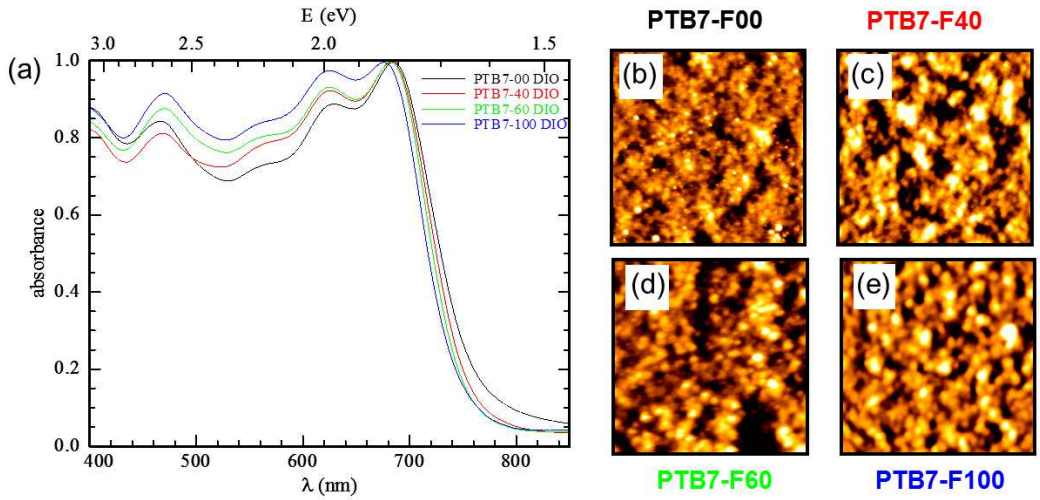

Figure 4.1:
a) Normalized absorption spectra of PTB7-Fxx:PC71BM films made of the solvent mixture chlorobenzene/DIO (97:3). b)-e) corresponding AFM topographic images.

In Fig. 4.1a, the absorption curves of active layers spin-coated from PTB7-Fxx:PC_{71}BM blend solutions with same concentration are presented. As seen from this figure, all the absorption curves follow a linear superposition of the corresponding individual spectra [2], implying that significant ground-state charge transfer does not occur in these films [3].
Figure 4.1b-e presents the AFM images of active layers of PTB7-Fxx:PC_{71}BM films made of solvent chlorobenzene/DIO. From all the topography images with DIO, it is observed that the intermixing effect introduced by DIO is much more pronounced for the non-fluorinated blend film than for highly fluorinated films, as PC_{71}BM clusters are still visible in those films. Besides the topography and roughness information of the samples which can be obtained from AFM, the characteristic length scale of the surface structure is extracted via the power spectral density function (PSD) of AFM measurements. The PSD of the films is shown in Fig. 4.2a.

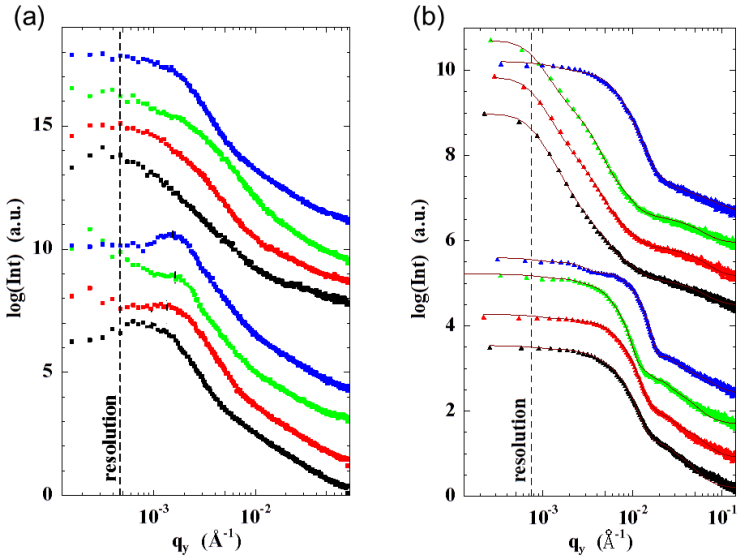

Figure 4.2:
(a) PSD curves of the AFM data of all the samples and (b) Out-of-plane cuts from the GISAXS 2d data. All curves are shifted along the y-axis for more clarity.

To access the inner film morphology, GISAXS measurements are performed on all samples made of different degree of fluorine content. By analyzing the out-of-plane cuts of the 2D GISAXS data via fitting them with a 1D paracrystal model within the frame of the distorted wave Born approximation (DWBA) (see Fig. 4.2b), the specific structural information is obtained. In this model, contributions from two different structure and form factors, as well as the resolution function, are considered. The most prevailing structure for as-spun films is $PC_{71}BM$ aggregated clusters at around 250 nm, which is comparable with the film surface structure extracted from PSD spectrum of AFM. After adding DIO, the domain sizes decrease from hundred nanometer length scale close to the excition diffusion length (25 nm), both on the film surface and inside the films due to DIO can selectively dissolve $PC_{71}BM$. Correspondingly, the structural peaks shift to higher q values. The extracted structure sizes for the varied degree of fluorination are in good agreement with the performance of the corresponding solar cell devices: The DIO included samples give rise to relatively higher efficiency due to the evident minimized structure size. Higher amount of fluorine give rise to smaller domain size inside the films, and thus higher charge dissociation rate and higher efficiency [4]. Further data analysis is still undergoing.

[1] M. A. Green, K. Emery, Y. Hishikawa, W. Warta, E. D. Dunlop, *Prog. Photovolt: Res. Appl.*, **21**, 827 (2013)

[2] H. Wang, X. Yu, C. Yi, H. Ren, C. Liu, Y. Yang, S. Xiao, J. Zheng, A. Karim, S. Z. D. Cheng, X. Gong, *J. Phys. Chem. C*, **117**, 4358 (2013)

[3] A. C. Arias, J. D. Mackenzie, R. Stevenson, J. J. M. Halls, M. Inbasekaran, E. P. Woo, D. Richards, R. H. Friend, *Macromolecules*, **34**, 6006 (2001)

[4] S. Guo, J. Ning, V. Körstgens, Y. Yuan, E. M. Herzig, S. V. Roth, J. Perlich, P. Müller-Buschbaum, in preparation (2014)

4.2 Structural degradation in excitonic solar cells

C. J. Schaffer, C. M. Palumbiny, M. A. Niedermeier, C. Jendrzejewski, G. Santoro[1], S. V. Roth[1], P. Müller-Buschbaum

[1] DESY, Hamburg, Germany

With their potential for a cheap and versatile source of electricity, organic photovoltaics provide a promising technology with a vast variety of applications due to their mechanical flexibility and their potential semitransparent appearance. Thus, research has not only been focused on the increase of power conversion efficiency of organic solar cells but also on processing methods and their stability. With reported efficiencies as high as 12% and the evidenced potential of being fabricated by roll-to-roll printing, this technology has advanced closely towards mass production [1]. However, less improvement was found concerning the stability of organic photovoltaics. With typical lifetimes in the order of several thousand operating hours, organic solar cells are not yet competitive to their inorganic counterparts. Although several pathways of OPV degradation have been discovered by now, it is expected that further degradation mechanisms take place. One of these mechanisms arises from potential changes in the nanometer-scaled morphology of the active photovoltaic layer during solar cell operation. Although such an assumption has been stated frequently in literature, it could not be experimentally evidenced until the very first simultaneous in-situ investigation on the nano scale morphology and the photovoltaic performance of a model polymer solar cell during an early stage of operation has been presented in this year [2], which is the subject of the present report. Other than in inorganic solar cells, the energy of absorbed photons cannot be directly used to generate free charge carriers in inorganic solar cells. It needs to be transported as an exciton to an interface between conducting polymer and fullerene domains, where free charge carriers can consequently be generated. As the range of an exciton is limited by the exciton diffusion length, which is typically in a range of several up to few ten nanometers in a polymer, it is crucial that the morphology of the polymer-fullerene blend layer matches to the exciton diffusion length, since an exciton is lost if it cannot reach a domain interface before recombining. Thus, there is an effective volume fraction within the organic blend layer, where generated excitons can reach such an interface and split into free charge carriers, i.e. where absorbed photons can be converted to electrical power. By performing in-situ grazing incidence small angle X-ray scattering (see Fig. 4.3) on a running P3HT:PCBM (poly(3-hexylthiophen-2,5-diyl): [6,6]-phenyl-C61-butyric acid methyl ester), a growth both of domains and their inter distance could be observed, as depicted in Fig. 4.4 (R_2 and d_2). In a model these domains are assumed as standing cylinders which are surrounded

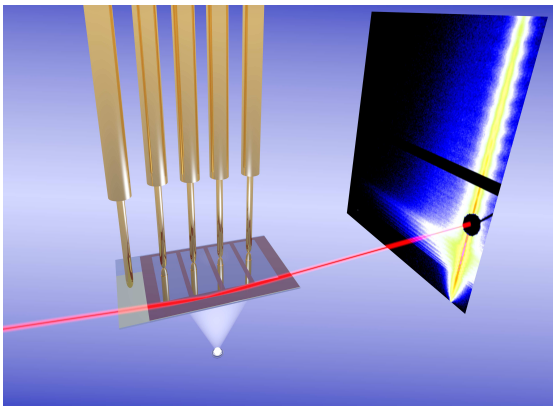

Figure 4.3:
Schematic representation of the experimental setup: The X-ray (coming from the left) impinges the active area of a polymeric solar cell and draws a scattering pattern on a 2-dimensional detector (right). Simultaneously, the solar cell is illuminated by simulated sun light (from the bottom). The IV-characteristics are probed via gold contacts (contacting the solar cell from the top).

by a belt where current generation is allowed (spots in the inlets of Fig. 4.5). In this model our observation implies an absolute loss of the overall volume where photons can be converted into an electric current. This results in a loss of short-circuit current (see black squares in Fig. 4.5).

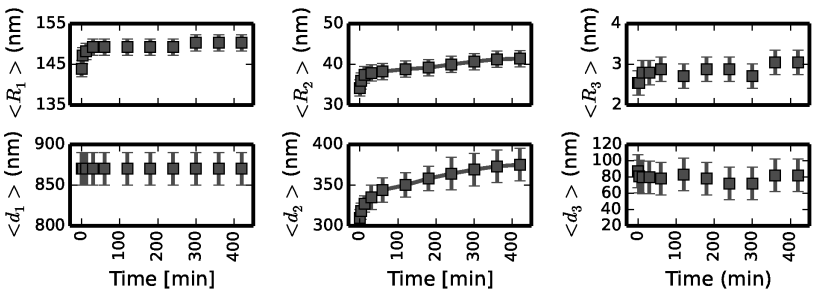

Figure 4.4:
Evolution of domain length scales with time: Modeling the data obtained from GISAXS reveals 3 different substructure length scales from which only the intermediate one leads to current generation. The corresponding domain sizes R_2 and inter distances d_2 display to grow with time.

As the current-voltage characteristics of the investigated solar cell could be simultaneously measured during the in-situ GISAXS experiment, the decay of short-circuit current could also be tracked during solar cell operation (dashed line in Fig. 4.5). From the very good agreement of measured and predicted short-circuit current we inferred that, in this case, the morphological changes are the main driving force for organic solar cell degradation, thus giving rise to a direct evidence of morphological degradation on a nanometer scale in organic photovoltaics.

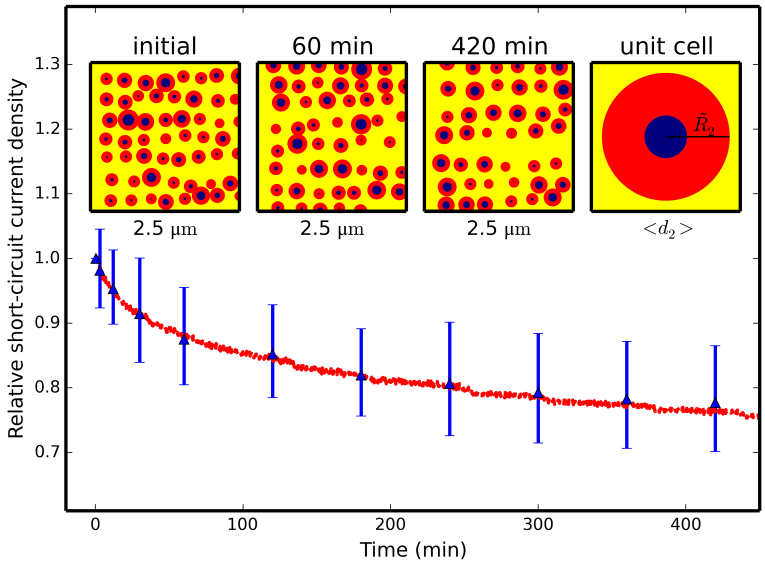

Figure 4.5:
Short-circuit current density and intermediate domain distribution as a function of time: The triangle markers represent the normalized short-circuit current as expected from GISAXS results (see Fig. 4.4) at different times. The dashed line shows the eventual normalized short-circuit current as measured as a function of time. The insets a)-c) show a simulated sketch of intermediate domain distribution (centered dots) and the active area around these domains (rings around centered dots). Inset d) displays a hypothetic unit cell corresponding to a square lattice.

[1] M. A. Green, K. Emery, Y. Hishikawa, W. Warta, E. D. Dunlop, *Prog. Photovolt. Res. Appl.* **21**, 827-837 (2013)

[2] C. J. Schaffer, C. M. Palumbiny, M. A. Niedermeier, C. Jendrzejewski, G. Santoro, S. V. Roth, P. Müller-Buschbaum, *Adv. Mater.* **25** (46), 6760-6764 (2013)

4.3 In-situ GIWAXS study of slot-die coated highly conductive PEDOT:PSS

C. M. Palumbiny, F. Liu[1], A. Hexemer[2], T. Russel[1], C. Wang[2], P. Müller-Buschbaum

[1] University of Massachusetts Amherst, Amherst, USA
[2] Advanced Light Source, LBNL, Berkeley, USA

The semi-transparency and potential to up-scale devices to large areas, makes organic electronics (OE) and organic photovoltaic devices (OPV) highly interesting for implementation e.g. into buildings. Further their adaptability due to their flexibility and light weight open up additional applications such as portable modules. One of the main advantages for all applications is the potential of easy up-scaling by printing technologies such as roll to roll (R2R) with slot die coating. However, most investigations of morphology, crystallinity and electronic properties of thin films for OPV are based on lab-scale techniques as spin coating. The growth of thin films, however, crucially depends on the conditions during film deposition and film treatment.

To follow the film formation in-situ, a self-made slot-die coater is implemented to the grazing incident wide angle X-ray scattering (GIWAXS) setup of the beamline 7.3.3. at the Advanced Light Source (ALS) of the Lawrence Berkeley National Laboratory (LBNL) in Berkeley. The slot die coater was realized in cooperation between UMass Amherst and ALS. With the high flux of the synchrotron beam and a low background due to a helium atmosphere, a good time resolution for the in-situ study of the film formation kinematics is realized.

Typically, oxide materials such as indium tin oxide (ITO) are used as transparent conductive electrodes (TCE) in the fabrication process for organic solar cells or light emitting diodes. ITO however has several drawbacks which become obvious if aiming for up-scaling of OEs. Its high cost of ITO and the limited existence of indium are limiting factors, but also the brittleness of ITO under bending [1] plays a crucial role. Thinking of flexible devices, this is one of the main advantages of OPV devices over conventional PV. Several attempts have been made to substitute ITO as an electrode. In this context, the polymer blend poly(3,4-ethylenedioxythiophene):poly(styrene-sulfonate) (PEDOT:PSS) has attracted high attention. This is mainly due to its advantageous properties such as transparency, easy processability, as dispersed in water and stability upon bending. Further, PEDOT:PSS is already implemented in organic electronic devices. To use PEDOT:PSS directly as an electrode, however, it is still lacking in conductivity. Blending with high boiling point co-solvents is known to increase the conductivity of PEDOT:PSS from 10 S/cm by three orders of magnitude. This makes it comparable to the conductivity of ITO and suitable as an electrode alternative in OEs.

In this study we investigate the structural evolution upon film drying for the polymer blend PEDOT:PSS dispersion in water (Heraeus Clevios PH1000, 1:2.5) doped with 6 vol% of ethylene glycol (EG). With this mixture conductivity values of PEDOT:PSS comparable to ITO conductivity can be realized as reported by Kim et al [2] and be used directly as an electrode which is flexible, transparent and stable upon bending. Since PEDOT has an anisotropic conductivity, special focus is on the $\pi - \pi$ stacking of the molecules within the crystallites from which the molecular orientation can be estimated [3]. It is known that adding non-acidic organic co-solvents with high boiling point and strong polarity, e.g. ethylene glycol (EG) as used in this work, increases the conductivity up to the order of 1000 S/cm, the order of ITO conductivity. Thereby, the co-solvent is believed to act as a structuring agent for the resulting film morphology and influences the crystallinity of the film.

For a good resolution in time and relevant statistics, measuring times of 5s without time delay were used and measured for a total time of 600 s. With this procedure, it is possible to follow

the structure evolution of EG post treated PEDOT:PSS during drying as shown in Fig. 4.6. The film was coated with a flow rate of 2 ml/min on an aligned silicon substrate which was kept at 50 °C for a homogeneous film.

Figure 4.6 shows the film formation from top to bottom. Directly after film deposition the scattering signal of water dominates the two dimensional scattering. With evaporation of the water, a strong signal of the randomly oriented PSS becomes apparent around $15.5\ \mathrm{nm}^{-1}$. Upon further drying of the film the scattering from the PEDOT $\pi - \pi$ stacking becomes evident at $18.5\ \mathrm{nm}^{-1}$ and increases in intensity compared to the PSS scattering indicating a crystallization of PEDOT during the drying of the film. As last step a shift in the PSS peak from $15.5\ \mathrm{nm}^{-1}$ to $13.0\ \mathrm{nm}^{-1}$ is observed. The shift to lower q values indicates a swelling of the PSS.

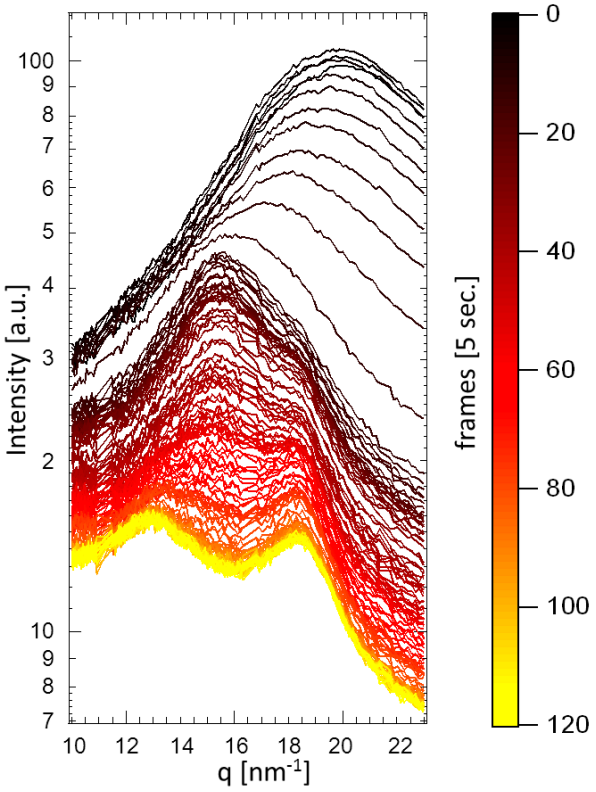

Figure 4.6:
In-situ evolution of slot die coated PEDOT:PSS doped with 6vol% EG. From top to bottom the dying of the film is shown, starting with the evaporation of water and ending with a dried highly conductive PEDOT:PSS film showing the scattering from PSS as well as from the PEDOT $\pi - \pi$ stacking.

Concluding, using the slot die coating deposition method and combining it with GIWAXS measurements, we are able to follow the film evolution during drying for highly conductive PEDOT:PSS. The film formation is divided into five film formation steps: water evaporation, appearance of a randomly oriented PSS scattering, PEDOT crystallization, increase is PEDOT crystalline amount and a swelling of the PSS. These results can be directly used for directed modification of PEDOT:PSS films for optimized properties and for R2R processing for practical devices.

[1] S.-I. Na, S.-S. Kim, J. Jo, D.-Y. Kim, *Adv. Mater.* **20**, (21), 4061-4067 (2008)

[2] Y. H. Kim, C. Sachse, M. L. Machala, C. May, S. V. Müller-Meskamp, L. Leo, *Adv. Funct. Mater.* **21**, (6), 1076-1081 (2011)

[3] C. M. Palumbiny, C. Heller, C. J. Schaffer, V. Körstgens, G. Santoro, S. V. Roth, P. Müller-Buschbaum, *under peer review* (2014)

4.4 The influence of solvent atmosphere on bulk heterojunction solar cells

W. Wang, S. Guo, J. Perlich[1], P. Müller-Buschbaum

[1] DESY, Hamburg, Germany

Organic solar cells have attracted tremendous attention in the last decades. Among different architectures of the solar cell, the morphology called bulk heterojunction (BHJ) plays an important role as it yields high device efficiencies [1]. Many ways are used to optimize the morphology of BHJ films such as thermal annealing, solvent annealing or solvent additive processing [2]. However, if a solar cell encapsulation is taken into account, it is also crucial to figure out how solvent atmosphere, evaporated from residual solvent, affects the solar cells, especially for the one treated with solvent.
For this purpose, BHJ solar cells, with the active layer of poly(3-hexylthiophen):[6,6]-phenyl C_{61}-butyric acid methyl ester (P3HT:PCBM) blends, are stored in solvent atmosphere to accelerate the related aging. It is found that the BHJ solar cells kept in solvent atmosphere for 5 days degrade. In order to gain the fundamental understanding, optical microscopy (OM) and atomic force microscopy (AFM) are used to reveal the final structure of aged BHJ films. Additionally, the crystalline structure is investigated with grazing incidence wide angle X-ray scattering (GIWAXS).
The BHJ solar cells are made of four different solvents, chlorobenzene (CB), toluene (T), xylene (Xy) and 1,2-dichlorobenzene (DCB), respectively. Two series of solar cells are prepared in the same condition. One is measured directly after the preparation, used as the references, and the other is kept in respective solvent atmosphere for 5 days. Through investigation of both series of solar cells photovoltaic performance, it is found that the cells kept in CB, T and Xy atmosphere show heavy degradation, with the efficiency reduced to values lower than 0.1% and the short circuit current (I_{SC}) lower than 0.5 mA/cm^2. In contrast, the solar cell aging in DCB atmosphere shows less degradation than the others, with efficiency of 0.74% and I_{SC} of 5.4 mA/cm^2.

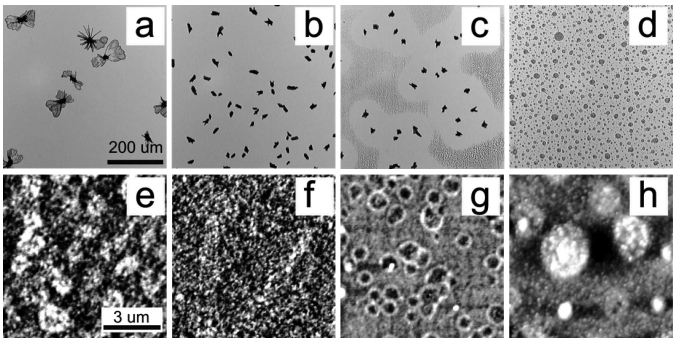

Figure 4.7:
OM and AFM images of BHJ films aging in a), e) CB; b), f) T; c), g) Xy; and d), h) DCB atmosphere for 5 days.

In order to investigate the surface morphology of the aged BHJ films, the OM images are shown in Fig. 4.7. The PCBM aggregates with micrometer length scales are observed in the BHJ films aging in CB, T and Xy atmosphere. The elongated PCBM aggregates lead to large scale segregation of the P3HT and PCBM components, which raises the probability of the recombination of excitons generated in P3HT phase, therewith the prominent decrease of I_{SC} of solar cells which age in CB, T and Xy atmosphere. Differently, the dewetting behavior of the blends instead of large PCBM aggregates is observed in the sample aging in DCB atmosphere. In order to probe the surface morphology in much smaller scale, AFM measurements are applied, escaping the PCBM aggregates region, and also shown in Fig. 4.7. The morphology of sample aging in CB or T atmosphere shows that P3HT and PCBM components still mix well, while for the sample aging in Xy atmosphere shows PCBM aggregates, distributing in

the mixing region. Among all the samples, the one aging in DCB atmosphere shows the finest mixture between P3HT and PCBM phase, which gives the reason for the highest I_{SC} of solar cell compared to the others, however the similar dewetting phenomena shown in OM image is also observed in this smaller scale. In addition, the roughness of all the samples can be extracted from the AFM measurements. All the samples show an increased surface roughness compared to the individual fresh sample, especially for the one kept in DCB atmosphere.
GIWAXS measurements are performed on the aged BHJ films to investigate the crystalline order of each component of P3HT and PCBM. The cake cuts in vertical and horizontal directions are shown in Fig. 4.8. In order to describe the P3HT crystalline information, (100), (200), (300) and (010) vectors are marked. (100) vector as well as its higher orders are scattered along the direction of P3HT side chain and (010) vector is scattered along the π-π stacking direction of P3HT. As observed in the image, just (100) and (010) peaks are clearly visible in the horizontal cake cuts, while (200) and (300) peaks also shows the strong scattering intensity in vertical cuts. Further, the lattice constants of P3HT crystallite are extracted from the peak position and the P3HT crystallite size is calculated from Scherrer's equation. All the aged samples show lattice constant around 1.70 nm for (100) vector, which is the same as the thermal annealed samples. However, the lattice constant of (010) direction is around 0.40 nm, 5% larger than that of thermal annealed samples (0.38 nm). The increase of the lattice constant in (010) direction can be explained by the diffusion of PCBM molecular to the space between P3HT π-π stacking. The crystallite size of P3HT is much smaller than that of thermal annealed samples, which is also the evidence that large PCBM aggregates hinder P3HT crystallization therefore the smaller crystallite size is observed. Additionally, the sample aging in DCB atmosphere shows quite smooth PCBM scattering peaks which are related to the randomly distributed PCBM amorphous phase or tiny crystallites, whereas for the sample aging in the other solvent atmosphere the PCBM scattering peaks are quite sharp or show lots of oscillations, even some with high intensity, which predicts that large PCBM crystallites are formed during aging period.

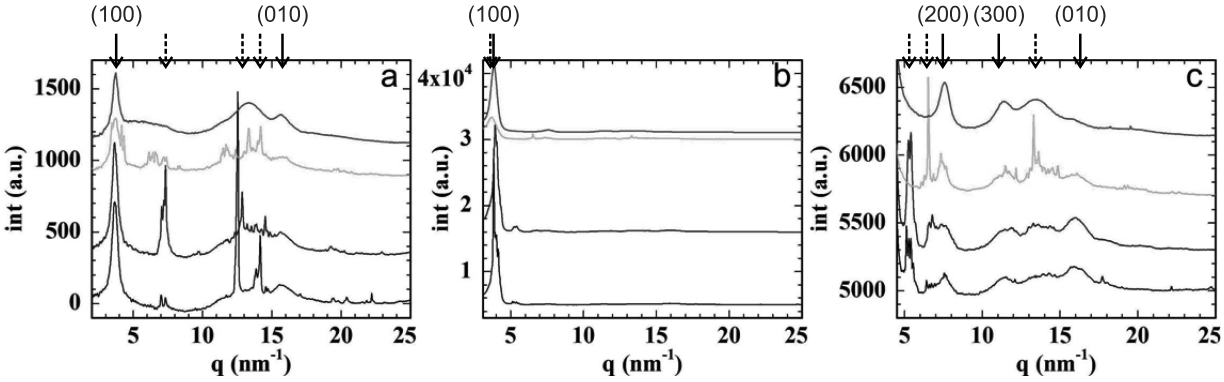

Figure 4.8:
GIWAXS cake cuts in a) horizontal direction and b) vertical direction of BHJ films aging in CB, T, Xy and DCB for 5 days, which are presented from bottom to the top. To clarify the higher order above P3HT (100) peak in vertical cuts, the curves are shifted in c). The solid arrow represents the reflection from P3HT and the dot arrow is related to PCBM.

In summary, BHJ solar cells age in solvent atmosphere. During aging period, large PCBM aggregates are formed, which decreases the mixing of P3HT:PCBM and also hinders the crystallization of P3HT. This is the main reason for solar cells degradation.

[1] C. Deibel, V. Dyakonov, *Rep. Prog. Phys.* **73**, 096401 (2010)

[2] M. A. Ruderer, S. Guo, R. Meier, H. Chiang, V. Körstgens, J. Wiedersich, J. Perlich, S. V. Roth, P. Müller-Buschbaum, *Adv. Funct. Mater.* **21**, 3382-3391 (2011)

4.5 Crystallinity of an aqueous-processable conducting polymer for applications in environmental friendly organic solar cells

S. Pröller, V. Körstgens, S. Yu[1], S. V. Roth[1], P. Müller-Buschbaum

[1] DESY, Hamburg, Germany

A widely used polymer for applications in the active layer of organic solar cells is poly(3-hexylthiophene) (P3HT). This polymer is object of several studies and one of the most investigated conducting polymers. P3HT is soluble in several organic solvents, among others chloroform, chlorobenzene or toluene. As these solvents are not environmental friendly and partly even toxic other polymers are needed on the way to eco-friendly organic solar cells. One possibility for fully 'green' organic solar cells is the use of polymers which can be dissolved in water. Poly[3-(potassium-6-hexanoate)thiophene-2,5-diyl] (P3P6T) is a derivative of P3HT having a potassium carboxylate salt side chain group. This side chain group yields P3P6T to be processable out of an aqueous solution. Thalluri et al. investigated among others P3P6T and found it to work well in hybrid solar cells [1]. However, they found the P3P6T layer to be amorphous when compared to the crystalline layer of P3HT. No other studies on the crystallinity of P3P6T are reported up to date.

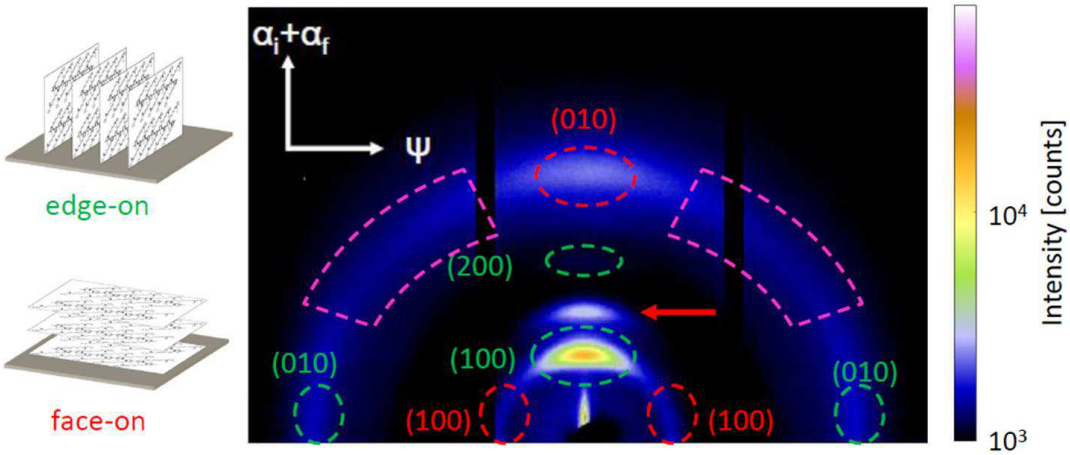

Figure 4.9:
Two dimensional GIWAXS data showing the diffraction pattern of a P3P6T film. Peaks arising from the crystallinity of the film are clearly visible. On the left part sketches of edge-on and face-on orientated crystals are shown. The respective peaks which are expected in the GIWAXS pattern are highlighted in green and red respectively. The crystal planes according to the well known P3HT are denoted. Further attributes are marked by a red arrow and purple boxes.

The crystallinity of a thin polymer film is of high interest in terms of efficient solar cells [2]. For high charge carrier mobility, local scale ordering appears to be essential [3]. As the UV/Vis absorption spectrum shows an absorption shoulder which can be attributed to crystal phases in the film, more detailed investigations are performed in order to elucidate and optimize the crystallinity of the P3P6T thin films. Therefore X-ray diffraction (XRD) as well as grazing incidence wide angle X-ray scattering (GIWAXS) are performed. The first one yields detailed information about the diffraction intensities while the latter one elucidates the orientation of a crystal due to the two dimensional detector.

In Fig. 4.9a recorded GIWAXS pattern is depicted. Furthermore, sketches of two possible crystal arrangements, edge-on and face-on, are shown. Due to the lack of literature for P3P6T, the data are compared to the well known diffraction patterns of P3HT [2]. The (100) and (010) crystal planes can clearly be attributed for both, the edge-on and face-on orientation. In vertical direction an additional peak, highlighted by a red arrow, is seen. Additionally, encircled in purple, a diffraction intensity in diagonal direction is found which could indicate a powder like distribution of the crystals. Detailed investigations on the crystal orientation results in predominantly edge-on oriented crystals. This, however, needs further explanations for the high intensity of the (010) peak in vertical direction.
A model of the crystal arrangement of P3P6T is proposed in Fig. 4.10. The inset shows the respective XRD pattern in vertical direction. The diffracting distances in the crystal model are highlighted with the same color as in the inset. Using this model, the high intensity of the peak at the (010) position can be explained by the distances between the side chain end groups to each other and the backbone. The peak which can not be seen in P3HT diffraction patterns in the vertical direction (red arrow in Fig. 4.9) can be explained the same way but to next nearest neighboring side chain end groups or backbones. The reason for the difference might be the higher electron density in the end groups. Furthermore, the ring-like diffraction intensity occurs from the distances between the side chains which are oriented in a diagonal manner.

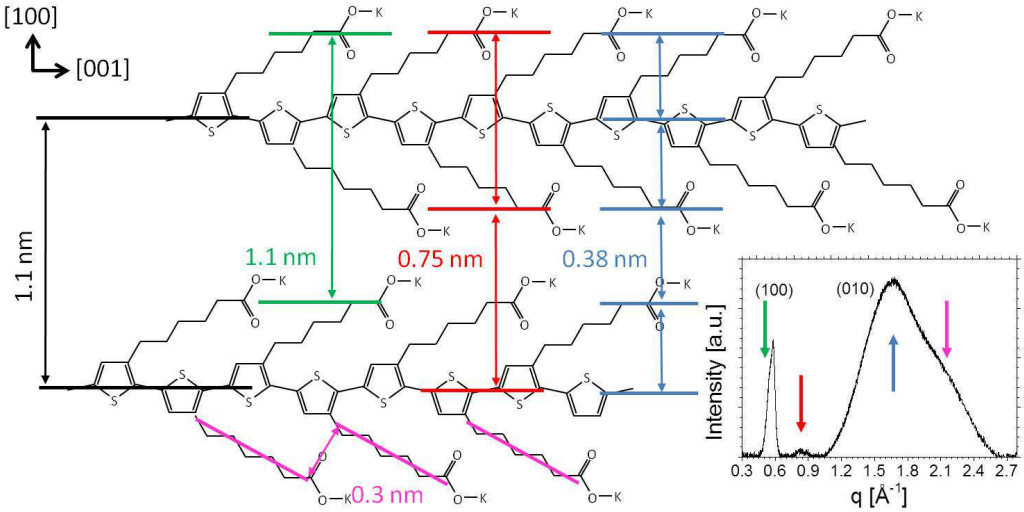

Figure 4.10:
A possible arrangement of the P3P6T in a crystal explaining the structures observed in the diffraction pattern. The inset shows a XRD pattern in which the observed crystal structures are highlighted by arrows in the respective color.

In conclusion, the crystalline properties of thin P3P6T films have been shown which further promotes the way to 'green' organic solar cells via the aqueous processable polymer. Using the proposed model, the different observed diffraction peaks can be explained.

[1] G. K. V. V. Thalluri, J.-C. Bolsace, A. Gadisa, M. Parchine, T. Boonen, J. D'Haen, A. E. Boyukbayram, J. Vandenbergh, T. J. Cleij, L. Lutsen, D. Vanderznde, J. Manca, *Sol. Energ. Mat. Sol. Cells* **95**, 3262-3268 (2011)

[2] U. Zhokhavets, T. Erb, G. Gobsch, M. Al-Ibrahim, O. Ambacher, *Chem. Phys. Lett.* **418**, 347-350 (2006)

[3] J. Rivnay, S. C. B. Mannsfeld, C. E. Miller, A. Salleo, M. F. Toney, *Chem. Rev.* **112**, 5488-5519 (2012)

4.6 Effect of solvent treatment on PTB7:$PC_{71}BM$ film system

B. Cao, S. Guo, J. F. Moulin[1], P. Müller-Buschbaum

[1] MLZ, Garching, Germany

Recently, organic photovoltaics have attracted tremendous attention due to its unique advantages such as lightweight, mechanically flexible and potentially low-cost compared with traditional silicon-based photovoltaics. Additionally, it has made rapid progress in the improvement of the power conversion efficiency, and has exceeded 10% in 2012 [1].
In the present research, the most promising polymer:fullerene bulk heterojunction PTB7:$PC_{71}BM$ system is investigated. It is reported previously by Heeger's group that methanol treatment performed after spin coating active layer can improve the device performance to certain extent. They ascribed the efficiency improvement as an increase in built-in voltage, decreased series resistance and increased mobilities [2]. However, there is no information about inner-film morphology provided, which is possibly a crucial point for the improvement of device performance [3]. Therefore, we examined the morphology of the active layers after different solvent treatment with time of flight - grazing incident small angle neutron scattering (TOF-GISANS) to investigate the morphological change induced by solvent treatment.

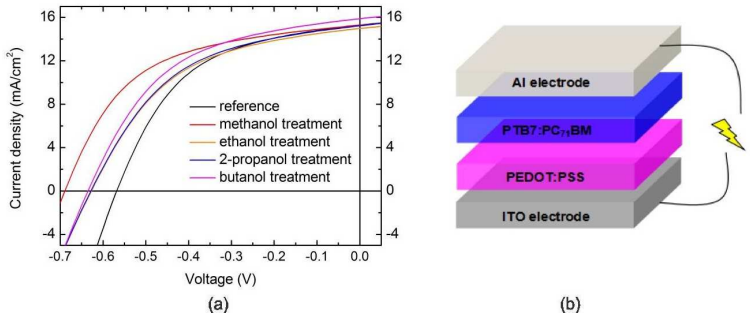

Figure 4.11:
a) Device performance of reference (without solvent treatment) and 4 devices with solvent treatment labeled on graph. b) Schematic sketch of a typical polymer:fullerene solar cell.

In the present investigation we focus on films which have been subjected to methanol, ethanol, 2-propanol and butanol treatment. As shown in Fig. 4.11, the efficiency of the reference solar cell is 4.26%, while those of solar cells with methanol, ethanol, 2-propanol and butanol treatment are 5.60%, 4.58%, 4.76% and 5.00%, respectively. It's obvious that with solvent treatments the device performance gets improved. In particular methanol treatment yields the best device performance. The improvement mainly results from the enhancement of the open circuit voltage and in crease of the fill factor.
To probe the inner-film morphology introduced by the different solvent treatments, a TOF-GISANS investigation is performed. From the 2D GISANS data at different neutron wavelengths horiziotal line cuts are extracted and fitted with one dimensional paracrystal model within the frame of the distorted wave Born approximation (DWBA). One reference sample (without solvent treatment) and four differently treated samples are compared in Fig. 4.12. Two form factors and structure factors are considered in this model. From the fitted data, a large object form factor of 500 nm and a small object form factor of 60 nm with a structure factor of 270 nm are obtained for the reference sample. For samples with different treatments, the large object form factor almost remains unchanged while the small object form

factor decreases to less than 50 nm with simultaneously decreased structure factors around 230 nm. This length scale is closer to the exciton diffusion length and thus, the decrease helps to explain the enhanced efficiency after solvent treatment. In addition, the structure/form factors at the surface and in the surface-near part (probed with higher wavelengths) are larger than inner-film structure/form factors (probed with smaller wavelengths). In summary, from our investigation, it is concluded that the morphology change introduced by the different solvent treatments can be considered as a reason leading to the improvement of the device performance. Further improvement on device performance and investigations are still in progress.

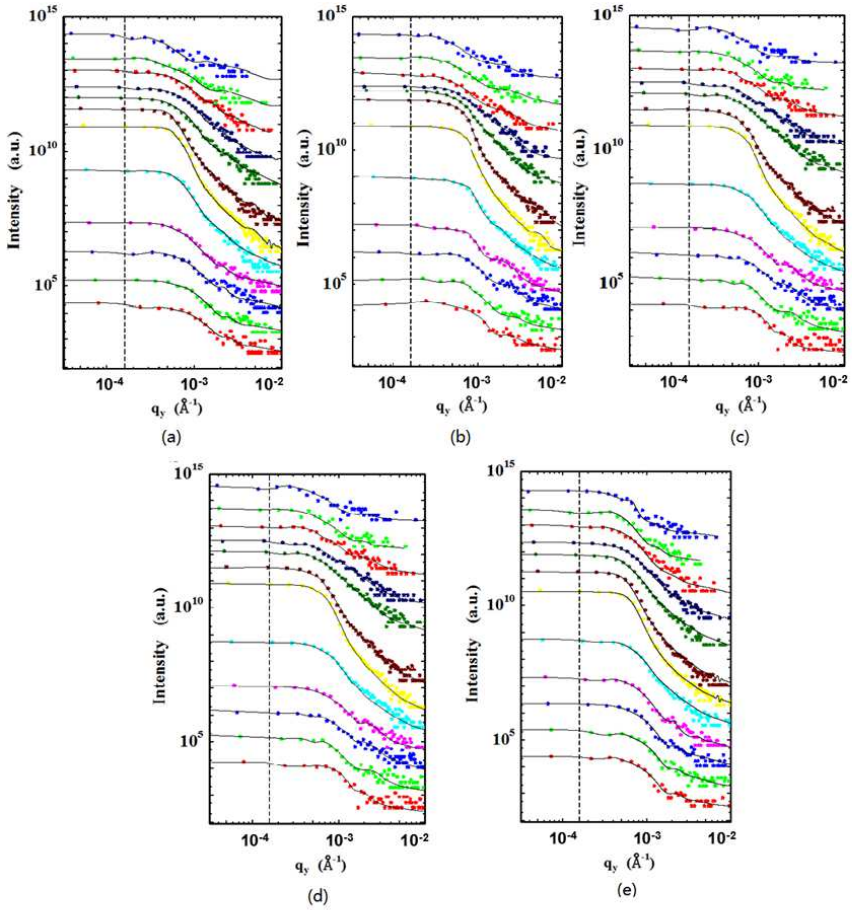

Figure 4.12:
Horizontal line cuts of the 2D GISANS data for samples with a) methanol, b) ethanol, c) 2-propanol, d) butanol treatment and e) the reference sample. Wavelengths are varying from 5.25 Å to 10.75 Å with a step of 0.5 Å. All curves are shifted along y-axis for clarity.

[1] M. A. Green, K. Emery, Y. Hishikawa, W. Warta, E. D. Dunlop, *Prog. Photovolt. Res. Appl.* **22**, 1-9 (2014)

[2] H. Zhou, Y. Zhang, J. Seifter, S. D. Collins, C. Luo, G. C. Bazan, T. Nguyen, A. J. Heeger. *Adv. Mater.* **20**, 1646-1652 (2013)

[3] M. A. Ruderer, R. Meier, L. Porcar, R. Cubitt, P. Müller-Buschbaum, *J. Phys. Chem. Lett.* **3**, 683-688 (2012)

4.7 Performance of P3HT:PCBM solar cells modified with iron oxide nanoparticles: a morphology study

D. Moseguí-González, S. V. Roth[1], P. Müller-Buschbaum
[1] DESY, Hamburg, Germany

One key feature of P3HT:PCBM solar cells that recently has aroused interest is the performance of such devices under magnetic stress. In the case of organic electronic devices, one possible route to incorporate magnetic fields consists in the addition of magnetic metal oxide nanoparticles to the system, which has been reported as a factor influencing the device performance [1]. Magnetic fields, amongst other effects, alter the position of the molecular energy levels, allowing "a priori" forbidden singlet-triplet spin transitions. Moreover, the presence of heavy metals enables a strong localized spin-orbit (L-S) coupling in the system, also increasing the rate of intersystem crossing [2]. Besides the effects of the presence of iron oxide nanoparticles on exciton energy transitions, the inclusion of nanoparticles in the organic device also alters the morphology of the components forming the active layer of the solar cell, regarding the size and arrangement of the domains of donor and acceptor materials. The mentioned influence of iron oxide nanoparticles on the morphology of the P3HT:PCBM blend films is characterized with the aid of grazing incidence small angle x-ray scattering (GISAXS) to understand the performance of organic solar cells. The GISAXS measurements were performed at the beamline P03 (DESY, Hamburg). Figure 4.13 displays the evolution of both, efficiency and fill factor, of P3HT:PCBM solar cells as a function of the concentration of iron oxide (Fe_3O_4) nanoparticles. The behavior of the efficiencies is closely related to that of the fill factor, as it is noticed from the trends in Fig. 4.13a-b. The maximum increase in efficiency is located in the region between 0.3 wt% and 1.0 wt% of Fe_3O_4 nanoparticles. The sample with 0.6 wt% of Fe_3O_4 nanoparticles shows an improvement in the efficiency of 10.5 % compared to the reference value (sample without nanoparticles). Accordingly, the evolution of the fill factor shows a similar behavior, yielding an increase of 12.2 % for the sample with the same weight percentage of Fe_3O_4 nanoparticles (0.6 wt%). The fill factor increases from 56.5 % for the reference sample to 63.5 % for the best solar cell with nanoparticles. These values are high for organic solar cells. Thus, the considerable improvement in the device performance is well-established by the incorporation of Fe_3O_4 nanoparticles.

When observing the evolution of the morphology, from the GISAXS data analysis we notice that the concentration of Fe_3O_4 nanoparticles has a major impact on medium-sized domains. The size and center to center distance of these domains have a major influence in the performance of the final device, since the typical distances involved are within the range of exciton diffusion length. These domains reach in size and also in center to center distance a local minimum around the range of the maximum solar cell performance. The mentioned decrease in size contributes to a more efficient exciton separation, eventually leading to a higher rate of separated charge carriers. Moreover, the impact of this morphology change in the behavior of the fill factor can be explained by the fact that, generally, the reduction of the domain size leads to smaller voids between domains. This fact is found to increase the mobility of electrons in PCBM domains. Moreover, the mobility of holes in the conjugated polymer is also strongly influenced by the orientation of the chains, thus by the morphology of the film [3].

With our finding we are able to show that the inclusion of metal oxide nanoparticles provides a promising improvement in the efficiency of polymer based solar cells. Besides the expected quantum effects caused by the presence of metal oxides and magnetic fields, the influence on the film morphology induced by the nanoparticles has also been found to have a beneficial impact on the performance of the final device.

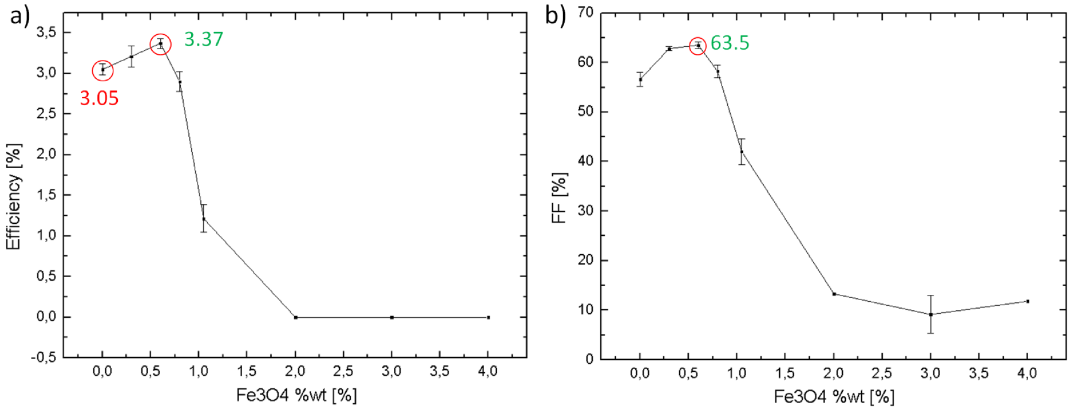

Figure 4.13:
a) Evolution of the efficiency of solar cells as a function of mass percentage of iron oxide nanoparticles. The range between 0.3 % and 1.0% shows the most efficient performance. b) Corresponding trend of the fill factor associated to the solar cells doped with different concentrations of iron oxide nanoparticles.

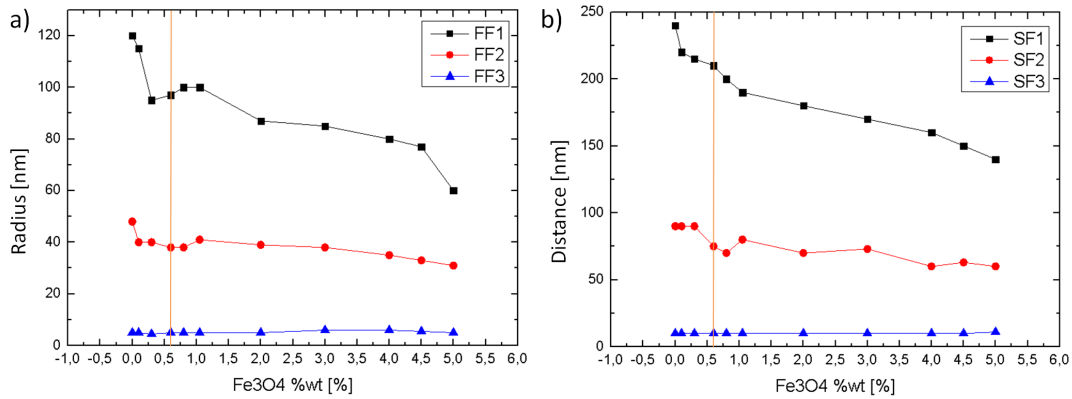

Figure 4.14:
a) Evolution of the domain sizes of bulk heterojunction P3HT:PCBM thin films as a function of mass percentage of iron oxide nanoparticles. Three different families corresponding to different sizes are displayed. In the range between 0.1 wt% and 0.8 wt% a local decrease in size for the medium-sized family is noticed. b) Corresponding trend of the structure size associated to the same thin films doped with different concentrations of iron oxide nanoparticles. Center-to-center distance also presents a local minimum at 0.8 % weight of Fe_3O_4.

The presented results open an interesting approach towards a better understanding of the role played by the different agents composing organic electronic devices, as well as a remarkable improvement of electric properties of the active components.

[1] W. Zhang, Y. Xu, H. Wang, C. Xu, S Yang, *Sol. Energ. Mat. Sol. Cells* **95**, 2880-2885 (2011)

[2] M. Arif, K. Yang, L. Li, P. Yu, S. Guha, *Appl. Phys. Lett.* **94**, (6), 063307 (2009)

[3] C. J. Brabec, V. Dyakonov, J. Parisi, N. Sacrifici, *Organic Photovoltaics. Concepts and realization.* Springer (2003)

4.8 Water-based P3P6T/C60 thin films for OSC applications

N. Hohn, D. Moseguí-González, P. Müller-Buschbaum

Organic solar cells (OSCs) offer a great potential due to low cost, large scale production and flexible design. For preparation of OSCs the water-soluble hole conducting polymer poly[3-(potassium-6-hexanoate)thiophene- 2,5-diyl] (P3P6T) is employed. For comparability reasons with the commonly studied P3HT:PCBM system, P3P6T is combined with an also water-soluble C60 fullerene derivative. Thus, both components of the active layer are processable for aqueous solutions and the manufacturing process of the active layer becomes more environmentally friendly as compared to common OSCs processing, which is based on organic solvents.

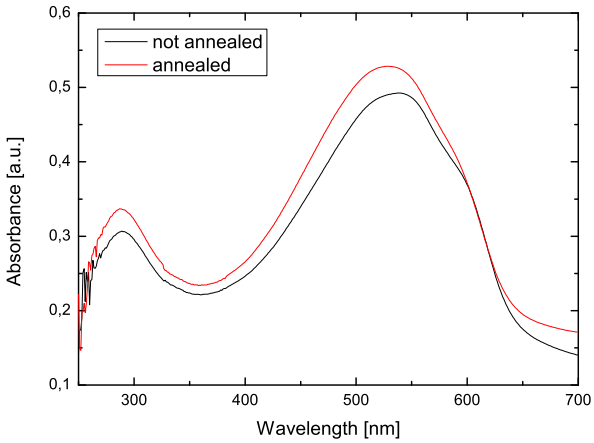

Figure 4.15:
UV/Vis spectrum of P3P6T/C60 bilayer before and after thermal annealing at 120° C for 30 minutes.

The study of the above mentioned system includes optimization steps to dissolve the polymer P3P6T and the C60 fullerene. Because the system is very sensitive to light and oxygen, it is crucial that the stirring time of the solution is as low as possible to still allow for the preparation of homogeneous thin films and, on the other hand, decreasing the performance of the OSC as little as possible. Furthermore the mixing behavior of the polymer/fullerene solution plays a huge role, as increasing the temperature was found to have a strong impact on the time needed to dissolve the mixture. Finally, as a last parameter to affect the solubility of our system, we needed to increase the pH-value of our solvent to dissolve the fullerene. Optimal conditions to dissolve both, polymer and fullerene separately, have been determined.
One possible approach for not dissolving both, fullerene and polymer, together in the pH-increased solution consists of working with two separate solutions. Therefore, the current investigations consist of the analysis of bilayer thin films. Concerning the UV/Vis and photoluminescence measurements, we already found promising results with regard to future solar cell preparation.
Figure 4.15 shows the absorbance of the bilayer directly after synthesis as well as after thermal annealing for 30 minutes at 120° C in nitrogen atmosphere. The energetically lower peak at 525 nm corresponds to the P3P6T layer absorption, whereas the peak at 290 nm is caused by the on top lying C60 layer. It is found that the annealing of the samples leads to a higher maximum absorption. This is an indication for higher crystallinity as the optical absorption correlates with the crystallinity for PCBM thin films [1]. Concerning the C60 peak (at the left side of the

absorption spectrum), an increase in absorption upon annealing is found, respectively. The peak position is slightly blue-shifted as compared to literature values of 335 nm of regular PCBM [2]. This blue-shift occurs due to the specific side-group functionalization of the employed PCBM derivative, which allows for water solubility.

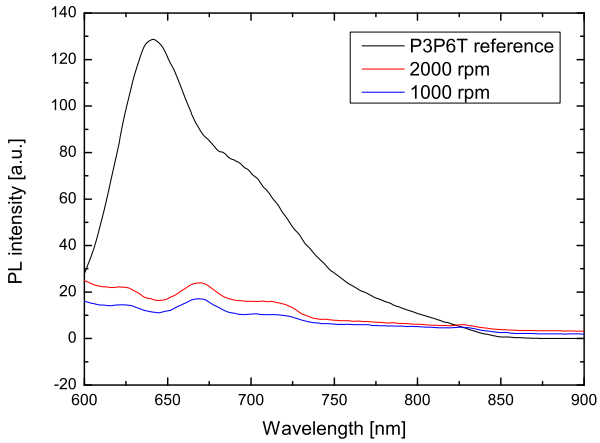

Figure 4.16: Photoluminescence of annealed bilayer structure for a 525 nm excitation wavelength

For further analysis the maximum absorption peaks from the UV/Vis spectra are determined and photoluminescence measurements are carried out (Fig. 4.16). The excitation wavelength corresponds to the determined maximum absorption wavelength of 525 nm. The reference of pure P3P6T exhibits a $\sim$ 6 times higher peak as compared to the bilayer sample. This result already indicates, that excitons are separated more efficiently, as the fluorescence signal drops. This means that the amount of radiative recombination is lowered as compared to the pure P3P6T. Moreover, it indicates is the presence of a layer of intermixed P3P6T and C60 [2]. In addition, we find a transition from the 2 peak structure in the reference to a 3 peak structure, which results from the P3P6T layer fine structure. The red-shift of the two right peaks is eventually a further evidence for a mixed bilayer due to a lower bandgap upon mixture. This feature bears the potential for future OSC application.

[1] U. Zhokhavets, T. Erb, G. Gobsch, M. Al-Ibrahim, O. Ambacher, *J. Chem. Phys. Lett.*, **418**, 347350 (2006)

[2] M. Ruderer, *Morphology of polymer-based films for organic photovoltaics*, PhD thesis, TUM (2012)

4.9 Implementing an OPV slot dye coating device for printed polymer solar cells

S. Günther, C. Schaffer, P. Müller-Buschbaum

Organic photovoltaics (OPV) is a new and highly investigated technology for photovoltaic devices that has the potential to solve the problems of large scale fabrication as well as materials costs, which most of the currently used PV technologies are faced with. Even though recent organic PV devices reach efficiencies of more than 10%, there is still a substantial amount of research and development to be done. That regards especially to analysis of morphology, which is a key parameter to efficient devices and also affects degradation as well as device lifetime. So far, in research studies the fabrication of slot die coated OPV modules has been addressed, including model studies, scaling-up of devices, use of different active layer materials or functional layers and substrates. However, despite this work there still remains a substantial amount of ambiguity regarding the slot die coating process itself. Therefore, particularly the processing method is of interest as it has an extensive influence on the morphology and structure of the created photoactive layers. Most of the currently investigated OPV devices are processed via spin coating although this technique is not very viable for large scale production. Thus, the influence of a printing method on the structural characteristics will be investigated on the basis of samples produced by positive shim mask slot die coating. This coating method for OPVs is a technique based on slot die coating that allows for very thin film application, provided that a very low viscosity solution (1mPa s) is used. For that purpose a new printing machine will be implemented that allows for further investigation of this coating technique.

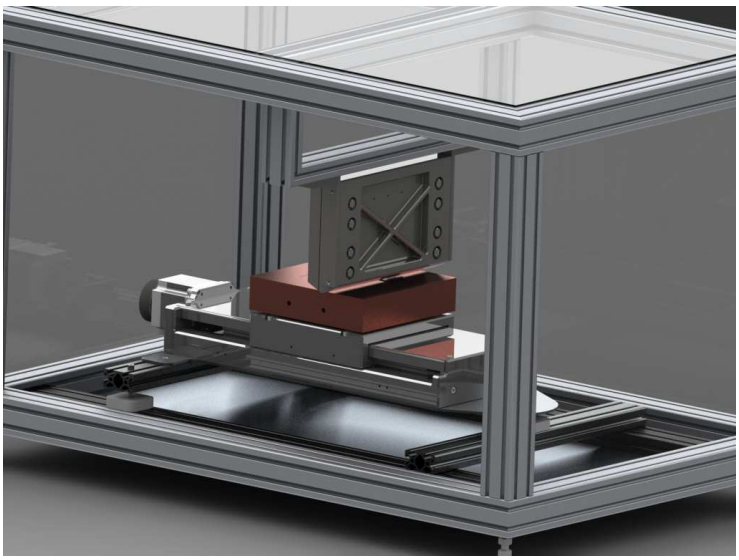

Figure 4.17:
Rendered image of the complete slot die assembly. The print head is fixed, hanging from the top part of the frame with a 100 - 300 micrometer spacing between substrate and shim mask.

This device is designed to provide the ability for coating multilayered solar cells in an one-dimensional direction by plotting different layers on top of each other, provided that all the used layer materials comply with the constraining coating device limits. The key feature however will be the uniform deposition of the photoactive layer and the effect on morphology in comparison to spin-coated active layers. The application of these layers is realized simply by translation of the coating substrate along the perpendicular direction of the print head. Due to the very close distance between substrate and shim mask a very planar movement of the substrate holder has to be guaranteed. The decision for the movement of the substrate is based on the idea of being able to compare the printed layers of this device to very large scale manufacturing, as it is done by roll-to-roll-coating (R2R). In the present work inelastic substrates, such as glass and silicon wafers, will be used first. With glass and silicon substrates the analysis of the printed films will be easier with X-ray based scattering methods, as compared to flexible substrates. Based

on the fundamental research of Krebs and Hong et al. [1, 2] a new coating head was designed, based on the principle of positive shim mask slot dye coating. Regardless of difficult technical requirements, due to the need of a very narrow spacing between translating parts and a rather low printing speed of 0.5 - 2 m/s, the technique of positive shim mask slot die coating allows for application of very thin films and homogeneous layer surfaces [3]. This is due to a lower viscosity of the printed solution and thus also a lower pressure in the printhead, which allows for the solution to wet the substrate surface in a more uniform manner.

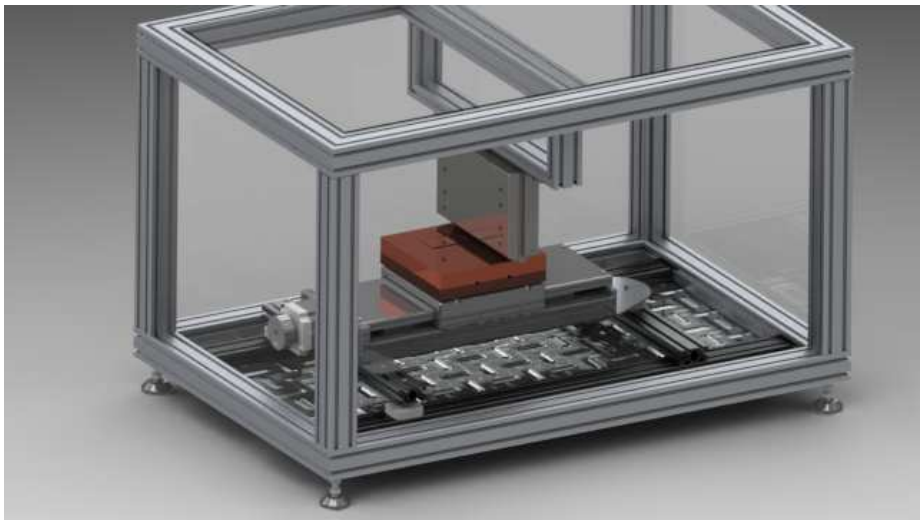

Figure 4.18:
Exploded view of the print head. In between the front and back parts of the printing head two masking interlayers are placed: One to create a drain and to guide the printed solution, the other one acts as the positive shim mask to determine the width of the printed layer.

The printing machine is designed to allow for the ability to heat the substrate up to a temperature of 80 centigrade, as well as for printing under a nitrogen atmosphere. The thereby created films will be analyzed using X-ray reflectivity (XRR), optical and atomic force microscopy (OM, AFM) and UV/Visible light spectroscopy (UV/Vis) as characterization methods. The morphology of these films on a nanometer scale is probed with grazing incidence wide and small angle scattering methods using X-rays and/or neutrons (GIWAXS/GISAXS/GISANS). The aim will be to compare the printed layers with spin-coated and spray-coated layers. Important device characteristics in these studies will be the morphology and structural differences in comparison between positive shim mask slot die coated layers and samples fabricated by other coating techniques. Slot-die coated BHJ structures based on blends consisting of poly(3-hexylthiophene) and fullerene derivative (6,6)-phenyl C61 butyric acid methyl ester (P3HT:PCBM) will be investigated. The primary points of interest will be shim length of the mask, temperature, atmospheric influences and coating speed.

[1] S. Hong, J. Lee, H. Kang, K. Lee, *Sol. Energ. Mat. Sol.* **27-35**, 112 (2013)

[2] F. C. Krebs, *Sol. Energ. Mat. Sol.* **465-475**, 93 (2009)

[3] F. C. Krebs, *Sol. Energ. Mat. Sol.* **394-412**, 93 (2009)

4.10 Aggregation control in organic photovoltaic blends

J. F. Martínez Grisales, E. M. Herzig, P. Müller-Buschbaum

Since the discovery of conductive polymers, organic photovoltaics has turned into a very active field of research. This is owed to the potential of the inexpensive and widely available energy of the sun and the resulting wide range of possible applications [1]. The solution processable thin film technology allows to produce shape versatile, light weight solar cells that offer a wide range of tunability [2]. The organic molecules used in this technology can be custom tailored for the applications involved. To fully exploit organic photovoltaics for efficient energy conversion processes the morphology of the active layer is a crucial parameter [3]. For example, the charge transport properties closely depend on the molecular arrangement of the semi-conduction polymers, i.e. the nanomorphology and the aggregation state of the polymer in the blend. This is due to the fact that for successful charge transport to occur, overlap of the π-conjugated parts of the polymers is necessary. Exploiting the properties of selective solvents we present a method to control the aggregation of a binary photovoltaic blend via the addition of a co-solvent. The system is thoroughly investigated using microscopy, and spectroscopy to gain fundamental understanding on the processes involved and to relate these to solar cell performance.
We study the classical binary system poly(3-hexylthiophene-2,5-diyl):phenyl-C_{60}-butyric-acid-methyl ester, P3HT:[60]PCBM using chlorobenzene (CB) as solvent. A second solvent, which is a poor solvent for P3HT, is chosen as a co-solvent additive (CSA). We add CSA in different volume percentages (0, 0.1, 1, 3, 7, 10 and 30%) to study how the co-solvent changes the aggregation of the polymer blend. This can be examined by measuring the absorption spectra of the different polymer blends. The choice to add a selective or "poor" solvent is sustained in studies performed in similar systems, which report an increase of charge carrier mobility [4] and absorption efficiency up to 30% [5].

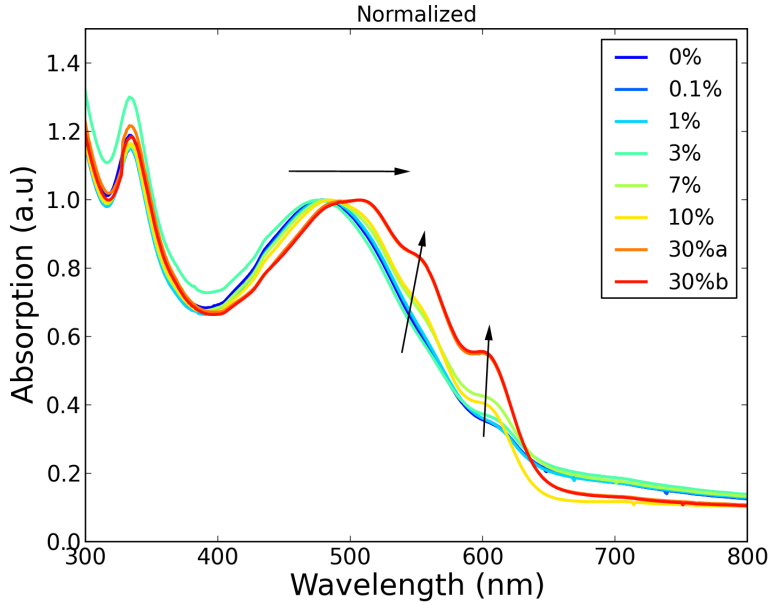

Figure 4.19: UV-Vis absorption measurements on P3HT:PCBM blends with varying content of CSA. The data is plotted with absorbance versus wavelength. The differently colored curves correspond to P3HT:PCBM blends with different volume contents of CSA. To make shifts in the peak positions more clear the data is normalized to the peak of absorbance of P3HT.

First results are shown in Fig. 4.19, where a red shift of the peak of absorption of P3HT from around 470 nm to approximately 500 nm is visible for large additions of CSA. Moreover, the formation of shoulders to this peak is visible at 550 nm and 600 nm, especially for the greatest volume content of CSA. It is worthy to point out that the absorption spectrum corresponding to

the PCBM behaves differently than for P3HT. While it remains similar for most volume contents of the additive a strong an unusual high absorption is observed for a medium PSA value.
To calculate the coefficient of absorption of this blend, the thickness of the layers is measured with the Dektak apparatus by scratching the surface layer in different areas and carrying out repeated measurements at different locations of one sample to get a good representative value of the thickness. The absorption coefficient spectra obtained using the obtained thicknesses are shown in Fig. 4.20. Interestingly the absorption coefficient spectra decrease in magnitude across the spectrum for films with a volume content of CSA higher than 3vol%. This observation, however, still needs to be interpreted with care because the CSA also changes the viscosity of the blend solution and therefore changes the quality of the obtained films.
This discrepancy is particularly visible in the values for the films with 30vol%. In this case the heterogeneity of the films leads to large errors on the thickness and therefore leads to widely diverging absorption coefficients. Further experiments are needed to clarify the behavior of the absorption coefficient upon the addition of the chosen CSA.

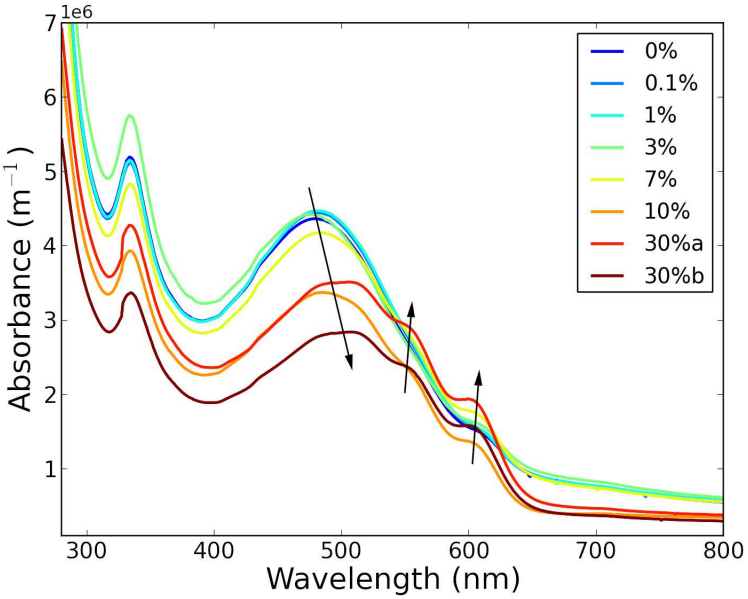

Figure 4.20: Absorption spectrum of P3HT:PCBM systems with different volume content of CSA. The discrepancy of the absorption in films with CSA content of 30vol% (namely a, and b) is due to the variations in thickness within the 30 % sample. The highly inhomogeneous distribution of the polymer film due to the high viscosity of these solutions renders the measurement position dependent.

To examine whether the CSA is the responsible of the decreasing absorption coefficient, the sample preparation process needs to be altered to improve film homogeneity. One approach will be to alter the spin coating conditions and to control the temperature while stirring and during spin coating. Furthermore, we will examine the influence of annealing on the absorption spectra. In combination with scattering experiments we plan to correlate the absorption behavior with information on the nanomorphology to gain systematic control over the aggregation behavior of the system. In combination with the use of these differently aggregated films in solar cells we want to study the effect on solar cell efficiency.

[1] E. M. Herzig, P. Müller-Buschbaum, *Acta Futura* **6**, 17-24 (2013)

[2] M. Scharber, N. Sariciftci, *Prog. Polym. Sci.* **38**, 1929-1940 (2013)

[3] M. A. Ruderer, P. Müller-Buschbaum, *Soft Matter* **7**, 5482-5493 (2011)

[4] C. Scharsich, R. H. Lohwasser, M. Sommer, U. Asawapirom, U. Scherf, M. Thelakkat, *J. Polym. Sci. Part. B* **6**, 442-453 (2012)

[5] Y. Sun, Y. Han, J. Liu, *Chi. Sci. Bull* **22**, 2767-2774 (2013)

5 Polymer-hybrid systems

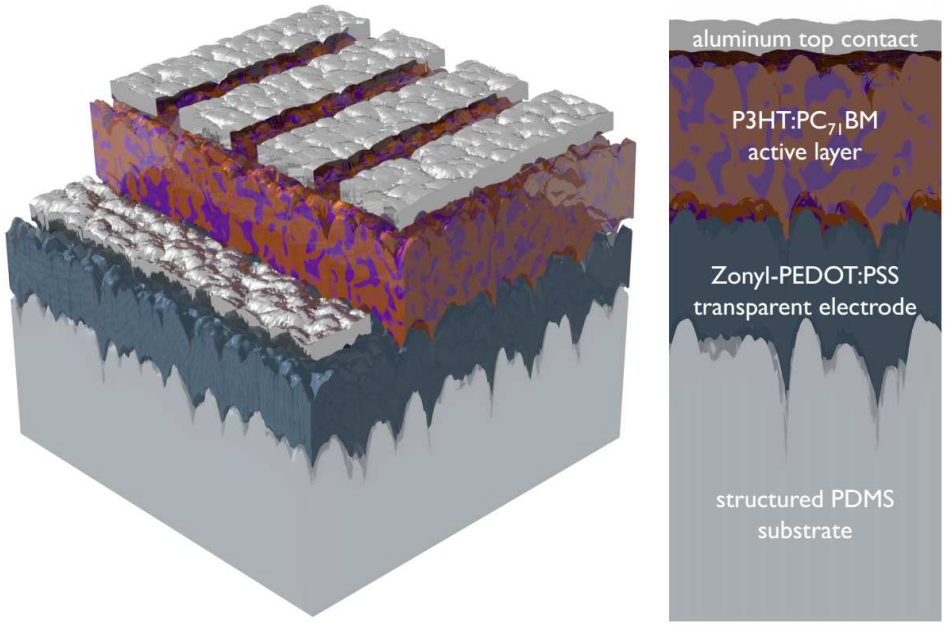

5.1 Spray pyrolysis deposition of titanium dioxide with foam like structure for photovoltaic applications

B. Su, S. Bernstorff[1], P. Müller-Buschbaum

[1] ELETTRA, Trieste, Italy

Titanium dioxide with foam-like nanostructure is receiving strong interest in photovoltaics, for example in hybrid solar cells [1], electrolyte solar cells and dye-sensitized solar cells (DSSCs). The nanoporous titania layers are responsible for the electron transporting and directing dye layers' structure. Spray pyrolysis is a process in which a thin film is deposited by spraying solution on a heated surface, where the constituents react to form a chemical compound [2]. In this report, we mainly focus on the effect of different concentrations of the sol-gel solution on the foam-like structure of titanium dioxide created via spray pyrolysis.
The amphiphilic diblock copolymer poly(styrene-b-ethylene oxide) (P(S-*b*-EO)) is used as a template copolymer. P(S-*b*-EO) was dissolved in 1,4-dioxane, which is a good solvent for both blocks. Afterwards, HCl is used as a bad solvent for the PS blocks, to induce micro-phase separation, and titanium tetraisopropoxide (TTIP) as a titania precursor. In the next step, the mixed solution is sprayed on pre-cleaned Si (100) substrates at $50°C$, the spray speed is set to 127.16 μl/s. The spray pyrolysis process involves a series of parameters, such as nozzle-sample distance, spray speed, substrate temperature, nitrogen flow pressure and spray interval time. To crystallize the TiO_2 films, the samples are put into a furnace and heated to $400°C$ for 4 hours. During this process, block copolymer is combusted, and titania nanostructures are formed. Different concentrations of TTIP in the sol-gel solution are investigated: 7 wt%, 6 wt%, 5 wt% and 4 wt% of TTIP.

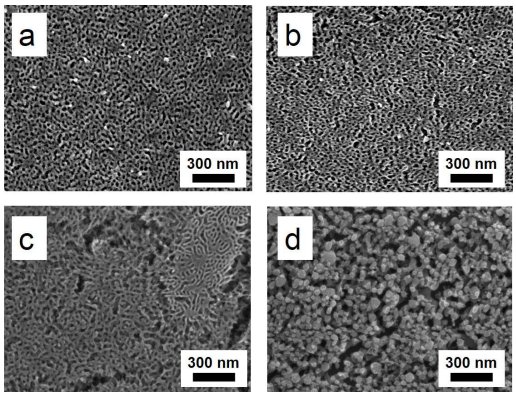

Figure 5.1:
SEM images of titanium dioxide films prepared from sol-gel solution, synthesized using a) 7 wt%, b) 6 wt%, c) 5 wt% and d) 4 wt% TTIP in sol-gel solution, and sintered at $400°C$.

Figure 5.1 shows the top view of titanium dioxide film after calcination with a foam like structure as probed by scanning electron microscope (SEM). The surfaces show a high quantity of small-size structures. With decreasing the weight ratio of TTIP, the morphology of the titania films is changed from a foam-like structure to nano-rods. In our study, such a critical processing parameter also affects the network morphology. For a more quantitative information about the nanostructure, in particular inside the films, the advanced scattering technique grazing incidence small angle x-ray scattering (GISAXS) is applied [3]. GISAXS experiments are performed at the Austrian SAXS Beamline of ELETTRA, Trieste Italy. The fixed incident angle is $\alpha_i = 0.484°$, the x-ray wavelength is λ = 0.154 nm and the sample-to-detector distance is d = 2.07 m. Figure 5.2 shows the 2d GISAXS data of titania films (left) and horizontal line cuts with fits (right), respectively. From the fitting of the horizontal line cuts, the structure factor and the structure distances can be obtained. The pore sizes of the samples with 7 wt%, 6 wt% and 5 wt% are 11.4 nm, 15.4 nm and 17.6 nm, respectively. The corresponding structure distances are 12.6 nm, 14.6 nm and 22.4 nm. For the 4 wt% sample, the nano-rod structure size is 7 nm and structure distance is 21 nm.

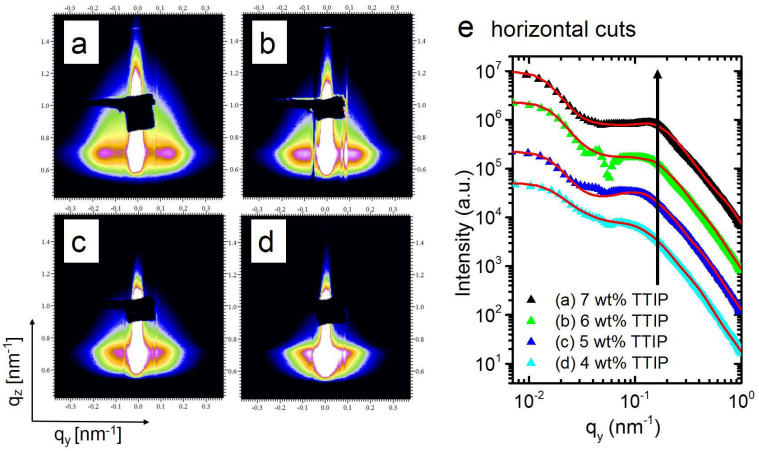

Figure 5.2:
2d GISAXS data of films prepared from a) 7 wt%, b) 6 wt%, c) 5 wt% and d) 4 wt% TTIP in sol-gel solution. e) corresponding horizontal line cuts for the different concentration of TTIP. The cuts are shifted along the intensity axis for illustrative purpose.

The influence of different sintering temperature on the films is also probed. Figure 5.3 shows the X-ray diffraction (XRD) measurement results, with the crystal size increasing from 7.5 nm to 23 nm by raising the sintering temperature. However, at $800°C$ the titania phase transition occurs, changing from the anatase to the rutile polymorph. The diffraction peaks were indexed on the basis of the rutile and anatase phases, using the JCPDS database files 21-1272 and 21-1276, respectively.

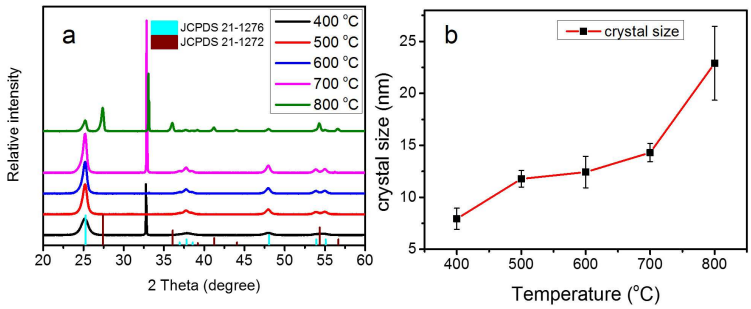

Figure 5.3:
a) X-ray diffraction results of different sintering temperatures for titania films and b) determined crystal sizes of the titania nanoparticles. The diffraction peaks were indexed on the basis of the rutile and anatase phases as explained in the text.

In conclusion, with decreasing the weight ratio of TTIP in the so-gel solution, the pore size is continuously increasing. However, when the amount of TTIP is reduced to 4wt%, the foam-like structure transforms into nano-rods. XRD data show that the crystal size of titania nanoparticles are growing with increasing sintering temperature. At $800°C$ the crystalline phase of titania changes from anatase to rutile, which might be disadvantageous for solar cell applications.

[1] J. F. Lin, W. B. Wang, C. C. Ho, J. H. Jou, Y. F. Chen, W. F. Su, *J. Phys. Chem. C* **116**, 1955–1960 (2012)

[2] J. B. Mooney, S. B. Radding, *Annu. Rev. Mater. Sci.* **12**, 81-101 (1982)

[3] P. Müller-Buschbaum, *Anal. Bioanal. Chem.* **376**, 3-10 (2003)

5.2 Low temperature route to porous titania nanostructures by block-copolymer assisted sol-gel method

L. Song, M. A. Niedermeier, P. Müller-Buschbaum

Nanostructured titania thin films have received great attention in different fields of applications such as photovoltaics, photocatalysis, and gas sensing. The main advantages are related to their chemical and optical stability, no toxicity and low cost. Titania, especially its anatase polymorph, has resulted in a fast upward trend in the field of hybrid solar cell, which consists of conjugated polymers and n-type inorganic nanocrystals. For solar cell applications, a large surface-to-volume ratio of the inorganic semiconductor is desirable, since the morphology influences charge carrier transport routes and the excition dissociation which occurs at the interface of the inorganic and the organic parts, therewith the probabilities of electron-hole recombination. So the porous titania nanostructures are particularly promising due to their morphology with a high surface area and an interconnected network.
Plenty of techniques have been developed to fabricate titania nanostructures, but most of them require a high temperature for calcination (400^{o}C-500^{o}C) [1,2], which limits the deposition of titania films on organic substrates and therewith flexible solar cells. Therefore, the low temperature synthesis of porous titania nanostructures is of promising application prospect, as it allows to be deposited on organic transparent electrodes such as poly(ethylene terephthalate) (PET) and poly(tetrafluoroethylene) (PTFE). Moreover, a reduction of synthesis temperature leads to a decreased energy requirement, resulting in lower costs and more environmentally friendly. Moreover, low temperature helps the stability of the titania nanostructure while the shrinkage and pattern collapse may occur at high temperature.

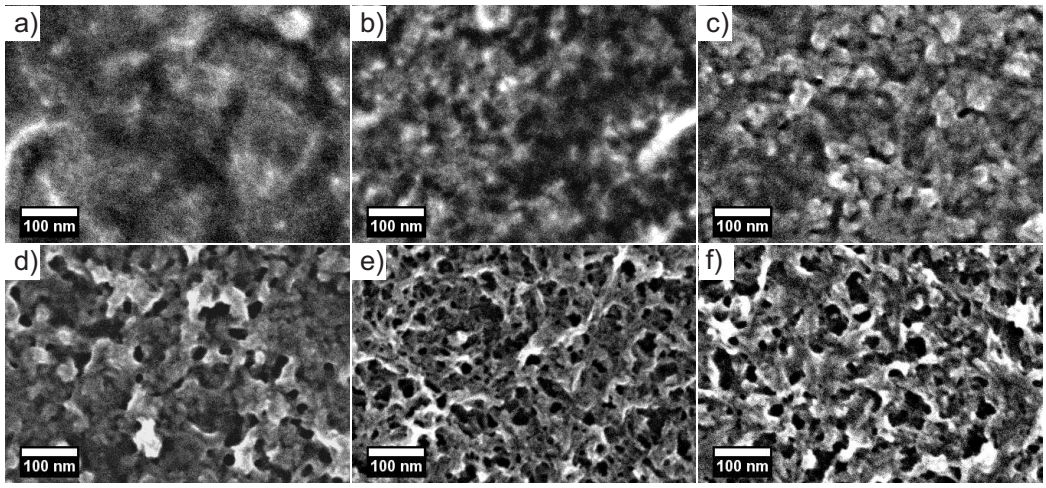

Figure 5.4:
SEM images of the titania films after different UV light irradiation times: a) 0h, b) 1h, c) 3h, d) 6h, e) 12h, f) 24 h.

To date, many low temperature approaches to synthesize porous titania nanostructures have been reported, including aqueous and nonaqueous routes [3,4]. In the present investigation, the porous titania nanostructures are prepared from sol-gel synthesis in combination with block copolymer templating as follows: a certain amount of the di-block copolymer polystyrene-block-polyethyleneoxide, denoted P(S-b-EO), is dissolved in N,N-dimethylformamide (DMF), which is a good solvent for both PS and PEO blocks. Then concentrated HCl and ethylene glycol-modified titanate (EGMT) are added slowly under vigorous stirring. In this step, the

EGMT is the titanium source and the concentrated HCl gives rise to the micro-phase separation as it is a selective solvent-a good solvent for the PEO block but a bad one for the PS block. The sol-gel reaction starts when HCl solution meets EGMT in the polymer solution, then the precursor converts to titania in the solution, where the titania is expected to disperse in the PEO domains. A fixed weight ratio of 1:1:10:100 of P(S-b-EO):EGMT:HCl:DMF is applied in this report. After this process completes, the whole solution is transferred to a hot plate(90 ^{o}C) for continuous stirring for 15min. Next it is deposited on the silica substrates by spin coating. In the end porous titania nanostructures are formed by removing the polymer matrix through UV irradiation.

To check the efficacy of UV light irradiation in removing the polymer matrix, different irradiation times are applied. The UV-light-induced changes of the titania films' morphologies are shown in Fig. 5.4. As seen from the SEM images of the low temperature titania samples, there is significant difference in their morphologies which induced by different UV light irradiation times. The contrast of Fig. 5.4a is not so sharp as the P(S-b-EO) is not conductive, indicating that the titania exists in the polymer matrix homogeneously and no aggregation. With the irradiation duration from 1 h to 6 h, the contrasts of the images become much sharper, which means the polymer is removed gradually with the increasing time of the UV irradiation. Up to 12 h or even 24 h, the obvious pores are demonstrated in Fig. 5.4e-f. The diameters of pores are around 20 nm.

In order to quantify the crystallization, the band gap of the titania films is measured by UV/Vis. The changes of the light absorbance are illustrated in Fig. 5.5. According to Lambert-Beer law and Tauc equation, the band gap can be calculated. The band gap of the titania film without UV light irradiation is about 3.54 eV while that of the titania film with 24 h is around 3.28 eV, showing a downward trend.

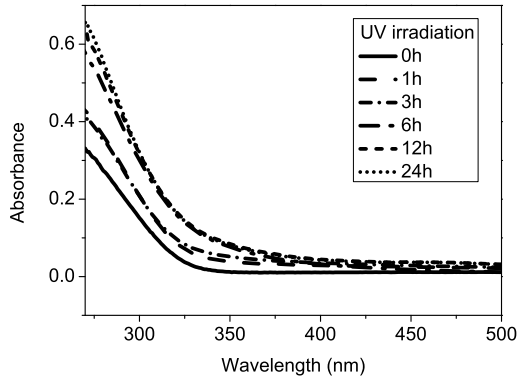

Figure 5.5:
UV/Vis absorbance data of the titania films after different UV light irradiation time.

In conclusion, the porous titania nanostructure is achieved at room temperature by the UV light irradiation, and its duration determines the extent of the polymer removing. The titania films are homogeneous, and the pore sizes are approximately 20 nm after 12 h UV light irradiation, no shrinkage or pattern collapse of the nanostructure are observed.

[1] M. A. Niedermeier, D. Magerl, Q. Zhong, A. Nathan, V. Körstgens, J. Perlich, S. V. Roth, P. Müller-Buschbaum, *Nanotechnology* **23**, 145602 (2012)

[2] S. Guldin, M. Kolle, M. Stefik, R. Langford, D. Eder, U. Wiesner, U. Steiner, *Adv. Mater.* **23**, 3664-3668 (2011)

[3] M. Rawolle, E. V. Braden, M. A. Niedermeier, D. Magerl, K. Sarkar, T. Fröschl, N. Hüsing, J. Perlich,P. Müller-Buschbaum, *ChemPhysChem* **13**, 2412-2417 (2012)

[4] M. Niederberger, M. H. Bartl, G. D. Stucky, *Chem. Mater.* **14**, 4364-4370 (2002)

5.3 A kinetic study of structural evolution in spray-deposited ZnO film for application in dye-sensitized solar cells

K. Sarkar, E. V. Braden, S. Pogorzalek, S. Yu[1], S. V. Roth[1], P. Müller-Buschbaum

[1] DESY, Hamburg, Germany

Parallel to the conventionally used titania (TiO_2) based dye-sensitized solar cells (DSSCs), zinc oxide (ZnO) has gradually emerged as a promising material for DSSCs. For efficient functioning of DSSCs, the morphology and the thickness of the metal oxide films play most important roles. A network-like morphology with high effective surface area acts as a scaffold for enhanced dye adsorption. This is of principle concern, since in DSSCs, the light is absorbed in the dye molecules. On the other hand, an optimum thickness of the metal oxide film is also important in order to ensure sufficient light absorption [1].
The present study focuses on optimizing these two crucial parameters in order to optimize the device performance. The ZnO nanostructures are synthesized via solution processing of a commercial ZnO precursor, namely zinc acetate dihydrate (ZAD). The industry-based spray deposition technique is used to deposit a 25 mg/ml solution of ZAD in N,N-dimethylformamide, which provides nanostructured ZnO morphologies with a scalable film thickness. Spray deposition is a fast process which involves complicated structural and morphology evolution [2]. In order to monitor such a dynamic process, a high time resolution is necessary which is provided by the powerful technique of grazing incidence small angle x-ray scattering (GISAXS).

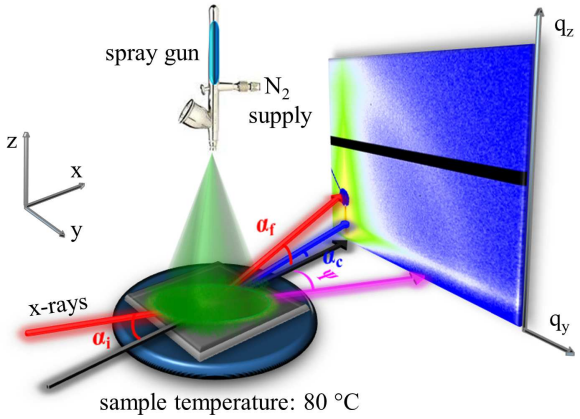

Figure 5.6:
A schematic representation of the experimental setup for GISAXS measurements on the in-situ spray deposited ZnO nanostructured film.

The schematic representation of the experimental setup is shown in Fig. 5.6. The structural evolution of a sprayed film is investigated via time-resolved GISAXS for an in-situ spray shot of 10 s. For a precise control over the spraying time, an automatized spray setup is used. To ensure fast drying and homogeneity of the film, the sample is kept heated at 80 °C throughout the experiment. The sample is exposed to an x-ray beam under a shallow angle of 0.34° as soon as the spray shot starts. The Pilatus 300k pixel noise free detector is used to acquire data for 30 s in total, over 600 frames each acquired over 0.05 s. The results obtained are summarized in Fig. 5.7.
The most interesting region in these scattering patterns, is the region around the material characteristic Yoneda peak. Hence, 5 pixels are integrated along q_z around the Yoneda peak position for each of the 600 frames and plotted in Fig. 5.7a with respect to the time axis. In the resulting mapping it is observed that the weak peak at $q_y = 1.5\ nm^{-1}$ appears already after 5 s spraying time as indicated by the dashed rectangle. The peak intensity is very weak as the counting time for each signal is kept low to achieve the high time resolution. This peak is attributed to the aggregation of ZnO nanoparticles which are deposited during spraying. It is also noted that the position of the peak stays constant for the remaining spray time and afterwards as highlighted by the dashed rectangle in Fig. 5.7b. The bottom ten curves in Fig. 5.7b corresponds to the data

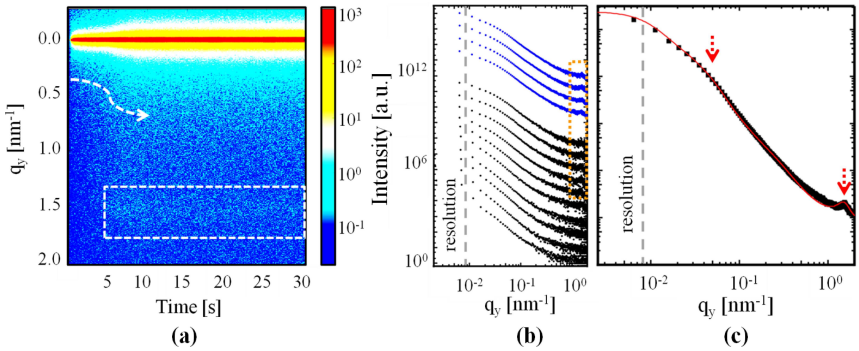

Figure 5.7:
a) 2D GISAXS data map plotted against time. An improvement in intensity at $q_z = 0$ nm^{-1} is marked by a dashed arrow. b) Horizontal line cuts for all frames plotted from bottom to top with increasing time. c) Integrated horizontal cut (symbols) with fit (solid line) to extract length scales in the film volume.

acquired during spraying and the top four curves indicate the data acquired after the spray shot for additional 20 s. Fig. 5.7c shows the predominant length scales extracted from the final dried film corresponding to 60 nm (at low q_y) and 3.4 nm (at high q_y) with a distribution of 15 and 4 nm respectively.

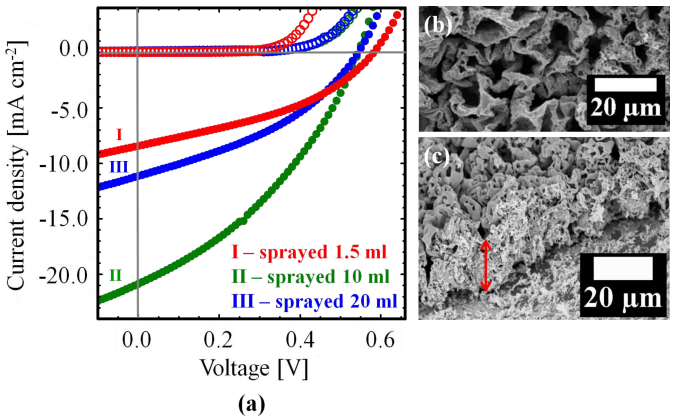

Figure 5.8:
a) I/V plots for measurements in dark (hollow circles) and under AM 1.5 illumination (filled circles) for solar cells with different ZnO film thicknesses. b) The SEM top and c) cross-sectional images of cell II. The arrow indicates the film thickness

For the final device characterization, DSSCs are prepared from sprayed ZnO films with different thicknesses. The related I/V curves are shown in Fig. 5.8a. The film prepared by spraying 10 ml of precursor solution shows the best performance with a power conversion efficiency of 4.1 % and a short circuit current density as high as 20.8 mA cm^{-2}. Figure 5.8b-c shows the surface and cross-sectional SEM images of the film respectively. Thus the network-like nanostructured morphology with nanometer length scales, obtained by spray deposition with an optimum thickness of 20 μm, results in a DSSC with reasonable device performance.

[1] A. Sacco, A. Lamberti, R. Gazia, S. Bianco, D. Manfredi, N. Shahzad, F. Cappelluti, S. Ma, E. Tresso *Phys. Chem. Chem. Phys.* **14**, 16203-16208 (2012)

[2] A. Abdellah, K. S. Virdi, R. Meier, M. Döblinger, P. Müller-Buschbaum, C. Scheu, P. Lugli, G. Scarpa *Adv. Funct. Mater.* **22**, 4078-4086 (2012)

5.4 A morphology study of ZnO/TiO_2 nanocomposite films for application in photovoltaics

E. V. Braden, K. Sarkar, S. V. Roth[1], P. Müller-Buschbaum

[1] DESY, Hamburg, Germany

Zinc oxide (ZnO) and titania (TiO_2), both have outstanding electrical and optical properties, which make them favorable for applications in hybrid solar cells. Conventionally, such hybrid solar cells contained either ZnO or TiO_2 [1,2]. In this study, composite nanostructured films containing both ZnO and TiO_2 are prepared. The nanostructures are synthesized using a sol-gel technique including an amphiphilic diblock copolymer as structure-giving agent. The copolymer used is poly(styrene-*block*-ethylene oxide), abbreviated as P(S-*b*-EO). Two different precursors, zinc acetate dihydrate (ZAD) and ethylene glycol-modified titanate (EGMT) are used as ZnO and TiO_2 sources respectively.
The polymer is dissolved in a pair of "good-selective" solvent which initiate micro-phase separation of the blocks, thereby forming micelles in the solution. ZAD and EGMT are added separately in such micellar solutions. Due to their polarity, the precursors preferentially get incorporated into the hydrophilic block of the copolymer. The precursors thereby interact in the limited volume producing nanostructures. The two sol-gels are finally mixed in varying volume fractions with 10 vol% increment in order to obtain a nanocomposite sol-gel which is spin-coated on silicon substrates. This is followed by a high temperature treatment which imparts crystallinity to the system and removes the copolymer template.

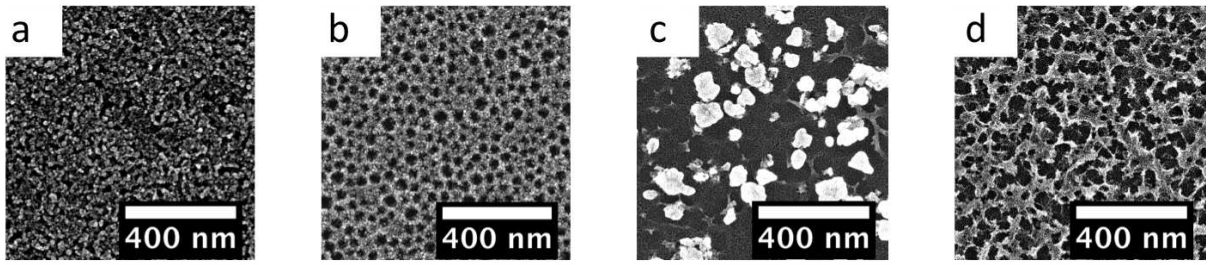

Figure 5.9:
Scanning electron microscopy images under high magnification. a) film with a molar fraction of ZnO to TiO_2 of 37.82 b) a fraction of 9.82 c) a fraction of 4.21 and d) a fraction of 1.05.

In Fig. 5.9 SEM images of the calcined nanocomposite films are depicted, which clearly show that the obtained structures dramatically vary in terms of morphology and length scales with different molar fractions of ZnO and TiO_2 in the system.

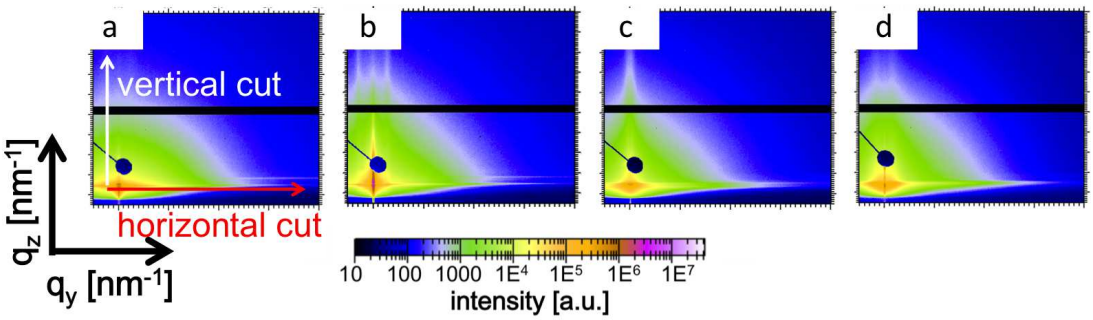

Figure 5.10: 2D data obtained with GISAXS. a)-d) refer to the samples depicted in Fig. 5.9.

In order to obtain statistically relevant information, the films are investigated at the beamline P03 of the PETRA III storage ring at DESY, Hamburg using grazing incidence small angle x-ray scattering (GISAXS). In Fig. 5.10 the characteristic 2D scattering patterns of the above-mentioned samples are presented. To obtain quantitative information about the structural length scales in the film volume, horizontal line cuts from the 2D GISAXS data (depicted in Fig. 5.10) are performed at the material sensitive Yoneda peak position as indicated by the red arrow in Fig. 5.10a. These data are presented in Fig. 5.11.

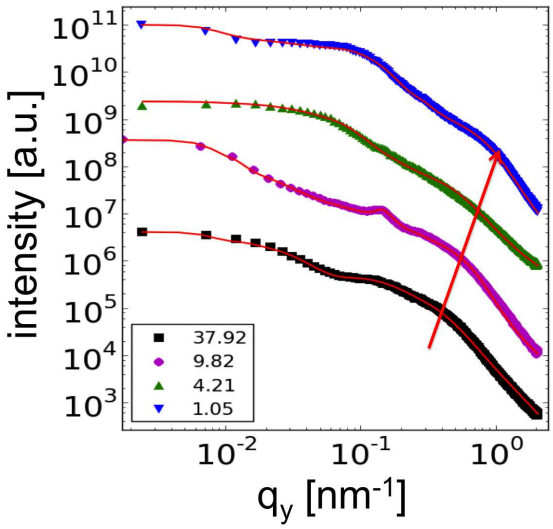

Figure 5.11:
Horizontal cuts of the 2Data at the q_y value of the Yoneda peak position shifted in intensity. The data shown belong to samples with a molar ratio of ZnO to TiO_2 of 37.92, 9.81, 4.21 and 1.05, respectively.

A model fit (indicated by the red line) considering two cylindrical form factors distributed over a 1D paracrystal lattice is used in the framework of distorted wave Born approximation (DWBA) to analyze the data. The form factors and the structure factors are associated with the predominant average cluster sizes and distances between the clusters respectively. The red arrow in Fig. 5.11 indicates a shift of the smaller form factor towards lower length scales (higher q_y values) with an increasing molar fraction of TiO_2 in the system, meaning a decrease in the cluster size of the nanostructures. This is in good agreement with the observations made from the SEM data. Hence, a template-assisted sol-gel route is shown to produce promising tunable nanocomposite (ZnO/TiO_2) morphologies for applications in hybrid photovoltaics.

[1] M. Rawolle, E. V. Braden, M. A. Niedermeier, D. Magerl, K. Sarkar, T. Fröschl, N. Hüsing, J. Perlich, P. Müller-Buschbaum, *Chem. Phys. Chem.* **13**, 2412-2417 (2012)

[2] K. Sarkar, M. Rawolle, E. M. Herzig, W. Wang, A. Buffet, S. V. Roth, P. Müller-Buschbaum *Chem. Sus. Chem.* **6**, 1414-1424 (2013)

5.5 Temperature-induced morphological changes of P(S-*b*-NIPAM) diblock copolymer embedded with cobalt ions

E. Metwalli, A. Gustschin, P. Müller-Buschbaum

Functional hybrid nanomaterials composed of metal nanoparticles dispersed in a polymer matrix are of high interest because of their potential applications in nanodevices for sensing, catalysis and high density memory storage devices.[1-3] The aim of the present report is to investigate a cobalt salt-diblock copolymer hybrid system which should be employed to guide cobalt metal ions in the micro-phase separated DBC morphology. Bulk samples and thin films of poly(styrene-*b*-N-isopropylacrylamide) P(S-*b*-NIPAM) with a PNIPAM volume fraction of 0.3 are prepared via solution casting and spin coating, respectively. The cobalt salt was Co(II)(bipy)Cl_2, based on a 2,2′ Bipyridine (bipy) complex. The bulk samples as well as thin films were prepared with different Co/PNIPAM weight ratios (R). The structural evolution of the bulk samples as a function of temperature was investigated using in situ small-angle x-ray scattering (SAXS). The thin films were investigated with grazing incidence small-angle x-ray scattering (GISAXS) and AFM after a post-treatment step at 100°C in an inert environment. All bulk samples (0 , 5, and 10 wt%) showed a micro-phase separated morphology at temperatures up to 240°C. Figure 5.12 shows the typical 2D SAXS images at room temperature and after heating up to 230°C.

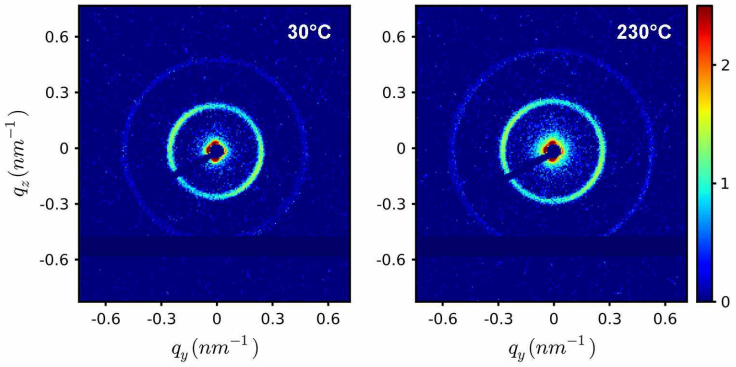

Figure 5.12:
SAXS 2D scattering patterns of bare P(S-*b*-NIPAM) DBC at 30°C and 230°C. The color bar is based on logarithmic intensity values. The dark blue stripe is a dead area of the Pilatus 300K detector.

A lamellar morphology was observed for samples with R = 0 wt% and 10 wt%. This micro-phase separation structure results from residual solvent and water molecules adsorbed during the solution casting step and the related swelling of the PINIPAM block, thereby giving rise to a higher effective PNIPAM volume fraction. The development of the lamellar spacing *d* and the thickness *l* of the PNIPAM block is shown in Fig. 5.13 with increasing temperature for samples with R = 0 wt% and 10 wt%. The data indicates that the PNIPAM block has the major influence on the change of the lamellar spacing. It also confirms that the cobalt salt is incorporated in the hydrophilic PNIPAM block since its thickness *l* is remarkably larger than in the bare DBC sample.
Cobalt salt-DBC hybrid films at different cobalt weight ratios (R = 0, 0.5, 2, 5, 10, and 30 wt%) were prepared. Upon increasing the metal salt content the lamellar spacing tends to continuously increase as revealed from GISAXS results (data is not shown). This is consistent with the SAXS data from the bulk samples indicating that the salt is selectively embedded in the PNIPAM block. However, the broadening of the corresponding peak with increasing concentrations indicates a high particle size distribution. The micro-phase separated morphology was further confirmed by AFM for some selected samples.
Figure 5.14a shows the lamellar phase of the as prepared R = 10 wt% sample. Interestingly, the lamellar spacing extracted from the AFM micrographs is remarkably larger than that provided

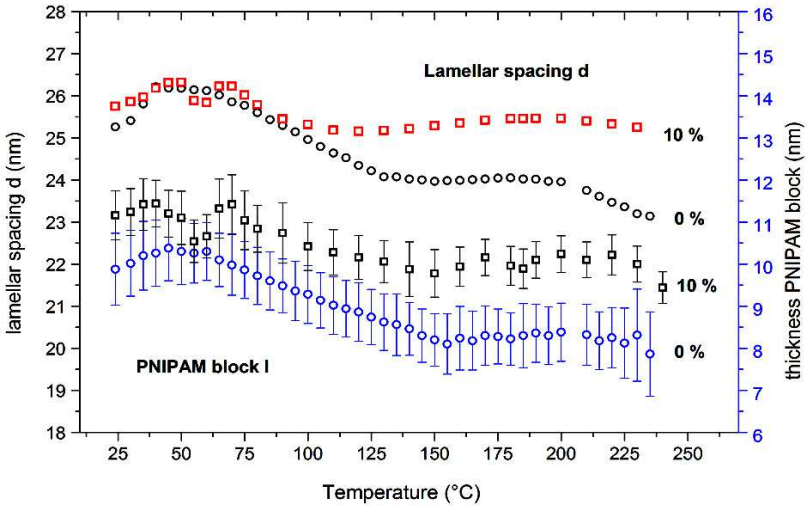

Figure 5.13:
Lamellar spacing d and thickness l of the PNIPAM block in cobalt salt-diblock copolymer hybrid bulk samples extracted from the SAXS data with increasing temperature. Bulk R = 0 wt% sample (circular data points) and R = 10 wt% (square data points).

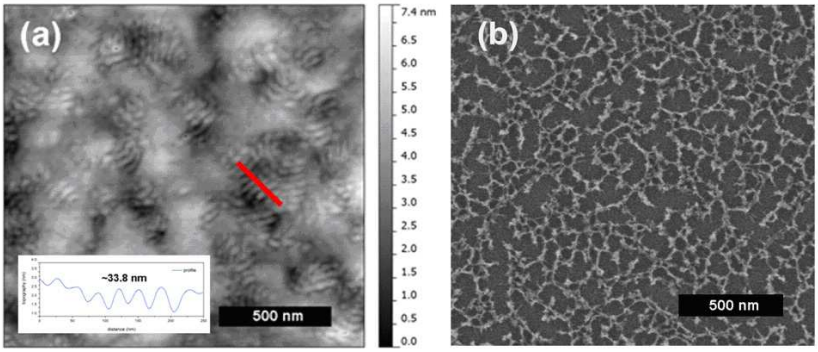

Figure 5.14:
a) AFM micrograph of the as prepared R = 10 wt% sample with an extracted topography profile. b) SEM image of the R = 30 wt% sample after 100°C annealing and oxygen plasma etching.

by GISAXS and SAXS data. This is explained by the different experimental conditions. The AFM scans are performed in ambient conditions while the SAXS/GISAXS data is collected in an evacuated chamber. Some selected hybrid films were further exposed to oxygen plasma etching to remove the polymer and then were examined with scanning electron microscopy (SEM). Figure 5.14b shows the residual structures of the R = 30 wt% sample after 100°C annealing and oxygen plasma etching. The wire like structures were presumably formed in the lamellar block and created a network like structure after the elimination of the polymer material. This interconnect nanowire structure with a percolation path is interesting for sensor related applications.

[1] E. Metwalli, S. Couet, K. Schlag, R. Röhlsberger, V. Körstgens, M. Ruderer, W. Wang, G. Kaune, S. V. Roth, P. Müller-Buschbaum, *Langmuir* **24**, 4265 (2008)

[2] E. Metwalli, J.-F. Moulin, J. Perlich, W. Wang, A. Diethert, S. V. Roth, P. Müller-Buschbaum, *Langmuir* **25**, 11815 (2009)

[3] E. Metwalli, V. Körstgens, K. Schlag, R. Meier, G. Kaune, A. Buffet, A. Couet, S. V. Roth, R. Röhlsberger, P. Müller-Buschbaum, *Langmuir* **29**, 6331 (2013)

5.6 Block copolymer electrolyte based membrane for lithium ion microbatteries

M. Rasool, E. Metwalli, H. Beyer[1], A. Eberle[1], H. Jha[1], H. A. Gasteiger[1], P. Müller-Buschbaum

[1] LS für Technische Elektrochemie, TUM, Garching, Germany

PEO based block copolymers are getting significant interest due to their conductivity and mechanical stability, which makes them especially suitable for applications such as lithium ion batteries. These conductive electrolyte membranes require defined conducting channels to transport charge carriers between electrodes and a supporting matrix to provide enough mechanical stability. Based on these requirements, the morphology of lithium ion-polymer hybrid films based on P(S-*b*-EO) block copolymer (BC) electrolyte is previously investigated [1-2]. The distinct relationship between the block copolymer morphology and its conductivity is still unclear. So in this report we employ both SAXS/WAXS and impedance spectroscopy to investigate this system. For SAXS/WAXS measurements, bulk samples were prepared using 50 mg/mL of P(S-*b*-EO) with different amount of LiTFSi (lithium salt) in THF solvent. The bulk sample solutions were brought on a thin mica window, where they were allowed to dry. After the complete drying of the sample, another mica window was used to sandwich it. The whole assembly was brought together using a stainless steel metal holder. All sample preparation was performed in a glove box. This sample assembly can be used for (SAXS/WAXS) experiments. Figure 5.15 shows (a) 2D SAXS and (b) WAXS scattering images for lithium diblock copolymer hybrid membrane with Li/EO ratio of 0.06 at $45\,^{\circ}\mathrm{C}$. In Fig. 5.16a WAXS and Fig. 5.16b SAXS profiles of the bulk sample of P(S-*b*-PEO) with Li/EO ratio of 0.06 at different temperatures are presented. The WAXS data show two diffraction peaks located at 1.36 and 1.66 nm^{-1}. These peaks were observed at temperatures below $55\,^{\circ}\mathrm{C}$ and then vanish at higher temperatures, which indicates the presence of PEO crystals below $55\,^{\circ}\mathrm{C}$. The SAXS data show the position of the first order peak at $45\,^{\circ}\mathrm{C}$ shifted from 0.168 to 0.186 nm^{-1} due to an increase in the interdomain spacing upon lithium ion incorporation. The data points show the reduced experimental data and the solid lines are the fits obtained using the Scatter software. A lamellar morphology of the lithium ion-polymer hybrid membrane is concluded. The domain size calculated from the SAXS profiles for Li/EO ratio of 0.06 varies from 35 to 63 nm with increasing temperature from $25\,^{\circ}\mathrm{C}$ to $105\,^{\circ}\mathrm{C}$. At $45\,^{\circ}\mathrm{C}$ the domain size increases from 50 to 60 nm. This shift can be seen in Fig. 5.16a at $45\,^{\circ}\mathrm{C}$.

Figure 5.17a shows the Nyquist plot of the lithium polymer hybrid membrane sandwiched between two Au electrodes. The conductivity data is fitted using an equivalent circuit as indicated in the inset in Fig. 5.17a. Conductivity was calculated from the fittings at different temperatures and presented in Fig. 5.17b. From Fig 5.17b, a systematic increase of conductivity with increasing temperature is observed, as indicated by the linear fit (red line) to the data points. As a conclusion, both morphology and impedance spectroscopy investigation is essential to better correlate the structure-conductivity relationship.

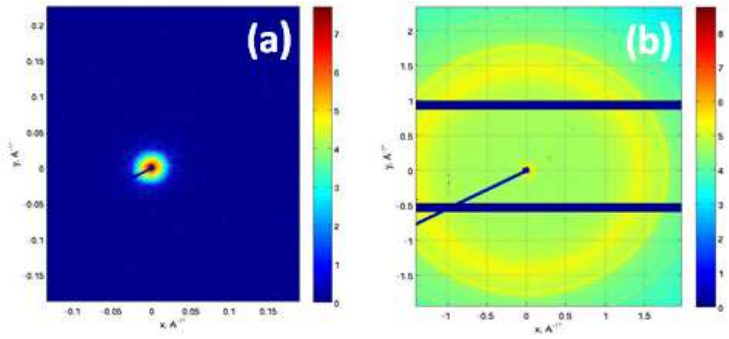

Figure 5.15:
a) SAXS and b) WAXS scattering images for lithium dibolock copolymer hybrid membrane with Li/EO ratio of 0.06 at $45\,^{\circ}\mathrm{C}$, the color bar is logarithmic intensity

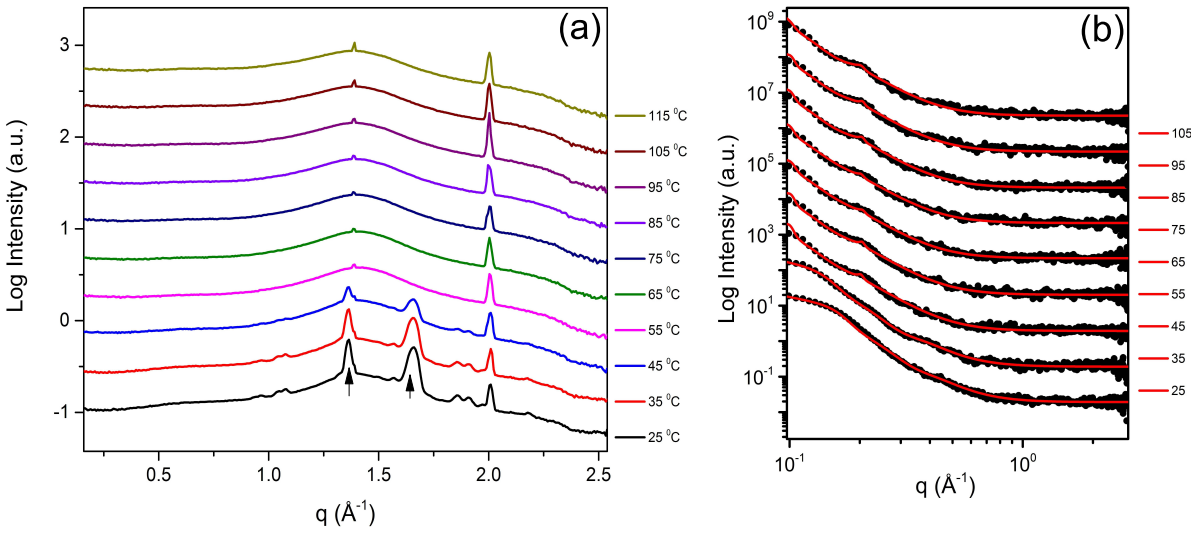

Figure 5.16:
a) WAXS and b) SAXS for lithium diblock copolymer hybrid membranes with Li/EO ratio of 0.06 at different temperatures. The WAXS data shows two diffraction peaks at temperatures below 55 °C that vanishes at higher temperatures. In the SAXS data the position of the first order peak is shifted at 45 °C, red lines are fits to the data points using the Scatter software.

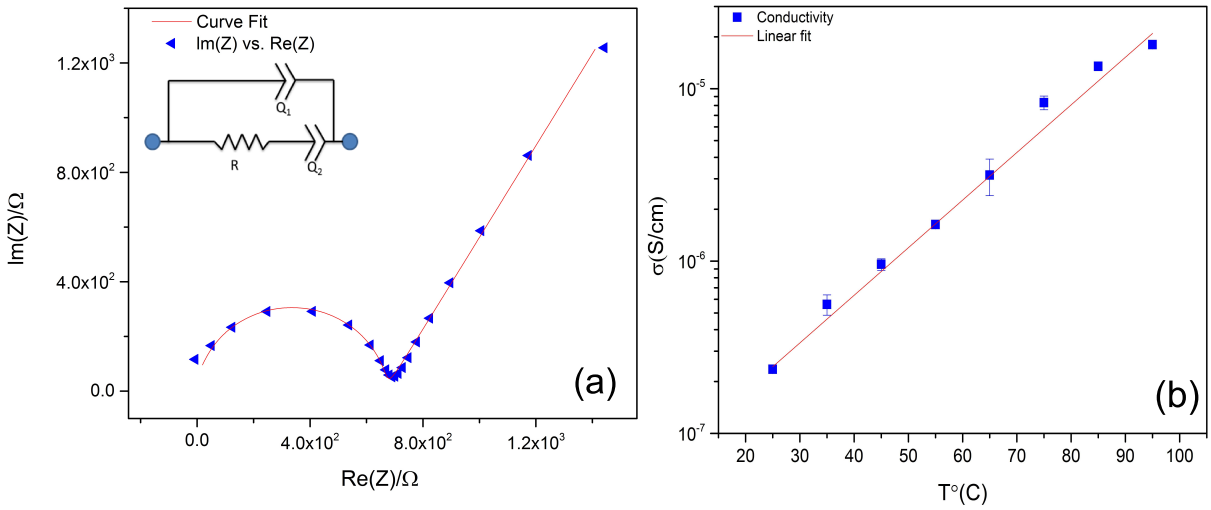

Figure 5.17:
a) Nyquist plot for lithium dibolock copolymer hybrid membrane with Li/EO ratio of 0.06 sandwiched between two Au electrodes. Symbols correspond to experimental data and the red curve corresponds to a fit using the proposed equivalent circuit. b) Conductivity values at different temperatures calculated from the fittings obtained from experimental data, red line corresponds to the linear fit.

[1] E. Metwalli, M. Nie, V. Körstgens, J. Perlich, S. V. Roth, P. Müller-Buschbaum, *Macromol. Chem. Phys.* **212**, 1742 (2011)

[2] W. S. Young, T. H. Epps, *Macromolecules* **45**, 4689-4697 (2012)

5.7 Aqueous processing of titania-nanoparticles for hybrid solar cells

C. Mayr, V. Körstgens, H. Iglev[1], P. Müller-Buschbaum

[1] Physik-Department E11, TUM, Garching, Germany

Hybrid solar cells combine the advantages of both materials they are made of. First, there is the conjugated polymer as electron donor and hole conductor with its high light absorbance and the possibility for roll-to-roll processing [1]. This manufacturing method is very economical and needs much less energy than e.g. the production for classical silicon solar cells. The use of polymers opens completely new areas of application, because the solar cells can be build flexible and lightweight. An inorganic electron acceptor and transporter is used as the second part of a hybrid active layer, which also contributes to the absorption and hence improves the total efficiency of the solar cell. Today, there is often the need for toxic organic solvents in the production of hybrid solar cells, which contradicts the idea of 'green' energy. Therefore, a potential way, which is more environmentally friendly, is using aqueous-processed active layers. Wei et al. presented in their work fill factors and efficiencies for aqueous processed solar cells up to 80 % and 2.14 %, respectively [2]. For the electron donor and acceptor we use a water soluble P3HT analogue and TiO_2 nanoparticles, respectively. The advantage of these particles is their size tunability, their high absorption coefficient and the high surface area. Thalluri et al. reached an efficiency of 0.70 % for a comparable system [3]. With the use of nanoparticles a large interfacial area with the polymer is facilitated. This bulk junction is desirable, because the movement of the electrically neutral excitons, which are generated during the light absorption, cannot be controlled. Therefore, a donor-acceptor interface is needed within the exciton diffusion length to successfully separate the charges and use the power of the absorbed photon.

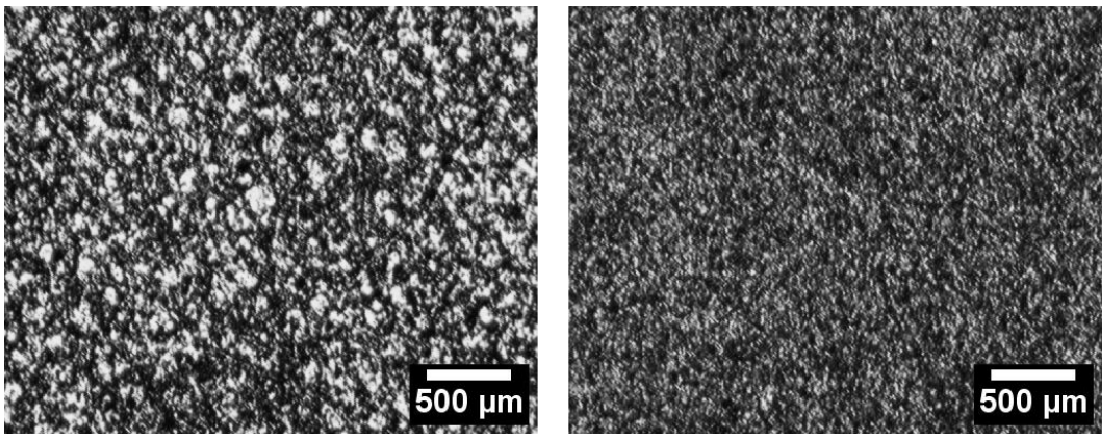

Figure 5.18:
Microscopy images with 10-fold magnification of the thin films containing P3P6T and 5μm titania particles (left) and 100 nm titania particles, respectively (right).

In our experiments we use two different titanium(IV)oxide powders by Sigma Aldrich as the metal electron acceptor. The average grain size of the particles is below 5 μm and below 100 nm, respectively. The second part of the hybrid film is the water soluble polymer poly[3-(potassium-6-hexanoate)thiophene-2,5-diyl] (P3P6T) from Rieke metals. 15 mg polymer were dissolved in 1 ml deionized water and stirred for four hours at 60 °C. The titania powder was dissolved in deionized water in a concentration of 10 mg/ml. The final film containing these two solutions has a weight ratio of titania to P3P6T of 2:1. Silicon substrates were acid cleaned for 15 minutes and thereafter treated with oxygen plasma to make its surfaces hydrophilic for the application of the aqueous based hybrid layer via spray casting. Figure 5.18 shows microscope images of

the TiO_2:P3P6T thin films with an average titanium(IV)oxide particle size below 5 μm on the left side and a particle size smaller than 100 nm on the right side, respectively. Both show the desired porous structure with a large interfacial area. As expected the latter blend has a finer distribution. Furthermore a hybrid layer containing of P3P6T and titania nanoparticles with an average size distribution of less than 100 nm was sprayed on a glass sample with the same approach as before. Figure 5.19 shows the graph of light absorbance of the active layer, normalized to its highest absorption. To see the contribution of the single components, we sprayed the pure polymer and the pure nanoparticles. It can be seen, that the polymer absorbs light mostly in the visible region, whereas the titanium(IV)oxide particles have the absorption peak in the UV region. The TiO_2:P3P6T blend combines both absorption regions and therefore uses the sunlight more efficiently.

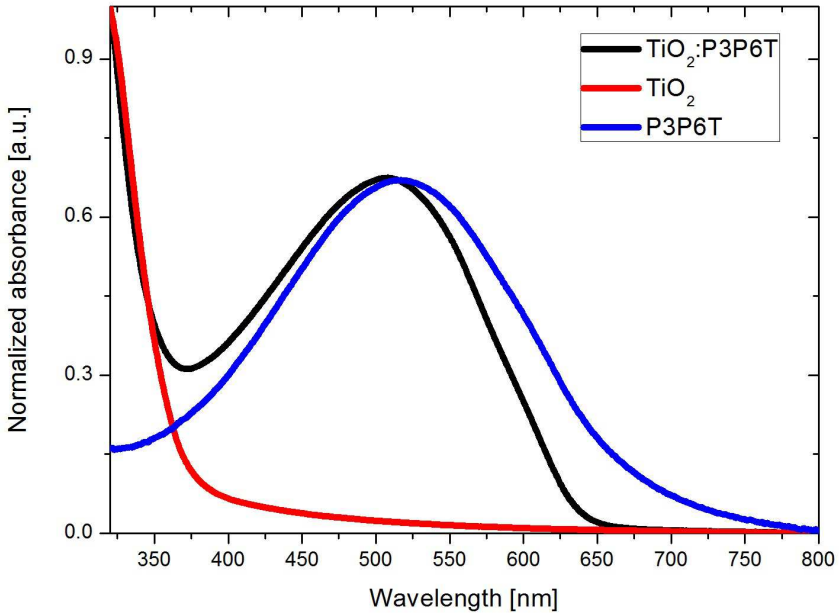

Figure 5.19:
Normalized absorbance of thin films consisting of the polymer, the 100 nm titanium(IV)oxide particles and the TiO_2:P3P6T active layer, respectively.

Our further investigations will focus on a mixture of titanium(IV)oxide particles of different sizes and with different concentrations to further improve the porous titania network. Also the parameters of spray coating will be changed to alter e.g. the film thickness. This is important in the final solar cell where we will investigate the photovoltaic performance. For the solar cell efficiency it is also crucial to have a crystalline structure in both the polymer and the metallic components of the active layer duo to the better charge conduction. Therefore, we will investigate the active layer with XRD and SEM measurements to characterize the crystalline structure and the surface structure, respectively.

[1] B. R. Saunders, *J. Coll. Inter. Sci.* **369**, 1-15 (2012)

[2] H. Wei, H. Zhang, H. Sun, B. Yang, *Nano Today* **7**, 316-326 (2012)

[3] G. K. V. V. Thalluri, J. Bolsee, A. Gadisa, M. Parchine, T. Boonen, J. D'Haen, A. E. Boyukbayram, J. Vandenbergh, T. J. Cleij, L. Lutsen, D. Vanderzande, J. Manca, *Sol. Energ. Mat. Sol.* **95**, 3262-3268 (2011)

5.8 Investigations toward high-efficiency dye-sensitized solar cells

Y. C. Rui, B. Su, P. Müller-Buschbaum

Dye-sensitized solar cells (DSSCs), with advantages of low cost, simple manufacture procedure and high theoretical energy conversion efficiency, have been attracting global attentions since the breakthrough work of O'Regan and Grätzel in 1991 [1]. A typical DSSC consists of a photoanode fabricated from mesoporous TiO_2 nanoparticles, dye molecules, iodide/triiodide redox couple, and a platinum counter-electrode. The energy conversion efficiency based on such materials has reached above 12% [2].
Several factors influence the efficiencies of the liquid electrolyte based DSSCs. Firstly, for the titania film, the thickness should be at least 10 μm, and the optimal thickness range is about 12 to 14 μm. If the film is too thin, the total surface area available to adsorb dye molecules will not to sufficient to absorb all incoming light. The conventional methods of fabricating the titania films are screen-printing or doctor-blading. Films made from spin-coating or spraying are usually too thin, which may be less than 2 μm in film thickness. With such thin films it is difficult to get a satisfactory efficiency in the DSSC approach. The titania pastes containing organic materials need to be sintered. Different organic materials need different sintering schedules. In the case of ethyl cellulose and terpineol based paste, the films should be gradually heated under an airflow at 325 °C for 5 min, at 375 °C for 5 min, and at 450 °C for 15 min, and finally, at 500 °C for 15 min. Pre-treatment and post-treatment are also the essential steps to guarantee a high efficiency. Pre-treatment is to form a compact titania layer between the FTO and mesoporous film, which can inhibit photoelectron recombination. The post-treatment is to obtain a well inter-connected porous film, which can also inhibit electron recombination. For the dye, ruthenium based small molecules are still the best choice, including N3, N719 and Black dye. After the sintering process, the hot photoanode film with a temperature about 80 °C should be immersed into the dye solution as soon as possible. The sensitization time is about 24 h. The pure electrolyte consisting only of iodine/triiodide as redox couple is not sufficient to reach high efficiencies, and some additives are necessary. A superior recipe provided by Ito et al. is as follows: The electrolyte employed was a solution of 0.6 M BMII, 0.03 M I_2, 0.10 M guanidinium thiocyanate and 0.5 M 4-tert-butylpyridine in a mixture of acetonitrile and valeronitrile (volume ratio, 85:15) [3].
After some initial material testing, DSSCs made from different materials were prepared and the *J-V* curves are shown in Fig. 5.20. The updated techniques indeed improve the DSSCs efficiencies.

Photoanode films made from tiny TiO_2 nanocrystallites, usually with the size about dozens of nanometers, exhibit high transparency and low utilization rate of incident light. Therefore, a bi-layer photoanode film with a light-scattering film placed on top of the nanocrystalline film has been adopted widely in state-of-the-art DSSCs as it increases the optical path of light and thereby enhances the photocurrent density. In our research, WER2-O Reflector Titania Paste purchased from Dyesol Corporation is used as the scattering layer while 18NR-T Titania Paste is used as the underlayer. Figure 5.21 shows an optical image of the photoanode with (right side) and without (left side) a scattering layer. Obviously, the scattering layer reflects a large portion of visible light back to the film, and improves the light harvesting of the photoanode. Figure 5.22 shows the *J-V* curves of DSSCs based on the photoanodes without and with a scattering layer. The short-circuit current density is increased after adding the scattering layers. The best DSSC shows a short-circuit current density (J_{sc}) of 15.5 mA cm^{-2}, an open-circuit voltage (V_{oc}) of 723 mV, and a fill factor (FF) of 68.0%, leading to an energy conversion efficiency (η) of 7.65%. Therefore the best achieved efficiency can exceed 8% after including several further optimization steps.

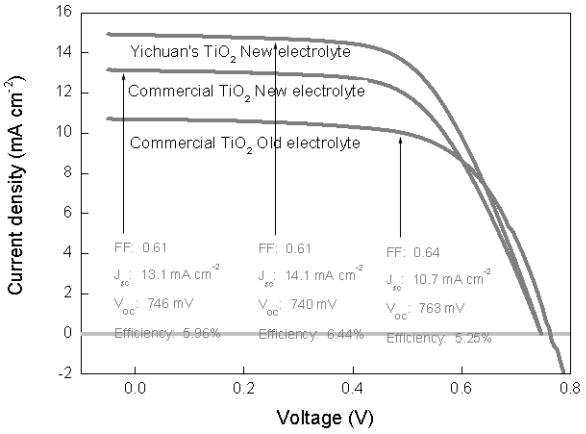

Figure 5.20: Example of *J-V* curves of DSSCs based on different materials as indicated.

Figure 5.21:
Optical image of the photoanode with (right side) and without (left side) a scattering layer.

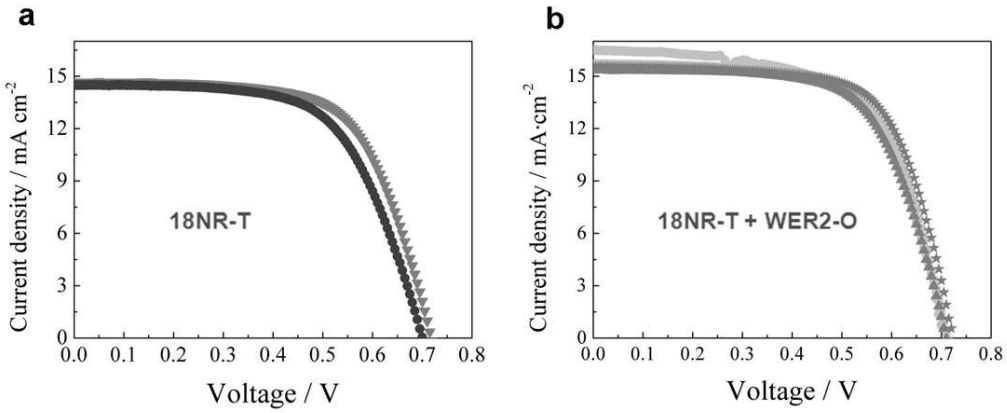

Figure 5.22:
Example of *J-V* curves of DSSCs based on the photoanodes without a) and with b) a scattering layer as explained in the text.

[1] B. Oregan, M. Grätzel, *Nature* **353**, 737-740 (1991)

[2] A. Hagfeldt, G. Boschloo, L. C. Sun, L. Kloo, H. Pettersson, *Chem. Rev.* **110**, 6595-6663 (2010)

[3] S. Ito, T. N. Murakami, P. Comte, P. Liska, C. Grätzel, M. K. Nazeeruddin, M. Grätzel, *Thin Solid Films* **516**, 4613-4619 (2008)

5.9 Low temperature route to nanostructured titania films

T. Widmann, W. Wang, L. Song, K. Sarkar, P. Müller-Buschbaum

In recent years hybrid solar cells have attracted an increasing interest of researchers. Typically the hybrid solar cells consist of a nanostructured inorganic semiconductor matrix filled with a hole conducting polymer. One of the most promising advantages of hybrid solar cells is the flexibility, which enables the production by a roll-to-roll process and in large scale. For this purpose, flexible substrates such as PET or other polymers are used. For the nanostructured hybrid layer, titania is a commonly used material. However most of the production routines of titania preparation include a high temperature calcination step at minimum of 400 °C or even at higher temperatures [1]. As flexible substrates such as PET or PEN can not stand temperatures above 150 °C, a low temperature synthesis route to nanostructured titania films is required.
For this purpose, a sol-gel synthesis in combination with micro-phase separation is used. Poly (styrene-block-ethylene oxide), denoted P(S-b-EO), an amphiphilic diblock copolymer, is used as the structure directing template and ethylene glycol-modified titanate (EGMT) as a novel titania precursor. By tuning the pH-value of the sol-gel, different crystalphases of the titania can be achieved. For the sol-gel, first of all P(S-b-EO) is dissolved in N,N-dimethylformamide (DMF) which is a good solvent for both polymer blocks. After stirring the solution for 30 min it is filtered with a 0.45 μm filter. Then HCl (37%) and EGMT are added and the solution is stirred again for 30 min and an additional 15 min at 90 °C. Finally, the sol-gel is spin-coated (2000 rpm, 60 s) on pre-cleaned silicon Si(100) substrates and annealed at 90 °C for 30 min. The spin-coating is repeated three times in order to get a higher film thickness as needed in hybrid solar cells. A value of about 50 nm is reached [2]. Larger layer thickness are difficult to realize as additional spin-coating will barely increase it. Finally, P(S-b-EO) needs to be extracted so that the titania layer can be backfilled with a conducting polymer later on. In order to extract the polymer from the nanostructured polymer/titania layer in a way that would leave a PET substrate intact, a low temperature extraction method is necessary. Different methods, UV-extraction and wet solvent extraction with 1,4-dioxane as solvent are used separately. Additionally, one sample is calcined at 400 °C as reference.

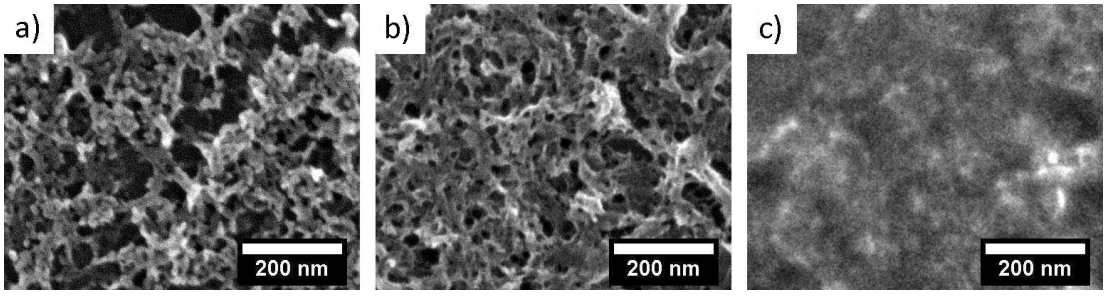

Figure 5.23:
SEM images of nanostructured titania layers treated with a) 4h calcination, b) 16 h UV-extraction and c) 2 min solvent extraction.

Figure 5.23 shows the SEM images of the reference sample treated with calcination at 400 °C for 4 h (a), a sample of the UV-chamber after 16 h of irradiation (b) and a sample after 2 min inside a 1,4-dioxane bath (c). As known, for the calcined sample the polymer is completely removed during the high temperature process. Clearly visible, the titania nanostructures are formed. A foam-like structure with a high diversity in pore-sizes of 20 - 100 nm is obtained. This foam like structure is still visible for the UV-irradiated sample, however the pore-sizes

of the foam structure are reduced to the range of 10 - 30 nm. For the sample treated with wet solvent extraction no structures but a featureless surface is visible. This indicates that most of the polymer is still left inside the titania layer. Hence the UV-extraction is found to remove the polymer most efficiently at a low temperature and will therefore be used in future experiments. For the application in hybrid solar cells a higher film thickness in the range of around 100 nm is required. Therefore, different deposition methods are investigated. Solution-casting, blade-casting and spray-coating are used as possible alternatives to spin-coating. The sol-gel is prepared in the same way as described above. For the blade-casting a silicon substrate is fixed with two tape-stripes, which also provide a fixed distance. 100 μl of the sol is cast on the substrate and distributed with a glass holder by pulling it over the tape. However, the surface cracks up completely during the drying process, so that no homogeneous film is obtained. The same happens to the solution-cast layer where 250 μl of the sol are deposited on a leveled substrate and dried with silica gel and under ambient conditions respectively.
Finally, the possibility of spray-coating the sol-gel is investigated. Again the sol-gel is prepared as above and then sprayed onto pre-cleaned silicon substrates heated to 100 °C. With an airbrush spray gun the sol is sprayed with a 5 s break every 10 s and finally the sample is annealed at 100°C for 30min. However, shortly after the annealing, droplets in the range of 100 - 500 nm start to form on top of the sample as seen in Fig. 5.24a. They form most likely due to solvent trapped inside the film. Therefore an inhomogeneous film was acquired. In order to remove the droplets and attain a more homogeneous film, the break time was increased to 10 s and the annealing time to 20 h. By doing so, we are able to hinder the formation of droplets on the sample. Moreover, a more homogeneous film was created, shown in Fig. 5.24b.
Via spray-coating the film thickness can reach up to several micrometer which would allow an application in dye sensitized solar cells. Thinner films in the range of hindered of nanometer for hybrid solar cells are feasible as well, because by adjusting the amount of sol-gel sprayed on the sample the thickness can be tuned.

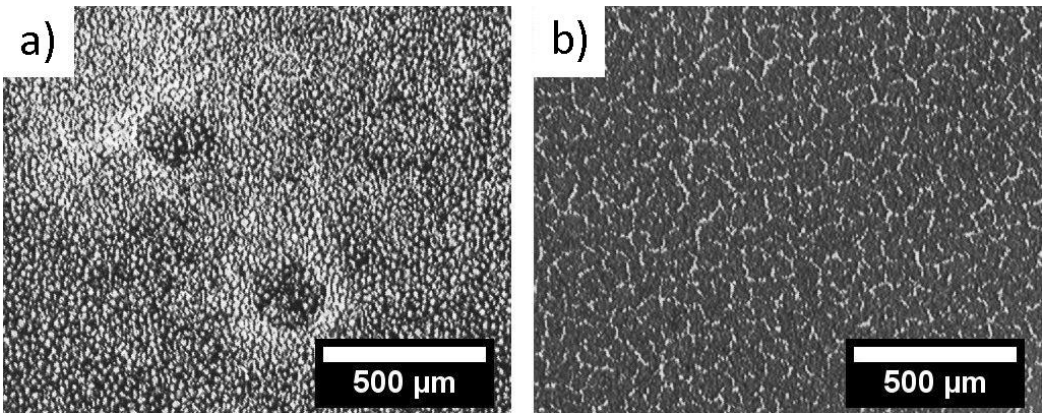

Figure 5.24:
Microscope images of spray-coated samples with annealing times of a) 30 min and b) 20 h.

In summary a nanostructured titania film with a good porosity was achieved and spray casting was found as a suitable method to tune the film thickness for application in hybrid solar cells.

[1] J. Weickert, R. B. Dunbar, H. C. Hesse, W. Wiedemann, L. Schmidt-Mende, *Adv. Mater.* **23**, 1810-1828 (2011)

[2] M. Rawolle, E. V. Braden, M. A. Niedermeier, D. Magerl, K. Sarkar, T. Fröschl, N. Hüsing, J. Perlich, P. Müller-Buschbaum, *Chem. Phys. Chem.* **13**, 2412-2417 (2012)

6 Dynamics

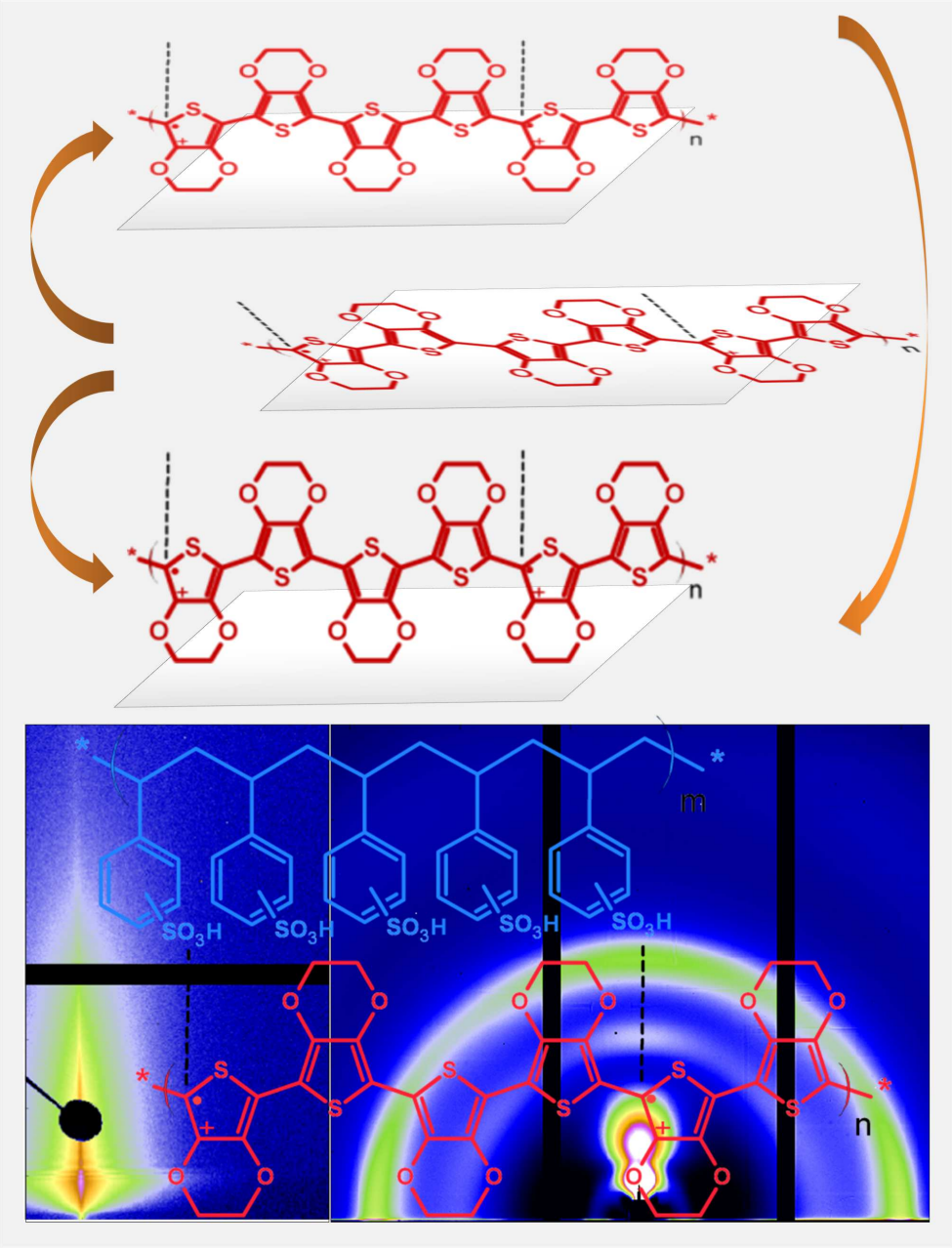

6.1 Investigation of kinetic processes accompanying the demixing transition of thermo-responive polymer solutions

M. Philipp, U. Müller[1], R. Aleksandrova[1], R. Sanctuary[1], P. Müller-Buschbaum, J. K. Krüger[1]

[1] University of Luxembourg, Luxembourg, Luxembourg

Stimuli-responsive polymer solutions undergo phase separation when subjected to external stimuli, like changes of temperature, pH or ionic strength. Poly(N-isopropylacrylamide) (PNIPAM) is a classical thermo-responsive polymer, which has attracted much attention because of its sharp lower critical solution temperature type (LCST-type) demixing transition in aqueous environment at about 33 °C. The PNIPAM molecules are subjected to a coil-to-globule transition during phase separation. The molecular collapse and partial dehydration of the PNIPAM chains is followed by a much slower process, namely the aggregation of the macromolecules, occuring typically on the time scale of minutes to hours. These kinetic processes lead to PNIPAM-rich aggregates with diameters of several 100 nm to micrometers embedded in a water-rich phase [1].

Depending on the most relevant physicochemical processes, different laws may govern the growth of the PNIPAM-rich domains in the phase-separated state. Depending on the elastic properties and the temperature-dependent attraction energy of the colliding PNIPAM-rich clusters, more or less fractal aggregates are expected to grow during phase separation. Amongst others, the depth of temperature jumps into the demixed state, the heating rate, the polymer concentration and the presence of ions can influence the growth kinetics and hence the resulting structures of the demixing polymer solution.

In the current study, we study purely elastic properties of PNIPAM solutions in dependence of temperature, space and time. The longitudinally polarized hypersonic velocity, as well as the longitudinal elastic modulus were indeed already shown to be highly sensitive to the LCST-type demixing transition of PNIPAM solutions [2]. As depicted in Fig. 6.1, we are able to discriminate different kinetic processes, which are related to the phase separation into PNIPAM-rich and PNIPAM-poor domains, as well as kinetics connected to the impact of gravitation on the on-going phase separation. In order to study the reversibility of the phase transition, the remixing transition is also analysed upon cooling the priorly demixed solutions.

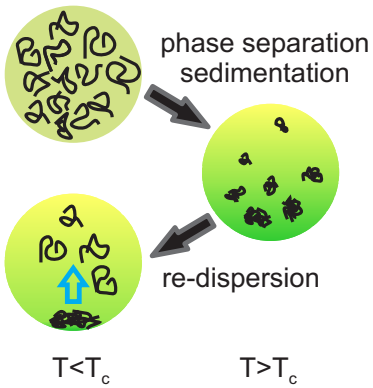

Figure 6.1:
Schematic drawing of the kinetic processes studied near the demixing transition temperature T_c of aqueous PNIPAM solutions.

Our Brillouin spectroscopic investigations were performed on a modified six-pass tandem Brillouin spectrometer of the Sandercock type in collaboration with the group of Prof. Krüger at the University of Luxembourg [2-4]. The PNIPAM homopolymer (M_n = 20 - 25 kg/mol) was

purchased from Sigma-Aldrich Chemie GmbH, Taufkirchen. Details of the experimental investigations are given in [2-4]. The hypersonic velocity v_L was determined from the Brillouin spectra determining the positions of the Brillouin doublets.

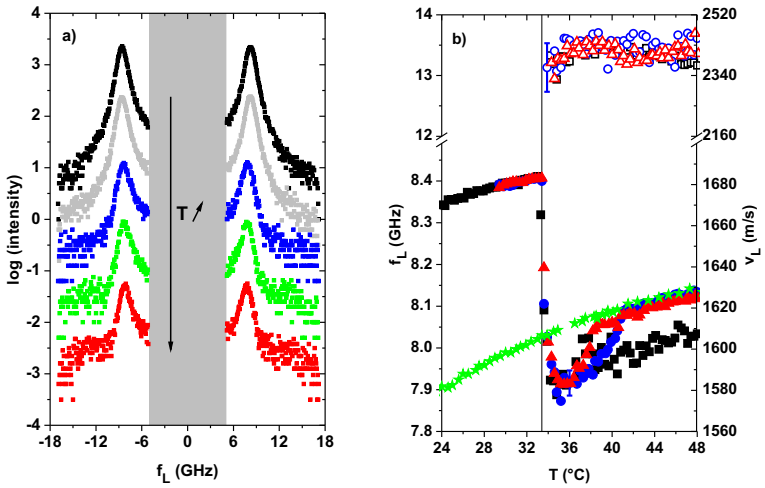

Figure 6.2:
a) Logarithmic representation of Brillouin spectra recorded in the middle of the cuvette during heating a 10 mass% PNIPAM solution across the demixing transition temperature (from T_c-2°C to T_c+1°C). The central Rayleigh line is omitted due to technical reasons. For clarity, the spectra are shifted vertically. b) Hypersonic frequency/hypersonic velocity versus temperature recorded at the bottom (black squares), in the middle (red triangles) and at the top (blue dots) of the cuvette while heating the 10 mass% solution or distilled water (green stars). Filled symbols: low frequency phonon branch, open symbols: high frequency phonon branch.

In Fig. 6.2a are represented typical Brillouin spectra recorded in the middle of the cuvette across the demixing transition of the 10 mass% PNIPAM solution. One clearly sees that a second Brillouin doublet arises at about 15 GHz during phase separation. It can be attributed to the growth of PNIPAM-rich aggregates, which possess gel-like mechanical consistency and which are embedded in the PNIPAM-poor phase. In Fig. 6.2b is indicated an overview over the evolution of the hypersonic velocity versus temperature for three different positions in the cuvette upon heating. As discussed in [4], this study allows gaining insight into the interplay between the growth kinetics of PNIPAM-rich domains and sedimentation kinetics upon heating, and the re-dispersion of the PNIPAM-rich agglomerates and homogenization upon cooling across the demixing transition.

M.P. thanks the Fonds National de la Recherche (Luxembourg) for the receipt of a Marie Curie cofunded AFR Postdoc grant.

[1] A. Meier-Koll, V. Pipich, P. Busch, C. M. Papadakis, P. Müller-Buschbaum, *Langmuir* **28**, 8791-8798 (2012)

[2] M. Philipp, U. Müller, R. Aleksandrova, R. Sanctuary, P. Müller-Buschbaum, J. K. Krüger, *Soft Matter* **8**, 11387-11395 (2012)

[3] M. Philipp, U. Müller, R. Aleksandrova, R. Sanctuary, P. Müller-Buschbaum, J. K. Krüger, *Soft Matter* **9**, 5034-5041 (2013)

[4] M. Philipp, U. Müller, R. Aleksandrova, R. Sanctuary, P. Müller-Buschbaum, J. K. Krüger, *Soft Matter* **9**, 9887-9896 (2013)

6.2 Molecular interactions and hydration in thermo-responsive polymers probed with FTIR spectroscopy

A. Schulte[1], M. Philipp, C. J. Schaffer, P. Müller-Buschbaum

[1] also at: University of Central Florida, Orlando, USA

Poly(N-isopropyl acrylamide) (PNIPAM) and other thermo-responsive polymers undergo a reversible coil-to-globule transition, after which the chains collapse and aggregate into bigger globules, in water above its lower critical solution temperature (LCST) [1]. PNIPAM is among the thermoresponsive polymers well studied in solution. However, less is known about properties of bound water molecular changes at the lower critical solution temperature. Vibrational spectroscopic probes are sensitive to chemical bonding and micro-structural changes and complement small angle scattering techniques that are used to study morphology. We apply Fourier-transform infrared (FTIR) spectroscopy is developing into a sensitive tool to monitor subtle molecular changes [2].
In initial experiments we have investigated PNIPAM films prepared from polymer provided by Sigma-Aldrich (SA) and Polymer Standard Systems (PS). The molecular masses are 20 - 25 kg/mol (SA) and 20.5 kg/mol mass averaged (PS), respectively. The LCS temperature for solutions of 20 mass% homopolymer are slightly different, namely 32.4 ^oC for SA and 29.5 ^oC for PS. This raises the question of the molecular origin of this variation. Therefore we conducted FTIR experiments to elucidate molecular differences. The polymers were dissolved in chloroform, and thin films (390 nm thickness) were prepared by spin coating on silicon substrates. FTIR spectra were measured with a Bruker Equinox 55 spectrometer equipped with a DTGS detector. Per spectrum 128 scans were accumulated at a resolution of 2 cm^{-1}.

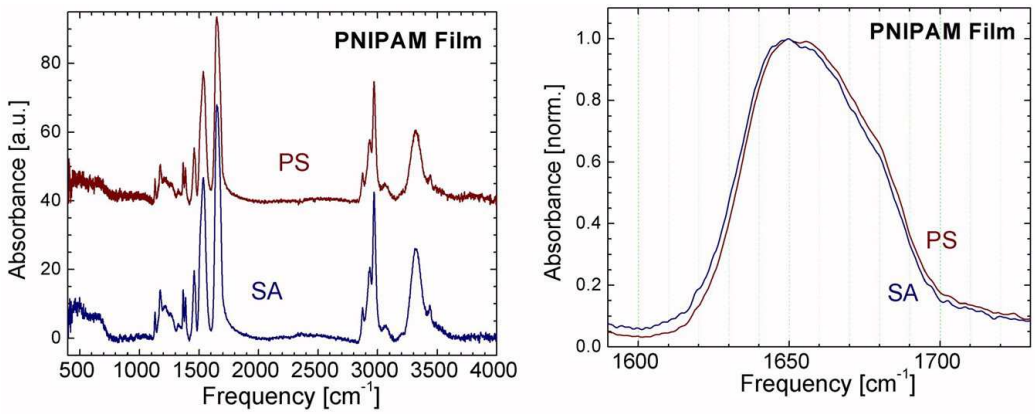

Figure 6.3:
Mid-infrared spectra of PNIPAM films in the fingerprint region (left). Samples were made from polymers obtained from two different manufacturers (labelled SA and PS). The panel on the right displays the Amide I band region. The small shift can be attributed to differences in tacticity of the polymers.

A comparison of the mid-infrared spectra of PNIPAM films from PS and SA polymers is presented in Fig. 6.3. The band the near 3,300 cm^{-1} is attributed to the hydrogen-bonded N–H stretching vibration, while the C–H stretching vibration bands occur in the range of 3,000–2,800 cm^{-1}. The intense band near 1650 cm^{-1} has been assigned to the amide I vibration. It involves the carbonyl group. This band is shifted to higher wavenumber in the PS film. Katsumoto et al. [3] have conducted a study of the role of tacticity in the infrared spectra. In tacticity controlled samples they reveal a systematic shift of the Amide I band. On the other hand, it has been established that the phase separation temperature of PNIPAM depends on the tacticity of

the polymer [4]. Thus, the tacticity appears to be different in the nominally identical polymers prepared by PS and SA.
The dynamics of the hydration water plays a major role in the coil-to-globule transition. To investigate the molecular structural changes a PNIPAM solution (25 mass%) of polymer from Sigma-Aldrich was dissolved in D_2O. The sample was measured in a transmission cell in which the polymer solution was sandwiched between two IR transmitting ZnS windows. Infrared spectra below and above the LCST are shown in (Fig. 6.4). The pattern of spectral bands is reminiscent of that in the films. In addition to the polymer bands (which are broadened compared to the thin films) the O-D stretching frequency is seen in the spectral region near 2500 cm^{-1}.

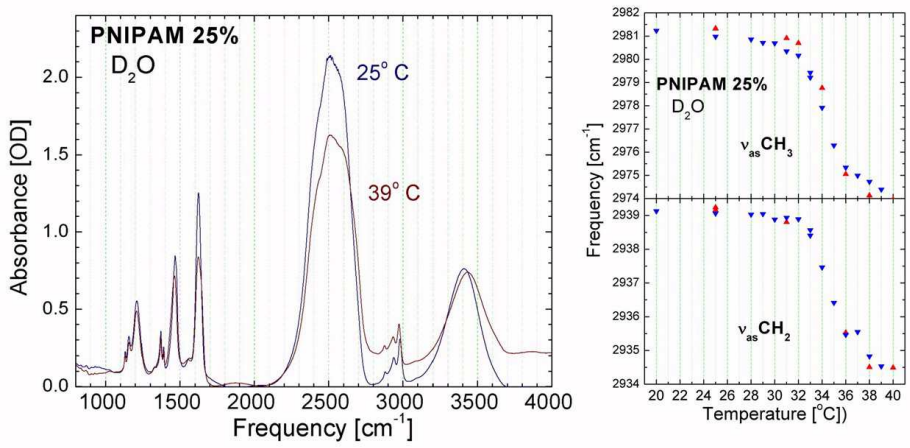

Figure 6.4:
FTIR spectra of PNIPAM films at variable temperature (left). The spectra probing polymer, film hydration, and D_2O solvent. Spectral changes occur in the C-H region (film – solution), the Amide region (deuteration on the N-H protons), and the water bands. The panel on the right displays the peak frequencies of bands in the C-H spectral region as a function of temperature. Different symbols indicate data from heating and cooling processes, respectively. A significant shift occurs across the LCST transition.

As a function of temperature the spectra show significant changes. This is illustrated for the peak positions of bands in the C-H stretch region in Fig. 6.4. Across the phase transition the peak positions shift to lower frequency in an almost step-like manner. The onset temperature is in good agreement with the LCST from turbidity measurements.
FTIR spectroscopy in combination with variations in temperature provides a means to probe conformational changes across the LCST transition and the behavior of the hydration water bands. It also yields information on molecular changes between polymer in solution and in thin film form. The technique can be applied to a wide range of materials. In ongoing experiments hydration changes in thin PNIPAM films [5] and other thermo-responsive polymers are investigated.
This work has been financially supported by the DFG in the priority program SPP 1259 'Intelligente Hydrogele' (MU1487/8). A. S. thanks the University of Central Florida for research support.

[1] H. G. Schild, Prog Polym Sci 17:163-249, *Prog. Polym. Sci.* **17**, 163-249 (1992)

[2] B. Sun, Y. Lin, P. Wu, H. W. Siesler, *Macromol.* **41**, 1512-1520 (2008)

[3] T. Hasegawa, S. Tatsuta, Y. Katsumoto, *Anal. Bioanal. Chem.* **398**, 2203-2209 (2010)

[4] B. Ray, Y. Okamoto, M. Kamigaito, M. Sawamoto et al., *Polym. J.* **37**, 234-237 (2005)

[5] A. Schulte, M. Philipp, C. J. Schaffer, P. Müller-Buschbaum, *DPG Frühjahrstagung*, CPP 54.62 (2014)

6.3 Dehydration behaviour of phase separating PNIPAM solutions

M. Philipp, K. Kyriakos, L. Silvi[1], W. Lohstroh[1], W. Petry[1], J. K. Krüger[2], C. M. Papadakis, P. Müller-Buschbaum

[1] MLZ, Garching, Germany

[2] University of Luxembourg, Luxembourg, Luxembourg

Thermo-responsive polymers exhibit in aqueous solution a demixing transition which is of the lower critical solution temperature (LCST) type. Such polymer solutions undergo phase separation upon heating above the demixing temperature T_c. Due to their sharp phase transition lying at about 32°C, thermo-responsive poly(N-isopropyl acrylamide) (PNIPAM) systems are widely studied. They have large application potential, for instance in the field of biotechnology [1].

The demixing transition leads to the collapse of PNIPAM chains in aqueous environment, which is followed by the growth of PNIPAM-rich aggregates, being embedded in a water-rich phase [2]. This structural re-organization is accompanied by a dehydration of the PNIPAM molecules. Despite the relevance of this dehydration process for the demixing transition, it has only been roughly characterized and understood. A highly cooperative dehydration of the macromolecules could be responsible for the sharpness of the demixing transition observed for PNIPAM solutions [3].

We studied the dehydration process of a concentrated PNIPAM solution during its phase separation by analysing the local diffusion behaviour of water molecules. The decrease of the hydration number, being defined as the number of water molecules being bound to one NIPAM monomer, was investigated across the demixing transition. Furthermore, we started to elucidate the impact of the molecular dehydration process on macroscopic properties. Of particular interest were such properties, which are closely related to the order parameter of the demixing transition, like the mass density and elastic properties [4-6]. Due to the large excess volumes observed at the demixing transition, it is actually also called a volume phase transition.

Quasi-elastic neutron scattering (QENS) experiments were carried out on the proton dynamics of H_2O and PNIPAM at the time-of-flight spectrometer TOF-TOF at the MLZ in Garching. PNIPAM homopolymer (M_n = 20 - 25 kg/mol) was purchased from Sigma-Aldrich Chemie GmbH, Taufkirchen and used to prepare a 20 mass% PNIPAM solution. The QENS spectra of this PNIPAM solution were recorded at ten tempertures lying in the vicinity of the demixing transition temperature. The central parts of representative QENS spectra below and above the demixing transition are given in Fig. 6.5a. These datasets were fitted using a model scattering function consisting of the sum of an elastic contribution, represented by a delta-function, and two Lorentzian curves (see lines in Fig. 6.5a). These Lorentzian lines are assigned to two water populations, which can be resolved in the selected energy window. The narrow quasi-elastic line is attributed to strongly associated water below the demixing temperature, which belongs to the hydration shells of PNIPAM molecules. The broad quasi-elastic Lorentzian is related to almost freely moving H_2O molecules, which diffusion behaviour is only slightly hindered in this concentrated PNIPAM solution. The line widths versus q can be described for both water populations by the model of isotropic jump diffusion. This means that an H_2O molecule stays at a given position for a certain residence time before it jumps over a distance of about 0.1 to 0.2 nm to another position. We observe that the residence times, which typically lie in the picosecond time range, strongly decrease for the hydration shell water above the demixing transition temperature. From this it follows that the hydration shells are gradually released above T_c.

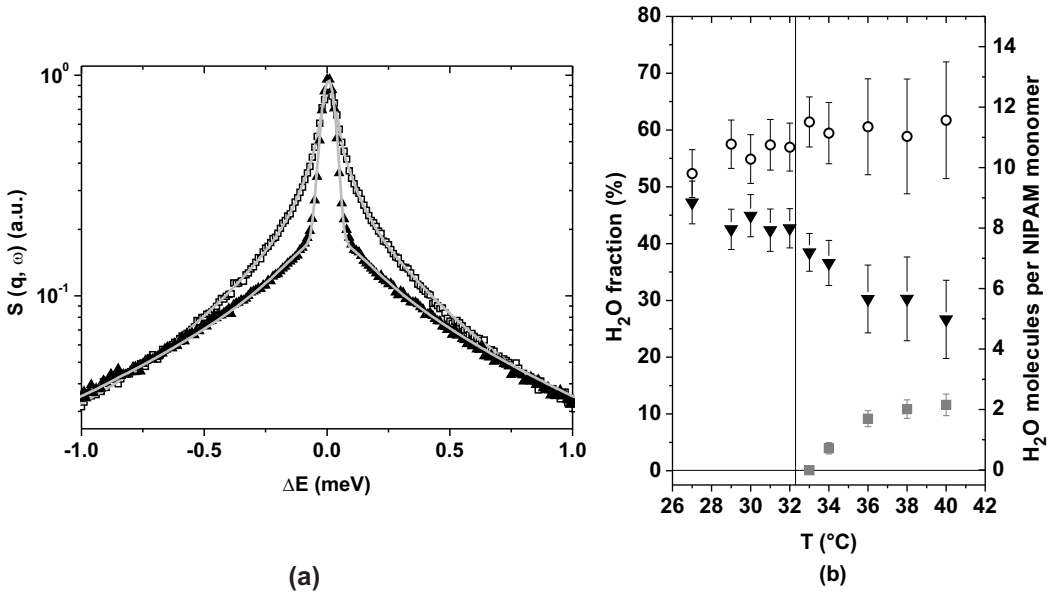

Figure 6.5:
a) Central part of the quasi-elastic neutron scattering spectra versus energy transfer for a 25 mass% PNIPAM solution at 27 °C (open black squares) and 40 °C (full triangles). Fits are represented by grey lines. The demixing transition temperature T_c lies at 32.2 °C. b) fraction/number of H_2O molecules per NIPAM monomer of very strongly associated water (hydrated above T_c; grey squares), strongly associated water (hydrated below T_c; triangles) and almost freely moving water (dots). Both axis are valid for all curves.

In Fig. 6.5b are represented the number of H_2O molecules per NIPAM monomer of strongly associated water, belonging to the hydration shells below T_c and almost freely moving water. These numbers are extracted from the areas of the Lorentzian lines. Remarkably, above T_c arises a scattering contribution of very strongly associated water, which cannot be resolved in the chosen energy window. In accordance with infrared spectroscopic findings, we surmise that only the hydrophobically associated water of the hydration shells is released during the partial dehydration of PNIPAM above T_c. Finally, first investigations were made in order to better understand the impact of the dehydration of water molecules on the excess volume related to the demixing transition.

M.P. thanks the Fonds National de la Recherche (Luxembourg) for the receipt of a Marie Curie cofunded AFR Postdoc grant.

[1] M. A. Cole, N. H. Voelcker, H. Thissen, H. J. Griesser, *Biomaterials* **30**, 1827-1850 (2009)

[2] A. Meier-Koll, V. Pipich, P. Busch, C. M. Papadakis, P. Müller-Buschbaum, *Langmuir* **28**, 8791-8798 (2012)

[3] F. Tanaka, T. Koga, H. Kojima, N. Xue, F. Winnik, *Macromolecules* **44**, 2978 (2011)

[4] M. Philipp, U. Müller, R. Aleksandrova, R. Sanctuary, P. Müller-Buschbaum, J. K. Krüger, *Soft Matter* **9**, 5034-5041 (2013)

[5] M. Philipp, U. Müller, R. Aleksandrova, R. Sanctuary, P. Müller-Buschbaum, J. K. Krüger, *Soft Matter* **9**, 9887-9896 (2013)

[6] U. Müller, M. Philipp, M. Thomassey, R. Sanctuary, J. K. Krüger, *Thermochim. Acta* **555**, 17-22 (2013)

6.4 Phonons and the thermodynamics of Fe

M. Leitner, J. Neuhaus[1], N. Karl, W. Petry, B. Hennion[2], A. Hiess[3]

[1] MLZ, Garching, Germany
[2] Laboratoire Léon Brillouin, CEA Saclay, France
[3] Institut Laue-Langevin, Grenoble, France (now at ESS, Lund, Sweden)

Apart from its being the base of steel metallurgy, elemental iron and its polymorphism is of great current interest for fundamental solid-state physics. Specifically, the transformation sequence bcc(α)-fcc(γ)-bcc(δ), with a ferromagnetic transition in the low-temperature α phase, is unique among the elements, and especially the existence of the high-temperature δ phase has been claimed by conflicting theoretical investigations to be due to either electronic/magnetic or vibrational effects. Here we report on temperature-dependent phonon dispersions for all phases obtained by inelastic neutron scattering, from which we deduce the vibrational contributions to thermodynamics. We show that the existence of γ-Fe is due to increased entropy contributed equally by electronic and phononic subsystems, while δ-Fe is stabilized nearly exclusively by its vibrational entropy. This corroborates the general finding of high-temperature transformations to open structures as being due to increased vibrational freedom [1].
The measurements on α-Fe were done at spectrometer E7 at the HMI, Berlin on single crystals grown by recrystallization at the Max-Planck-Institut für Metallforschung, Stuttgart. By in-beam cycling through the $\alpha \leftrightarrow \gamma$-transition a large γ grain has been grown and measured at spectrometer IN3 at the ILL, Grenoble, while large δ single crystals have been grown by zone melting in the combined crystal growth and measurement furnace and measured at the spectrometer 1T at the LLB, Saclay. For all measurements a pyrolytic graphite monochromator and analyzer were used in constant final wave-vector mode.

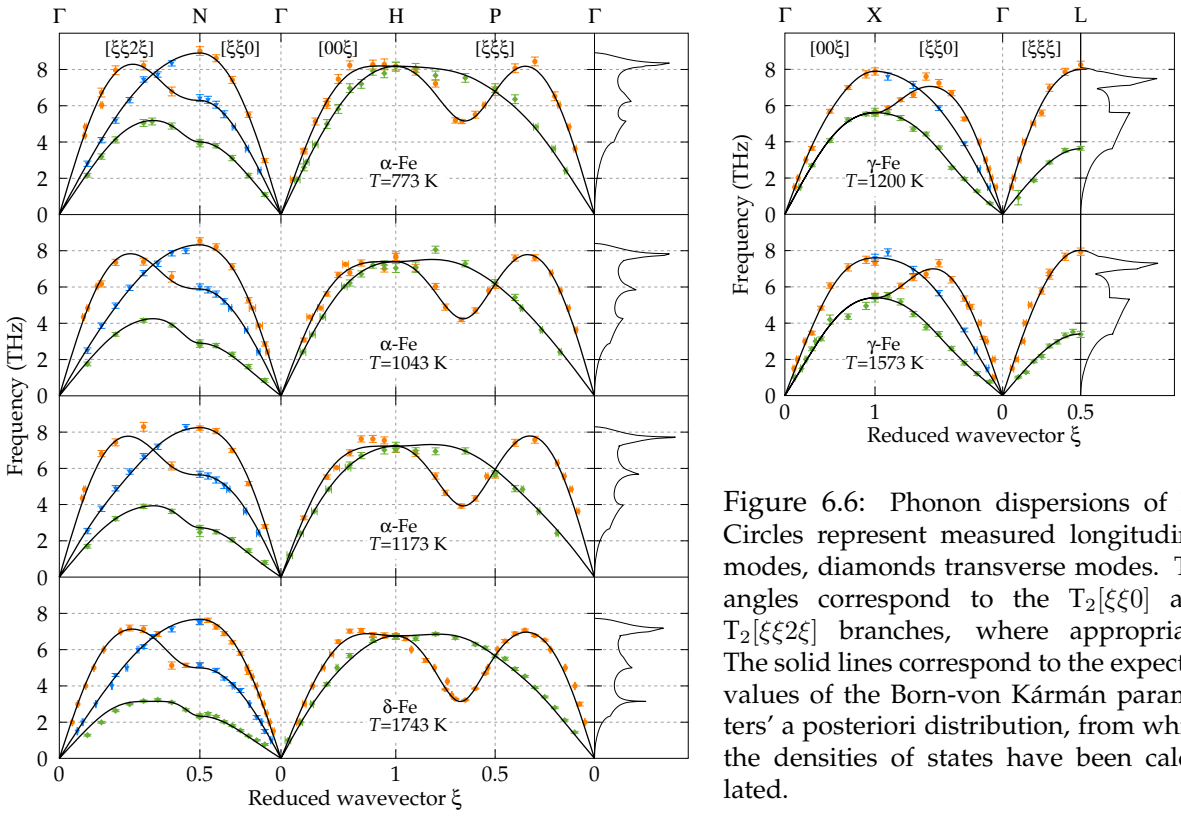

Figure 6.6: Phonon dispersions of Fe. Circles represent measured longitudinal modes, diamonds transverse modes. Triangles correspond to the $T_2[\xi\xi 0]$ and $T_2[\xi\xi 2\xi]$ branches, where appropriate. The solid lines correspond to the expected values of the Born-von Kármán parameters' a posteriori distribution, from which the densities of states have been calculated.

The resulting phonon dispersions are presented in Fig. 6.6. The anharmonic softening with rising temperature is clearly visible; it is most pronounced in the transverse branches $T_1[\xi\xi 2\xi]$ and $T_1[\xi\xi 0]$ of the bcc phases. These anomalies are indicative for latent instabilities towards a transition to a close-packed structure [1], being connected to the shearing of close-packed planes. For a further quantitative evaluation we describe the measured phonon dispersions at each temperature by a Born-von Kármán model (the quasi-harmonic assumption). In the framework of Bayesian inference, we assumed a prior distribution of BvK-constants modelled as independent Gaussians that favours short-range interactions of predominantly axial character. The modelled phonon dispersions according to the corresponding a posteriori means are displayed in Fig. 6.6. The very satisfactory fit confirms the adequacy of the prior assumptions.
From the obtained BvK-parameter distributions the vibrational contribution to the system's thermodynamics can be computed. The most evident way to report these results is by way of Debye temperatures, exemplified here for the entropy: for a given temperature of measurement T the Debye temperature $\Theta_S(T)$ is defined so that the entropy of the crystal modelled by the considered Born-von Kármán parameters at T is equal to the entropy of the Debye system with characteristic temperature $\Theta_S(T)$. The obtained values are presented in Fig. 6.7; they show how the anharmonic phonon softening leads to decreasing Debye temperatures and therefore high-temperature entropies that are increased compared to the harmonic extrapolation from low temperatures.

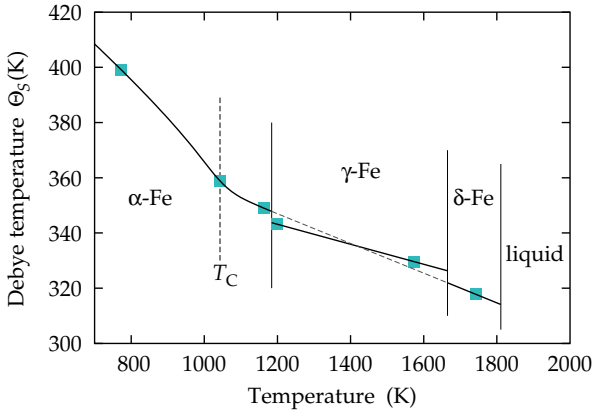

Figure 6.7:
Debye temperature defined via the vibrational entropy as a function of temperature.

Apart from the smooth softening within the regions of the respective phases, our results imply that $\Theta_S(T)$ is discontinuous at the phase transitions, which is to be expected for first-order transitions. Extrapolating our data to the transition temperatures shows that the vibrational entropy makes up about 40% of the total excess entropy (determined from the known total latent heat of the phase transition) at the $\alpha\leftrightarrow\gamma$-transition, the rest being due to an increased entropy of the electronic system, while for the $\gamma\leftrightarrow\delta$-transition the vibrational contribution alone can explain the total excess entropy within the error bars. In contrast, the vibrational contribution to the increase in internal energy is at both transitions below 10% of the total value.
The quoted results lead to the following conclusions: The $\alpha\leftrightarrow\gamma$-transition is for the larger part due to the increased electronic entropy of γ-Fe compared to paramagnetic α-Fe, which is energetically stabilized by local magnetic correlations also above T_C. At the temperature of the $\gamma\leftrightarrow\delta$-transition, however, the magnetic fluctuations in the bcc phase have decayed, so that the difference in electronic entropy is small. The transition to truly paramagnetic bcc Fe costs energy as known form first-principles calculations [2], which is covered by the increased high-temperature vibrational entropy of the open bcc structure.

[1] W. Petry, *J. Phys. IV* **05**, C2-15–C2-28 (1995)

[2] D. J. Singh, W. E. Pickett, H. Krakauer, *Phys. Rev. B* **43**, 11628–11634 (1991)

6.5 Rotational and diffusive motions of hydrogen in Magnesium Borohydride

L. Silvi, W. Lohstroh[1]

[1] MLZ, Garching, Germany

Complex p-metal hydrides are of interest for hydrogen storage material in mobile application due to their light weight. Borohydrides are largely ionic compounds with a general formula M(BH_4), consisting of a metal cation M^{n+} and a tetrahedral complex formed by 4 hydrogens covalently bonded to the boron atom $[BH_4]^-$. In particular Magnesium Borohydride $Mg(BH_4)_2$ has a theoretical hydrogen capacity of 14.8 wt%. The thermal stability up to 300°C is not suitable for reversible storage application, but there is a general interest in its properties as complex metal hydride [1]. Magnesium Borohydride can be found in different crystal structures, but the most stable, up to the decomposition temperature (530K), is the orthorhombic (space group $Fddd$) β-$Mg(BH_4)_2$.

An attempt to study the rotational and diffusive motion of the $[BH_4]^-$unit has been done with the use of quasielastic neutron scattering. Measurements have been performed at the time-of-flight spectrometer TOFTOF.
The sample was synthesized at the Karlsruhe Institute of Technology with the isotope substitution ^{11}B, $Mg(^{11}BH_4)_2$. Approximately 164 mg of powder were filled into an Aluminum flat cell, with an estimated neutron transmission of 90%. The incident wavelength was $2.5\mathring{A}$, yielding a resolution of 500 μeV (FWHM) at the elastic peak and a dynamical range up to $4.5\mathring{A}^{-1}$. Measurements were taken between 200 and 500 K.
Rotational and diffusive motions of the tetrahedra can be described by jump rotation or movements of the H atom around equilibrium positions. The scattering function $S(Q,\omega)$ can be modeled by:

$$S(Q,\omega) = A_0\delta(\omega) + \sum A_n L_n(\Gamma_n,\omega) \tag{6.1}$$

where

$$EISF = A_0 = \frac{I_{el}}{I_{el} + I_{inel}} \tag{6.2}$$

is the elastic incoherent structure factor (EISF) and $L_n(\Gamma_n,\omega)$ Lorentzian functions with half width at half maximum (HWHM) $\Gamma_n = 1/\tau_n$. τ_n is the average residence time between successive jumps . Usually the EISF shows some Q-dependence, indicating differend type of motions. For this reason it is necessary to explore large area of the dynamical range (Q,ω) in order to capture all the quasi elastic contributions.
For the analysis, the data have been fitted using a δ-function and two Lorentzians, which were numerically convoluted with the resolution function (measurements done with a vanadium sample), see Fig. 6.8.

The HWHM of L_1, Γ_1, is in the order of 0.4-0.7 meV, whereas for L_2, Γ_2 is in the order of 4-8 meV (Fig. 6.9). For the fitting routine, Γ_1 has been kept constant, with a value according to the best fit, and Γ_2 is kept free to adjust to the experimental values. The values for Γ_2 are not constant, showing a dispersion in Q. This means that in this time scale the $[BH_4]^-$motion is not localized, indicating a kind of diffusive motion. It also strongly deviates from a pure diffusive motion (Q^2 law).

The EISF has been calculated according to equations that have been reported previously (Fig. 6.10). Any attempt to fit theoretical models , like 120 or 90 ° rotations around C_3 and C_2 axis failed, indicating a more complex reorientation motions. Note, that the current experimental

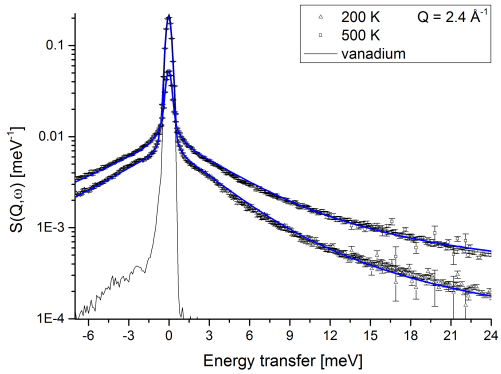

Figure 6.8:
$S(Q,\omega)$ of $Mg(BH_4)_2$ at 300 and 500 K, and the vanadium resolution function. Blue lines are fits to the data.

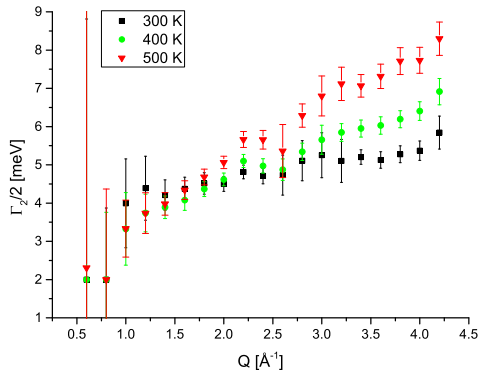

Figure 6.9: HWHM of L_2 at different temperatures.

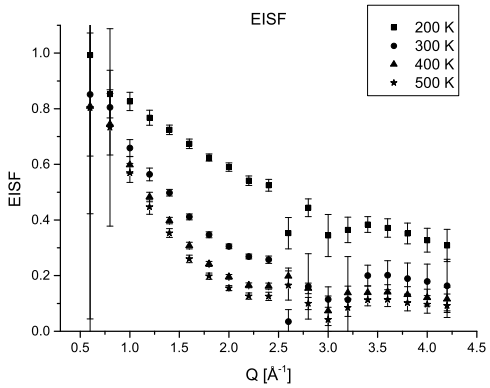

Figure 6.10: EISF for different temperatures.

data cover a large Q-range compared to ref. [2]. Further investigation will be done according to more complex motions of hydrogen considering translational-diffusive mechanisms.

[1] R. Cerny, Y. Filinchuk, H. Hagemann, K. Yvon, *Angew. Chem. Int. Ed.* **46**, 5765-5767 (2007)

[2] D. Blanchard, M. D. Riktor, J. B. Maronsson, H. S. Jacobsen, J. Kehres, D. Sveinbjornsson, E. Gil Bardaji, A. Leon, F. Juranyi, J. Wuttke, B. C. Hauback, M. Fichtner, T. Vegge, *J. Chem. Phys. C* **116**, 2013-2023 (2012)

7 Methodological and instrumental developments

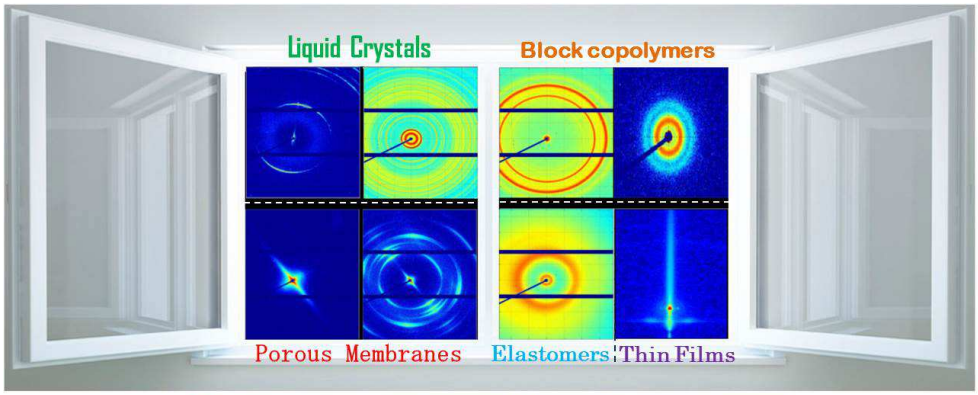

7.1 Initial changes in nanoparticle films under laminar flow conditions followed with in-situ GISAXS microfluidics

V. Körstgens, G. Santoro[1], S. V. Roth[1], P. Müller-Buschbaum

[1] DESY, Hamburg, Germany

Microfluidic processes accompanied with structural changes at the solid-liquid interface can be monitored with in-situ grazing incidence small angle x-ray scattering (GISAXS) [1, 2]. In this study the initial structural changes of composite films of nanospheres in a polyelectrolyte matrix upon the flow of water are demonstrated. These composite films representing a simple model for biofilms were prepared in small dimensions that they fit the channel of the microfluidic device [2]. Channel grooves with a width of about 0.9 mm are established on top of microscope glass slides with adhesive tape. Subsequently blade coating of a viscous solution of sodium alginate with dispersed polystyrene spheres of 105 nm diameter is performed. After drying and removing the adhesive tape, films in narrow stripes of 2 cm length with a width below 1 mm and a film thickness of about 7 μm remain on top of the glass substrate. Rinsing of the dry films with a 1M solution of $CaCl_2$ deliver a second type of sample where the divalent calcium ions physically cross-link the alginate matrix.

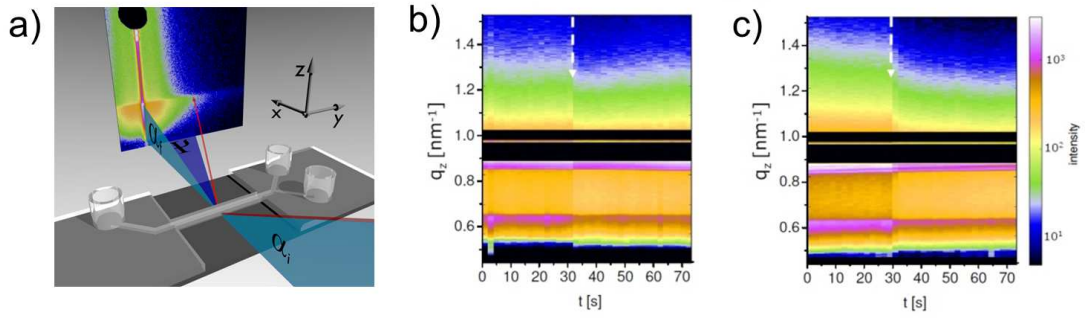

Figure 7.1:
a) Sketch of GISAXS geometry with microfluidic cell. An x-ray beam hits the surface with an incident angle α_i. Scattered intensity at an exit angle α_f and out of plane angle Ψ is recorded with a two-dimensional detector. b) Composite images of vertical cuts for a microfluidic experiment with water and a film of polystyrene spheres dispersed in a sodium alginate film c) same for film physically cross-linked with calcium ions; white arrows mark the frame at which the channel is completely filled with water for the first time.

The GISAXS experiments were performed at the MiNaXS instrument P03 [3] of the synchrotron PETRA III at DESY, Hamburg, Germany. The wavelength λ = 0.109 nm and a sample-to-detector distance D_{SD} = 3705 mm with an incidence angle α_i = 0.45° were used. A moderately micro-focused x-ray beam leads to a footprint of the beam closely matching the width of the microfluidic channel. The GISAXS signal was recorded with a Pilatus 300k area detector from DECTRIS Ltd. (Baden, Switzerland). In Fig. 7.1a the GISAXS measurement geometry together with the microfluidic device is shown. The x-ray beam hits the surface under the incident angle α_i. The response of an initially dry film to laminar flow was probed in such a way that the flow direction was opposite to the scan direction of the microfluidic device. A flow of water was installed by a syringe pump (nemesys, Cetoni GmbH) with 0.01 ml/min. X-ray exposures for 1 s in step widths of 125 μm were recorded. From the subsequent individual 2D GISAXS data vertical cuts at Ψ=0 are composed. In Fig. 7.1b (spheres in sodium alginate matrix) and Fig. 7.1c (spheres in cross-linked alginate matrix) distances of 5 mm along the channel in y-direction are covered. The experiment starts with a dry film and the liquid begins to fill the channel before laminar flow is

established. The first frame at which the x-ray beam hits the channel with its cross-section completely filled with liquid is observed by the distinct drop in intensity due to absorption of the x-ray beam by the liquid. Close to the full front of liquid, which fills the channel, the individual frames (before the white arrow, around t = 30 s) correspond not necessarily to a completely dry film. A precursor of liquid wets the surface of the film and initiates structural changes of the film even before the full cross-section of the channel is filled.
Information about lateral structures can be achieved from horizontal line cuts. The dry films show two distinct shoulders (black curves in Fig. 7.2a-b, marked with blue arrows). The curves show from bottom to top the evolution of the scattered intensity during the in-situ microfluidic experiment. The first light grey curves represent the situation where the channel is completely filled for the first time, as noticed by the distinct drop in intensity. It becomes clear that a structural change of the film does not only develop when the channel is completely filled (light grey curves in Fig. 7.2) but already starts before (dark grey curves in Fig. 7.2).

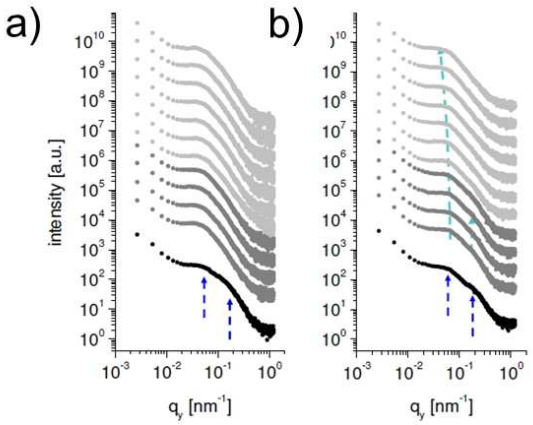

Figure 7.2:
Horizontal line cuts: (a) Microfluidic experiments with water and a sodium alginate film with dispersed polystyrene spheres (b) same for film physically cross-linked with calcium ions. The black curves on the bottom constitute the initially dry films, curves on top show the microfluidic experiment in light grey with completely filled channel, grey curves below show influence of precursor of liquid. Each curve represents the sum of three subsequent measurement comprising 6 seconds.

For the sodium alginate film (Fig. 7.2a) the precursor of liquid, which wets the film, smoothens the two distinct structural features. Immediately upon water contact one shoulder transforms into a more prominent peak, indicating a loss of small scale structures. Finally, as sodium alginate is water soluble, a complete dissolution of the film occurs on longer timescales. For a film which is physically cross-linked with calcium ions the process is slowed down. The precursor of liquid does not lead to an immediate smoothening or structural change. Only at full water contact one shoulder transforms into a reasonably prominent peak, witnessing the loss of small scale structures. With ongoing flow of water the scattering curves further transform as seen by a shift of the peak positions towards smaller q_y values. These changes are due to a coarsening of structures (indicated by the light blue line in Fig. 7.2b). This corresponds to the swelling of the physically cross-linked film increasing the distance of polystyrene spheres in the alginate matrix.
The combination of GISAXS and microfluidics gives the opportunity to investigate the structural changes that precede the detachment of composite films and nanoparticle aggregates. In combination with an observation on longer time and larger size scale (e.g. with optical microscopy) a complete description of detachment processes will be accessible and may serve as a model for the behaviour of biofilms attached to microfluidic devices.
This work has been financially supported by the BMBF (grant number 05K10WOA).

[1] J.-F. Moulin, S. V. Roth, P. Müller-Buschbaum, *Rev. Sci. Instrum.* **79**, 015109 (2008)

[2] V. Körstgens, M. Philipp, D. Magerl, M. A. Niedermeier, G. Santoro, S. V. Roth, P. Müller-Buschbaum, *RSC Advances* **4**, 1476-1479 (2014)

[3] A. Buffet, A. Rothkirch, R. Döhrmann, V. Körstgens, M. M. Abul Kashem, J. Perlich, G. Herzog, M. Schwartzkopf, R. Gehrke, P. Müller-Buschbaum, S. V. Roth, *J. Synchr. Rad.* **19**, 647-653 (2012)

7.2 Real time investigation of metal nanoparticles growth on solid surfaces

E. Metwalli, M. Schindler, Y. Yao, W. Wang, G. Gümüssoy, S.V. Roth[1], P. Müller-Buschbaum

[1] DESY, Hamburg, Germany

Nanoparticles are important for many technological applications, including catalysis, recording media, thin film technology, optoelectronic, magnetic sensors, and anti-bacterial surfaces. The properties of the nanoparticles are related their size and shape. Physical sputtering of metal on chemically/energetically different surfaces can result in formation of different nanoparticles sizes and shapes. Therefore, the growth kinetics of metal nanoparticles on solid supports has crucial consequences on the structure and physical properties of the prepared active hybrid surfaces. The metal growth kinetics on solid surfaces does not only depend on the sputtering conditions but also on the surface properties where the metal nanoparticle are growing on. In order to understand the effect of surface chemistry/energy on the metal growth kinetics of metal, in situ real-time grazing incidence small-angle x-ray scattering (GISAXS) is employed. With high time resolution of the measurements, the formation/growth of metal nanoparticle can be systematically monitored.

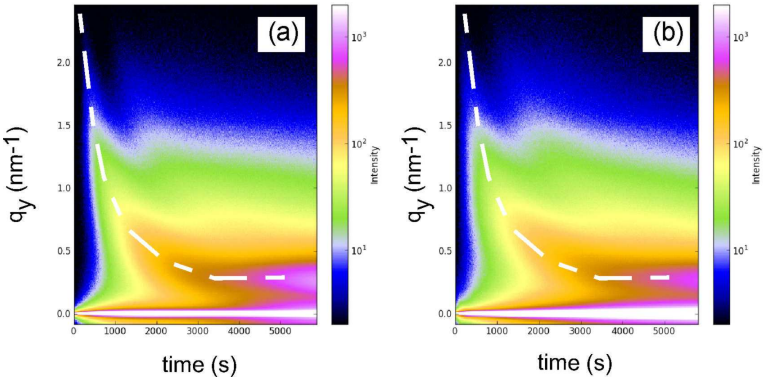

Figure 7.3:
The q_y time mapping (at a constant q_z value) of 2D GISAXS data during gold sputtering on a) PEHA and b) PMMA films. The intensity of the overall scattering pattern increases with increasing metal upload (deposition time). The dashed lines shows the time evolution of the metal characteristic peak moving from very large to lower q_y values before it stays at a constant q_y value

In the present report we used the DC sputtering technique to investigate the deposition of Au metal onto different surfaces namely soft poly(ethylhexylacrylate) (PEHA; Tg = 188 K) and hard poly(methylmethacrylate) (PMMA; Tg 378 K) films. We have investigated the formation and growth kinetics of Au nanoparticles on these surfaces. The main sputtering chamber is pumped down by a two-stage turbo molecular pump that brings the chamber into a base pressure of 1.5 x 10^{-8} mbar. Then the deposition was performed at an argon pressure of 1.5 x 10^{-2} mbar and at a deposition rate of 1.2 nm/min. The in situ GISAXS measurements were carried out at beamline P03 of PETRA storage ring at DESY, Hamburg. The sample inside the sputtering chamber was placed horizontally at an incidence angle α_i = 0.5° to the incidence x-ray beam. 2D GISAXS data were collected on a noise-free high resolution Pilatus-300k detector with a ten-milliseconds time-resolution.
The real-time GISAXS technique systematically monitors the metal nanoparticle growth behavior and provides details on the geometric structure of metal nanoparticles as the atoms in the

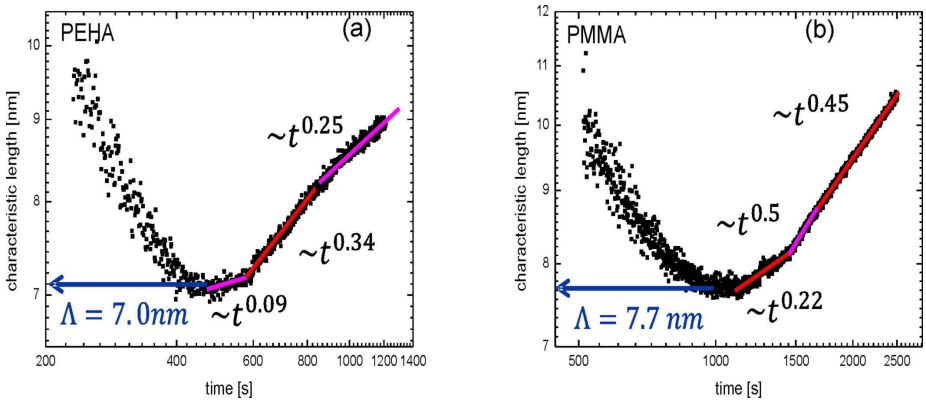

Figure 7.4:
The interparticle distance between growing nanoparticles as a function of sputtering time for a) PEHA and b) PMMA films.

gas phase are condensed on the solid surface with increasing deposition time. Figure 7.4a-b shows the characteristic metal interparticle distances of growing nanoparticles as a function of time under the same sputtering conditions for both PEHA and PMMA films. The data interestingly shows that the metal nucleation/growth occurs at a slower rate for the low glass transition temperature T_g polymer (PEHA) film as compared with the high T_g polymer (PMMA) film. The intensity of the metal characteristic peak in the GISAXS data is found to increase with time because of the high scattering power of the metal atom. The latter peak is a characteristic of the inter-particle distance as a function of metal load while its width (FWHM) is a fingerprint of the polydispersity of the nanoparticles.
Eventually, under the same sputtering conditions the metal particle migration seems to be much faster [1] on the silicon substrate (data is not shown) compared with the investigated polymer films. From Fig. 7.4, it is obvious that the adatom migration on the substrate surface is one of the most important mechanisms that control the nanoparticle formation/growth. As the metal atoms arrive at the polymer surface, they migrate on/in the film and when two of them are near neighbors, they form a stable nucleus and remain on the surface. If an atom does not combine with another one, it may evaporate back in the gas phase instead. With increasing the metal upload, many random nucleation sites are formed. When the distance between the two neighboring islands are less than the diffusion length of the atoms in the films, the density of nuclei reaches saturation. After that, all arriving adatoms are captured by the islands either directly or after diffusion along the film surface to minimize their energy. The diffusion of gold nanoparticles on the PMMA surface is found to be faster than that on the PEHA film (Fig. 7.4) as indicted by the fast particle growth on the PMMA film. This diffusion is mainly determined by the metal-polymer interaction which depends mainly on the chemistry, stiffness, and surface topography of the films [2-4].

[1] M. Schwartzkopf, A. Buffet, V. Körstgens, E. Metwalli, K. Schlage, G. Benecke, J. Perlich, M. Rawolle, A. Rothkirch, B. Heidmann, G. Herzog, P. Müller-Buschbaum, R. Röhlsberger, R. Gehrke, N. Stribeck, S. V. Roth, *Nanoscale* **5**, 5053 (2013)

[2] E. Metwalli, S. Couet, K. Schlage, R. Röhlsberger, V. Körstgens, M. Ruderer, W. Wang, G. Kaune, S. V. Roth, P. Müller-Buschbaum, *Langmuir* **24**, 4265 (2008)

[3] E. Metwalli, J.-F. Moulin, J. Perlich, W. Wang, A. Diethert, S. V. Roth, P. Müller-Buschbaum, *Langmuir* **25**, 11815 (2009)

[4] E. Metwalli, V. Körstgens, K. Schlage, R. Meier, G. Kaune, A. Buffet, A. Couet, S. V. Roth, R. Röhlsberger, P. Müller-Buschbaum, *Langmuir* **29**, 6331 (2013)

7.3 New capabilities in laboratory instrumentation

A. Schulte[1], C. J. Schaffer, P. Müller-Buschbaum, C. M. Papadakis

[1] also at: University of Central Florida, Orlando, USA

Sample environment for FTIR spectroscopy under variable external conditions

One of the principal probes of molecular structure and chemical bonding is infrared absorption. It reveals the vibrational spectrum of a material and its physical state providing a non-destructive in-situ probe without need for labelling [1]. To complement scattering probes of soft matter we have put a Bruker Equinox 55 FTIR spectrometer back into operation and constructed a new sample environment. The FTIR spectrometer enables analysis with both contact and non-contact IR sample stages. The Michelson interferometer uses a KBr substrate beamsplitter with a spectral range from 650 - 8000 cm^{-1}. The FTIR is equipped with a DTGS and mercury-cadmium-telluride (MCT) photoconductive detectors. Due to the CO_2 and water vapor absorption the sample compartment needs to be purged with dry air continously. To this end a new purge unit was implemented that allows for fast sample change and baseline stability over hours. We have added a variable temperature stage and new sample holders that are well suited for measurements over the range from 0 to 90 ^oC on samples in solution or thin film form. We employ a transmission geometry that enables us to measure films down to the ten nanometer range. Samples under investigation include stimuli-responsive polymers and organic solar cell materials.

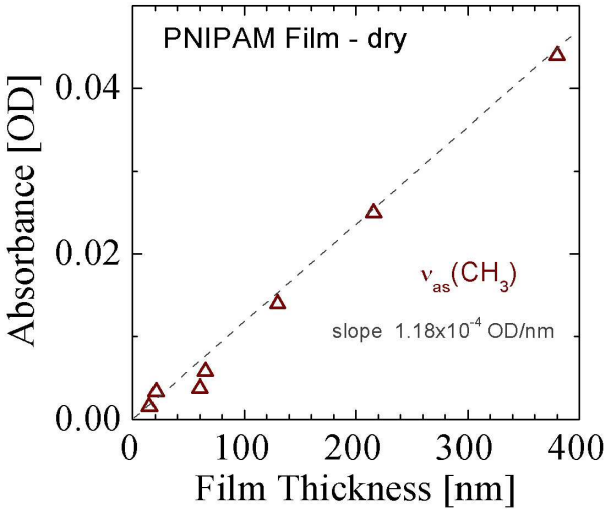

Figure 7.5:
Absorbance of the anitsymmetric C-H stretching mode in dry PNIPAM films as a function of film thickness. The thickness was measured independently with a profilometer. Note the linear relation between absorbance and film thickness.

FTIR spectroscopy usually covers the entire range from 600 cm^{-1} upwards with particular sensitivity for the finger print range in organic systems. In combination with variations in temperature it provides a means to probe conformational changes across the LCST transition and the behavior of the hydration water bands. We can also obtain information on molecular changes between polymer in solution and in thin film form. In ongoing experiments hydration changes in thin Poly(N-isopropyl acrylamide) (PNIPAM) films [2] and other thermo-responsive polymers are investigated. Fig. 7.5 illustrates the capabilities of the instrument. The measured absorbance of dry PNIPAM films decreases linearly with the film thickness over the range from 400 to 20 nm. The thickness was measured independently with a profilometer (Dektak).

In thin film devices such as polymeric solar cells an understanding of the relation between microstructure and functional properties is key to improve materials performance. For instance, the stability of solar cells under the influence of temperature or extended exposure to illumination is of considerable interest. FTIR spectroscopy, when coupled with controlled variations in external parameters, lends itself to the investigation of molecular changes of solar cell materials under operating conditions. Our development of the FTIR sampling environment has enabled such investigations.

A compact high pressure generating system for experiments on soft matter

Pressure is a fundamental thermodynamic variable and its influence is seen at different levels, from determining phase equilibria to changing the rate of a chemical reaction to altering conformational states of biological macromolecules. In stimuli-responsive polymers pressure is conjugate to temperature and high pressure experiments can help to elucidate the role of the hydrophobic interaction in phase changes, for instance the coil to globule transition.

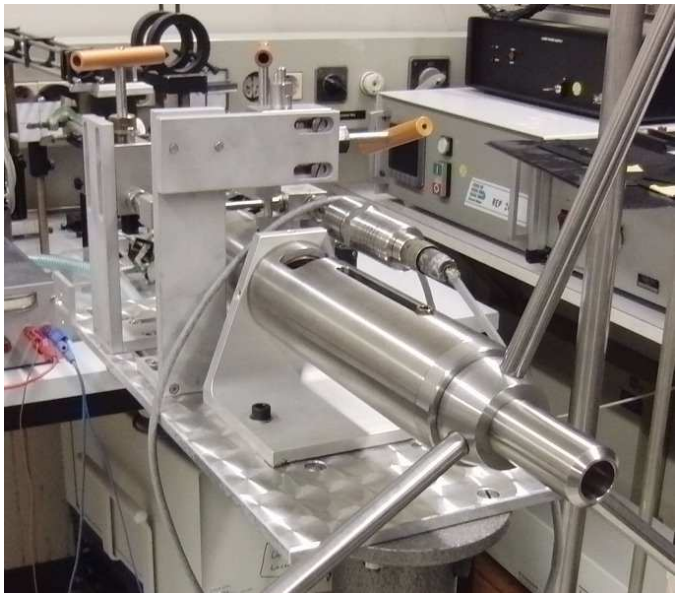

Figure 7.6:
Hydrostatic pressure generating system for the range 1 to 7000 bar.

We have assembled a compact high pressure system that can be interfaced to various high pressure cells. The hydrostatic pressure generator employs liquids as a pressurizing medium and the pressure can be continously and reversibly varied between 1 and 7000 bar. Including all valves, a liquid reservoir, and pressure gauge it fits on a baseplate with size 45x20 cm^2. Due to its small footprint it is highly transportable.
We plan to employ the high pressure generating system in experiments to investigate phase changes in soft matter such as stimuli-responsive polymers. Experiments include turbidity and dynamic light scattering at variable temperature and pressure.
This work has been financially supported by the DFG in the priority program SPP 1259 'Intelligente Hydrogele' (MU1487/8). A. S. thanks the University of Central Florida for research support.

[1] P. R. Griffiths, J. A. de Haseth, *Fourier transform infrared spectrometry*, Wiley (2007)

[2] A. Schulte, M. Philipp, C. J. Schaffer, P. Müller-Buschbaum, *DPG Frühjahrstagung*, CPP 54.62 (2014)

7.4 Applications for the combination of GISAXS and microfluidics with adapted x-ray beam sizes

V. Körstgens, G. Santoro[1], S. V. Roth[1], P. Müller-Buschbaum

[1] DESY, Hamburg, Germany

The combination of microfluidics and grazing incidence small angle x-ray scattering (GISAXS) allows for the investigation of structural changes at the solid-liquid interface [1, 2]. One of the prerequisites for useful measurements is to match the footprint of the x-ray beam with the width of the microfluidic channel. The size of the footprint of the incident beam under the given shallow angle should be that small that an extensive over-illumination of the sample not in contact with the fluid is prevented. In an experiment following the attachment of gold nanoparticles to a polymer coated substrate we show the utilization of a perfectly adapted microfocused x-ray beam at the beamline P03, DESY, Hamburg [3].

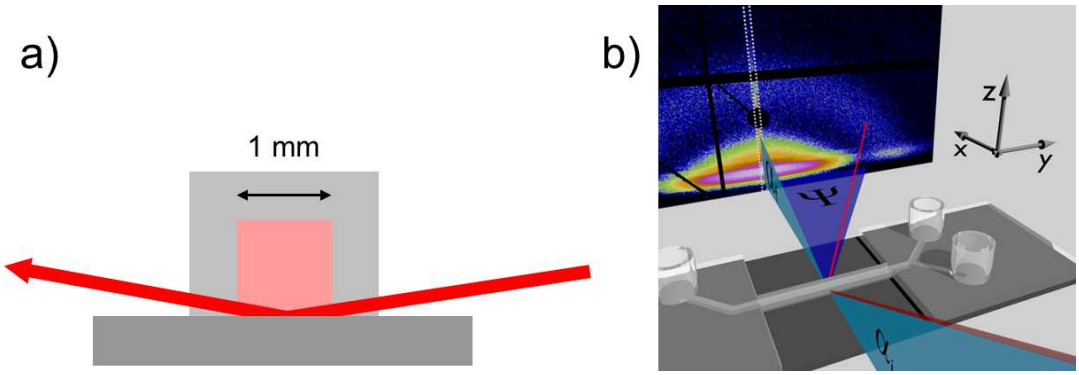

Figure 7.7:
a) Sketch of the x-ray beam transmitting the microfluidic channel walls and the footprint on the sample surface. b) GISAXS set-up with microfluidic cell, the incoming x-ray beam with the incident angle α_i is depicted in red. Scattered intensity with the exit angle α_f and the out of plane angle Ψ is recorded on a 2D detector.

We investigate an initially dry polymer film of poly(ethyleneimine) (molecular weight M_w = 750000 g/mol, Sigma-Aldrich, Germany) on a silicon substrate. GISAXS data were collected with a 2D detector Pilatus 1M (Dectris Ltd., Switzerland) at a sample to detector distance of 2455 $\pm$ 1 mm. The incident angle α_i was 0.46°. A micro-focused x-ray beam with a size of about 7 x 5 μm^2 (h x v) was used. The attachment of gold nanoparticles of 10 nm diameter out of aqueous dispersion (Cytodiagnostics, Canada) was studied. A flow of the dispersion of 0.02 ml/min was realized with a syringe pump (Nemesys, Cetoni, Germany). The microfluidic cell was moved perpendicular to the x-ray beam (along the y-axis, with x-ray beam oriented along the x-axis and the surface normal along the z-axis) with 50 μm steps opposed to the direction of the flow in the microfluidic channel. From the 2D GISAXS data line cuts were extracted.
The course of the microfluidic experiment can be followed by combining vertical line cuts at $q_y = 0$ integrated over several pixels (box surrounded by dotted line in Fig. 7.7b in a composite image for different times (see Fig. 7.8a). The vertical line cuts give structural information in the direction of the surface normal. Three different regimes can be distinguished in the composite image (separated by red dashed lines in Fig. 7.8a: 1) The scattering originating from the dry film, 2) scattering from a pre-cursor of liquid which wets the surface and 3) scattering in case the channel is completely filled and the attachment process of nanoparticles can be followed. The increasing intensity in the Yoneda peak is indicating the nanoparticle attachment (see grey dashed arrow in Fig. 7.8a). Information about the lateral structure is given by horizontal line

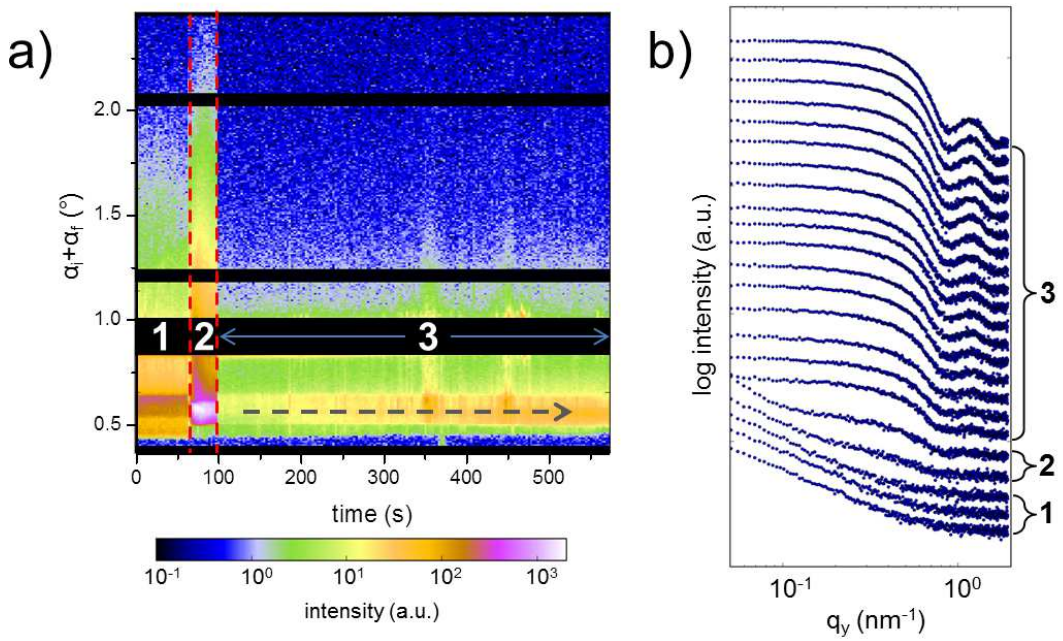

Figure 7.8:
a) Composite image of vertical cuts at $q_y = 0$ for 210 consecutive measurements scanning the microfluidic channel along y-direction while gold nanoparticles attach to the polymer thin film; see text for numbers indicating different regimes in the microfluidic experiment. b) Horizontal line cuts for in-situ microfluidic experiment as sum of 10 consecutive measurements; intensity is shifted for clarity along intensity-axis with the initially dry film at the bottom.

cuts (Fig. 7.8b). The increase in intensity of a peak originating from the form factor of spheres (marked with black arrow in Fig. 7.8b) is observable and shows the proceeding coverage of the polymer film with gold nanoparticles. For clarity, the scattering curves of 10 consecutive measurements have been added up for the curves shown in Fig. 7.8b. The numbers to the right of the curves in Fig. 7.8b correspond to the regimes of the microfluidic experiment as assigned in Fig. 7.8a.
The combination of microfluidic devices and GISAXS technique allows for a multitude of investigations at the solid-liquid interface. Beside attachment and detachment processes, swelling and structural reorganization of thin films, as well as particle growth and mixing experiments under flow conditions can be followed in-situ. The full capability of this method is accessible if a microfocused x-ray beam is used with a beamsize resulting in a footprint matching the channel width of the microfluidic device as closely as possible.

This work has been financially supported by the BMBF (grant number 05K10WOA).

[1] J.-F. Moulin, S. V. Roth, P. Müller-Buschbaum, *Rev. Sci. Instrum.* **79**, 015109 (2008)

[2] V. Körstgens, M. Philipp, D. Magerl, M. A. Niedermeier, G. Santoro, S. V. Roth, P. Müller-Buschbaum, *RSC Advances* **4**, 1476-1479 (2014)

[3] G. Santoro, A. Buffet, R. Döhrmann, S. Yu, V. Körstgens, P. Müller-Buschbaum, U. Gedde, M. Hedenqvist, S. V. Roth, Rev. Sci. Instrum. 85, 043901 (2014)

7.5 Ultrananocrystalline diamond films - a grazing-incidence small-angle X-ray scattering study

H. Sternschulte[1], I. Staudinger, A. Sepe, J. Perlich[2], S. V. Roth[2], S. Ghodbane[3], D. Steinmüller-Nethl[3], C. M. Papadakis

[1] nanoTUM, TU München, Garching, Germany
[2] DESY, Hamburg, Germany
[3] KOMET rhoBeSt GmbH, Innsbruck, Austria

Ultra nanocrystalline diamond (UNCD) films feature small grain sizes of less than 10 nm and a smooth surface with roughness RMS values down to 10 nm. They represent a homogeneous material with isotropic material properties. Furthermore, both p- and n-type doped UNCD films are available with high carrier concentrations, a requirement for applications in sensing-devices based, e.g., on electrochemistry. UNCD films are grown in a chemical vapor deposition process with a high secondary nucleation rate. The obtained films are composed of separated single crystal diamond grains with rounded shapes which are embedded randomly oriented in an amorphous carbon-hydrogen matrix. To obtain information about the grain size and the distance of the grains in the matrix, UNCD films are usually studied by transmission electron microscopy (TEM), which, however requires a highly sophisticated preparation. An alternative method to obtain structural information is grazing-incidence small-angle X-ray scattering (GISAXS) which allows to determine the shape of the grains, their size and size distribution as well as their distance without any sample preparation with excellent sampling statistics. For the analysis of the GISAXS data, information about the scattering length density (SLD) and the surface roughness of the UNCD film were determined independently by X-ray reflectometry (XRR) measurements.

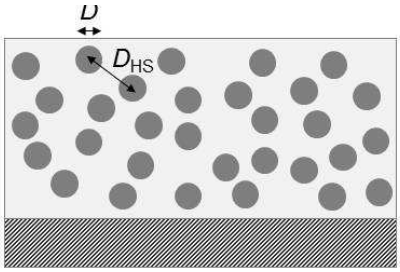

Figure 7.9:
Model used for modeling the GISAXS images.

An undoped UNCD film with homogeneous film thickness of 3.8 μm was deposited on pre-cleaned (2 $\times$ 3) cm^2 Si(001) substrates by using a modified hot filament technique with a precursor gas mixture of pure CH_4 and H_2. To obtain a plane sample, the substrate temperature had to remain in the range of 760-770°C all along the diamond growth process. XRR measurements were carried out using a D5000 diffractometer (Siemens). The XRR curve was fitted with a model of a homogeneous film on a sbstrate. This way, the surface roughness as well as the scattering length density and the absorption of the film were determined. GISAXS measurements were performed at beamlines BW4 and P03, both at HASYLAB, DESY, Hamburg. As detectors, a MarCCD camera or PILATUS 300k were used. The GISAXS images were modelled using the FitGISAXS software [1] using the DLSs and absorption values from XRR as input parameters. The diamond nanoparticles were modeled as monodisperse spheres of diameter D (Fig. 7.9). Their correlation within the film plane was approximated as a two-dimensional liquid. As a fitting parameter, the ratio of the centre-to-centre distance between the spheres, D_{HS}, and D, was used. The hard-sphere volume fraction, η_{HS}, was fixed at 0.1. Representative 2D images are shown in Fig. 7.10a-c. Intensity maxima are visible at $q_y = 0.28 - 0.36$ nm^{-1} which have a round shape and extend from the horizon to higher q_z values. Their intensity decays towards

high q_z values due to the scattering geometry in grazing incidence. These maxima are caused by the scattering from the diamond nanocrystallites which have an electron density different from the surrounding amorphous matrix and having a certain average distance from each other.

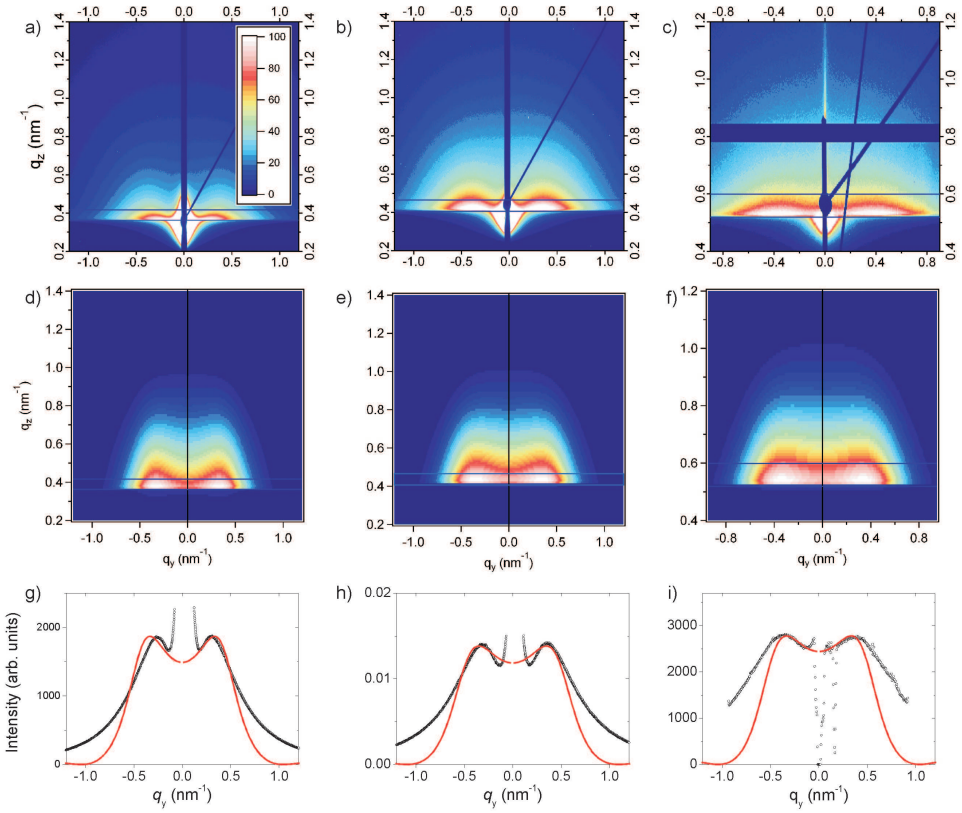

Figure 7.10:
Measured GISAXS images at the incident wave vectors k_{iz} a) 0.191 nm^{-1}, b) 0.239 nm^{-1}, and c) 0.346 nm^{-1}; d)-f) Corresponding simulated images; g)-i) Corresponding intensity profiles (black circles) and model curves (red lines). The blue lines parallel to q_y in a)-f) denote the regions over which was integrated to obtain the profiles in g)-i).

The model resulted consistently in 2D images showing scattering of similar shape as the experimental ones (Fig. 7.10d-f). The sphere diameter, D, and the average centre-to-centre distance of the spheres, D_{HS}, were determined from 1D line profiles summed over a stripe narrow in q_z and extending along q_y (Fig. 7.10g-i). In the 1D profiles, the q_y positions of the intensity maxima as well as their peak heights were matched by varying the parameters. Then, the 2D GISAXS image was generated, and the overall shape of the intensity maxima in the 2D images was verified. This procedure resulted for all images in $D = 8.0 - 8.5$ nm and $D_{HS} = 10.4 - 11.9$ nm. We conclude that the diamond crystallites are close to spherical and do not touch each other but there is a minimum distance between them of $2 - 4$ nm. GISAXS gave statistically relevant information in a non-destructive way.

[1] D. Babonneau, *J. Appl. Cryst.* **43**, 929 (2010)

[2] H. Sternschulte, I. Staudinger, A. Sepe, C. M. Papadakis, J. Perlich, S. V. Roth, S. Ghodbane, D. Steinmüller-Nethl, *Diam. Relat. Mater.* **37**, 68 (2013)

7.6 Structural changes in a simple model biofilm investigated with in situ SAXS microfluidics

V. Körstgens, V. Haramus[1], P. Müller-Buschbaum

[1] Helmholtz-Zentrum Geesthacht, outstation at EMBL/DESY, Hamburg, Germany

Biofilms are aggregates of micro-organisms formed at solid-liquid interfaces mostly in aqueous environments. The micro-organsisms in a biofilm are dispersed in a matrix of polymers and oligomers like polysaccharides, proteins and lipids. For the investigation of biofilms in fluidic systems the constitution of model composite systems is advantageous. Our model system consists of spherical polystyrene nanoparticles in a matrix of algal alginate. This is a simple model system for bacterial biofilms of *Pseudomonas aeruginosa* which in its mucoid form consist to a large extent of bacterial alginate [1].
Structural changes at the solid-liquid interface of these films can be monitored with in-situ grazing incidence small angle x-ray scattering (GISAXS) [2]. In this study the initial structural changes of composite films of nanospheres in a polyelectrolyte matrix upon the flow of water were demonstrated with a microfluidic device especially designed for GISAXS. The advantage of the microfluidic device is that is also possible to perform experiments in transmission. For this it is necessary to attach the film to be investigated not on the substrate, as done for GISAXS experiments, but to the channel walls of the microfluidic channel. It has to be noted that for structural investigations of statistical relevance in transmission a certain film thickness is necessary.

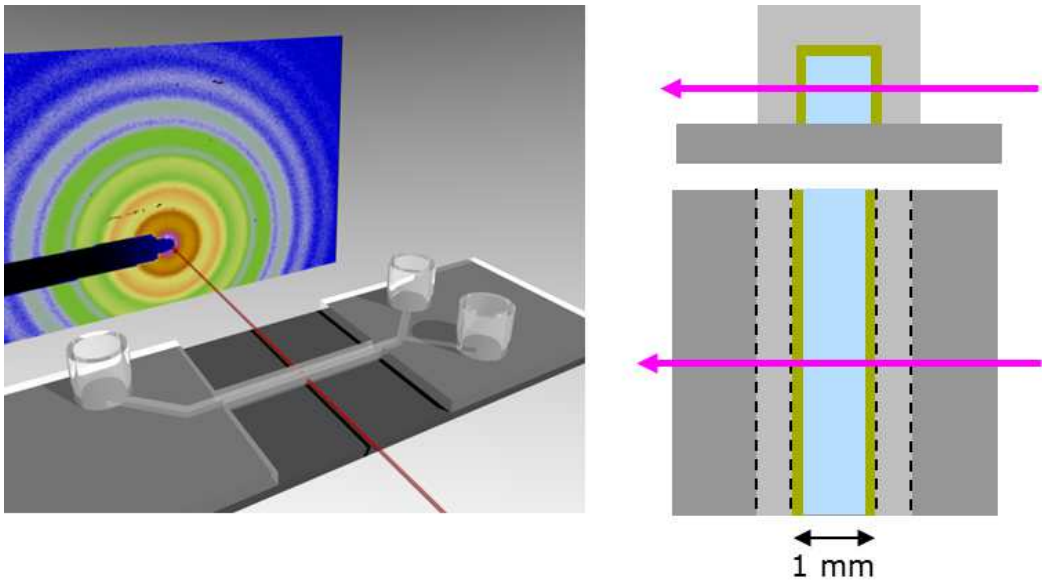

Figure 7.11:
Sketch of SAXS geometry with microfluidic cell. On the right side the transmission of an x-ray beam through the microfluidic channel is shown in side and top view. The composite film is produced in a way that it is attached to both channel walls and the top of the channel

Composite films of several μm representing a simple model for biofilms were prepared via solution casting inside the microfluidic channel. A dispersion of spherical polystyrene spheres with a diameter of 120 nm in algal alginate is used for the preparation of the films. Rinsing of the dry films with a 1M solution of $CaCl_2$ delivers a second type of sample where the divalent calcium ions physically cross-link the alginate matrix. As shown in Fig. 7.11 the final film covers the inside of the channel, both channel walls and the top of the channel. The SAXS experiments were

performed at the BioSAXS instrument P12 of the synchrotron PETRA III at DESY, Hamburg, Germany. An energy of 10 keV with a focal x-ray spot of 0.2 mm x 0.12 mm was used. The SAXS signal was recorded with a Pilatus 2M area detector from DECTRIS Ltd. (Baden, Switzerland). For the flow experiments the microfluidic channel out of cyclic olefine with the dry film attached to its channel walls is put on a clean glass substrate and clamped mechanically together. A flow of water with 0.02 ml/min was installed with a Cetoni syringe pump constituting laminar flow conditions. The sample is probed at different positions along the channel at a constant height of about 0.5 mm from the glass substrate. The 2D detector pattern shown in Fig. 7.11 gives just a small cutout of the full image collected for a dry film with the large detector.

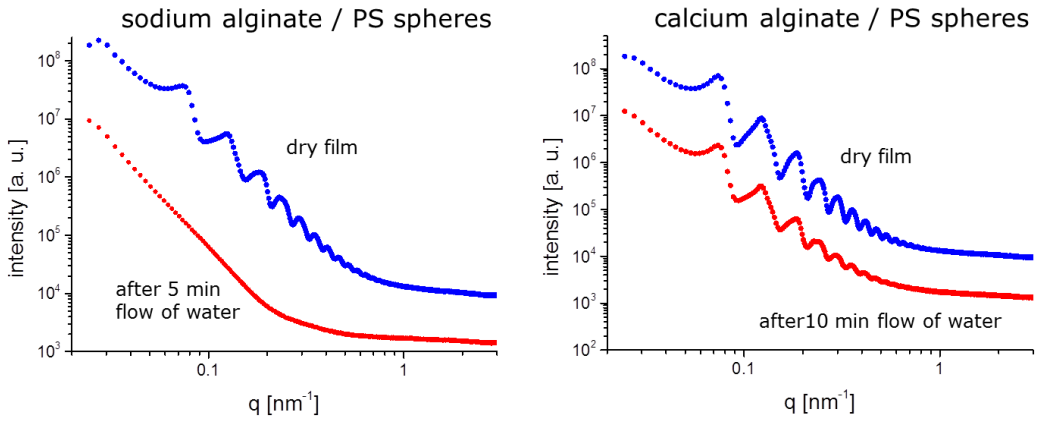

Figure 7.12:
Microfluidic experiments with water and a sodium alginate film with dispersed polystyrene spheres (left side) same for film physically cross-linked with calcium ions (right side). The top blue curves constitute the initially dry films, red curves below show the microfluidic experiment after 5 min and 10 min of flow of water, respectively.

The initially dry films show distinct oscillations in the scattering curve arising from the form factor of the monodisperse polystyrene spheres (blue curves in Fig. 7.12). The red curves in Fig. 7.12 represent the situation after some minutes of flow with water in the microfluidic experiment. Already in the single 1 s measurements of Fig. 7.12 illustrate the general difference of the films investigated. The composite film of sodium alginate is completely dissolved after 5 min whereas the physically cross-linked composite film is stable for at least 10 min. The shift of intensity for the cross-linked film (right side in Fig. 7.12) before and during the flow of water is caused by the absorption in the completely filled channel. The microfluidic experiments were performed with consecutive measurements and analysis of the data will in combination with GISAXS experiments on similar systems allow the description of the structural changes in the films preceeding a potential final detachment or dissolution of the composite film as it is observed for the sodium alginate composite films.

This work has been financially supported by the BMBF (grant number 05K10WOA).

[1] V. Körstgens, H. C. Flemming, J. Wingender, W. Borchard, *J. Microbiol. Meth.* **46**, 9-17 (2001)

[2] H. C. Flemming, J. Wingender, *Nature Rev. Microbiol.* **8**, 623-633 (2010)

[3] V. Körstgens, M. Philipp, D. Magerl, M. A. Niedermeier, G. Santoro, S. V. Roth, P. Müller-Buschbaum, *RSC Advances* **4**, 1476-1479 (2014)

8 Teaching and outreach

8.1 Lectures, seminars and lab courses

Spring semester 2013

Prof. Dr. Peter Müller-Buschbaum, *Angewandte Physik: Polymerphysik 2*
Prof. Dr. Christine Papadakis, *Grundlagen der Experimentalphysik 2 (LB-Technik)*
Prof. Dr. Christine Papadakis, Dr. Ezzeldin Metwalli Ali, *Nanostructured Soft Materials II*
Prof. Dr. Peter Müller-Buschbaum, Prof. Dr. Christine M. Papadakis,
Seminar über Struktur und Dynamik kondensierter Materie
Prof. Dr. Peter Müller-Buschbaum, Prof. Dr. Christine M. Papadakis, *Seminar: Polymere*
Prof. Dr. Peter Müller-Buschbaum, Prof. Dr. Christine M. Papadakis,
Studentenseminar: Grundlegende Phänomene der Physik der weichen Materie
Prof. Dr. Peter Müller-Buschbaum, *Seminar: Aktuelle Probleme der organischen Photovoltaik*
Prof. Dr. Peter Müller-Buschbaum, Prof. Dr. Christine M. Papadakis,
Bachelor-Seminar: Funktionelle weiche Materialien
Prof. Dr. Winfried Petry, Prof. Dr. Peter Böni, Prof. Dr. Wolfgang Häußler, Prof. Dr. Klaus Schreckenbach, *Seminar über Neutronen in Forschung und Industrie*
Prof. Dr. Winfried Petry, *Blockseminar Erasmus Mundus MaMaSELF Summerschool*

Fall semester 2013/2014

Prof. Dr. Peter Müller-Buschbaum, *Experimentalphysik 1 für MSE*
Prof. Dr. Peter Müller-Buschbaum, *Angewandte Physik: Polymerphysik 1*
Prof. Dr. Peter Müller-Buschbaum, Dr. Ezzeldin Metwalli Ali, *Nanostructured Soft Materials 1*
Prof. Dr. Christine Papadakis: *Sabbatical*
Prof. Dr. Peter Müller-Buschbaum, Prof. Dr. Christine M. Papadakis,
Seminar über Struktur und Dynamik kondensierter Materie
Prof. Dr. Peter Müller-Buschbaum, Prof. Dr. Christine M. Papadakis, *Seminar: Polymere*
Prof. Dr. Peter Müller-Buschbaum, Prof. Dr. Christine M. Papadakis,
Studentenseminar: Grundlegende Phänomene der Physik der weichen Materie
Prof. Dr. Peter Müller-Buschbaum, *Seminar: Aktuelle Probleme der organischen Photovoltaik*
Prof. Dr. Winfried Petry, Prof. Dr. Peter Böni, Prof. Dr. Wolfgang Häußler
Seminar über Neutronen in Forschung und Industrie

Lab courses 2013

Theoretische und praktische Einführung in AFM (Fortgeschrittenenpraktikum)
Thermische Analyse (Fortgeschrittenenpraktikum)
Neutronenstreuung am FRM II (Fortgeschrittenenpraktikum)
JCNS Laboratory Course - Neutron Scattering (Forschungspraktikum)

8.2 Conferences and public outreach

C. M. Papadakis
Tag der Physikerin
Garching, 31 Jan 2013

Day of the Female Physicist 2013

Already for the third time, the Day of the Female Physicist took place on January 31, 2013 at the Physics Department. After an introduction by the dean, Prof. Johannes Barth, Prof. Laura Fabbietti from the Physics Department and the Excellence-Cluster „Origin and Structure of the Universe" gave a talk about "Mini big bangs in the lab – what comes out?" Afterwards, Dr. Stephanie Handschuh-Heiß, Wissenschaftszentrum Weihenstephan für Ernährung, Landnutzung und Umwelt, Gender Management, reported on her investigation on "Studies of physics at TUM: Criteria for the choice of the university. Results from an opinion survery among male and female students of physics in the beginning of their studies". A poster session enabled an extensive exchange among the participants.

P. Müller-Buschbaum, W. Petry
Lehrerfortbildung 'Physik von Zukunftsmaterialien'
37. Edgar-Lüscher-Seminar
Zwiesel, 12 – 14 Apr 2013

Programm

Freitag, 12. April 2013

13.00 - 14.30	Studienberatung der TUM
15.00 - 15.30	Begrüßung
15.30 - 16.45	**Magnetoelektrische Komposite als hochempfindliche Magnetfeldsensoren** *Prof. Dr.-Ing. Eckhard Quandt, Universität Kiel*
16.45 - 17.30	Diskussion und Kaffeepause
17.30 - 18.15	**Hochtemperatursupraleiter** *Prof. Dr. Rudolf Gross, TUM WMI*
18.45 - 19.00	Diskussion

Samstag, 13. April 2013

09.00 - 10.15	**Datenspeicher** *Prof. Christian Pfleiderer, TUM*
10.15 - 11.00	Diskussion und Kaffeepause
11.00 - 12.15	**Photodetektoren, optische Materialien, CCD Kamera** *Prof. Paola Lugli, TUM*
12.15 -12.30	Diskussion
14.30 - 15.45	**Metalle erinnern sich – von den physikalischen Grundlagen bis zu Anwendungen von Formgedächtnislegierungen** *Prof. Dr.-Ing Gunther Eggeler, Ruhr-Universität Bochum*
15.45 - 16.30	Diskussion und Kaffeepause
16.30 - 17.45	**Displays basierend auf organischen Leuchtdioden** *Tobias Schmidt, Universität Augsburg*
17.45 - 18.00	Diskussion

Sonntag, 14. April 2013

09.00 - 10.15	**Entwicklung von nichtmetallischen Handy-Antennen** *Dr. Martin Letz, SCHOTT AG, Mainz*
10.15 - 11.00	Diskussion und Kaffeepause
11.00 - 12.15	**Thermoresponsive Polymere** *Dr. Martine Philipp, TUM*
12.15 - 13.00	Diskussion, Themenfindung für das 38. Seminar

Organisation

Prof. Dr. Peter Müller-Buschbaum
TUM

Prof. Müller-Buschbaum befasst sich in seiner Forschungsarbeit mit der Entwicklung polymerbasierter Materialien mit neuartigen Struktur-Eigenschaftsbeziehungen. Strukturen aus leitfähigen Polymeren und deren Anwendungen für die Photovoltaik sind ein Schwerpunkt der Arbeiten.

Prof. Dr. Winfried Petry
TUM

Prof. Petry ist Ordinarius am Lehrstuhl E13 des Physik-Departments, Leiter des Prüflabors für Technische Physik, wissenschaftlicher Direktor der Forschungsneutronenquelle Heinz Maier-Leibnitz (FRM-II), Betreuungsprofessor des Physik Departments für die Bayerische Elite-Akademie und Vorsitzender der Arbeitsgemeinschaft Metall- und Materialphysik der Deutschen Physikalischen Gesellschaft.

Organisatorische Hinweise

Organisation vor Ort:

StD Heribert Strunz,	*Gymnasium Zwiesel*
StD Wolfgang Achatz,	*Gymnasium Zwiesel*
StR Claus Starke,	*Gymnasium Zwiesel*
OStR Christian Stoiber,	*Gymnasium Zwiesel*

Email:
sekretariat@gymnasium-zwiesel.de

Hinweise:

- Alle Veranstaltungen finden in der Aula des Gymnasiums Zwiesel statt. Die Teilnehmer erhalten am Ende des Seminars für 5,- € eine CD mit sämtlichen Vorträgen.
- Die Mensa des Gymnasiums ist während des Seminars geöffnet (Mittagessen, Kaffeepausen).
- Buch- und Lehrmittelausstellung in der Aula

37. Edgar-Lüscher-Seminar

am Gymnasium Zwiesel

Freitag, 12. April 2013, bis Sonntag, 14. April 2013

Schirmherr:
Prof. Dr. Dr. h.c. mult. Wolfgang Herrmann, *Präsident der TUM*

Veranstalter:
Ltd. OStD , *Ministerialbeauftragter für die Gymnasien in Niederbayern*

Wissenschaftliche Leitung:
Prof. Dr. Peter Müller-Buschbaum, *TUM*
Prof. Dr. Winfried Petry, *TUM*

GYMNASIEN NIEDERBAYERN
Gymnasium Zwiesel

W. A. Herrmann, T. Hamacher, W. Lang, M. Lienkamp, P. Müller-Buschbaum, H. Spliethoff, U. Stimming
Colloqium 'Research towards innovative energy systems and materials'
3rd Colloquium of the Munich School of Engineering
Garching, 4 Jul 2013

P. Müller-Buschbaum
Lehrerfortbildung 'Energiewandlung und Energiespeicherung'
Edgar-Lüscher-Lectures
Dillingen, 30 Sep – 2 Oct 2013

EDGAR–LÜSCHER–LECTURES LEITERSHOFEN/AUGSBURG 2013
Thema: Energiewandlung und Energiespeicherung
Datum: Montag, 30. September bis Mittwoch, 2. Oktober 2013
Tagungsort: Exerzitienhaus St. Paulus in Leitershofen, einem Ortsteil der Stadt Stadtbergen bei Augsburg
Veranstalter: Akademie für Lehrerfortbildung Dillingen und TU München
wissenschaftliche Leitung: Prof. Dr. Peter Müller-Buschbaum, Technische Universität München.

Programm

Montag, 30. 09. 2013
15:00 – 15:30 Prof. Dr. Peter Müller-Buschbaum (Physik-Department, TUM)
Begrüßung

15:30 – 17:00 Prof. Martin Brandt (Walter Schottky Institut, TUM)
Physikalische Grundlagen der Energiespeicherung

18:30 – 20:00 Dr. Claudia Lintz (BMW group)
Batteriesysteme für die Anwendung in Fahrzeugen

Dienstag, 01. 10. 2013
8:30 – 10:00 Prof. Tom Nilges (Chemie, TUM)
Anoden- und Kathodenmaterialentwicklung

10:00 – 10.30 Kaffeepause

10:30 – 12:00 Dr. Arnd Garsuch (BASF)
Batteriematerialentwicklung in der Industrie

15:30 – 17:00 Dr. Norbert Wagner (DLR, Stuttgart)
Post-Lithiumionenbatterien

18:30 – 20:00 Dr. Holger Fink (ZAE Bayern)
Redox-Flow Batterien für elektrische Grossspeicher

Mittwoch, 02. 10. 2013
8:30 – 10:00 Dr. Michael Hofmann (Forschungs-Neutronenquelle Heinz Maier-Leibnitz, FRM II)
Strukturuntersuchungen an Materialien zur Energiespeicherung

10:00 – 10.30 Kaffeepause

10:30 – 12:00 Dr. Alexander Hirnet (Varta Storage GmbH)
Batteriesysteme für die stationäre Speicherung

Ab 12:00 Prof. Dr. Peter Müller-Buschbaum / StD Werner Ettinger
Lehrgangsabschluss

R. Gehrke, P. Müller-Buschbaum, S. V. Roth
International workshop 'GISAXS 2013'
Hamburg, 7 – 9 Oct 2013

From October 7 to October 9, 2013 the workshop 'GISAXS2013' was held in Hamburg, Germany. GISAXS2013 was a continuation of the very successful series of three international GISAXS workshops at DESY in 2005, 2007 and 2011 (http://gisaxs2011.desy.de) and the GISAS2009 satellite conference to the XIV SAS conference in Oxford (UK). This workshop brought together different communities working in the field of thin films, nanostructures, surfaces and interfaces, to gain insights to the very powerful method of grazing incidence small angle x-ray scattering. In invited lectures the possibilities and new trends in GISAXS were highlighted. One poster session allowed for a profound discussion among the participants. This workshop addressed students, experienced researchers, senior scientists working in the field of and exploiting the potentials of GISAXS in the area of thin film technology.

07.10.2013						
Chair		Start	End	Title	Speaker	Location
	Registration	08:30	10:00			
Roth		10:00	10:20	Welcome	Organizers	Auditorium (Bldg. 5)
Roth		10:20	11:10	A general introduction to GISAXS: Basics and fundamentals	Müller-Buschbaum	Auditorium (Bldg. 5)
Roth		11:10	12:00	Application of GISAXS to the study of ion-sputtered surfaces and sputter-deposited thin films	Babonneau	Auditorium (Bldg. 5)
	Lunch Break	12:00	13:00			
Roth		13:00	13:30	Photon-Science at DESY	Weckert	Auditorium (Bldg. 5)
Müller-Buschbaum		13:30	14:20	HiPGISAXS	Hexemer	Auditorium (Bldg. 5)
Müller-Buschbaum		14:20	15:10	GIWAXS measurements on laser sintered metal oxide nanoparticles	Notthoff	Auditorium (Bldg. 5)
	Coffee break	15:10	16:00			
Müller-Buschbaum		16:00	16:50	Solvent vapor treatment of nanostructured thin films - in-situ, real-time GISAXS studies	Papadakis	Auditorium (Bldg. 5)
Müller-Buschbaum		16:50	17:40	Towards in-situ observation of resistive switching: filament detection in SrTiO3 thin films by GISAXS	Klemradt	Auditorium (Bldg. 5)
	Break	17:40	18:00			
		18:00	21:00	Poster session		Auditorium (Bldg. 5)
08.10.2013						
Chair		Start	End	Title	Speaker	Location
Gehrke		09:00	09:30	Advanced grazing incidence scattering at P03/MiNaXS	Roth	Auditorium (Bldg. 5)
Gehrke		09:30	10:20	Polymer brushes as the ultimate precision tool	Gutmann	Auditorium (Bldg. 5)
	Coffee break	10:20	10:50			
Müller-Buschbaum		10:50	11:40	Mesostructured Metal Oxide Thin Films with Cubic Pore Symmetry: Preparation, Properties, and Applications	Brezesinski	Auditorium (Bldg. 5)

Müller-Buschbaum		11:40	12:10	Technical Development Projects for the DESY Research Infrastructure	Gehrke	Auditorium (Bldg. 5)
	Lunch	12:10	13:10	Photo 13:00 Foyer		
Roth		13:10	14:00	Growth kinetics of metal nanoparticles on polymer thin films	Metwalli	Auditorium (Bldg. 5)
Roth		14:00	14:50	Retrieving indirect structural and chemical information of nanoparticles in vitreous matrix by combined synchrotron radiation techniques	Malachias	Auditorium (Bldg. 5)
Roth		14:50	15:40	Structure and Dynamics of Microemulsions Adjacent to Planar Walls	Frielinghaus	Auditorium (Bldg. 5)
Roth		15:40	16:00	Division into groups for tutorials	Tutors	Auditorium (Bldg. 5)
	Coffee break	16:00	16:30			Canteen Annex
Roth		16:30	17:00	Safety Instruction	Roth	Canteen Annex
	Break	17:00	17:30			
		17:30	19:30	Practical course	Philipp, Benecke, Bommel, Schwartzkopf	Seminar rooms
	Dinner	19:30	23:00			Canteen
09.10.2013						
Chair		Start	End	Title	Speaker	Location
		09:30	11:30	Practical course	Philipp, Benecke, Bommel, Schwartzkopf	Seminar rooms
	Lunch	11:30	13:00			
		13:00	15:00	Practical course	Philipp, Benecke, Bommel, Schwartzkopf	Seminar rooms
	Break	15:00	15:30			
Roth		15:30	16:00	Closure	Roth	Auditorium (Bldg. 5)

C. M. Papadakis, D. Wöll
Workshop 'Fluorescence correlation spectroscopy in polymer science'
Garching, 10 – 11 Oct 2013

Workshop "Fluorescence correlation spectroscopy in polymer science"

October 10-11, 2013, the workshop "Fluorescence correlation spectroscopy in polymer science" was organized by Prof. Christine Papadakis and Dr. Dominik Wöll (Universität Konstanz) and was held at the Physics Department.
For more than 40 years, fluorescence correlation spectroscopy (FCS) has been used and developed to the powerful and broad method it is today. So far however, its main focus has been systems in life sciences and pharmacology. In recent years, FCS found its way into polymer science, e.g. to determine critical micelle concentrations in amphiphilic block copolymer solutions, to investigate polymer hydrogels, to follow dynamics at interfaces, to study hydrodynamic flow and to unravel the evolution of molecular motion in polymerizing solutions. These new aspects have led to methodological developments, such as double focus fluorescence cross-correlation spectroscopy, multi-color FCS and full correlation FCS. The improved technical possibilities allowed for an investigation of various polymer systems and fostered the development of suitable sample environments.
The workshop aimed at bringing together scientists working in this exciting field. It comprised three invited talks, given by Prof. Walter Richtering (RWTH Aachen), Dr. Kaloyan Koynov (MPI for Polymer Research, Mainz) and Dr. Peter Košovan (Charles University, Prague). Twelve submitted talks as well as a number of posters shown during the poster session gave additional insight into this growing field. A bavarian dinner enabled scientific and personal exchange.

Thursday, October 10th		
13:00 – 13:10	Welcome address	
13:10 – 13:40	**Kaloian Koynov (invited)** Max-Planck-Institute for Polymer Research Mainz	Fluorescence Correlation Spectroscopy Studies of Tracer Dynamics in Dense Polymer Systems
13:40 – 14:00	**Maren Dill** Universität Konstanz	Parallel Detection of Translational and Rotational Diffusion during Radical Polymerization with Full Correlation Fluorescence Correlation Spectroscopy (fcFCS)
14:00 – 14:20	**David Schäffel** Max-Planck-Institute for Polymer Research Mainz	Dual Color FCCS Directly Monitors Coalescence of Polymer Nanodroplets and the Dynamic Equilibrium Exchange Kinetics of Copolymer Micelles
14:20 – 14:50	***Coffee break***	
14:50 – 15:10	**Daniela Täuber** Technische Universität Chemnitz	Fluorescence Correlation Spectroscopy in Thin Films on Reflecting Substrates
15:10 – 15:30	**Petr Štěpánek** Academy of Sciences of the Czech Republic, Prague	Investigation of Nanoparticle Coating by Fluorescence Correlation Spectroscopy
15:30 – 15:50	**Felix Koberling** PicoQuant GmbH, Berlin	Time-Correlated Single Photon Counting Based FCS – From Absolute Diffusion Parameters to Species Selective Spectroscopy
16:00 – 18:00	**Poster session**	
19:30 –	***Dinner***	

Friday, October 11th		
09:00 – 09:30	**Walter Richtering (invited)** RWTH Aachen University	Spatially Resolved Diffusion in Gels
09:30 – 09:50	**Deborah Sandrin** Heinrich-Heine-Universität Düsseldorf	FCS Studies of Dye Photostability in Polymer Hydrogel
09:50 – 10:10	**Ludger Harnau** Max-Planck-Institute for Intelligent Systems, Stuttgart	Dynamics of Semidilute Polymer Solutions Studied by Fluorescence Correlation Spectroscopy and Centrifugal Nanofiber Spinning
10:10 – 10:30	**Konstantinos Kyriakos** Technische Universität München	Novel Thermoresponsive Polymers in Various Architectures
10:30 – 11:00	***Coffee break***	
11:00 – 11:30	**Petr Košovan (invited)** Charles University, Prague	Complex Tracer Diffusion Dynamics in Polymer Solutions
11:30 – 11:50	**Dominik Würsch** University of Regensburg	Solvent Annealing Studies of Conjugated Polymers at the Single-Molecule Level
11:50 – 12:10	**Eugene Petrov** Max-Planck-Institute Martinsried	Fluorescence Correlation Spectroscopy of Rod-Like DNA Origami on Freestanding Lipid Membranes
12:10 – 12:30	**Carolin Ganas** Technische Universität Berlin	Water Soluble Inter-Polyelectrolyte Complexes for Application in Drug Delivery

12:30 – 12:50	**Jan Ebenhan** Interdisciplinary Research Unit, Halle	Probing the Membrane Structure of Hybrid Lipid-Polymer GUVs on Different Scales with Advanced Fluorescence Correlation Techniques
12:50 – 13:00	Closing Remarks	

Poster session (Thursday, 16:00-18:00)		
1	**Mikheil Doroshenko** Max-Planck-Institute for Polymer Research, Mainz	Phase Separation Dynamics in a Polymer Blend Studied by Confocal Microscopy and Fluorescence Correlation Spectroscopy
2	**Margarita Dyakonova** Technische Universität München	Structure and Disintegration of Nanoparticles from Clinically Relevant Polymers
3	**Felix Schmieder** Technische Universität Chemnitz	Photon-Correlation Fourier Spectroscopy
4	**Apostolos Vagias** Max-Planck-Institute for Polymer Research, Mainz	Fluorescence Correlation Spectroscopy Studies of Molecular Tracer Mobility in Responsive Grafted Hydrogels
5	**Natalya Vishnevetskaya** Technische Universität München	Polymeric Nanoparticles for Drug Delivery
6	**Jiří Pánek** Institute of Macromolecular Chemistry, Prague	Comparative Study of Critical Micelle Concentration of Block and Gradient Poly(2-oxazoline)s
7	**Jan Martin Nölle** Universität Konstanz	FCS Studies on the Diffusion of Molecular and Macromolecular Probes in Polymerizing Systems

C. M. Papadakis
Schnupperstudium für Abiturientinnen
Garching, 31 Oct 3013

One day trial study at the Physics Department for girls

October 31, 2013, the one day trial study took place at the Physics Department, already for the second time. On this day, female high school students (11th grade or higher) had the opportunity to get detailed information about the studies of physics. The trial study was organized by Dr. Andreas Hauptner, and he together with two female physics students supervised the girls.

The women's representative of the Department, Prof. Papadakis welcomed the girls and gave them a short introduction to the Physics Department. Afterwards, they carried out an experiment with optical interferometry, which is usually taught in the first year's physics lab course. At this, the girls installed a Michelson interferometer and adjusted it. By means of a computer, they analyzed the oscillations of a mirror surface quantitatively. After a common lunch in the Mensa, they tried the slides in the maths building! Afterwards, they visited the lecture Experimental Physics 3, where the refractive index of metals and the color of objects were in the focus, and related demonstration experiments were shown. Finally, they followed a guided tour through the research reactor FRM II.

On this day, the girls could "sniff" into the physics studies and get answers to their questions.

G. G. Simeoni
Technical meeting on neutron scattering at high-pressure
Garching, 10 – 11 Dec 3013

10-11th December 2013

Heinz Maier-Leibnitz Zentrum, Garching

TECHNICAL MEETING ON NEUTRON SCATTERING AT HIGH-PRESSURE

Introduction
The characterization of the physical and chemical properties of the condensed matter under extreme environmental conditions is one of the big challenge of nowadays and next-future science. Despite some unique peculiarities of the neutron scattering, however, the high pressure investigations at large scale neutron facilities have been significantly limited so far due to the big size of the typical samples and other further technical restrictions. As a matter of fact, even the existing high pressure equipments are far from being routinely operated and taken into account when designing a new line of research. Any progress in this direction represents therefore a huge potential source of scientific development, whose technical feasibility is supported by the unprecedented results achieved in the field the focusing Neutron Optics over last few years.

Scope
General scope of the meeting is to promote the high-pressure investigations at the Heinz Maier-Leibnitz Zentrum.
It is intended to be a 1,5 day kick-off meeting, bringing together few people from different scientific areas, already involved in the high-pressure research and/or active in the neutron scattering. The scientific case will be left aside during this first phase, unless strictly connected with the discussion of the technical details. The information will be collected in a technical document, which will provide a rational base for any further MLZ scientific discussion on the topics, including the request of financing "neutron research at high pressure".

Topics
It will be discussed about existing equipments and expertise (complementary techniques included), basic infrastructures and technical support required before, during and after the experiments. Great attention will be also payed to the major safety aspects (laboratories, tools, testing place, etc) and the main issues for the proper handling of the HP-equipment (loading procedure, activation etc).

Location
Glaspalace, Heinz Maier-Leibnitz Zentrum, Garching

Organizer - Contacts
Dr. G. G. Simeoni
giovanna.simeoni@frm2.tum.de
0049 - (0)89 - 28914975

Administration and accommodation:
Mrs. S. Valentin-Hantschel
silvia.valentin-hantschel@frm2.tum.de

8.3 Service to the community

Prof. Dr. Peter Müller-Buschbaum:

- since 11/2012 Member of 'Peer Review Panel 3 – Surfaces & Interfaces' of 'Diamond Light Source Ltd'
- since 9/2012 Associate Editor of journal ACS Applied Materials & Interfaces of the American Chemical Society
- since 1/2012 Member of the Scientific Selection Panel of the Helmholtz-Zentrum Berlin für Materialien und Energie (HZB)
- since 2011 Mitglied im European Spallation Source (ESS) Scientific Advisory Panel (Reflectivity)
- since 2011 German representative at the European Polymer Federation (EPF) for polymer physics
- since 2011 elected member of 9th Committee Research with Synchrotronstrahlung (KFS), Section User Matters
- since 2010 spokesman of the regenerative engergies section (NRG) at the Munich School of Engineering (MSE) of TU Munich
- since 2010 member of TUM.Energy at TU Munich
- since 2010 spokesman of the energy section at the Physics Department/TU Munich
- since 2010 German representative at the ESUO - European Synchrotron User Organization
- since 2008 chairman of 'HASYLAB User Committee (HUC)' at the synchrotron radiation laboratory HASYLAB in Hamburg

Prof. Dr. Christine Papadakis:

- member of the Project Review Panel 5: 'Soft Condensed Matter/Scattering' at HASYLAB, DESY, Hamburg

- member of the subcommittee 'College 9: Structure and Dynamics of Soft-Condensed Matter' at Laue-Langevin Institute (ILL), Grenoble

- women's representative of the Physics Department at TU München

Prof. Dr. Winfried Petry:

- since 1999 liaison professor of Bayerische Eliteakademie (Bavarian Leadership Academy) and since May 2011 member of the curatorium

- since 2007 member of the Steering Comittee of the Laue Langevin Institute and chairman of the instrumentation review panel of the CEA Leon Brillouin Laboratory

9 Publications, talks and funding

9.1 Publications

- J. Adelsberger, I. Grillo, A. Kulkarni, M. Sharp, A. M. Bivigou-Koumba, A. Laschewsky, P. Müller-Buschbaum, C. M.Papadakis
Kinetics of aggregation in micellar solutions of thermoresponsive triblock copolymers - influence of concentration, start and target temperature
Soft Matter **9**, 1685-1699 (2013)

- M. Al-Hussein, M. Schindler, M. A. Ruderer, J. Perlich, M. Schwartzkopf, G. Herzog, B. Heidmann, A. Buffet, S. V. Roth, P. Müller-Buschbaum
In-situ X-ray study of the structural evolution of gold nano-domains by spray deposition on thin conductive P3HT films
Langmuir **29**, 2490-2497 (2013)

- V. Antonelli, W. Lohstroh, H. Baier
Feasibility study of a large chopper disk for a TOF spectrometer
Proceedings of the 19th International Conference on Composite Materials, Montreal (2013)

- B. N. Balzer, M. Gallei, K. Sondergeld, M. Schindler, P. Müller-Buschbaum, M. Rehahn, T. Hugel
Cohesion mechanisms of polystyrene-based thin polymer films
Macromolecules **46**, 7406-7414 (2013)

- C. Bousige, S. Rols, J. Ollivier, H. Schober, P. Fouquet, G. G. Simeoni, V. Agafonov, V. Davydov, H. Kataura, P. Launois
From one-dimensional crystal to a one-dimensional liquid: a comprehensive dynamical study of a textbook system, C60 peapods
Phys. Rev. B **87**, 195438 (2013)

- C. Brandt, C. Baur, A. Caon, P. Müller-Buschbaum, C. Zimmermann, T. Andreev
The influence of high temperatures on radiation damage of GaInP2/GaAs/Ge triple junction cells
IEEE J. of Photovoltaics **3**, 904-908 (2013)

- H. Breitkreutz, R. Jungwirth, A. Röhrmoser, W. Petry, S. Van den Berghe, A. Leenaers, E. Koonen, P. Lemoine, M. Rpiert, H. Palancher, M.-C. Anselmet, C. Jarousse, B. Stepnik, D. Geslin, Y. Calzavara, H. Guyon
The development of dispersed UMo as a high performance research reactor fuel in Europe
Transactions RRFM 2013, St. Petersburg, Russia, (21 - 25 Apr 2013)

- H. Breitkreutz, A. Röhrmoser, W. Petry
Monolithic UMo based fuel element designs for FRM II
Transactions RRFM 2013, St. Petersburg, Russia, (21 - 25 Apr 2013)

- H. Ceeh, J. A. Weber, Ch. Hugenschmidt, M. Leitner, P. Böni
First measurements with the Munich 2D-ACAR spectrometer on Cr
J. Phys. Conf. Ser. **443**, 012094 (2013)

- H. Ceeh, J. A. Weber, M. Leitner, P. Böni, Ch. Hugenschmidt
The source-sample stage of the new two-dimensional angular correlation of annihilation radiation spectrometer at Technische Universität München
Rev. Sci. Instrum. **84**, 043905 (2013)

- H.-Y. Chiang, M. Mayer, T. Zweifel, R. Jungwirth, W. Petry
RBS studies on heavy ion irradiation induced diffusion in UMo/Transition metal/Al fuel
Transactions RRFM 2013, St. Petersburg, Russia, (21 - 25 Apr 2013)

- H-Y. Chiang, T. Zweifel, H. Palancher, A. Bonnin, L. Beck, P. Weiser, M. Döblinger, C. Sabathier, R. Jungwirth, W. Petry
Evidence of amorphous interdiffusion layer in heavy-ion irradiated U-8wt%Mo/Al interfaces
J. Nucl. Mater. **440**, 117-123, (2013)

- R. Döhrmann, S. Botta, A. Buffet, G. Santoro, K. Schlage, M. Schwartzkopf, S. Bommel, J. F. H. Risch, R. Mannweiler, S. Brunner, E. Metwalli, P. Müller-Buschbaum, S. V. Roth
A new highly automated sputter equipment for in-situ investigation of deposition processes with synchrotron radiation
Rev. Sci. Instr **84**, 043901 (2013)

- S. Ener, T. Mehaddene, B. Pedersen, M. Leitner, J. Neuhaus, W. Petry
Vibrational properties of Ni–Mn–Ga shape memory alloy in the martensite phases
New J. Phys. **15**, 123016 (2013)

- S. K. Filippov, J. M. Franklin, P. V. Konarev, P. Chytil, T. Etrych, A. Bogomolova, M. Dyakonova, C. M. Papadakis, A. Radulescu, K. Ulbrich, P. Stepanek, D. I. Svergun
Hydrolytically Degradable Polymer Micelles for Drug Delivery: A SAXS/SANS Kinetic Study
Biomacromolecules **14**, 4061-4070 (2013)

- Z. Fu, Y. Zheng, Y. Xiao, S. Bedanta, A. Senyshyn, G. G. Simeoni, Y. Su, U. Ruecker, P. Koegerle, Th. Brueckel
Coexistence of magnetic order and spin-glass-like phase in the pyrochlore antiferromagnet Na3Co(CO3)2Cl
Phys. Rev. B **87**, 214406 (2013)

- T. Glomann, G. J. Schneider, J. Allgaier, A. Radulescu, W. Lohstroh, B. Farago, D. Richter
Microscopic Dynamics of Polyethylene Glycol Chains Interacting with Silica Nanoparticles
Phys. Rev. Lett. **110**, 178001 (2013)

- M. Gruber, M. Rawolle, J. Wagner, D. Magerl, U. Hörmann, J. Perlich, S. V. Roth, A. Opitz, F. Schreiber, P. Müller-Buschbaum, W. Brütting
Correlating structure and morphology to device performance of molecular organic donor-acceptor photovoltaic cells based on Diindenoperylene (DIP) and C60
Adv. Energy Mat. **3**, 1075-1083 (2013)

- S. Guo, M. A. Ruderer, M. Rawolle, V. Körstgens, C. Birkenstock, J. Perlich, P. Müller-Buschbaum
Evolution of lateral structures during the functional stack build-up of P3HT:PCBM based bulk heterojunction solar cells
ACS Appl. Mater. Interfaces **5**, 8581-8590 (2013)

- T. Gutberlet, H. Hilbig, R. E. Beddoe, W. Lohstroh
New insights into water bonding during early tricalcium silicate hydration with quasielastic neutron scattering
Cement and Concrete Research **51**, 104 (2013)

- E. M. Herzig, P. Müller-Buschbaum
Organic Photovoltaic Cells for Space Applications
Acta Futura **6**, 17-24 (2013)

- E. T. Hoppe, A. Sepe, M. Haese-Seiller, J.-F. Moulin, C. M. Papadakis
Density profile in thin films of polybutadiene on silicon oxide substrates: A TOF-NR study
Langmuir **29**, 10759-10768 (2013)

- Y. J. Jeong, J. M. Park, H. J. Ryu, Y. S. Lee, W. J. Kim, R. Jungwirth, H.-Y. Chiang, T. Zweifel, W. Petry
Heavy ion irradiation of nitride and silicon coated UMo/Al and UMoTi/Al fuel
Transactions RRFM 2013, St. Petersburg, Russia, (21 - 25 Apr. 2013)

- R. Jungwirth, H. Palancher, A. Bonnin, C. Bertrand-Drira, C. Borca, V. Honkomäki, C. Jarousse, B. Stepnik, S. H. Park, X. Iltis et al.
Microstructure of as-fabricated Umo/Al (Si) plates prepared with ground and atomized powder
J. Nucl. Mater. **438**, 246 - 260 (2013)

- R. Jungwirth, T. Zweifel, H.-Y. Chiang, W. Petry, S. van den Berghe, A. Lennaers
Heavy ion irradiation of UMo/Al samples PVD coated with Si and ZrN layers
J. Nucl. Mater. **434**, 296-302,(2013)

- W. Kipnusu, M. Elmahdy, M. Treß, M. Fuchs, E. Mapesa, D.-M. Smilgies, J. Zhang, C. M. Papadakis, F. Kremer
Molecular order and dynamics of nanometric thin layers of poly(styrene-b-1,4-isoprene) diblock copolymers
Macromolecules **46**, 9729-9737 (2013)

- M. Kofu, T. Kajiwara, J. S. Gardner, G. G. Simeoni, M. Tyagi, A. Faraone, K. Nakajima, S. Ohira-Kawamura, M. Nakano, O. Yamamuro
Magnetic relaxations in a Tb-based single molecule magnet studied by quasielastic neutron scattering
Chem. Phys. **427**, 147-152 (2013)

- P. Kohn, Z. Rong, K. Scherer, A. Sepe, M. Sommer, P. Müller-Buschbaum, R. Friend, U. Steiner, S. Hüttner
Crystallization-induced 10-nm structure formation in P3HT/PCBM blends
Macromolecules **46**, 4002-4013 (2013)

- A. Laschewsky, P. Müller-Buschbaum, C. M. Papadakis
Thermo-responsive amphiphilic di- and triblock copolymers based on poly(N-isopropylacrylamide) and poly(methoxy diethylene glycol acrylate): aggregation and hydrogel formation in bulk solution and in thin films
Prog. Colloid Polym. Sci. **140**,15-34 (2013)

- W. Lohstroh
Materials for energy storage
in Nanotechnology and Energy: Science, Promises and Limits, Editors J. Lambauer, U. Fahl, A. Voss, Singapore, Pan Stanford Publishing Pte. Ltd, Singapore (2013)

- E. Metwalli, V. Körstgens, K. Schlage, R. Meier, G. Kaune, A. Buffet, S. Couet, S. V. Roth, R. Röhlsberger, P. Müller-Buschbaum
Cobalt nanoparticles growth on a block copolymer thin film: A time resolved GISAXS study
Langmuir **29**, 6331-6340 (2013)

- H. Morhenn, S. Busch, H. Meyer, D. Richter, W. Petry, T. Unruh
Collective intermolecular motions dominate the picosecond dynamics of short polymer chains
Phys. Rev. Lett. **111**, 173003 (2013)

- U. Müller, M. Philipp, M. Thomassey, R. Sanctuary, J. K. Krüger
Temperature modulated optical refractometry: A quasi-isothermal method to determine the dynamic volume expansion coefficient
Thermochim. Acta **555**, 17-22 (2013)

- P. Müller-Buschbaum
Grazing incidence small angle neutron scattering: Challenges and possibilities
Polymer Journal (invited review) **45**, 34-42 (2013)

- M. A. Niedermeier, I. Groß, P. Müller-Buschbaum
Structuring of titania thin films on different length scales via combining block copolymer assisted sol-gel templating with wet-imprinting
J. Mater. Chem. A **1**, 13399-13403 (2013)

- M. A. Niedermeier, M. Rawolle, P. Lellig, V. Körstgens, E. M. Herzig, A. Buffet, S. V. Roth, J. S. Gutmann, T. Fröschl, N. Hüsing, P. Müller-Buschbaum
Low temperature sol-gel synthesis of polymer/titania hybrid films based on custom made poly(3-alkoxy thiophene)
Chem. Phys. Chem. **14**, 597-602 (2013)

- M. A. Niedermeier, G. Tainter, B. Weiler, P. Lugli, P. Müller-Buschbaum
Fabrication of hierarchically structured titania thin films via combining nano imprint lithography with block copolymer assisted sol-gel templating
J. Mater. Chem. A **1**, 7870-7873 (2013)

- S. Ng, E. Metwalli, P. Müller-Buschbaum, J. Plank
Occurrence of intercalation of PCE superplasticizers in calcium aluminate cement under actual application conditions, as evidenced by SAXS analysis
Cement & Concrete Research **54**, 191-198 (2013)

- N. Paul, M. Müller, A. Paul, E. Guenther, I. Lauermann, P. Müller-Buschbaum, M. Ch.Lux-Steiner
Molecularly imprinted conductive polymers for controlled trafficking of neurotransmitter at solid-liquid interfaces;
Soft Matter **9**, 1364-1371 (2013)

- N. Paul, A. Paul, S. Mattauch, P. Müller-Buschbaum, P. Böni, M. Ch. Lux-Steiner
  Interfacial engineering of polymer multilayers with polarized biomolecules: a new approach in growing supramolecular layer structures
  Soft Matter **9**, 10117-10128 (2013)

- W. Petry
  Neutronenstrahlung
  Buchbeitrag in: H. Bullinger, H. Jürgens, W. Rohmert (Herausg.) bearbeitet von H. Schmidtke Handbuch der Ergonomie, Bundesamt für Wehrtechnik und Beschaffung, ISBN: 9783-927038-70, (2013)

- M. Philipp, U. Müller, R. Aleksandrova, R. Sanctuary, P. Müller-Buschbaum, J. K. Krüger
  Immense elastic nonlinearities at the demixing transition of aqueous PNIPAM solutions
  Soft Matter **9**, 5034-5041 (2013)

- M. Philipp, U. Müller, R. Aleksandrova, R. Sanctuary, P. Müller-Buschbaum, J. K. Krüger
  Kinetic processes at the demixing transition of PNIPAM solutions
  Soft Matter **9**, 9887-9896 (2013)

- M. Rawolle, K. Sarkar, M. A. Niedermeier, M. Schindler, P. Lellig, J. S. Gutmann, J.-F. Moulin, M. Haese-Seiller, A. Wochnik, C. Scheu, P. Müller-Buschbaum
  Infiltration of polymer hole-conductor into mesoporous titania structures for solid-state dye-sensitized solar cells
  ACS Appl. Mater. Interfaces **57**, 19-729 (2013)

- R. Richter, U. E. Berger, S. Dullinger, F. Essl, M. Leitner, M. Smith, G. Vogl
  Spread of invasive ragweed: climate change, management and how to reduce allergy costs
  J. Appl. Ecol. **50**, 1422–1430 (2013)

- R. Richter, S. Dullinger, F. Essl, M. Leitner, G. Vogl
  How to account for habitat suitability in weed management programmes?
  Biol. Inv. **15**, 657–669 (2013)

- M. A. Ruderer, P. Müller-Buschbaum
  Solvent effects in polymer based organic photovoltaics
  in Polymers for Energy Storage and Conversion, edt. Vikas Mittal, 137-162, Wiley-Scrivener (2013)

- M. A. Ruderer, C. Wang, E. Schaible, A. Hexemer, T. Xu, P. Müller-Buschbaum
  Morphology and optical properties of P3HT:MEH-CN-PPV blend films
  Macromolecules **46**, 4491-4501 (2013)

- A. A. Rudov, E. S. Patyukova, I. V. Neratova, P. G. Khalatur, D. Posselt, C. M. Papadakis, I. I. Potemkin
  Structural changes in lamellar diblock copolymer thin films upon swelling in non-selective solvents
  Macromolecules **46**, 5786-5795 (2013)

- K. Sarkar, M. Rawolle, E. M. Herzig, W. Wang, A. Buffet, S. V. Roth, P. Müller-Buschbaum
  Custom-made morphologies of ZnO nanostructured films templated by a P(S-b-EO) diblock copolymer via sol-gel technique
  Chem. Sus. Chem. **6**, 1414-1424 (2013)

- C. J. Schaffer, C. M. Palumbiny, M. A. Niedermeier, C. Jendrzejewski, G. Santoro, S. V. Roth, P. Müller-Buschbaum
A direct evidence of morphological degradation on a nanometer scale in polymer solar cells
Adv. Mat. **25**, 6760-6764 (2013)

- R. Schenk, W. Petry, B. Stepnik, C. Jarousse, G. Bourdat, C. Moyroud, M. Grasse
FRMII/CERCA UMo atomizer project status
Transactions RRFM 2013, St. Petersburg, Russia, (21 - 25 Apr 2013)

- M. Schindler, S. Pröller, T. Geue, P. Müller-Buschbaum
Near-interface composition in pressure sensitive adhesives at the adhesive-adherent interface
Macromol. React. Eng. **7**, 549-554 (2013)

- G. Schneider, T. Glomann, J. Allgaier, A. Radulescu, W. Lohstroh, B. Farago, D. Richter
Rich molecular dynamics of polymer melts in nanocomposites
Proceeding of the Polymer Processing Society 29th annual meeting, Nürnberg, (2013)

- M. Schwartzkopf, G. Benecke, A. Buffet, D. Erb, B. Heidmann, G. Herzog, V. Körstgens, E. Metwalli, J. Perlich, M. Rawolle, A. Rothkirch, K. Schlage, P. Müller-Buschbaum, R. Röhlsberger, R. Gehrke, N. Stribeck, S. V. Roth
From atoms to layers: in situ gold growth kinetics during sputter deposition
Nanoscale **5**, 5053-5062 (2013)

- A. Sepe, P. Černoch, P. Štěpánek, E. T. Hoppe, C. M. Papadakis
Creation of lateral structures in diblock copolymer thin films during vapor uptake and subsequent drying - effect of film thickness
Eur. Polym. J. **50**, 87-96 (2014)

- M. Stana, M. Leitner, M. Ross, B. Sepiol
Studies of atomic diffusion in Ni-Pt solid solution by x-ray photon correlation spectroscopy
J. Phys.: Condens. Matter **25**, 065401 (2013)

- H. Sternschulte, I. Staudinger, A. Sepe, C. M. Papadakis, J. Perlich, S. V. Roth, S. Ghodbane, D. Steinmüller-Nethl
Grazing-incidence small-angle X-ray scattering study on ultrananocrystalline diamond films
Diam. Rel. Mater. **37**, 68-73 (2013)

- J. Wang, W. H. de Jeu, M. Speise, A. Kreyes, U. Ziener, D. Magerl, M. Philipp, P. Müller-Buschbaum, M. Möller, A. Mourran
Biaxial alignment of block copolymer-complex lamellae
Soft Matter **9**, 1337-1343 (2013)

- J. A. Weber, P. Böni, H. Ceeh, M. Leitner, Ch. Hugenschmidt
First 2D-ACAR Measurements on Cu with the new Spectrometer at TUM
J. Phys. Conf. Ser. **443**, 012092 (2013)

- Y. Xiao, S. You, Y. Yao, T. Zheng, C. Lin, S. V. Roth, P. Müller-Buschbaum, W. Steffen, L. D. Sun, C. H. Yan, J. S. Gutmann, M. Yin, J. Fu, Y. J. Cheng
Generalized synthesis of mesoporous rare earth oxide thin films through amphiphilic ionic block copolymer templating
Eur. J. Inorg. Chem. **2013**, 1251-1257 (2013)

- S. Yu, G. Santoro, K. Sarkar, B. Dicke, P. Wessels, S. Bommel, R. Döhrmann, J. Perlich, M. Kuhlmann, E. Metwalli, J. F. H. Risch, M. Schwartzkopf, M. Drescher, P. Müller-Buschbaum, S. V. Roth
  Formation of Al nanostructures on Alq3: An in situ grazing incidence small angle X-ray scattering study during RF sputter deposition
  J. Phys. Chem. Lett. **4**, 3170-3175 (2013)

- J. Zhang, D. Posselt, A. Sepe, X. Shen, J. Perlich, D.-M. Smilgies, C. M. Papadakis
  Structural evolution of perpendicular lamellae in diblock copolymer thin films during solvent vapor treatment investigated by grazing-incidence small-angle X-ray scattering
  Macromol. Rapid Commun. **34**, 1289-1295 (2013)

- Q. Zhong, E. Metwalli, M. Rawolle, G. Kaune, A. M. Bivigou Koumba, A. Laschewsky, C. M. Papadakis, R. Cubitt, P. Müller-Buschbaum
  Structure and thermal response of thermoresponsive polystyrene-block-poly(methoxydiethylene glycol acrylate)-block-polystyrene films
  Macromolecules **46**, 4069-4080 (2013)

- Q. Zhong, J. Adelsberger, M. A. Niedermeier, A. Golosova, A. M. Bivigou Koumba, A. Laschewsky, S. S. Funari, C. M. Papadakis, P. Müller-Buschbaum
  The influence of selective solvents on the transition behavior of poly(styrene-b-monomethoxydiethylene glycol-acrylate-b-styrene) thick films
  Colloid. Polym. Sci. **291**,1439-1451 (2013)

- T. Zweifel, H.-Y. Chiang, H. Palancher, A. Bonnin, L. Beck, P. Weiser, M. Döblinger, C. Sabathier, R. Jungwirth, F. Charollais, P. Lemoine, W. Petry
  Heavy ion irradiation on monolithic UMo/Al layer systems: Interdiffusion layer analysis using TEM and NANO-XRD
  Transactions RRFM 2013, St. Petersburg, Russia, (21 - 25 Apr 2013)

- T. Zweifel, H. Palancher, A. Leenaers, A. Bonnin, V. Honkimaki, R. Tucoulou, S. van den Berghe, R. Jungwirth, F. Charollais, W. Petry
  Crystallographic study of Si and Zrn coated U-Mo atomised particles and of their interaction with Al under thermal annealing
  JNM **442**, 124-132 (2013)

9.2 Talks

- M. Dyakonova, A. Bogomolova, S. Filippov, A. Radulescu, C. M. Papadakis
  Structure and disintegration of nanoparticles from clinically relevant polymers
  DPG Frühjahrstagung, Regensburg, 10 – 15 Mar 2013

- E. M. Herzig
  Ternary Blends in Organic Photovoltaics
  Lehrstuhl für Nanoelektronik, München, 30 Oct 2013

- S. Jaksch, K. Kyriakos, J. Zhang, I. Grillo, A. Schulz, R. Jordan, C. M. Papadakis
  The collapse transition of poly(2-oxazoline) gradient copolymers - a multistep transition
  DPG Frühjahrstagung, Regensburg, 10 – 15 Mar 2013

- V. Körstgens, S. V. Roth, P. Müller-Buschbaum
  Microfluidics and GISAXS at the MiNaXS Beamline
  SAXS/WAXS satellite workshop of DESY User Meeting, Hamburg, 24 – 25 Jan 2013

- K. Kyriakos, M. Philipp, J. Adelsberger, S. Jaksch, A. Miasnikova, A. Laschewsky, I. Grillo, P. Müller-Buschbaum, C. M. Papadakis
  Cononsolvency in P(S-b-NIPAM) diblock copolymers in aqueous solutions
  6th Internal Biannual Science Meeting, Grainau, 10 – 13 Jun 2013

- K. Kyriakos, M. Philipp, J. Adelsberger, S. Jaksch, A. Miasnikova, A. Laschewsky, I. Grillo, P. Müller-Buschbaum, C. M. Papadakis
  Cononsolvency in P(S-b-NIPAM) diblock copolymers in aqueous solutions
  European Polymer Congress EPF 2013, Pisa, Italy, 16 – 21 Jun 2013

- K. Kyriakos, C. Psylla, S. Ottinger, A. Miasnikova, A. Laschewsky, P. Müller-Buschbaum, C. M. Papadakis
  Novel thermoresponsive polymers in various architectures
  Workshop Fluorescence Correlation Spectroscopy in Polymer Science, Garching, 10 – 11 Oct 2013

- M. Leitner, J. Neuhaus, N. Karl, W. Petry, B. Hennion, A. Hiess
  The role of phonons in the thermodynamics of Fe
  DPG Frühjahrstagung, Regensburg, 10 – 15 Mar 2013

- M. Leitner, J. Neuhaus, N. Karl, W. Petry, B. Hennion, A. Hiess
  Temperature-dependent phonons in Fe: Implications on thermodynamics and diffusion
  dyProSo XXXIV, Wien, 15 – 19 Sep 2013

- W. Lohstroh, L. Silvi, J. Neuhaus, W. Petry
  A cold chopper spectrometer for ESS
  4th In-kind contribution Meeting for ESS - IKON 4, Lund, 25 – 27 Sep 2013

- D. Magerl, D. Egger, A. Miasnikova, A. Laschewsky, P. Müller-Buschbaum
  Investigation of a multiresponsive hydrogel based on poly(methoxydiethylenglycol acrylate) (PMDEGA) with azobenzene moieties
  DPG Frühjahrstagung, Regensburg, 10 – 15 Mar 2013

- E. Metwalli, V. Körstgens, A. Buffet, J. Perlich, K. Schlage, S. V. Roth, P. Müller-Buschbaum
  Growth kinetics of metal nanoparticles on polymer surfaces
  SAXS/WAXS satellite workshop of DESY User Meeting, Hamburg, 24 Jan 2013

- E. Metwalli, V. Körstgens, A. Buffet, J. Perlich, K. Schlage, S. V. Roth, P. Müller-Buschbaum
  Growth kinetics of metal nanoparticles on polymer surfaces
  DPG Frühjahrstagung, Regensburg, 10 – 15 Mar 2013

- E. Metwalli, Y. Yao, J.-F. Moulin, M. Haese-Seiller, P. Müller-Buschbaum
  Millisecond time resolved investigation of metal nanoparticles growth on polyme films
  6th Internal Biannual Science Meeting, Grainau, 10 – 13 Jun 2013

- E. Metwalli, V. Körstgens, A. Buffet, J. Perlich, K. Schlage, S. V. Roth, P. Müller-Buschbaum
  Real time monitoring of metal nanoparticles growth on polymer templates
  EPF2013, Pisa, 16 – 21 Jun 2013

- E. Metwalli
  Real time monitoring of metal nanoparticles growth on polymer templates
  Invited talk at LMU, München, 1 Jul 2013

- E. Metwalli, V. Körstgens, A. Buffet, J. Perlich, K. Schlage, S. V. Roth, P. Müller-Buschbaum
  Millisecond time resolved investigation of metal nanoparticles growth on polyme films
  6th Int. Workshop on Polymer/Metal Nanocomposites, Toulouse, 16 – 18 Sep 2013

- E. Metwalli
  Growth Kinetics of Metal Nanoparticles on Polymer Surfaces
  Invited talk at GISAXS 2013, DESY, Hamburg, 7 – 9 Oct 2013

- H. Morhenn, T. Unruh
  Glassy dynamics in molecular liquids
  Assessment and Strategy Seminar LKS FAU Erlangen Nürnberg, Murau, Austria,
  25 – 28 Feb 2013

- H. Morhenn, S. Busch, T. Unruh
  Local, global and collective dynamics in a short polymer system
  DPG Frühjahrstagung, Regensburg, 10 – 15 Mar 2013

- P. Müller-Buschbaum
  Polymer and hybrid nanostructures for applications in organic solar cells investigated with advanced x-ray techniques
  Center for NanoScience (CeNS) Kolloquium, Munich, 11 Jan 2013

- P. Müller-Buschbaum
  GISAXS and GIWAXS measurements for the detection of the inner morphology in organic solar cells
  SAXS/WAXS satellite workshop of DESY User Meeting, Hamburg, 24 – 25 Jan 2013

- P. Müller-Buschbaum
  Report of the HASYLAB User Committe (HUC): report 2012
  DESY User Meeting, Hamburg, 24 – 25 Jan 2013

- P. Müller-Buschbaum
  Polymer and hybrid nanostructures for applications in organic solar cells investigated with advanced x-ray techniques
  Physics Seminar, University of Luxembourg, Luxembourg, 29 Jan 2013

- P. Müller-Buschbaum
  Solar cells using hybrid materials
  Workshop 'Environmentally Responsible Hybrid Functional Materials' of the University of Alberta, München, 20 Feb 2013

- P. Müller-Buschbaum
  Polymer and hybrid nanostructures for applications in organic solar cells investigated with advanced x-ray techniques
  Cavendish Laboratory Seminar, Cambridge, UK, 22 Feb 2013

- P. Müller-Buschbaum
  Determination of the inner morphology of organic solar cells with grazing incidence small angle neutron scattering
  DPG Frühjahrstagung, Regensburg, 10 – 15 Mar 2013

- P. Müller-Buschbaum
  Thin films of thermo-responsive amphiphilic di- and triblock copolymers: swelling and thermal response
  SPP 1259 Intelligente Hyrogele Abschlusskolloquium, Aachen, 18 – 20 Mar 2013

- P. Müller-Buschbaum, M. A. Ruderer, R. Meier, S. Guo, C. M. Palumbiny, D. Magerl, L. Porcar, R. Cubitt
  Determination of the inner morphology of organic solar cells with grazing incidence small angle neutron scattering
  245th American Chemical Society National Meeting, New Orleans, USA, 7 – 11 Apr 2013

- P. Müller-Buschbaum
  Tailoring titania nanostructures
  Kick-off Meeting OLYMP, Regensburg, 24 Apr 2013

- P. Müller-Buschbaum
  Polymer and hybrid nanostructures for applications in organic solar cells investigated with advanced x-ray techniques
  SFB Kolloquium, Bayreuth, 6 May 2013

- P. Müller-Buschbaum
  The applied method of grazing incidence scattering
  6th Internal Biannual Science Meeting, Grainau, 10 – 13 Jun 2013

- P. Müller-Buschbaum
  Phase separation and molecular intermixing in polymer-fullerene bulk heterojunction thin films
  European Polymer Congress EPF 2013, Pisa, Italy, 17 – 21 Jun 2013

- P. Müller-Buschbaum
  Modeling grazing incidence small angle x-ray and neutron scattering data
  Emerging Themes in Analysis of Grazing Incidence Small Angle Scattering Data Workshop, Abingdon, UK, 1 – 2 Jul 2013

- P. Müller-Buschbaum
  Organic photovoltaics at TUM
  Interface Science for Photovoltaics ISPV workshop 2013, Munich, 4 Jul 2013

- P. Müller-Buschbaum
  Tailoring Titania Nanostructures for Solar Cell Applications
  Symposium Nanosystems for Solar Energy Conversion, Munich, 24 – 26 Jul 2013

- P. Müller-Buschbaum
  Grazing incidence X-ray scattering techniques for the investigation of organic solar cells
  International Congress on X-Ray Optics and Microanalysis ICXOM22, Hamburg, Sep 2013

- P. Müller-Buschbaum
  Polymer-metal oxide nanocomposites prepared by self-assembly of nanoparticles in block copolymer films
  6th International Workshop on Polymer/Metal Nanocomposites in Toulouse, France, 15 – 18 Sep 2013

- P. Müller-Buschbaum
  A general introduction to GISAXS: Basics and fundamentals
  GISAXS 2013, Hamburg, 7 – 10 Oct 2013

- P. Müller-Buschbaum
  Polymer and hybrid nanostructures for applications in organic solar cells investigated with advanced x-ray techniques
  Physikalisches Kolloquium der TU Darmstadt, Darmstadt, 15 – 16 Nov 2013

- P. Müller-Buschbaum
  Polymer and hybrid nanostructures for applications in organic solar cells investigated with advanced x-ray techniques
  Seminar Chair for Laser- and X-Ray Physics, Munich, 6 Dec 2013

- C. M. Palumbiny, C. Heller, C. J. Schaffer, V. Körstgens, G. Santoro, S. V. Roth, P. Müller-Buschbaum
  Highly conductive PEDOT:PSS for flexible structured ITO-free solar cells
  DPG Frühjahrstagung, Regensburg, 10 – 15 Mar 2013

- C. M. Palumbiny, C. Heller, C. J. Schaffer, V. Körstgens, G. Santoro, S. V. Roth, P. Müller-Buschbaum
  Highly conductive PEDOT:PSS as electrode for flexible structured ITO-free organic electronics: A morphological study
  3rd Colloquium of the Munich School of Engineering, Garching, 4 Jul 2013

- C. M. Palumbiny, C. Heller, C. J. Schaffer, V .Körstgens, G. Santoro, S. V. Roth, P. Müller-Buschbaum
  Highly conductive PEDOT:PSS as electrode for flexible structured ITO-free organic electronics: A morphological study
  EuroTech ISPV meeting, Garching, 17 Jul 2013

- C. M. Papadakis
  Thermo-responsive amphiphilic di- and triblock copolymers: micelle formation, collapse and aggregation behavior and segmental dynamics
  Abschlusskolloquium SPP 1259 Intelligente Hydrogele, Aachen, 19 – 20 March 2013

- C. M. Papadakis, A. Sepe, J. Zhang, I. I. Potemkin, D.-M. Smilgies, D. Posselt
  What happens during solvent vapor treatment of block copolymer thin films – in-situ, real-time studies with grazing-incidence small-angle X-ray scattering
  XXIX Panhellenic Conference on Solid-State Physics and Materials Science, Athens, Greece, 22 – 25 Sep 2013

- C. M. Papadakis
  Solvent vapor treatment of nanostructured thin films - in-situ, real-time GISAXS studies
  GISAXS 2013, Hamburg, 07 – 09 Oct 2013

- C. M. Papadakis
  Micellar solutions and gels from thermoresponsive block copolymers - structures and their changes
  Lomonosov Moscow State University, Russia, 29 Nov 2013

- C. M. Papadakis
  Micellar solutions and gels from thermoresponsive block copolymers - structures and their changes
  University of Patras, Greece, 05 Dec 2013

- W. Petry
  Licht im Dunkel - Neutronen für Grundlagenforschung, Ingenieurswissenschaften und Medizin
  Think big – Großgeräte in der Physik, Symposium des BAdW Forums Technologie, 19 Apr 2013

- W. Petry
  Forschungsmöglichkeiten in allen Bereichen der Physik am FRM II
  Ringvorlesung des Physik-Departments der TU München: Einführung in Aspekte akuteller Forschung, München, 24 Apr 2013

- W. Petry
  Neutrons for functional materials
  CENEM Workshop, Erlangen, 18 Jun 2013

- W. Petry
  Neutrons for Energy
  Journées de la Diffusion Neutronique 21, Sète, France, 21 Jun 2013

- W. Petry
  Neutrons are (like) light
  Nobody's is perfect - Nanostructure in X-ray Light - Symposium in honor of the 80th birthday of Johann Peisl, 14 Sep 2013

- W. Petry
  Panel: Kerntechnik Made in Germany - Quo vadis?
  Podiumsdiskussion im Rahmen des DAtF Kompetenznetzwerks Hochschule und Forschung, 23 – 24 Sep 2013

- W. Petry
  Neutronen für Forschung, Medizin und Industrie
  ARD Wissenschafts-Journalisten, 24 Oct 2013

- M. Philipp, P. Müller-Buschbaum
  Thermoresponsive Polymere
  37. Edgar-Lüscher-Seminar: Physik von Zukunftsmaterialien, Zwiesel, 12 – 14 Apr 2013

- M. Philipp, P. Müller-Buschbaum
  GISAS in soft matter
  Workshop on Grazing Incidence Scattering Software, Garching, 9 – 10 Apr 2013

- M. Philipp, K. Kyriakos, W. Lohstroh, L. Silvi, C. M. Papadakis, P. Müller-Buschbaum
  Water dynamics at the demixing transition of PNIPAM solutions
  6th Internal Biannual Science Meeting, Grainau, 10 – 13 Jun 2013

- M. Philipp, P. Müller-Buschbaum
  Mechanical and structural instabilities around the volume phase transition of PNIPAM solutions
  Seminar of the Leibniz-Institut für Polymerforschung Dresden, Dresden, 18 Sep 2013

- M. Philipp, P. Müller-Buschbaum
  Introduction into FitGISAXS
  GISAXS 2013, Hamburg, 7 – 9 Oct 2013

- M. Philipp, J. K. Krüger, P. Müller-Buschbaum
  Immense elastic nonlinearities at transition phenomena in soft matter
  Seminar of the Institut de Sciences des Materiaux de Mulhouse, Mulhouse, France, 23 Oct 2013

- D. Posselt, M. Trapp, W. Lohstroh, C. M. Papadakis, T. Gutberlet
  Structure and dynamics of phospholipid membranes doped with 1-alkanols
  Third Annual Niels Bohr International Academy Workshop on ESS Science: Crossing Space and Time Domains with SAS and QENS, Copenhagen, Denmark, 24 – 28 Jun 2013

- G. G. Simeoni
  Critical and supercritical phenomena: structure by dynamics
  6th Internal Biannual Science Meeting, Grainau, 10 – 13 Jun 2013

- G. G. Simeoni, R. Valicu, N. Rasmussen, J. Weber, G. Borchert, P. Boeni, J. Neuhaus, W. Petry
  Focusing adaptive optics for neutron spectroscopy
  International Workshop on Neutron Optics and Detectors 2013, Ismaning, 2 – 5 Jul 2013

- G. G. Simeoni, R. Valicu, N. Rasmussen, J. Weber, G. Borchert, P. Boeni, F. Yang, F. Kargl, T. Kordel, D. Holland-Moritz, A. Meyer, J. Neuhaus, W. Petry
  Neutron spectroscopy under extreme-environment conditions
  ESS Science Symposium on Neutron Scattering at Extreme Conditions, Edinburgh, 5 – 6 Jul 2013

- G. G. Simeoni, S. Gepraegs, M. Opel, A. Mancini, L. Malavasi
  Exotic behaviour in novel manganites
  3rd International Workshop on McPhase, Berlin, 6 – 9 Aug 2013

- G. G. Simeoni, S. Gepraegs, M. Opel, A. Mancini, C. Milanese, L. Malavasi
  Chemical pressure effects in novel doped rare-earth manganites
  European High Pressure Research Group International Meeting EHPRG 51, London, 1 – 6 Sep 2013

- R. Tietze, S. Dürr, S. Lyer, N. Taccardi, P. Wasserscheid, L. Canella, F. Wagner, W. Petry, C. Alexiou
  Phantom studies of neutron capture of boron containing magnetic nanoparticles
  Biomed Tech, Berlin, Sep 2013

- N. Vishnevetskaya, M. Dyakonova, A. Bogomolova, S. K. Filippov, A. Miasnikova, C. M. Papadakis
  Polymeric nanoparticles for drug delivery
  5th Mamaself Status Meeting, Rigi Kulm, Switzerland, 21 – 24 May 2013

- Y. Yao, E. Metwalli, J.-F. Moulin, M. Haese-Seiller, P. Müller-Buschbaum
  Structure investigation of polymer-metal nanocomposite films using time-of-flight grazing incidence small angle neutron scattering
  DPG Frühjahrstagung, Regensburg, 10 – 15 Mar 2013

- J. Zhang
  Structural evolution of diblock copolymer thin films with perpendicular lamellae during solvent vapour treatment investigated by GISAXS
  SAXS/WAXS satellite workshop of DESY User Meeting, Hamburg, 24 – 25 Jan 2013

- J. Zhang, A. Sepe, D. Posselt, J. Perlich, D-M. Smilgies, and C. M. Papadakis
  Structural evolution in diblock copolymer thin films during solvent vapor treatment
  SAXS/WAXS satellite workshop of DESY User Meeting, Hamburg, 24 – 25 Jan 2013

- J. Zhang
  Structural evolution in diblock copolymer thin films during solvent vapor treatment investigated by GISAXS
  Cornell University, Ithaca NY, USA, 1 Mar 2013

- J. Zhang, A. Sepe, D. Posselt, J. Perlich, D.-M. Smilgies, and C. M. Papadakis
  GISAXS study of diblock copolymer thin films with perpendicular lamellar structure during solvent vapor treatment and drying
  DPG Frühjahrstagung, Regensburg, 10 – 15 Mar 2013

9.3 Posters

- J. Adelsberger, A. Kulkarni, I. Grillo, M. Sharp, A. M. Bivigou-Koumba, A. Laschewsky, P. Müller-Buschbaum, C. M. Papadakis
  Kinetics of aggregation in micellar solutions of thermoresponsive triblock copolymers: influence of concentration, start and target temperature
  DPG Frühjahrstagung, Regensburg, 10 – 15 March 2013

- D. Aravopoulou, M. Souli, K. Kyriakos, A. Miasnikova, C. M. Papadakis, A. Kyritsis
  Neutron scattering, dielectric and thermal studies on thermoresponsive polymers of complex architecture
  XXIX Panhellenic Conference on Solid-State Physics and Materials Science, Athens, Greece, 22 – 25 Sep 2013

- M. Dyakonova, M.-T. Popescu, N. Stavrouli, Z. Iatridi, C. Tsitsilianis, C. M. Papadakis
  Multiresponsive polymer networks studied by small angle neutron scattering
  6th Internal Biannual Science Meeting, Grainau, 10 – 13 Jun 2013

- M. Dyakonova, S. K. Filippov, P. Chytil, A. Bogomolova, A. Radulescu, C. M. Papadakis
  Structure and disintegration of nanoparticles from clinically relevant polymers
  European Polymer Congress of European Polymer Federation (EPF), Pisa, 16 – 21 Jun 2013

- M. Dyakonova, S. K. Filippov, P. Chytil, A. Bogomolova, A. Radulescu, C. M. Papadakis
  Structure and disintegration of nanoparticles from clinically relevant polymers
  Workshop "Fluorescence correlation spectroscopy in polymer science", Garching, 10 – 11 Oct 2013

- E. M. Herzig, K. Wagenbauer, V. Körstgens, W. Wang, Y. Yao, A. Buffet, S. V. Roth, P. Müller-Buschbaum
  Tuning of crystal Orientation in Organic Photovoltaics
  Spring School SPP1355, Weinböhla, 19 – 22 Mar 2013

- E. M. Herzig, K. Wagenbauer, M. Niedermeier, M. Rawolle, K. Sarkar, K. Scherer, J. Perlich, S. V. Roth, P. Müller-Buschbaum
  Three component organic photovoltaic systems
  Tag der Physikerin, Garching, 31 Jan 2013

- E. M. Herzig, A. R. Akhtar, P. Deimel, A. Naumann, C. M. Palumbiny, W. Wang, S. Guo, G. Tainter, J. Perlich, S. Yu, S. V. Roth, P. Müller-Buschbaum
  Control over crystallization and crystallite orientation in conducting polymer blend films
  DPG Frühjahrstagung, Regensburg, 10 – 15 Mar 2013

- E. M. Herzig, A. R. Akhtar, A. Naumann, S. Guo, G. Tainter, J. Zhang, J. Perlich, S. V. Roth, C. M. Papadakis, P. Müller-Buschbaum
  Influence of third polymeric component on OPV performance and morphology
  GISAXS 2013, Hamburg, 7 – 9 Oct 2013

- E. M. Herzig, A. R. Akhtar, A. Naumann, S. Guo, G. Tainter, J. Perlich, P. Müller-Buschbaum
  Influence of Third Polymeric component on OPV Performance and Morphology
  Soltech Workshop, Großhadern, 24 – 26 Jul 2013

- D. Jehnichen, D. Pospiech, G. He, P. Friedel, J. Zhang, C. M. Papadakis, J. Perlich
  Characterization of PPMA-PMMA block copolymer films with modified gold nanoparticles
  GISAXS 2013, Hamburg, Germany, 7 – 9 Oct 2013

- V. Körstgens, M. Philipp, S. V. Roth, P. Müller-Buschbaum
  Microfluidics and microGISAXS - nanoscopic in situ characterization at the solid-liquid interface
  DESY User Meeting, Hamburg, 24 – 25 Jan 2013

- V. Körstgens, D. Magerl, N. Paul, M. Philipp, J. Perlich, S. V. Roth, P. Müller-Buschbaum
  Early stages of nanoparticle attachment to polyelectrolyte layers - in-situ GISAXS investigations with microfluidics and dipcoating
  DPG Frühjahrstagung, Regensburg, 10 – 15 Mar 2013

- V. Körstgens, M. Philipp, S. V. Roth, P. Müller-Buschbaum
  Microfluidics and microGISAXS - nanoscopic in situ characterization at the solid-liquid interface
  DPG Frühjahrstagung, Regensburg, 10 – 15 Mar 2013

- V. Körstgens, M. Philipp, S. V. Roth, P. Müller-Buschbaum
  Microfluidics and microGISAXS - Nanoscopic in-situ characterization at the solid-liquid interface
  GISAXS 2013, Hamburg, 7 – 9 Oct 2013

- K. Kyriakos, M. Philipp, J. Adelsberger, S. Jaksch, A. Miasnikova, A. Laschewsky, I. Grillo, P. Müller-Buschbaum, C. M. Papadakis
  Conosolvency of PNIPAM in water/methanol mixed solutions
  DPG Frühjahrstagung, Regensburg, 10 – 15 March 2013

- K. Kyriakos, S. Ottinger, C. Psylla, A. Miasnikova, A. Laschewsky, P. Müller-Buschbaum, C. M. Papadakis
  Novel thermoresponsive polymers in various architectures
  DPG Frühjahrstagung, Regensburg, 10 – 15 March 2013

- L. Song, M. A. Niedermeier, P. Müller-Buschbaum
  Thin Films of Sponge-like Titania Nanostructures with Controllable Thickness
  DPG Frühjahrstagung, Regensburg, 10 – 15 Mar 2013

- L. Song, M. A. Niedermeier, P. Müller-Buschbaum
  Fabrication of sponge-like titania nanostructures by the combination of sol-gel synthesis
  3rd Colloquium of the Munich School of Engineering, Garching, 4 Jul 2013

- L. Song, M. A. Niedermeier, P. Müller-Buschbaum
  Fabrication of sponge-like titania nanostructures by the combination of sol-gel synthesis
  GISAXS 2013, Hamburg, 7 – 9 Oct 2013

- W. Lohstroh, L. Silvi
  Hydrogen Motion in $LiBH_4$
  International Conference on Neutron scattering, Edinburgh, UK 8 – 12 July 2013

- D. Magerl, X.-P. Qiu, F. M. Winnik, M. Rawolle, G. Herzog, S. V. Roth, P. Müller-Buschbaum
  A comparison of the morphology and thermoresponsive switching behavior in thin films of cyclic and linear PNIPAM
  GISAXS 2013, Hamburg, 7 – 9 Oct 2013

- E. Metwalli, V. Körstgens, A. Buffet, J. Perlich, K. Schlage, S. V. Roth, P. Müller-Buschbaum
  Millisecond time resolved GISAXS investigation of metal nanoparticles growth on soft and hard surfaces
  DESY User Meeting, Hamburg, 25 Jan 2013

- H. Morhenn, S. Busch, T. Unruh
  Molecular dynamics at the onset of self-diffusion
  ICNS 2013, Edinburgh, United Kingdom, 8 – 13 Jul 2013

- D. Moseguí González, C. Palumbiny, J. Perlich, S. V. Roth, P. Müller-Buschbaum
  Effect of patterning on film morphology and device performance of BHJ organic solar cells
  DPG Fr"uhjahrstagung, Regensburg, 10 – 15 Mar 2013

- D. Moseguí González, C. M. Palumbiny, M. A. Niedermeier, R. Meier, S. V. Roth, J. Perlich, P. Müller-Buschbaum
  Characerization of patterned polymer thin films for the application in organic photovoltaics using GISAXS
  GISAXS 2013, Hamburg, 7 – 9 Oct 2013

- S. Miyatsu, M. Kofu, M. Sadakiyo, T. Yamada, H. Kitagawa, M. Tyagi, V. Garcia-Sakai, G. Simeoni, W. Lohstroh, O. Yamauro
  Quasielastic neutron scattering study on dynamics of water and ammonia molecules confined in porous coordination polymers
  International Conference on Neutron scattering, Edinburgh, UK, 8 – 12 Jul 2013

- C. M. Palumbiny, C. Heller, C.J. Schaffer, V. Körstgens, G. Santoro, S. V. Roth, P. Müller-Buschbaum
  Highly conductive PEDOT:PSS as electrode for flexible structured ITO-free organic electronics: a morphological study
  Tag der Physikerin, Garching, 8 Feb 2013

- C. M. Palumbiny, C. Heller, C. J. Schaffer, V. Körstgens, G. Santoro, S. V. Roth, P. Müller-Buschbaum
  Highly conductive PEDOT:PSS as electrode for flexible structured ITO-free organic electronics: a morphological study
  Nanosystems for the solar cell, LMU, 24 – 26 Jul 2013

- C. M. Palumbiny, C. Heller, C. J. Schaffer, V. Körstgens, G. Santoro, S. V. Roth, P. Müller-Buschbaum
  Highly Conductive PEDOT:PSS as electrode for flexible structured ITO-free organic electronics: a morphological study
  Advanced Light Source (ALS) User Meeting, Berkleley, USA, 7 – 9 Oct 2013

- C. M. Palumbiny, C. Heller, C. J. Schaffer, V. Körstgens, G. Santoro, S. V. Roth, P. Müller-Buschbaum
  Highly conductive PEDOT:PSS as electrode for flexible structured ITO-free organic electronics: a morphological study
  Material Research Society (MRS) Fall Meeting, Boston, USA, 1 – 6 Dez 2013

- W. Petry
  Electronic correlations and structural transitions
  TRR80 Begutachtung, Augsburg, 16 – 17 Jul 2013

- M. Philipp, U. Müller, O. Astasheva, J. K. Krüger, P. Müller-Buschbaum
  Elastic anomalies at the volume phase transition of aqueous PNIPAM solutions
  Tag der Physikerin, Garching, 31 Jan 2013

- M. Philipp, U. Müller, R. Aleksandrova, R. Sanctuary, P. Müller-Buschbaum, J. K. Krüger
  About the elastic nature of the demixing transition of aqueous PNIPAM solutions
  DPG Frühjahrstagung, Regensburg, 10 – 15 Mar 2013

- S. Pröller, V. Körstgens, K. Sarkar, H. Iglev, P. Müller-Buschbaum
  Morphology studies for titania nanoparticle based hybrid solar cells
  DPG Frühjahrstagung, Regensburg, 10 – 15 Mar 2013

- S. Pröller, V. Körstgens, K. Sarkar, J. Werhahn, H. Iglev, P. Müller-Buschbaum
  Hybrid solar cells based on TiO_2-nanoparticles and water soluble polymer
  3rd Colloquium of the Munich School of Engineering, Garching, 4 Jul 2013

- S. Pröller, V. Körstgens, K. Sarkar, H. Iglev, P. Müller-Buschbaum
  New device setup for titania nanoparticle based hybrid solar cells
  6th Internal Biannual Science Meeting, Grainau, 10 – 13 Jun 2013

- C. Psylla, K. Kyriakos, S. Ottinger, A. Miasnikova, A. Laschewsky, P. Müller-Buschbaum, C. M. Papadakis
  Novel thermoresponsive polymers in various architectures
  6th Internal Biannual Science Meeting, Grainau, 10 – 13 Jun 2013

- M. Schindler, E. Metwalli, S. Roth, P. Müller-Buschbaum
  Growth kinetics of metal films sputtered on adhesive polymer films followed with in-situ GISAXS
  DPG Frühjahrstagung, Regensburg, 10 – 15 Mar 2013

- A. Sepe, D. Posselt, C. M. Papadakis
  Identification of good conditions for solvent vapor annealing of block copolymer thin films
  DESY User Meeting, Hamburg, 25 Jan 2013

- A. Sepe, D. Posselt, K. Swiatek, J. Zhang, S. Jaksch, R. Steinacher, J. Perlich, D. M. Smilgies, C. M. Papadakis
  Improvement of the lamellar structure in block copolymer thin films by solvent vapor treatment
  DPG Frühjahrstagung, Regensburg, 10 – 15 March 2013

- A. Sepe, D. Posselt, S. Jaksch, K. H. Swiatek, R. Steinacher, J. Zhang, J. Perlich, D.-M. Smilgies, C. M. Papadakis
  Guiding reorganization in block copolymer thin films on the nanoscale by judicious control of solvent vapor conditions
  GISAXS 2013, Hamburg, Germany, 7 – 9 Oct 2013

- L. Silvi, W. Lohstroh, G. Simeoni, J. Neuhaus, W. Petry
  A cold chopper spectrometer for the ESS
  DPG Frühjahrstagung, Regensburg, 10 – 15 Mar 2013

- L. Silvi, W. Lohstroh, J. Neuhaus, W. Petry
  Development of a cold chopper spectrometer
  International Conference on Neutron scattering, Edinburgh, UK, 8 – 12 July 2013

- L. Silvi, W. Lohstroh
  Hydrogen Dynamics in $LiBH_4$
  Gordon Research Conference: Hydrogen–Metal Systems, Lucca, Italy, 14 – 19 Jul 2013

- H. Sternschulte, I. Staudinger, C.M. Papadakis
  Grazing-incidence small-angle X-ray study on ultra nanocrystalline diamond films
  DESY User Meeting, Hamburg, 25 Jan 2013

- H. Sternschulte, I. Staudinger, A. Sepe, J. Perlich, S. V. Roth, S. Ghodbane, D. Steinmüller-Nethl, C. M. Papadakis
  Ultrananocrystalline diamond - a grazing-incidence small-angle X-ray scattering study
  GISAXS 2013, Hamburg, Germany, 7 – 9 Oct 2013

- B. Su, M. A. Niedermeier, M. Rawolle, P. Müller-Buschbaum
  Foam-like structures of titania films for application in hybrid photovoltaics
  DPG Frühjahrstagung, Regensburg, 10 – 15 Mar 2013

- B. Su, M. A. Niedermeier, M. Rawolle, P. Müller-Buschbaum
  Foam-like structures of titania films for application in hybrid photovoltaics
  SolTech Workshop, Würzburg, 11 – 13 Apr 2013

- B. Su, M. A. Niedermeier, M. Rawolle, L. Song, S. Bernstorff, P. Müller-Buschbaum
  Foam-like structures of titania films for application in hybrid photovoltaics
  3rd Colloquium of the Munich School of Engineering, Garching, 4 Jul 2013

- B. Su, M. A. Niedermeier, M. Rawolle, L. Song, S. Bernstorff, P. Müller-Buschbaum
  Foam-like structures of titania films for application in hybrid photovoltaics
  Nanosystems for Solar Energy Conversion, LMU Munich, 24 – 26 Jul 2013

- N. Vishnevetskaya, M. Dyakonova, A. Bogomolova, S. K. Filippov, A. Miasnikova, C. M. Papadakis
  Polymeric nanoparticles for drug delivery
  6th Internal Biannual Science Meeting, Grainau, 10 - 13 Jun 2013

- N. Vishnevetskaya, M. Dyakonova, A. Bogomolova, S. K. Filippov, A. Miasnikova, C. M.Papadakis
  Polymeric nanoparticles for drug delivery
  Workshop Fluorescence Correlation Spectroscopy in Polymer Science, Garching, 10 – 11 Oct 2013

- W. Wang, M. A. Ruderer, E. Metwalli, S. Guo, K. H. Scherer, S. V. Roth, J. Perlich, P. Müller-Buschbaum
  The morphology of flexible all polymer solar cell
  Tag der Physikerin, Garching, 31 Jan 2013

- W. Wang, M. Philipp, D.Magerl, J.-F. Moulin, P. Müller-Buschbaum
  The influence of processing additives on the morphology of bulk herterojunction films
  DPG Frühjahrstagung, Regensburg, 10 – 15 Mar 2013

- W. Wang, M. Philipp, D. Magerl, E. M. Herzig, J.-F.Moulin, P. Müller-Buschbaum
  The influence of processing additives on the morphology of bulk heterojunction films in organic photovoltaics
  3rd Colloquium of the Munich School of Engineering, Garching, 4 Jul 2013

- Y. Yao, E. Metwalli, J.-F. Moulin, P. Müller-Buschbaum
  Magnetic nanoparticles embedded in thin block copolymer films
  Tag der Physikerin, Garching, 31 Jan 2013

- J. Zhang, D. Posselt, A. Sepe, X. Shen, J. Perlich, D. M. Smilgies, C. M. Papadakis
  Structural evolution of perpendicular lamellae in diblock copolymer thin films during solvent vapor treatment investigated by grazing-incidence small-angle X-ray scattering
  GISAXS 2013, Hamburg, 7 – 9 Oct 2013

9.4 Invited talks at the chair

- Dr. Anastasia Malliopoulou, Aristotle University of Thessaloniki, Greece
  Applications of PV systems in Greek market from my experienced point of view
  16 Jan, 2013

- Prof. Igor I. Potemkin, Lomonosov Moscow State University, Russia
  Control of nanodomains orientation in block copolymer films
  11 Feb 2013

- Dr. Theo Lohmüller, Ludwig-Maximilians-Universität München
  Nanolithography by plasmonic heating and optical manipulation of gold nanoparticles
  15 May 2013

- Thomas Zinn, Jülich Centre for Neutron Science, Jülich
  Time-resolved small-angle neutron scattering: probing kinetics on the nanoscale
  22 May 2013

- Priv.-Doz. Dr. Doris Pospiech, Institute for Polymer Research (IPF), Dresden
  Methacrylate-based block copolymers as platform for nanostructured materials and hybrids
  29 May 2013

- Dr. Sergey Filippov, Institute of Macromolecular Chemistry, Czech Academy of Sciences, Prague
  A comprehensive study of the inner structure of a highly efficient drug delivery systems: macromolecular HPMA-based nanoparticles with cholesterol for solid-tumor targeting
  5 Jun 2013

- Dr. Heide Götz, European Patent Office, and Dr. Florian Siebel, DPMA
  Seminar on research possibilities in Espacenet (European Patent Office) and Depatisnet (German Patent Office)
  19 June, 2013

- Prof. Dr. Dina Fattakhova-Rohlfing, Ludwig-Maximilians-Universität München
  Metal oxide nanoarchitectures for energy conversion and storage
  26 Jun 2013

- Prof. Costas Tsitsilianis, University of Patras, Greece
  Injectable hydrogels from model responsive macromolecules
  2 Jul 2013

- Dr. Dominik Wöll, Zukunftskolleg/Fachbereich Chemie, Universität Konstanz
  Diffusion of single molecules and single particles in polymer systems studied with fluorescence microscopy
  3 Jul 2013

- Miriam Engel, Department Nanostrukturtechnik, Universität Duisburg-Essen
  Reduced Coulomb interaction in organic semiconductors for the use in solar cells
  Jul 10, 2013

- Gülayse Gürsoy, Marmara University, Istanbul, Turkey
  Applications of low pressure plasmas in different branches of industries
  17 Jul 2013

- Dr. Jean-Francois Moulin, HZG at MLZ, Garching
  REFSANS instrument and data handling
  31 Jul 2013

- Dr. Anatoly Berezkin, MPI für Eisenforschung, Düsseldorf
  Reaction-induced microphase separation at the interface between two reactive polymer melts
  14 Oct 2013

- Prof. Alfons Schulte, University of Central Florida, Orlando, USA
  Micro-spectroscopic approaches to soft matter
  15 Oct 2013

- Steffen Säubert, Forschungs-Neutronenquelle Heinz Maier-Leibnitz, Garching
  Isothermal Transformation Kinetics in Uranium Molybdenum Alloys
  30 Oct 2013

- Lorenz Sykora, Technical University of Denmark and TUM
  Fabrication and optimization of micro- and nanostructured surfaces. First results and further steps
  31 Oct 2013

- Dr. Ilja Gunkel, Lawrence Berkeley National Lab, USA
  In situ GISAXS studies of block copolymer thin films during solvent vapor annealing
  6 Nov 2013

- Prof. Apostolos Kyritsis, National Technical University of Athens, Greece
  Hydration studies in polymer hydrogels - The input of dielectric measurements
  12 Nov 2013

- Irina Mitina, FH Düsseldorf
  Review on studying and international research activity in the field of solar energy
  13 Nov 2013

- Stefan Huber, Technische Universität München
  Thermische Analyse von Polymeren
  20 Nov 2013

- Ida Berts, Ludwig-Maximilians-Universität München
  Hyaluronan gels, composites, and coatings studied with SANS and neutron reflectometry
  27 Nov 2013

- Dr. Matthias Ruderer, BMW Group, Munich
  Elastomers in automotive applications
  4 Dec 2013

- Dr. Stefan Guldin, Ecole Polytechnique Fédérale de Lausanne, Switzerland
  Soft matter self-assembly as a design tool for inorganic photonic nanoarchitectures
  11 Dec 2013

- Priv.-Doz. Dr. Thomas Gruhn, Universität Bayreuth
  Phase behavior of polymer blends with reversible crosslinks – A self-consistent field theory study
  18 Dec 2013

- Bruno Baumeister, MLZ, Garching
  Construction, commissioning and characterization of a sputtering device for the production of cylindrical targets for 99Mo production
  18 Dec 2013

9.5 Funding

Deutsche Forschungsgemeinschaft:

- Within DFG priority program SPP 1259:
  Struktur und Kinetik stimuli-responsiver, dünner Hydrogelfilme aus amphiphilen Blockcopolymeren
  Grant Number: MU 1487/8-3
  Project Leader: Prof. Dr. Peter Müller-Buschbaum

- Within DFG priority program SPP 1355:
  Controlled morphologies by molecular design and nano-embossing
  Grant Number: MU 1487/13-3
  Project Leader: Prof. Dr. Peter Müller-Buschbaum

- *Zweifach und orthogonal schaltbare Blockcopolymere aus zwitterionischen und thermoresponsiven Blöcken: Synthese und Strukturen in Lösung und im dünnen Film*
  Grant Number: MU 1487/17-1
  Project Leader: Prof. Dr. Peter Müller-Buschbaum

- *In-situ Untersuchungen zu Kondensation, Nukleation und Wachstum von Metallfilmen und Nanostrukturen auf organischen Oberflächen während Sputterbeschichtung*
  Grant Number: MU 1487/18-1
  Project Leader: Prof. Dr. Peter Müller-Buschbaum

- *In-situ Eigenspannungsanalyse an Verbundgusskörpern mittels Neutronendiffraktometrie*
  Grant Number: PE 580/12-1
  Project Leader: Prof. Dr. Winfried Petry

- *In-situ-Messung deformationsinduzierter Martensitbildung in ausferritischem Gusseisen (ADI)*
  Grant Number: PE 580/14-1
  Project Leader: Prof. Dr. Winfried Petry

- Within DFG priority program SPP 1259:
  Struktur und Kinetik stimuli-responsiver, dünner Hydrogelfilme aus amphiphilen Blockcopolymeren
  Grant Number: PA 771/4-3
  Project Leader: Prof. Dr. Christine Papadakis

- *Structural changes in block copolymer thin films during solvent vapor treatment*
  Grant Number: PA 771/10-1
  Project Leader: Prof. Dr. Christine Papadakis

- *Zweifach und orthogonal schaltbare Blockcopolymere aus zwitterionischen und thermoresponsiven Blöcken: Synthese und Strukturen in Lösung und im dünnen Film*
  Grant Number: PA 771/14-1
  Project Leader: Prof. Dr. Christine Papadakis

Bundesministerium für Bildung und Forschung:

- *MiNaXS-Microfluidik: Entwicklung und Aufbau des Mikrofluidik Messplatzes am Instrument MiNaXS am Synchrotron PETRA III*
  Grant Number: 05K10WOA
  Project Leader: Prof. Dr. Peter Müller-Buschbaum

Bayerisches Staatsministerium für Bildung und Kultus, Wissenschaft und Kunst:

- Im Rahmen der Munich School of Engineering (MSE):
  Solar Technologies Go Hybrid (SolTech) - Forschungsnetzwerk TUM.solar
  Project Leader: Prof. Dr. Peter Müller-Buschbaum
- Im Rahmen der Munich School of Engineering (MSE): Netzwerk Regenerative Energien
  Aufbau eines interdisziplinären Netzwerks aus Lehrstühlen der Technischen Universität München und anderen Forschungseinrichtungen zur Förderung der Forschungsaktivitäten im Bereich der regenerativen Energien
  Project Leader: Prof. Dr. Peter Müller-Buschbaum
- Seedfunding im Rahmen der Energy Valley Bavaria (Munich School of Engineering, MSE)
  Tailored TCO nanostructures for PV applications (Tailor TCO)
  Project Leader: Prof. Dr. Peter Müller-Buschbaum
- Nachwuchsgruppe im Rahmen des Energy Valley Bavaria (Munich School of Engineering, MSE)
  Organische Photovoltaik
  Project Leader: Dr. Eva M. Herzig

Others:

- Im Rahmen des Internationalen Graduiertenkollegs: Material Science of Complex Interfaces (CompInt)
  Degradation und Alterung in Polymeren Mischungsfilmen für die Photovoltaik
  Project Leader: Prof. Dr. Peter Müller-Buschbaum
- Im Rahmen des Internationalen Graduiertenkollegs: Material Science of Complex Interfaces (CompInt)
  Strukturelle Änderungen in nanostrukturierten Blockcopolymerfilmen - Zeitaufgelöste in-situ-Untersuchungen mit Röntgenkleinwinkelstreuung unter streifendem Einfall
  Project Leader: Prof. Dr. Christine Papadakis
- Forschungskooperation mit der Freien Universität Berlin
  Organic and hybrid photovoltaic devices for Energy and Biomedical applications
  Project Leader: Prof. Dr. Peter Müller-Buschbaum; Co-Project Leader: Prof. Dr. Martha Ch. Lux-Steiner

- Forschungskooperation mit Kao Corporation, Japan
  Analysis of the near-surface composition profile of water-sensitive adhesive polymer films
  Project Leader: Prof. Dr. Peter Müller-Buschbaum

- Im Rahmen des Exzellenzclusters Nanosystems Initiative Munich (NIM)
  Nanosystems for Energy Conversion
  Pricipal Investigator: Prof. Dr. Peter Müller-Buschbaum

- Forschungskooperation mit der Technischen Universität Dresden
  Untersuchung der Mineralisierung organischer Moleküle mit Neutronenkleinwinkelstreuung zum Verständnis der Verstopfung von Membranfiltern bei der Aufbereitung von Abwässern
  Project Leader: Prof. Dr. Wohlfgang Uhl (Technische Universität Dresden); Co-Project Leader: Prof. Dr. Winfried Petry, Dr. Dietmar Schwahn

- Im Rahmen des Projektbezogenen Personenaustauschs mit Tschechien (Deutscher Akademischer Austausch Dienst, DAAD)
  Klinisch relevante makromolekulare Nanopartikel mit Cholesterin
  Project Leader: Prof. Dr. Christine Papadakis; Co-Project Leader: Dr. Sergey Filippov (Institute of Macromolecular Chemistry of Academy of Sciences of the Czech Republic, IMC).

- Im Rahmen des Projektbezogenen Personenaustauschs mit Griechenland (Deutscher Akademischer Austausch Dienst, DAAD
  Stimuli-responsive hydrogels from model associative block copolymers
  Project Leader: Prof. Dr. Christine Papadakis; Co-Project Leader: Prof. Constantinos Tsitsilianis (University of Patras)

- Im Rahmen des Bayerischen Hochschulförderprogramms zur Anbahnung internationaler Forschungskooperationen
  Novel smart amphiphilic polymers of complex architecture
  Project Leader: Prof. Dr. Christine Papadakis; Co-Project Leader: Prof. Apostolos Kyritsis (National Technical University of Athens, NTUA)

Technische Universität München:

- Im Rahmen der International Graduate School of Science and Engineering (IGSSE)
  Interface Science for Photovoltaics - a EuroTech GreenTech Initiative
  Project Leader: Prof. Dr. Peter Müller-Buschbaum

10 The chair

10.1 Staff

Chair: Prof. Dr. Winfried Petry

Head: Prof. Dr. Peter Müller-Buschbaum

Professor:

Prof. Dr. Christine Papadakis

Fellows:

Dr. Eva M. Herzig
Dr. Volker Körstgens
Dr. Wiebke Lohstroh
Dr. Ezzeldin Metwalli Ali
Dr. Jürgen Neuhaus
Dr. Martine Philipp
Dr. Dietmar Schwahn
Dr. Giovanna Giulia Simeoni
Dr. Jianqi Zhang

PhD students:

Hsin-Yin Chiang
Margarita Dyakonova
Fabian Fuchs
Shuai Guo
Tobias Hollmer
Tanja Huber
Sebastian Jaksch
Konstantinos Kyriakos
Xiaohu Li
David Magerl
Humphrey Morhenn
Daniel Moseguí González
Martin Niedermeier
Claudia Palumbiny
Monika Rawolle
Yichuan Rui
Kuhu Sarkar
Christoph Schaffer
Robert Schenk
Markus Schindler
Martin Schmiele
Luca Silvi
Lin Song
Christian Steyer
Bo Su
Natalya Vishnevetskaya
Weijia Wang
Stephan Wlokka
Yuan Yao
Tobias Zweifel

Diploma students:

Simon Brunner
Christoph Heller
Weiguo Lu
Daniel Moseguí González
Christian Reiter

Master students:

Lukas Augsbach
Bruno Baumeister
Erik Braden
Herbert Caller
Biye Cao
Sebastian Günther
Ali Hassan
Nuri Hohn
Christian Jendrzejewski
Che-Hung Lin
Wei Liu
Avishek Maity
Felipe Martinez
Christoph Mayr
Stephan Pröller
Christina Psylla
Majid Rasool
Johannes Schlipf
Xuhu Shen
Gregory D. Tainter
Rosa Maria Torrademe
Natalya Vishnevetskaya
Rui Wang
Tobias Widmann
Xiaohan Zhang

Bachelor students:

Melis Aça
Marc Appleton
Jessica Böhm
Tobias Buchmann
Francisco Caballero
Constantin Dory
Alex Gustschin
Andreas Heine
Manuel Koller
Stefan Pogorzalek
Javier Roldán
Josef Sapper
Sebastian Simeth
Jochen Wolf

Students assistants:

Ali Aghebat Rafat
Erik Braden
Manuela Heiß
Che-Hung Lin
Evangelos Makrygiannis
Anna Naumann
Christina Psylla
Sebastian Simeth

Technical/administrative staff:

Erik Faber
Susanna Fink
Reinhold Funer
Raffael Jahrstorfer
Josef Kaplonski
Matthias Maier
Dieter Müller
Jandal Ringe
Marion Waletzki

10.2 Graduations

- **Accomplished PhD theses**

  Monika Rawolle
  Structuring and filling of titania films for applications in photovoltaics

  Robert Schenk
  Development of Umo powder production for use in high density uranium fuel

  Sebastian Jaksch
  Phasenverhalten von Poly(2-Oxazolinen) in wässriger Lösung

  Martin Niedermeier
  Novel structuring routines of titania films for application in photovoltaics

- **Accomplished diploma theses**

  Daniel Moseguí-González
  Micro- and nanostructuring of thin film layers for the application in organic photovoltaics

  Jan Christoph Heller
  Kontrollierte Morphologien durch molekulares Design und Nanostrukturierung für die Anwendung in der organischen Photovoltaik

  Weiguo Lu
  Mesostrukturierte Hybridsolarzellen

  Christian Reiter
  Methodenentwicklung, Kalorimetrie und Messen der Dichte von hochdichten Kernbrennstoffen

  Simon Brunner
  Blockcopolymere für Anwendungen als Feststoffelektrolyte in der Energiespeicherung

- **Accomplished master theses**

  Xuhu Shen
  GISAXS Simulation of Complex Lamellar Structure

  Gregory D. Tainter
  Microstructuring of inorganic-organic hybrid materials for application in photovoltaics

  Natalya Vishnevetskaya
  Polymeric nanoparticles for drug delivery

  Rui Wang
  Hybrid Solar Cells based on ZnO Nanostructures

  Stephan Pröller
  Structure and Function of Nanoparticle-Based Hybrid Solar Cells

  Christian Jendrzejewski
  Systematic investigation on ternary bulk heterojunction solar cells based on PTB7:PC70BM

  Che-Hung Lin
  Cononsolvency in Self-Assembled Thermo-Responsive Polymers

  Steffen Säubert
  Time Temperature Transformation Kinetics of Uranium Molybdenum Alloys

  Bruno Baumeister
  Construction, commissioning and characterization of a sputtering device for the production of cylindrical targets for 99Mo production

- **Accomplished bachelor theses**

  Jochen Wolf
  Realizing flexibility and artificial structures for organic solar cells

  Marc Appleton
  Ternary systems for application in organic photovoltaics

  Andreas Heine
  Intelligent materials - stimuli-responsive reversible hydrogels from triblock polyelectrolytes

  Sebastian Simeth
  Verteilung von Wasserstoff in ultrananokristallinen Diamantschichten -Strukturbestimmung mit Kleinwinkelneutronenstreuung

  Tobias Buchmann
  Nanoparticles via laser ablation for solar cells

  Manuel Koller
  Kontrolle der Adhäsion durch Oberflächenanreicherung

  Constantin Dory
  Polymer based thin films for new concepts of energy storage

  Alexander Gustschin
  Cobalt metal grown in block copolymer films via in-situ thermal reduction of metal ions

  Stephan Pogorzalek
  Tailoring ZnO nanostructures for hybrid solar cells

  Francisco Caballero
  Impact of aluminum contact deposition parameters on the metal-organic interface of polymer solar cells measured by X-ray reflectivity

  Javier Roldán
  Influence of aluminum contact deposition parameters on the characteristics of polymer solar cells

  Dominik Weidlich
  Bestimmung der Tiefendosis bei einer epidermalen Radioisotopentherapie mit Rhenium -188

  Matthias Knoelker
  Aufbau eines Reaktornetzwerkes zur Bestrahlung von Ho-166- Microspheres für Selektive Interne Radiotherapie (SIRT)

  Matthias Dodenhöft
  Metallurgraphische Untersuchung von Umo

10.3 Guests

- Dr. Anastasia Malliopoulou, University of Thessaloniki, Greece
  16 Jan 2013
- Prof. Dorthe Posselt, Roskilde University, Denmark
  25 - Jan - 05 Feb 2013
- Prof. Igor I. Potemkin, Andrey Rudov, Lomonosov Moscow State University, Russia
  11 Feb 2013
- Wycliffe Kipnusu, University of Leipzig
  07 Feb 2013, 29-30 April 2013
- Priv.-Doz. Dr. Doris Pospiech, Institut für Polymerforschung, Dresden
  29 May 2013
- Dr. Sergey Filippov, Dr. Jiri Panek, Anna Bogomolova, Institute of Macromolecular Chemistry, Academy of Sciences of the Czech Republic, Prague
  03-07 Jun 2013
- Prof. Costas Tsitsilianis, University of Patras, Greece
  29 Jun - 6 Jul 2013
- Dr. Dominik Wöll, Universität Konstanz
  3 Jul 2013
- Prof. Dr. Alfons Schulte, University of Central Florida, Orlando, USA
  since 16 Aug 2013
- Rina Iikubo, Kao Corporation, Tokyo, Japan
  01 Sep 2012 – 31 Aug 2013
- Dr. Neelima Paul
  1 Oct 2011 – 31 Aug 2013
- Dr. Anatoly Berezkin, MPI für Eisenforschung, Düsseldorf
  14 Oct 2013
- Prof. Walter Richtering, RWTH Aachen
  28/29 Oct 2013
- Katerina Bikas, National Technical University of Athens
  29 Oct – 30 Nov 2013
- Teodoa Popescu, National Technical University of Athens
  11-15 November 2013
- Kostas Raftopoulos, National Technical University of Athens
  11-14 November 2013
- Prof. Apostolos Kyritsis, National Technical University of Athens
  12-15 November 2013
- Jiří Pánek, Anna Bogomolova, University of Prague
  9 - 14 Dec 2013

- Prof. Thomas Gruhn, Universität Bayreuth
  18 Dec 2013